ELECTROMECHANICS MODELLING OF THE EFFECTS OF MYOCARDIAL INFARCTION ON LEFT VENTRICULAR REMODELLING

LEONG CHIN NENG

FACULTY OF ENGINEERING
UNIVERSITY OF MALAYA
KUALA LUMPUR

2020

ELECTROMECHANICS MODELLING OF THE EFFECTS OF MYOCARDIAL INFARCTION ON LEFT VENTRICULAR REMODELLING

LEONG CHIN NENG

THESIS SUBMITTED IN FULFILMENT OF THE REQUIREMENTS FOR THE DEGREE OF DOCTOR OF PHILOSOPHY

FACULTY OF ENGINEERING
UNIVERSITY OF MALAYA
KUALA LUMPUR

2020

UNIVERSITY OF MALAYA

ORIGINAL LITERARY WORK DECLARATION

Name of Candidate: **Leong Chin Neng**

Matric No: **HHC 130015**

Name of Degree: **Doctor of Philosophy**

Title of Project Paper/Research Report/Dissertation/Thesis ("this Work"):

Electromechanics Modelling of the Effects of Myocardial Infarction on Left Ventricular Remodelling

Field of Study: **Biomedical engineering**

I do solemnly and sincerely declare that:

(1) I am the sole author/writer of this Work;
(2) This Work is original;
(3) Any use of any work in which copyright exists was done by way of fair dealing and for permitted purposes and any excerpt or extract from, or reference to or reproduction of any copyright work has been disclosed expressly and sufficiently and the title of the Work and its authorship have been acknowledged in this Work;
(4) I do not have any actual knowledge nor do I ought reasonably to know that the making of this work constitutes an infringement of any copyright work;
(5) I hereby assign all and every rights in the copyright to this Work to the University of Malaya ("UM"), who henceforth shall be owner of the copyright in this Work and that any reproduction or use in any form or by any means whatsoever is prohibited without the written consent of UM having been first had and obtained;
(6) I am fully aware that if in the course of making this Work I have infringed any copyright whether intentionally or otherwise, I may be subject to legal action or any other action as may be determined by UM.

Candidate's Signature Date:

Subscribed and solemnly declared before,

Witness's Signature Date:

Name:

Designation:

ELECTROMECHANICS MODELLING OF THE EFFECTS OF MYOCARDIAL INFARCTION ON LEFT VENTRICULAR REMODELLING

ABSTRACT

Myocardial infarction (MI) is one of the diseases with the highest mortality rate. Following MI, myocardium experiences abrupt changes in its loading condition due to the presence of infarct. In response to such changes, myocytes undergo adaptations to maintain homeostasis. However, maladaptation can happen and lead to remodelling, in which the left ventricle (LV) gradually loses its function and eventually turns into heart failure. Nevertheless, the mechanisms underlying LV remodelling are still poorly understood. In this study, a generic LV model was developed, incorporating realistic fibre orientation and excitable contracting myocardium. It was demonstrated that the developed model is capable of reproducing physiological LV functions, including action potential propagation, LV pressure and cavity volume, LV twisting and wall thickening. Subsequently, the generic LV model was utilised to investigate the effects of the infarct state on LV regional mechanics, including the interaction between non-contractile infarct and contractile myocardium. It was found that infarct transmural extent (TME) is more important than infarct size in determining LV regional mechanics impairments. Neighbouring contractile myocardium and non-contractile infarct induce a mechanical tethering effect, which elevates with infarct TME, at the border zone (BZ). Such mechanical tethering causes the BZ to have high systolic fibre stress, elevated energy expenditure and reduced myocardial energy efficiency, which are believed to give rise to infarct extension. The generic LV model was then modified into a patient-specific model, incorporating patient-specific infarcted LV geometry and optimised regional material properties, to study the correlation between infarct extension and myocardial mechanics impairments, including the underlying mechanisms responsible for the impairments. Among the observed myocardial mechanics impairments, only the

depressed myocardial energy efficiency was found to be correlated with infarct extension. The depressed myocardial energy efficiency was due to inadequate generation of contraction force, which, at least in part, owing to inadequate stretching of myocardium at end-diastole (the Frank-Starling law). Although a stiff infarct can prevent infarct expansion, results of this study showed that it can also cause the neighbouring myocardium to be under stretched at end-diastole, thereby depressing the generated contraction force and energy efficiency during systole, which were found to be correlated with infarct extension of the neighbouring myocardium.

Keywords: myocardial infarction, infarct TME, LV regional mechanics, LV remodelling, infarct extension.

PEMODELAN ELEKTROMEKANIK KESAN-KESAN PENGINFARKAN MIOKARDIUM TERHADAP PEMODELAN SEMULA VENTRIKEL KIRI

ABSTRAK

Penginfarkan miokardium (PM) merupakan salah satu penyakit dengan kadar kematian tertinggi. Selepas PM, keadaan bebanan miokardium mengalami perubahan yang drastik disebabkan oleh kewujudan infark. Sebagai tindak balas terhadap perubahan tersebut, miosit mengalami penyesuaian demi mengekalkan homeostasis. Tetapi, salah penyesuaian boleh berlaku dan menyebabkan pemodelan semula, di mana ventrikel kiri (VK) semakin menghilangi fungsi-fungsinya, sehingga -sampai ke tahap kegagalan jantung. Walaupun demikian, pemahaman terhadap mekanisma yang menyebabkan pemodelan semula VK masih tidak mencukupi. Dalam kajian ini, satu model VK umum telah dibina, menggabungkan orientasi serat dan pengecutan miokardium yang realistik. Model VK tersebut telah ditunjukkan berkemampuan untuk mereplikasikan fungsi-fungsi VK secare fisiologi, termasuk penyebaran aksi potensi, tekanan and isipadu VK, pemutaran dan penebalan dinding VK. Seterusnya, model VK umum ini digunakan untuk menyiasat kesan-kesan keadaan infark terhadap mekanik serantau VK, termasuk interaksi antara infark tidak berkontraksi dan miokardium berkontraksi. Ia didapati bahawa transmural infark lebih penting daripada saiz infark dalam menentukan kerosakan mekanik serantau VK. Miokardium berkontraksi dan infark tidak berkontraksi bersebelahan mendorongi satu kesan tambatan mekanikal, yang mana meningkat dengan peningkatan transmural infark, di zon sempadan (ZS). Tambatan mekanikal tersebut mengakibatkan ZS mengalami stres pengecutan serat yang tinggi, peningkatan penggunaan tenaga miokardium dan penurunan kecekapan tenaga myokardium, yang dipercayai akan menyebebkan pelanjutan infark. Model VK umum tersebut kemudiannya diubahsuai menjadi model berkhusus pesakit, menggabungkan geometri VK berinfark berkhusus pesakit dan sifat-sifat bahan serantau

yang telah dioptimumkan, demi mengaji perhubungan antara pelanjutan infark dan kerosakan mekanik miokardium, termasuk mekanisma yang mengakibatkan kerosakan tersebut. Antara kerosakan mekanik miokardium yang dijumpai, hanya penurunan kecekapan tenaga myokardium yang didapati berkait dengan pelanjutan infark. Penurunan kecekapan tenaga myokardium ini berpunca daripada penghasilan daya kontraksi yang tidak mencukupi, yang mana sekurang-kurangnya, disebabkan oleh peregangan miokardium yang tidak mencukupi pada diastolik akhir (hukum Frank-Starling). Walaupun infark yang liat dapat menolong dalam pencegahan pengembangan infark, ia didapati boleh manjadikan miokardium bersebelahan berada dalam keadaan beregangan rendah, seterusnya menurunkan penghasilan daya kontraksi dan kecekapan tenaga, yang mana didapati berkait dengan pelanjutan infark di miokardium bersebelahan tersebut.

Kata kunci: penginfarkan miokardium, transmural infark, mekanik serantau VK, pemodelan semula VK, pelanjutan infark.

ACKNOWLEDGEMENTS

First of all, I would like to express my utmost gratitude to my supervisors: Associate Professor Lim Einly, Associate Professor Socrates Dokos and Associate Professor Andri Andriyana, for their guidance throughout this project. Their expertise, invaluable insights and encouragement greatly helped me overcame challenges encountered in this study.

I would also like to thank Scientia Professor Nigel H. Lovell, Dr. Liew Yih Miin and Dr. Amr Al Abed for giving their intellectual support and feedback on many key works in this project. My heartfelt gratitude is also extended to the collaborators involved in this study: Professor Yang Faridah Abdul Aziz, Professor Chee Kok Han, Dr. Sridhar, Siti Salwa and Mohd Azwan, for their expertise and assistance in collecting the much needed clinical data for this project. This project would not be accomplished without their professional support.

Special thanks go to my colleagues, both at University of Malaya (UM) and University of New South Wales (UNSW), especially Chan Bee Ting, Jamil Mokhtar, Wan Naimah, Azam Ahmad Bakir, Leong Chen Onn, Guo Tianruo, Ng Chun Yi, Khalid Alonazi, Yousef Alharbi and Abdulrahman Alqahtani. It is my pleasure to work with all of you. I would also like to express my acknowledgement to the postgraduate coordinator of the Graduate School of Biomedical Engineering (GSBME), UNSW, Associate Professor Megan Lord, and the management teams of Faculty of Engineering UM, GSBME UNSW and Institute for Advanced Studies UM, for sorting out the administrative issues faced during my candidature.

I am also grateful to Malaysia Hall Sydney for providing me a comfortable accommodation during my time in Sydney, which served as a relief for stress and homesickness while I was thousands of miles away from my homeland. Not forgetting

also MyPhD scholarship and IPS Dual PhD Fund, for giving me a golden opportunity to take up this Joint PhD program.

Last, but not the least, my greatest gratitude to my family, girlfriend, friends and housemates. Thank you for giving me your moral support and patience, a heaven for my emotional relief.

TABLE OF CONTENTS

LIST OF FIGURES

LIST OF TABLES

LIST OF SYMBOLS AND ABBREVIATIONS

List of Symbols

C_0	material overall stiffness
C_p	Windkessel model peripheral capacitance
d	distance
D	electrical conductivity
$\hat{\mathbf{e}}$	tangent basis vector
E	Green-Lagrange strain tensor
f, s and r	fibre, sheet and radial components respectively
G	reciprocal of distance
i, j and k	local orthogonal coordinate system axis components
I	dimensionless slow inward current
I_s	dimensionless external stimulus current
J	determinant of deformation gradient tensor
k_0	spring constant per unit area
p	Lagrangian multiplier
P_A	arterial blood pressure
P_{LV}	left ventricular pressure
Q_A	blood ejection rate
$\mathbf{r}$	rigid transformation matrix
R_c	Windkessel model aortic root impedance
R_p	Windkessel model peripheral impedance
$\mathbf{R}$	rotational matrix
S	second Piola-Kirchhoff stress tensor
$S^m_{m\cap n}$	intensity profile of intersection line on slices m and n

t	time
t_s	local active contraction time
t_x, t_y and t_z	translations along x, y and z axes respectively
$\mathbf{t}$	translation vector
T_0	active stress parameter
T_a	active stress
$\mathbf{u}_c$, $\mathbf{u}_l$ and $\mathbf{u}_r$	circumferential, longitudinal and radial base unit vectors respectively
$\mathbf{v}$	image voxel vector
V	dimensionless transmembrane potential
V_{LV}	left ventricular cavity volume
W	strain energy function
$W_{m\cap n}$	intensity of ROI mask at the intersection line of slices m and n
β	transmurality index
δ	Kronecker delta
ζ	distance between actual and reference geometries
θ	myocardial fibre angle
λ	sarcomere length
λ_0	reference sarcomere length
$\mu S^m_{m\cap n}$	mean of $S^m_{m\cap n}$
ϕ_x, ϕ_y and ϕ_z	rotation about x, y and z axes respectively
χ	infarct index
Ψ	material properties
ω	work density

List of Abbreviations

$[Ca^{2+}]_i$	free intracellular Ca^{2+} concentration
ACE	angiotensin converting enzyme
AP	action potential
AV	atrioventricular
BZ	border zone
Ca^{2+}	calcium ions
CICR	Ca^{2+}-induced Ca^{2+}-release
CMR	cardiac magnetic resonance imaging
CO	cardiac output
DT	diffusion tensor
EC	excitation-contraction
ECM	extracellular matrix
EDPVR	end-diastolic pressure-volume relationship
EDV	end-diastolic volume
EF	ejection fraction
ESPVR	end-systolic pressure-volume relationship
ESV	end-systolic volume
FE	finite element
FSSL	fibre stress-strain loop
I_{Ca}	inward Ca^{2+} current
IVC	isovolumic contraction
IVR	isovolumic relaxation
IZ	infarct zone
K^+	potassium ions
L-TR	large and transmural infarct model

L-XTR	large but nontransmural infarct model
LA	left atrium
LGE	late gadolinium enhancement
LV	left ventricle
LX	long axis
MI	myocardial infarction
MMP	matrix metalloproteinase
MMP-1	interstitial collagenase
MT-MMP	membrane type matrix metalloproteinase
Na^+	sodium ions
NCX	Na^+/Ca^{2+} exchange channel
NORMAL	healthy LV model
NPR	non-perfused region
OBJ	objective function
ODE	ordinary differential equation
P_{SYS}	peak systolic pressure
PDE	partial differential equation
PR	perfused region
PV	pressure-volume
RA	right atrium
ROI	region of interest
ROS	reactive oxygen species
RV	right ventricle
RZ	remote zone
S-TR	small but transmural infarct model
SA	sinoatrial

$SL_{(RZ)}$	sarcomere length profile at remote zone
SR	sarcoplasmic reticulum
STEMI	ST-elevation myocardial infarction
SV	stroke volume
SX	short axis
TIMP	tissue inhibitor of metalloproteinase
TME	transmural extent
TN-I	troponin-I
TN-C	troponin-C
TNF	tumour necrosis factor
TRxx	infarct LV models with varying infarct TMEs
WDD	work density dissipation
ZNCC	zero-normalised cross-correlation
α-SMA	α-smooth muscle actin

LIST OF APPENDICES

CHAPTER 1: GENERAL INTRODUCTION

1.1 Introduction

Myocardial infarction (MI), or commonly known as heart attack, affects more than 7 million people each year worldwide, and remains as one of the most common causes of morbidity and mortality (White & Chew, 2008). It occurs when there is insufficient blood flowing to the heart, mostly due to sudden blockage of a coronary artery owing to the formation of a blood clot or thrombus. The treatment for MI, which aims to restore the blood flow to the heart, either removing the clot with thrombolysis or reopening the occluded coronary artery with introduction of a stent, is performed as early as possible following MI. However, in most cases, the heart has been exposed to a prolonged period of inadequate blood supply. As a result, a part of the heart muscle is damaged and an infarct is formed.

Unlike skeletal muscle, damage to the heart muscle can be irreversible even after blood flow restoration, causing the heart muscle to lose its mechanical function and subsequently altering the myocardial mechanical loading. To maintain cardiac homeostasis, the left ventricle (LV) undergoes some changes in response to the alteration in myocardial loading (Choi et al., 2011). However, these changes can be pathological, which result in adverse remodelling of the LV. Ventricular remodelling involves deleterious structural alterations of LV, and such remodelling leads to the degeneration of ventricular function over time, eventually giving rise to heart failure, in which the heart fails to pump sufficient cardiac output to meet normal bodily requirements. Furthermore, heart failure following MI is the main cause of late mortality and morbidity (Cahill & Kharbanda, 2017). Therefore, early prediction and treatment for ventricular remodelling are important in reducing the mortality rate of MI patients.

Over the past few decades, experimental and clinical studies have been carried out extensively, to investigate the mechanisms that may contribute to ventricular remodelling. With recent advancement in imaging techniques, LV deformation and myocardial fibre orientation are accessible via tagged (Notomi et al., 2005) and diffusion tensor (DT) (Helm, Beg, Miller, & Winslow, 2005) cardiac magnetic resonance imaging (CMR) respectively, whilst myocardial scar can be rendered using late gadolinium enhancement (LGE) CMR (Dall'Armellina et al., 2011). Although such advancement allows better capture of myocardial mechanics, stress-related information is still out of reach through imaging techniques.

Therefore, computational finite element (FE) method has become an alternative to comprehend the LV remodelling mechanisms, as it offers a more complete visualisation of myocardial mechanics, including stress-related information. Over the last few decades, there has been much improvement in computational power, imaging techniques and modelling techniques, facilitating heart FE modelling, even up to the subject-specific level. For example, FE models have been employed in earlier studies to examine ventricular function with different patch materials (Tang, Yang, Geva, Gaudette, & Pedro, 2011), estimate LV segmental contractility (Chabiniok et al., 2012) and predict acute effects of cardiac resynchronisation therapy (Sermesant et al., 2012).

Nevertheless, to date, the mechanisms underlying LV remodelling are still poorly understood. Numerical investigation on the LV remodelling mechanisms is highly beneficial as it not only helps in predicting future remodelling events, but also facilitates treatment planning.

1.2 Problem Statement

Although it is widely believed that the state of an infarct is significant in determining remodelling process, it is debatable which infarct state variable plays a more crucial role

than the others. More importantly, in-depth study on the effects of the infarct states on LV regional mechanics is lacking. Besides, LV regional mechanics variables that potentially causing LV remodelling are also speculative, including their underlying mechanisms.

1.3 Objectives

The main goal of this study is to establish a patient-specific LV model, which allows the examination of mechanics that possibly contributes to LV remodelling in MI patients. To do this, an LV FE framework will be developed, incorporating realistic fibre orientation and excitable contracting myocardium. Patient-specific models will then be generated from the developed framework, and validated by optimising regional material properties to minimise the mismatch between the simulated myocardial walls and clinically obtained CMR data at several selected cardiac phases. The optimised models will then be used to analyse the correlation between LV remodelling and myocardial mechanics variables, and their underlying causal factors.

Therefore, the objectives of this thesis include:

- To establish a 3D electromechanical LV model with simplified generic geometry, incorporating realistic fibre orientation, action potential (AP) propagation and excitable contracting myocardium.
- To investigate the effects of infarct state on LV regional mechanics, including the interaction between ischemic and nonischemic myocardium, using the constructed generic LV model.
- To modify the generic LV model into patient-specific, incorporating patient-specific infarcted LV geometry and optimised regional material properties.

- To examine the correlation between LV remodelling and myocardial mechanics variables, including their underlying causal factors.

1.4 Thesis Layout

The layout of this thesis is based on the chronology of each study performed during the project. Chapter 2 presents the heart physiology, and the state of art pertaining to LV remodelling and heart modelling.

In Chapter 3, the development of a generic LV model is described, including its validation against available clinical data. A preliminary study on the significance of infarct transmural extent (TME) versus infarct size on LV regional mechanics is also included in this chapter.

Chapter 4, which is an extension to Chapter 3, discusses the role that infarct TME has on LV regional mechanics, which is believed to be the driving force for infarct extension. The importance of mechanical interaction between ischemic and nonischemic myocardium is also highlighted in this chapter.

Chapter 5 presents the modification of the developed generic LV model in Chapter 3 into patient-specific models, including the optimisation of regional material properties to resemble the deformation captured from CMR images. The correlation of LV remodelling and myocardial mechanics is then analysed. Subsequently, the potential mechanisms underlying infarct extension are also discussed. The chronology of work done in Chapters 3, 4 and 5 is illustrated in Figure 1.1.

Lastly, Chapter 6 concludes the present study and suggests potential works in the future.

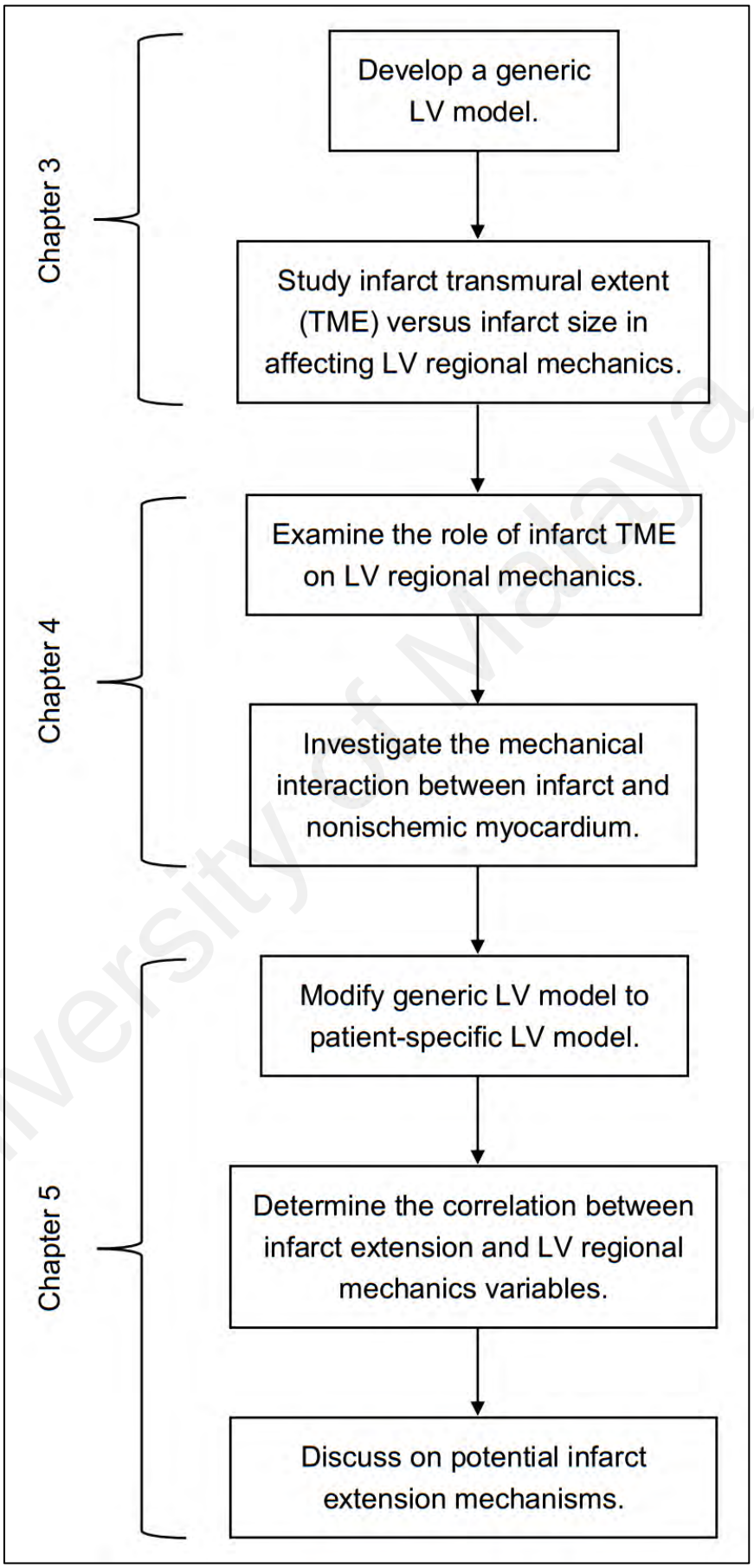

Figure 1.1: Chronology of work done in Chapters 3, 4 and 5.

CHAPTER 2: LITERATURE REVIEW

2.1 Background

2.1.1 Heart Anatomy and Physiology

Heart is an organ responsible for circulating blood throughout the whole body. It has four chambers, namely left atrium (LA), left ventricle (LV), right atrium (RA) and right ventricle (RV), as illustrated in Figure 2.1. The LA receives blood from the lungs and pumps it to the LV, which in turn pumps the blood to the rest of the body. On the other hand, the RA receives blood from the rest of the body and pumps it to the RV, which in turn pumps the blood to the lungs (Doyle, 2011).

The heart has four valves: mitral, aortic, tricuspid and pulmonary valves, which control the blood flow direction. Mitral valve prevents the backflow of blood from the LV to the LA; aortic valve prevents the backflow of blood from the aorta to the LV; tricuspid valve prevents the backflow of blood from the RV to the RA, whilst pulmonary valve prevents the backflow of blood from the pulmonary artery to the RV. The mitral and tricuspid valves are called atrioventricular (AV) valves because they are located in between the atria and ventricles. Conversely, the aortic and pulmonary valves are called semilunar valves, owing to the shape of their leaflets (Doyle, 2011).

2.1.2 Heart Wall Thickness and Histology

Wall thickness of the heart chambers varies according to their workload. The atria, under low pressure, pump blood only to the neighbouring ventricles, therefore have relatively thin walls. In contrast, the ventricles, under higher pressure, pump blood over greater distances, therefore have thicker walls. On top of that, the LV has a thicker wall than the RV, corresponding to its higher afterload. As compared to the RV, which pumps against the afterload provided by the pulmonary circulation, the LV has to pump blood against a much higher pressure over a greater distance throughout the whole body

(Tortora & Derrickson, 2012). The relatively higher workload of the LV explains also why the LV is the most commonly failing heart chamber.

Heart wall is made up of three layers, which are endocardium (the innermost layer), middle myocardium and epicardium (the outermost layer). The endocardium is a thin layer of endothelium overlaying a thin layer of connective tissue, providing smooth lining for the chambers of the heart, thus minimising the surface friction as blood flows through. The epicardium contains blood vessels, lymphatics and vessels that supply the myocardium. The middle myocardium, which comprises approximately 95% of the heart wall and responsible for the pumping action of heart, is composed of cardiac

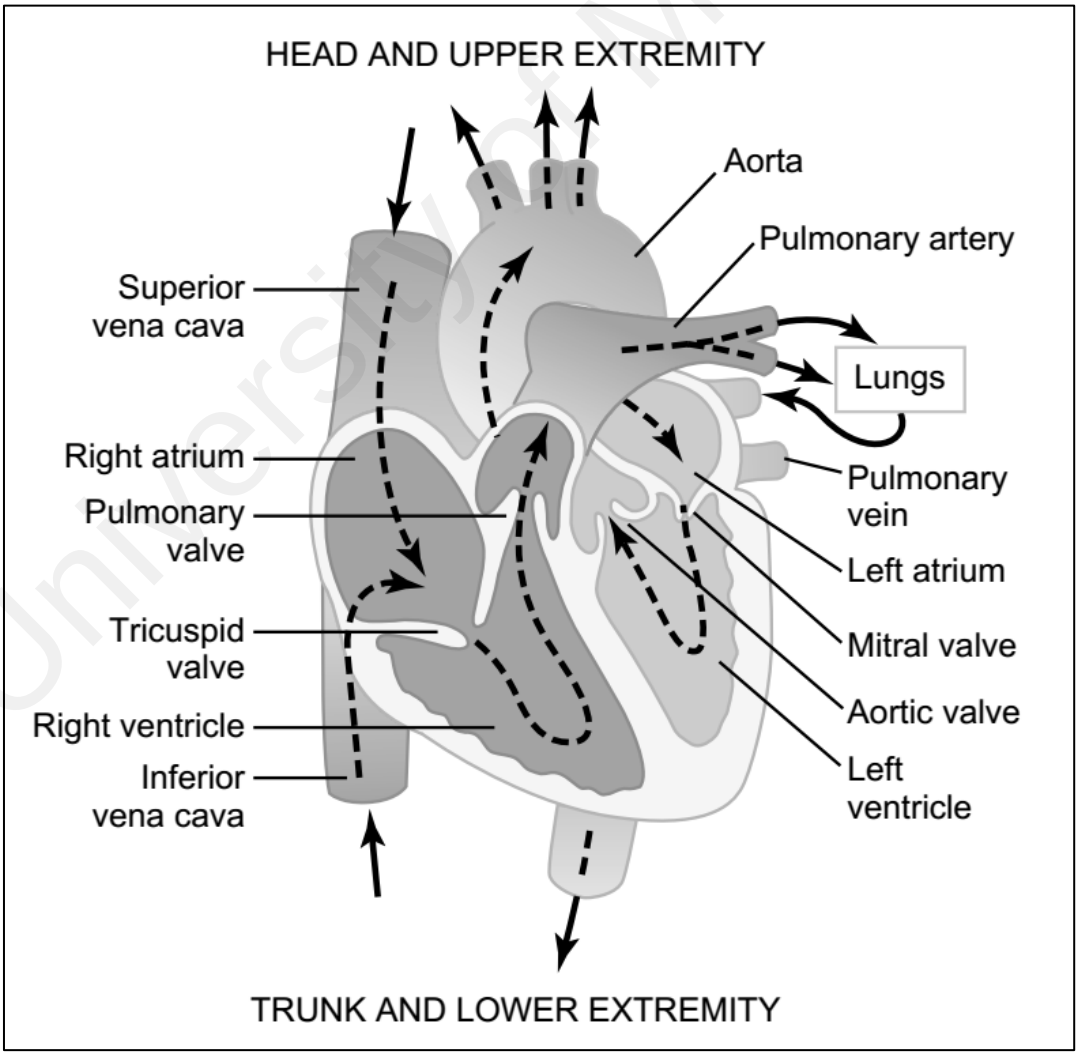

Figure 2.1: Structure of the heart, with arrows indicating the direction of blood flowing through the heart chambers and valves (Guyton & Hall, 2006).

muscle tissue (contracting cardiomyocytes) (Tortora & Derrickson, 2012). The cardiac muscle tissue is wrapped with extracellular matrix (ECM), and organised in bundles. Each myocyte can be divided into myofibril filaments, which consist of repeating sarcomeres, with each sarcomere is made up of actin and myosin myofilaments (Doyle, 2011). The actin filaments extend from the peripheral ends, which are known as the Z-disks, towards the middle of sarcomere, whilst myosin filaments extend peripherally from the middle region, with parts of the actin and myosin filaments overlapping each other, as illustrated in Figure 2.2. In between the myosin filaments and Z-disks, there is titin protein. Titin uncoils when the cardiac muscle is stretched, and recoils when the stretch is removed. The titin, together with the ECM, defines the passive material properties of myocardium. Besides, the elastic recoil of titin after myocardial contraction contributes to diastolic suction, an essential part of ventricular filling (LeWinter & Granzier, 2014).

The LV wall is composed of layered organisation of myocytes (about 70%) and interstitial matrix (about 30%) (Holzapfel & Ogden, 2009). The myocyte layers are separated by a branched, continuous network, namely perimysium, which comprises weaves of wavy collagen fibres in a proteoglycan matrix (Robinson, Geraci, Sonnenblick, & Factor, 1988). Perimysium allows myocyte layers to slip past each other, promoting the necessary rearrangement of the myocyte layers during the contraction of myocardium (Purslow, 2008). On the other hand, individual myocytes are separated by a continuous network of connective tissue called endomysium, which consists of weaves of fine and wavy collagen fibres embedded in a proteoglycan matrix. The endomysial collagen fibrils, which is parallel to the myocyte surface, form a planar network that connects neighbouring myocytes, keeping them registered within the myocyte sheet (Intrigila, Melatti, Tofani, & Macchiarelli, 2007).

The orientation of muscle fibre is an important determinant of the passive and active ventricular mechanics. It varies transmurally across the myocardial wall, and such variation differs regionally in both LV and RV. A number of studies (Ashikaga et al., 2007; Streeter, Spotnitz, Patel, Ross, & Sonnenblick, 1969) had been carried out to

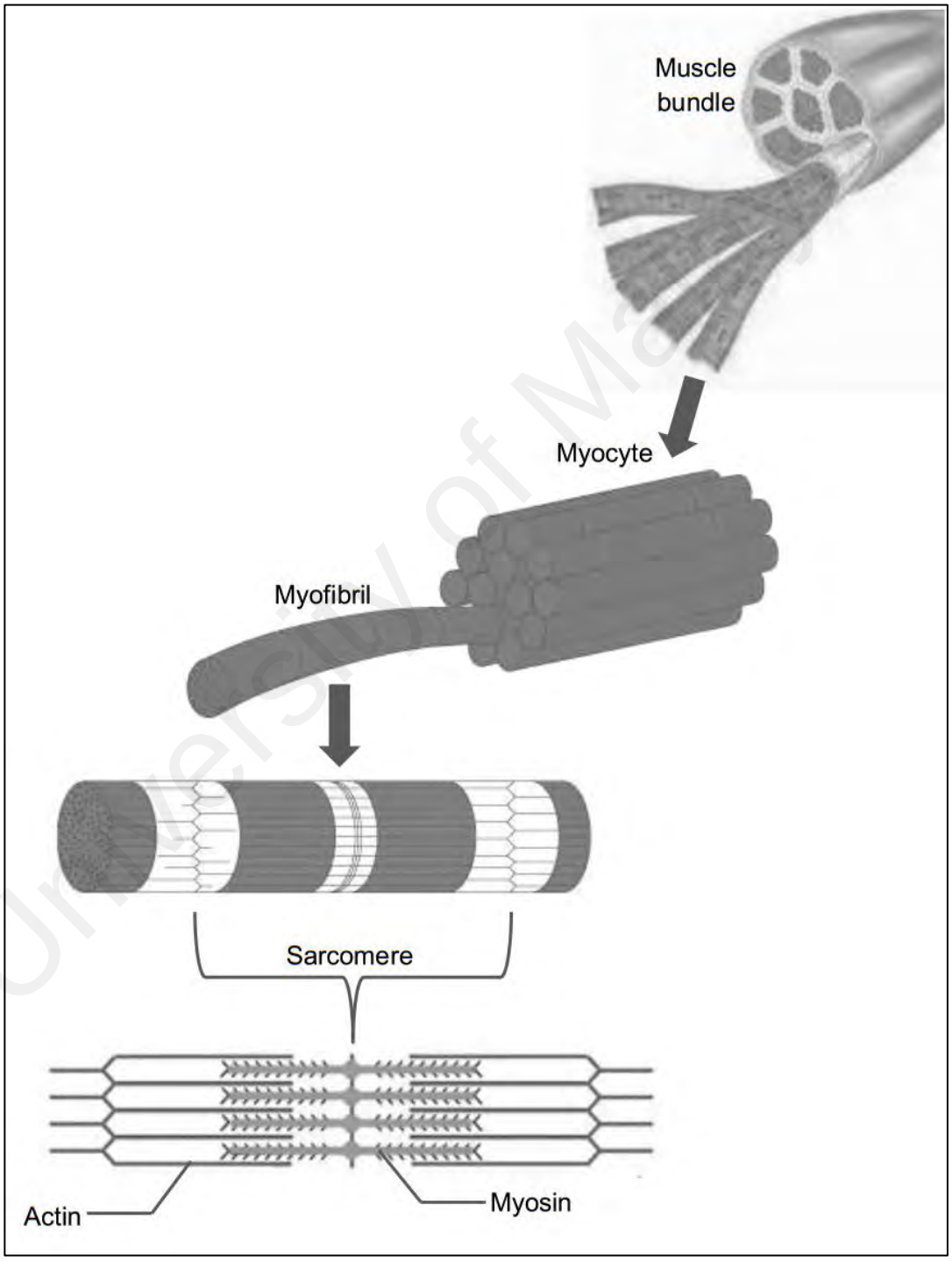

Figure 2.2: Histology of cardiac muscle, with each muscle bundle is composed of myocytes, which comprise myofibrils. Each myofibril consists of repeating sarcomeres, which are made up of actin and myosin myofilaments.

quantify the muscle fibre orientation across the myocardium. It was found that fibre angle changes smoothly from about +60° (at the endocardium) to about -60° (at the epicardium) across the LV free wall. Furthermore, no significant variation in fibre angle was observed between diastole and systole phases (Streeter et al., 1969).

2.1.3 Action Potential Conduction

Pumping action of the heart is initiated by an electrical current, known as action potential (AP). The study of electrical activity of the heart, including the propagation of AP throughout the heart, is called cardiac electrophysiology.

i. The electrical activity begins in sinoatrial (SA) node located in the RA wall. The SA node is the pacemaker of heart. It spontaneously triggers the AP, which then propagates throughout both atria to initiate atrial contraction.

ii. From the atrial myocardium, the AP travels to AV node, which is located in the interatrial septum. Due to differences in cell structure in the AV node, conduction of the AP slows down noticeably, providing considerable time for the atria to pump their blood into the ventricles.

iii. From the AV node, the AP propagates down into the interventricular septum via the bundle of His, which is the only path where the AP can propagate from the atria to the ventricles.

iv. From the bundle of His, the AP enters the right and left bundle branches and reaches the heart apex.

v. Finally, the AP enters the Purkinje fibres and propagates upwards to the ventricular walls, initiating ventricular contraction.

The sequence of the AP conduction throughout the heart, as described above, is exhibited in Figure 2.3 (Tortora & Derrickson, 2012).

2.1.4 Action Potential and Myocardial Contraction

Myocardium at rest, during diastole, has a negative membrane potential (about -90 mV). When triggered by an AP, its voltage-gated sodium ion (Na^+) channels open, allowing rapid inflow of Na^+ into cytosol. The membrane potential rises abruptly and becomes positive (about +20 mV). This process of shifting in membrane potential is called depolarisation. Upon depolarisation, a series of ion channels is activated and controlled transfer of ions, including calcium (Ca^{2+}) and potassium (K^+) ions, is initiated (Tortora & Derrickson, 2012). The inflow of Ca^{2+}, via a series of chemical reactions, triggers myocardial contraction, developing force by means of physical interaction between the actin and myosin myofilaments. This series of events, from the depolarisation to the contraction of the myocardium, is referred as cardiac excitation-contraction (EC) coupling (Bers, 2002). Due to complexity in nature of the EC coupling process, it will be covered in more details in Section 2.2.

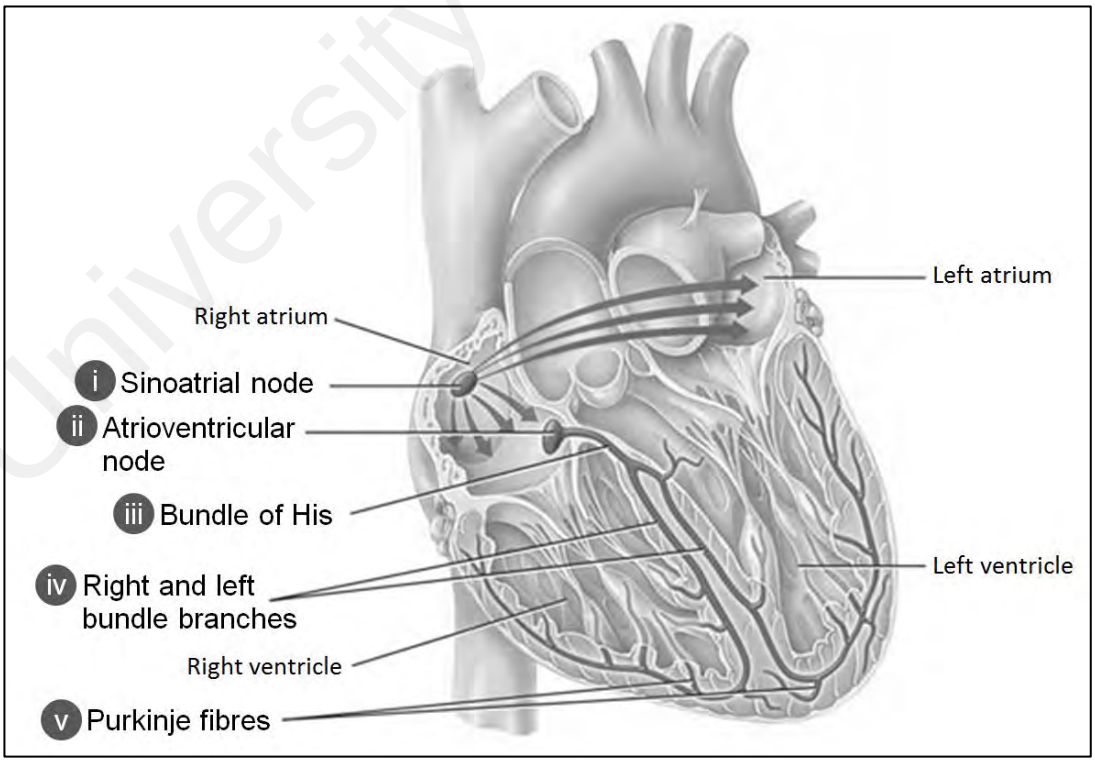

Figure 2.3: Conduction of action potential (AP) from the sinoatrial (SA) node, through the atrioventricular (AV) node, bundle of His, right and left bundle branches, and Purkinje fibres, to get to the entire ventricles (Tortora & Derrickson, 2012).

The inflow of Ca^{2+} is balanced by the outflow of K^+, sustaining the depolarisation state (Tortora & Derrickson, 2012), as illustrated in Figure 2.4. This period of maintained depolarisation is called plateau, and lasts for about 0.2 s (Guyton & Hall, 2006). After myocardial contraction, additional outflow of K^+, couples with the termination of Ca^{2+} inflow, restores the negative resting membrane potential (-90 mV), a process referred as repolarisation (Tortora & Derrickson, 2012).

Myocardium has a refractory period, a time interval during which a second excitation cannot be triggered. A normal refractory period of ventricles is 0.25 to 0.3 s (Guyton & Hall, 2006), longer than their contraction period, such that another contraction cannot be initiated before relaxation (Tortora & Derrickson, 2012).

2.1.5 Left Ventricular Cycle

An LV cycle comprises of a series of events that occur in the LV during each heartbeat. It consists of diastolic phase, a period of time during which the LV is under relaxation and filled with blood, and systolic phase, a period of time during which the LV is contracting. Figure 2.5 shows a standard Wiggers diagram, illustrating the different events in an LV cycle. LV diastole consists of isovolumic relaxation (IVR),

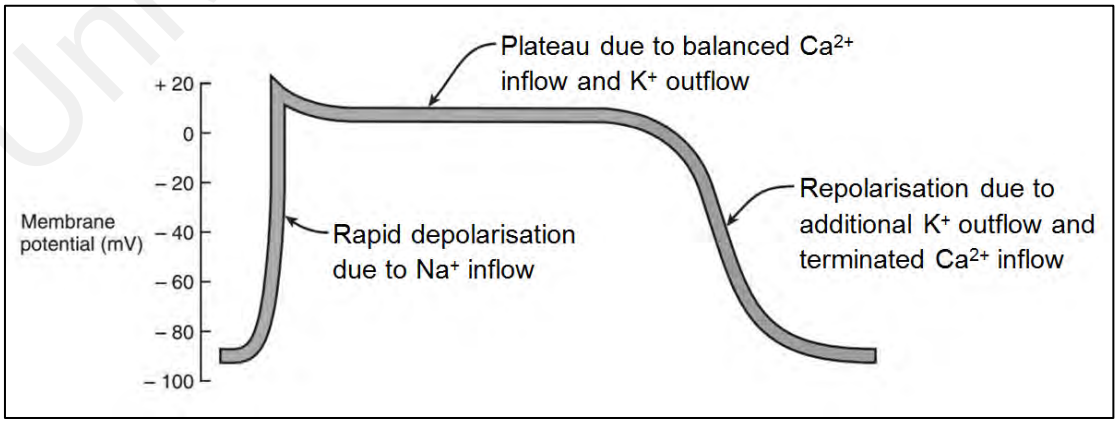

Figure 2.4: Ventricular membrane potential when an action potential is generated (Tortora & Derrickson, 2012). Na^+: sodium ion; Ca^{2+}: calcium ion; K^+: potassium ion.

rapid inflow or rapid filling, diastasis and atrial systole, whilst LV systole consists of isovolumic contraction (IVC) and ejection (Guyton & Hall, 2006):

i. During rapid filling, the LV pressure is lower than the LA pressure due to continual relaxation of the LV, which causes a large amount of blood accumulated in the LA during LV systole to flow rapidly into the LV. The period of rapid filling lasts for about one-third of diastole and ends when the LV completes its relaxation.

ii. During the middle phase of diastole, i.e. diastasis, the LV stops relaxing. The difference between the LV and LA pressures is minimal, thereby allowing only a small amount of blood flowing into the LV.

iii. During atrial systole, the LA contracts, pumping more blood into the LV, elevating both LV volume and pressure.

iv. At IVC, the LV starts to contract, generating an increase in the LV pressure, which closes the mitral valve. The LV pressure continues to rise until it exceeds the aortic pressure (about 80 mmHg) and opens the aortic valve, entering the ejection phase. Since both the mitral and aortic valves are closed during IVC, the LV contracts with no emptying, thus maintaining the LV volume. Consequently, this phase is referred as isovolumic contraction (IVC).

v. Immediately after the opening of the aortic valve, blood is ejected out from the LV. During the first half of the ejection phase, the LV pressure elevates, pumping blood out rapidly. During the second half of the ejection phase, LV pressure drops with blood continues to be ejected but at a slower rate, owing to the force-velocity relationship, in which contraction force generated declines with an increase in shortening velocity of myocyte filaments. The ejection ends

when the LV pressure falls below the aortic pressure, at which moment the aortic valve closes again, entering the IVR phase.

vi. During IVR, the LV continues to relax, dropping the LV pressure rapidly, with the LV volume is maintained. The IVR ends when the LV pressure falls below the LA pressure, causing the mitral valve to open and entering another LV cycle.

2.1.6 Cardiac Output

A healthy adult LV has an end-diastolic volume (EDV) of about 120 ml. During systole, the LV ejects about 70 ml of blood, which is called stroke volume (SV), leading to an end-systolic volume (ESV) of about 50 ml. The ratio of SV to EDV (SV/EDV) is

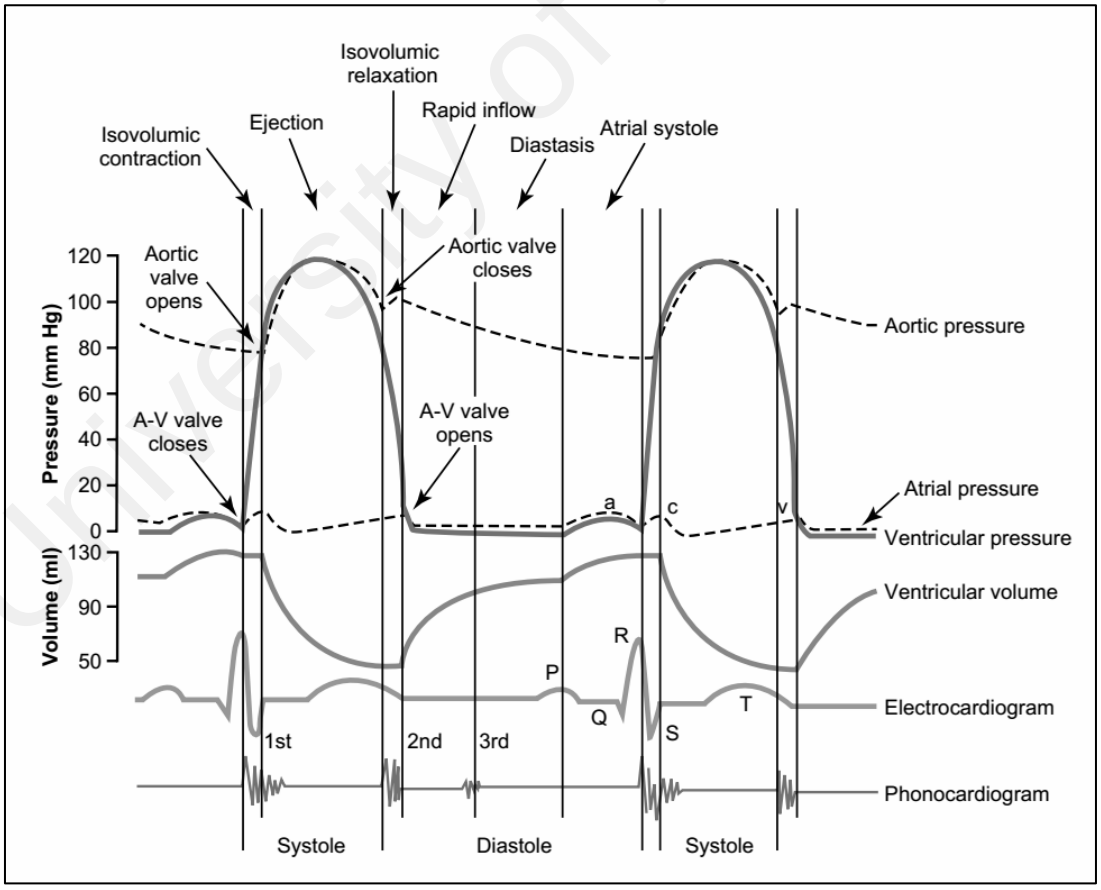

Figure 2.5: Wiggers diagram showing the different events of a left ventricular (LV) cycle: isovolumic contraction (IVC), ejection, isovolumic relaxation (IVR), rapid inflow, diastasis and atrial systole (Guyton & Hall, 2006).

called ejection fraction (EF), which is approximately 60% in a healthy adult. Cardiac output (CO), expressed as SV multiplied by heart rate, is the amount of blood ejected by LV in a minute. A healthy LV has a CO of about 5 L (Guyton & Hall, 2006).

However, under stressed conditions, for example during exercises, the EDV can reach 150-180 ml, with a large amount of blood flowing into the LV during diastole. The ESV can go as low as 10-20 ml, with the LV contracting strongly during systole. By both increasing the EDV and decreasing the ESV, the SV can be double of normal values (Guyton & Hall, 2006). Together with an increase in heart rate, the CO can be increased by several-fold.

2.1.7 Pressure-Volume Loop

Figure 2.6a shows an example of LV pressure-volume (PV) loop. It has four phases, namely filling, IVC, ejection and IVR; represented by a, b, c and d in the figure respectively. The slope of end-diastolic pressure-volume relationship (EDPVR) represents the reciprocal of LV compliance, whilst the slope of end-systolic pressure-volume relationship (ESPVR) denotes the inotropy of LV (Klabunde, 2011). The LV loop width indicates SV, whilst the area reveals the work output of LV in an LV cycle. To study the myocardial mechanics, three important factors have to be considered, which are preload, afterload and inotropy.

Preload refers to the stretching extent on the LV prior to contracting (Tortora & Derrickson, 2012), and is usually taken to be the end-diastolic pressure, corresponding to the end of filling curve in the PV loop (Guyton & Hall, 2006), as depicted in Figure 2.6b. With increased preload (red loop in the figure), the contraction force generated by myocardium is elevated, increasing the LV SV. On the contrary, a lower SV is obtained with decreased preload (green loop). This relationship is called the Frank-Starling law (Klabunde, 2011), or from a cellular perspective, the sarcomere length-force relations,

which explains the effect of greater contraction force generated with an increase in the resting sarcomere length of myocyte filaments.

Afterload refers to the pressure LV has to overcome prior to blood ejection (Tortora & Derrickson, 2012), and is usually taken to be the LV pressure while ejecting, corresponding to the ejection curve in the PV loop (Guyton & Hall, 2006), as demonstrated in Figure 2.6c. Augmented afterload (red loop in the figure) raises the workload LV has to overcome, depressing the shortening velocity of myocardium, thereby reducing the SV. In contrast, diminished afterload increases the myocardial

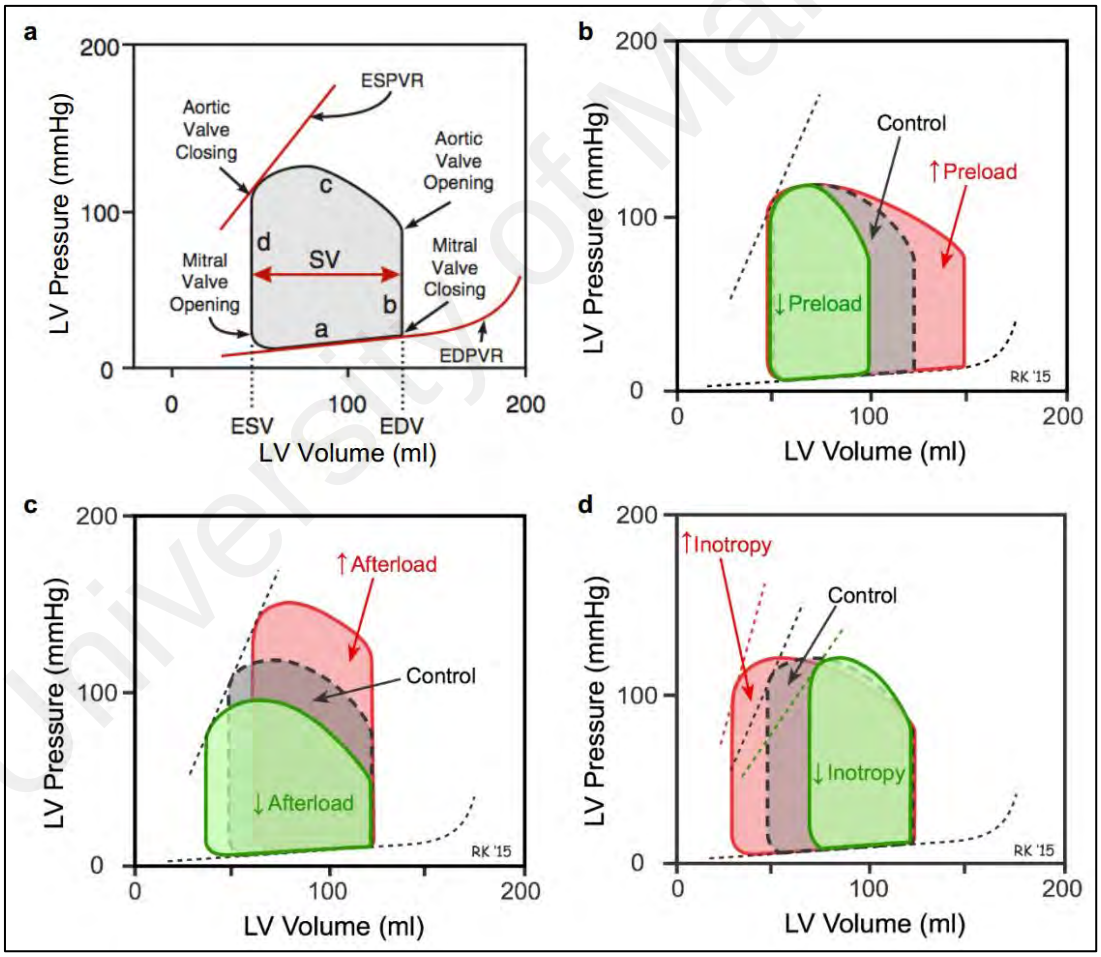

Figure 2.6: Pressure-volume (PV) loops under (a) control, and varying (b) preload, (c) afterload and (d) inotropy conditions (Klabunde, 2011). EDV: end-diastolic volume; ESV: end-systolic volume; SV: stroke volume; EDPVR: end-diastolic pressure-volume relationship; ESPVR: end-systolic pressure-volume relationship.

shortening velocity and also the SV (green loop). This effect is named the force-velocity relationship (Klabunde, 2011), which defines the inverse relation between the force generated and shortening velocity of myocardium.

Inotropy refers to the contractility of LV, and is represented by the ESPVR slope, as represented in Figure 2.6d. With increased inotropy (red loop in the figure), myocardium contracts at higher velocity, ejecting blood at a faster rate, lowering the ESV and elevating the SV. On the other hand, a lower myocardial shortening velocity, higher ESV and diminished SV are obtained with weaker inotropy (green loop) (Klabunde, 2011).

2.2 Cardiac Excitation–Contraction Coupling

Cardiac EC coupling refers to the series of events that occur from the electrical excitation to the contraction of myocardium. After the AP depolarisation, voltage-gated Ca^{2+} channels open and Ca^{2+} enter the cell as an inward Ca^{2+} current (I_{Ca}). The Ca^{2+} inflow initiates further Ca^{2+} release from the sarcoplasmic reticulum (SR). The combination of Ca^{2+} inflow and release rapidly raises the free intracellular Ca^{2+} concentration ($[Ca^{2+}]_i$), allowing Ca^{2+} to bind to the myofilament protein troponin C, which then triggers the contractile machinery. During myocardial contraction, the actin and myosin myofilaments rapidly slide past each other, causing the shortening of each sarcomere, and consequently, of each muscle fibre, thereby creating a twitch tension. Following contraction, Ca^{2+} are removed from the cytosol by several routes, which include SR Ca^{2+}-ATPase, sarcolemmal Na^+/Ca^{2+} exchanger, sarcolemmal Ca^{2+}-ATPase and mitochondrial Ca^{2+} uniporter, decreasing $[Ca^{2+}]_i$ and promoting dissociation of Ca^{2+} from the troponin, thereby allowing relaxation to occur (Bers, 2002). The process of cardiac EC coupling, as described above, is illustrated in Figure 2.7.

2.2.1 Activating Calcium Release

To trigger Ca^{2+}-induced Ca^{2+}-release (CICR) at the SR, $[Ca^{2+}]_i$ must first raise to a threshold level following depolarisation. Several routes have been proposed that can contribute to CICR (Figure 2.7). Myocytes have two forms of voltage-gated Ca^{2+} ion channels, namely L- and T-type. Upon depolarisation, both the L- and T-type channels open and Ca^{2+} enter the cytosol as inward Ca^{2+} currents ($I_{Ca,L}$ and $I_{Ca,T}$ respectively). However, $I_{Ca,T}$ is much weaker than $I_{Ca,L}$, and mostly non-functional (Sipido, Carmeliet, & Van de Werf, 1998; Zhou & January, 1998). Although Ca^{2+} inflow through the Na^+/Ca^{2+} exchange channels has also been proposed to contribute to CICR, it is much slower and ineffective as compared to $I_{Ca,L}$ (Sipido, Maes, & Van de Werf, 1997). Therefore, $I_{Ca,L}$ is the main Ca^{2+} source, and as long as it exists, it dominates other mechanisms in triggering CICR. Although Ca^{2+} ion channels are activated by depolarisation, their cytosolic side inactivation is Ca^{2+}-dependent. Therefore, during EC coupling, I_{Ca} is limited by high $[Ca^{2+}]_i$ (Peterson, DeMaria, & Yue, 1999; Zühlke, Pitt, Deisseroth, Tsien, & Reuter, 1999). In other words, both I_{Ca} and CICR (Sipido,

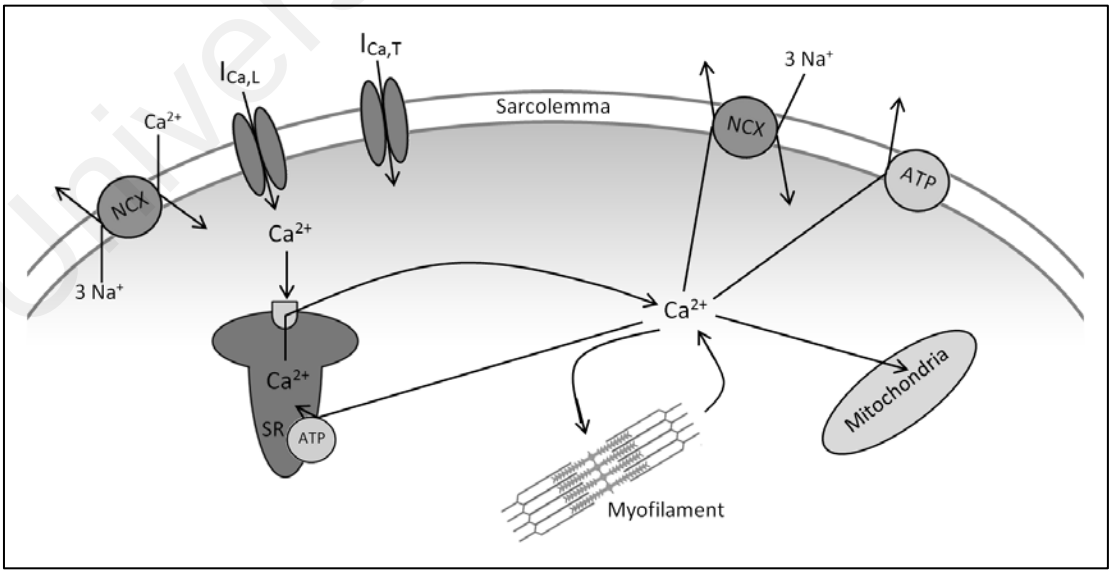

Figure 2.7: Ca^{2+} transport in a cardiomyocyte during a cardiac excitation-contraction coupling process. Ca^{2+}: calcium ions; Na^+: sodium ions; NCX: Na^+/Ca^{2+} exchanger; $I_{Ca,L}$: L-type calcium current; $I_{Ca,T}$: T-type calcium current; ATP: ATPase; SR: sarcoplasmic reticulum.

Callewaert, & Carmeliet, 1995) have local negative feedback on I_{Ca}, limiting Ca^{2+} inflow.

2.2.2 Role of the Sarcoplasmic Reticulum

A high SR Ca^{2+} content directly increases the amount of Ca^{2+} available for release, thereby enhancing its sensitivity to cytosolic Ca^{2+}, and dramatically increases the fraction of SR Ca^{2+} that is released when triggered by I_{Ca}. Conversely, a low SR Ca^{2+} content is less sensitive to cytosolic Ca^{2+}, and I_{Ca} can fail to activate the Ca^{2+} release from the SR (Bassani, Yuan, & Bers, 1995; Shannon, Ginsburg, & Bers, 2000). The failure in activation of the Ca^{2+} release from the SR promotes more Ca^{2+} inflow via I_{Ca} and Na^{+}/Ca^{2+} exchange, allowing the SR to reload, preparing for the next cycle of I_{Ca}. SR Ca^{2+} can be raised by increasing Ca^{2+} inflow, decreasing Ca^{2+} outflow, or increasing Ca^{2+} uptake into the SR (Bers, 2002).

2.2.3 The Role of Calcium in Contraction and Flow Balance

Myocyte contraction achieved via interactions of actin and myosin myofilaments. Adhering the actin, there is troponin-C (TN-C), which is a binding site for Ca^{2+} during EC coupling, and troponin-I (TN-I), which inhibits the binding of actin and myosin. When Ca^{2+} binds to TN-C, TN-I moves away from the myosin-binding site, promoting the binding and formation of crossbridge between the actin and myosin, which allows the actin and myosin to slide past each other and gives rise to the shortening of sarcomere. On the other hand, when Ca^{2+} dissociates from TN-C, TN-I inhibits the actin-myosin binding, restoring the sarcomere back to relaxation state (Klabunde, 2011).

There are two main factors that manipulate the strength of myocyte contraction, which are $[Ca^{2+}]_i$ and the sensitivity of myofilaments to Ca^{2+}. The myofilament sensitivity to Ca^{2+} is enhanced greatly by stretching of the myofilaments. This is due, in

part, to the reduction in interfilament lattice spacing and enhancement of TN-C affinity for Ca^{2+} during stretching (Klabunde, 2011), thereby intensifying the actin-myosin interaction (Fukuda, Sasaki, Ishiwata, & Kurihara, 2001). This nature of myofilaments is termed length-dependent Ca^{2+} sensitivity, which forms the sarcomere length-force relations and Frank-Starling law, in which the heart pumps harder with greater filling, an important cardiac autoregulatory response in adjusting CO.

Ca^{2+} must be transported out from the cytosol, lowering $[Ca^{2+}]_i$ to allow relaxation. This is accomplished by several pathways, in which their quantitative significance varies depending on species. For rabbits, which are believed to exhibit a quantitatively similar ventricular Ca^{2+} flow to human, 70% of Ca^{2+} are removed from the cytosol via SR Ca^{2+}-ATPase, 28% via sarcolemmal Na^+/Ca^{2+} exchange channels, leaving only a small amount of Ca^{2+} removed via sarcolemmal Ca^{2+}-ATPase and mitochondrial Ca^{2+} uniporter, with about 1% each (Figure 2.7) (Bassani, Bassani, & Bers, 1994).

2.2.4 Sarcoplasmic Reticular Ca^{2+}-ATPase Activity and Ventricular Function

In a heart failure scenario, the activity of SR Ca^{2+}-ATPase is depressed, and the removal of Ca^{2+} is counter-balanced by an enhanced activity of the Na^+/Ca^{2+} channels (Hasenfuss, 1998). This returns $[Ca^{2+}]_i$ to its resting state and allows relaxation to occur. However, at the same time, this affects the reload of Ca^{2+} into the SR, reducing SR sensitivity to I_{Ca} and limiting SR Ca^{2+} release, subsequently depressing ventricular contractile function. This may be a central cause of impaired contractile function in heart failure (Bers, 2002). Although less SR Ca^{2+} release promotes more Ca^{2+} inflow from I_{Ca}, still, $[Ca^{2+}]_i$ strongly depends on CICR, given that Ca^{2+} inflow from I_{Ca} is much lesser than CICR (Shannon et al., 2000). Furthermore, it has been found that SR Ca^{2+}-ATPase expression matches myocardial contractile function. SR Ca^{2+}-ATPase protein level is not only related to the potentiation of twitch tension with increased

stimulation frequency, but also significantly correlated with the frequency at which twitch tension is maximum. In other words, the force-frequency response of myocardium is closely matched to the SR Ca^{2+}-ATPase expression, suggesting that the myocardial contractile function, with respect to the force-frequency relation, is determined by SR Ca^{2+}-ATPase expression (Hasenfuss et al., 1994).

2.3 Myocardial Infarction

Myocardial infarction (MI) affects more than 7 million people each year worldwide, and is one of the diseases with the highest mortality rate (White & Chew, 2008). It happens when blood supply to the heart stops, causing damage to the heart muscle. Unlike skeletal muscle, damage to the heart muscle can be irreversible (even after reperfusion), causing ventricular remodelling, in which LV functionally degenerates over time, ultimately leading to heart failure. Therefore, understanding post-MI events is important to prevent, or at least delay, the progression of remodelling.

2.3.1 Post Myocardial Infarction

Myocardial wall consists of a muscular compartment composed of myocytes and an interstitial compartment that contains vasculature and ECM, which is composed of a collagen network (Sun et al., 2010). Following MI, intracellular oedema, which is an early indicator of cell damage, begins to accumulate, causing cell swelling, increasing tissue area, reducing interstitial space and enhancing infarct stiffness (Whittaker, Boughner, & Kloner, 1991). In addition, myocardial infarction lowers the tissue inhibitor of metalloproteinase (TIMP) expression, activates the latent matrix metalloproteinases (MMPs), and subsequently produces the matrix fragments (Frangogiannis, 2017). Meanwhile, neutrophils invade the infarct to clear necrotic myocytes, cellular debris and collagen network, which holds the myocytes in place (French & Kramer, 2007).

A few days after MI, the infarct enters a proliferative phase, in which formation of neovessels takes place, promoting extensive proliferation of fibroblasts. The fibroblasts become activated and differentiate into myofibroblasts, which synthesise a large amount of α-smooth muscle actin (α-SMA), contractile proteins and ECM proteins, including the collagen necessary for holding myocytes in place (Shinde & Frangogiannis, 2014). It has been suggested that α-SMA plays a crucial role in infarct contraction. However, its part in mediating fibroblast function is still remained unanswered, and a recent study has found that it is insufficient in exhibiting the contraction of the matrix (Shinde, Humeres, & Frangogiannis, 2017). Besides, overexpression of fibroblasts might promote diastolic and systolic dysfunction (Frangogiannis, 2014). In this phase, a wide range of matricellular proteins are deposited in the ECM, regulating cytokines and growth factors, such as transforming growth factor beta and angiotensin II (Frangogiannis, 2017; Murphy-Ullrich, 2001). Also in proliferative phase, monocytes infiltrate the infarct and differentiate into macrophages, phagocytising neutrophils, which undergo apoptosis after completely clearing the necrotic myocytes and cellular debris (French & Kramer, 2007). The degeneration of the vasculature, collagen damage and decrease in oedema cause a loss in the interstitial space (Whittaker et al., 1991).

After the proliferative phase, the infarct enters a maturation phase, in which fibroblasts undergo apoptosis and neovessels regress from the infarct, whilst the collagen-based matrix turns into a mature scar (French & Kramer, 2007). The entire process of scar formation can take weeks to months to complete (Fishbein, Maclean, & Maroko, 1978).

An infarct is the most vulnerable during the proliferative phase. Additional degradation of the collagen network, with the loss of collagen strut, which forms lateral connections between neighbouring myocytes, can severely depress the myocardial

stiffness (Whittaker et al., 1991). Under high distending pressure, for example during systole, the myocytes slide past each other by a mechanism called slippage (Weisman, Bush, Mannisi, Weisfeldt, & Healy, 1988), causing overdistension and systolic bulging of the myocardial wall (Whittaker et al., 1991). Soon after this, infarct expansion takes place, in which the infarcted myocardium dilates and expands (Gajarsa & Kloner, 2011). Therefore, it is important that a mature and strong scar, which resists further expansion, is formed as soon as possible (Whittaker et al., 1991).

2.3.2 Infarct Expansion

Infarct expansion is a process in which the infarct progressively becomes dilated and thinned (Schuster & Bulkley, 1979), as illustrated in Figure 2.8. It is a result of myocyte slippage following infarct distension, and not macrophagic removal of dead tissue (Hutchins & Bulkley, 1978). It has also been shown that the length of sarcomeres from the expanded infarct remains normal, indicating that the infarct expansion is a consequence of myocyte slippage, rather than the distension of sarcomeres (Linzbach, 1960).

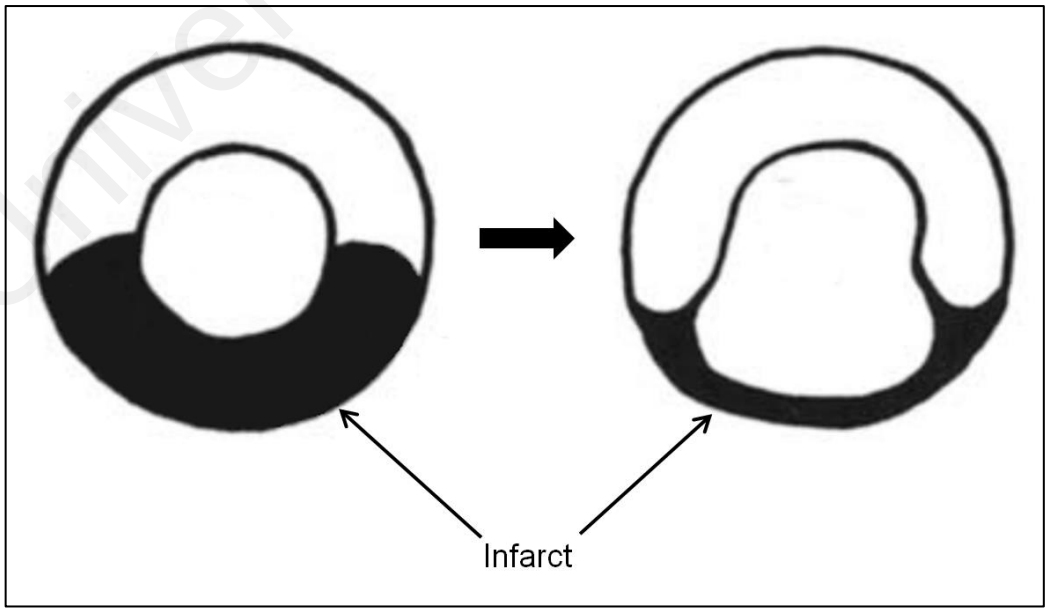

Figure 2.8: Ventricular changes with infarct expansion, in which myocardial wall progressively becomes dilated and thinned.

Infarct expansion contributes to ventricular remodelling, in which ventricle undergo pathologic structural changes and gradually losses its function. This process can give rise to complications such as aneurysm formation, congestive heart failure (Erlebacher et al., 1982), and myocardial rupture. The latter is an extreme consequence of infarct expansion, in which the expanded infarct is too thin to withstand the high distending pressure, and as a result, the ventricular wall ruptures. Moreover, infarct expansion significantly increases the patient mortality rate (Schuster & Bulkley, 1979).

Since infarct expansion is a result of infarct distension due to its incapability to withstand high systolic LV pressure, a small and well-healed infarct is safe from infarct expansion. This is supported by the observations that patients with small, nontransmural infarcts are not associated with LV remodelling. On the contrary, a large, transmural infarct is subject to abnormal loading and undergoes infarct distension with each heartbeat. It follows that the amount of stretching and the number of heartbeats the infarct experiences are crucial in determining the infarct expansion progression (French & Kramer, 2007).

Therefore, any treatments help in attenuating infarct distension are believed to be able to prevent, or at least slow down, infarct expansion. Angiotensin converting enzyme (ACE) inhibitors, which help lowering blood pressure, attenuate loading placed on infarct, thereby reducing the risk of infarct expansion. Therefore, ACE inhibitors are normally given to MI patients as early as possible (Antman et al., 2004). In a post-MI rat model, ventricular plication by suturing infarcted tissue had been shown to improve end-diastolic and end-systolic lengths, fractional shortening, LV contractility, and attenuate LV remodelling (Schwarz, Speakman, & Kloner, 2000). Myocardial patches, an alternative surgical method for strengthening the infarcted myocardium, have also been shown to aid in minimising infarct expansion (Leor & Cohen, 2004).

Infarct expansion is the first complication associated with LV remodelling that takes place following MI. Therefore, it has a role in determining subsequent progression of LV remodelling, and perhaps is also the most important complication associated with LV remodelling (French & Kramer, 2007). Although infarct expansion is not a result of myocardial necrosis, it can promote one by inducing abnormal loading on the viable myocardium (Hutchins & Bulkley, 1978).

It has been found that after MI, myocardium remote from the infarct progressively increases its segmental length at end-diastole, which is accompanied by elevated shortening ratio (the Frank-Starling law). The changes experienced by the remote myocardium are responses of the LV to compensate for the reduced work done by the infarct (Theroux et al., 1977). Such cavity enlargement is not due to acute distension of the myocardium, as the filling pressure of a chronic LV can be lower than that of an acute LV. These changes improve LV haemodynamics, including an observed reduction in the LV filling pressure and restoration of CO, but at the cost of LV enlargement (Mckay et al., 1986).

However, care has to be taken that patients with infarct expansion can demonstrate chronic dilation of the noninfarcted myocardium. The increased LV chamber size due to infarct expansion, as well as increased workload experienced by the noninfarcted myocardium, increases diastolic wall stress in the noninfarcted myocardium (Erlebacher et al., 1982). In accordance to Grossman hypothesis, volume overload (increased diastolic wall stress) initiates eccentric hypertrophy, in which sarcomeres are added in series, myocardial fibres elongate, and subsequently, the noninfarcted myocardium dilates (Grossman, Jones, & McLaurin, 1975).

Furthermore, the thinning and softening of the infarct following expansion decrease the infarct tensile strength, causing cavity dilation, and subsequently augmenting wall

tension (Schuster & Bulkley, 1979). The augmented wall tension results in an increase in oxygen demand that may exceed coronary supply (Erlebacher et al., 1982), leading to necrosis of the viable myocardium, and therefore infarct extension. It has been shown that the rate of infarct extension is related to the degree of infarct expansion (Hutchins & Bulkley, 1978).

Therefore, infarct expansion not only progressively alters the function of the infarcted myocardium, but also chronically alters the function of the noninfarcted myocardium (M. A. Pfeffer & Braunwald, 1990).

2.3.3 Infarct Extension

Following MI, myocardium can be categorised into three zones, namely infarct zone (IZ), border zone (BZ) and remote zone (RZ). IZ refers to the nonperfused myocardial region, BZ refers to the perfused but functionally impaired myocardial region, whilst RZ refers to the perfused and fully functional myocardial region.

Immediately after MI, the BZ is normally small, with its function impaired moderately (hypocontractile). However, as remodelling progresses, the BZ enlarges, and at the same time, its functional impairment becomes more severe. In other words, the BZ extends, recruiting adjacent RZ into the BZ, a process called nonischemic infarct extension. Meanwhile, functional profile of the BZ becomes closer or even identical to that of the IZ, a process called ischemic infarct extension (Jackson et al., 2002), as shown in Figure 2.9.

Infarct extension can initiate myocardial necrosis that spreads beyond the IZ and BZ, and may involve the entire LV. It explains the phenomenon, in which LV progressively becomes dilated and dysfunctional in some MI patients. Patients with infarct extension have an in-hospital mortality of more than four times higher than those without

extension (Muller et al., 1988). Furthermore, increasing amount of transmural necrosis following infarct extension can cause infarct expansion and its related complications. The combined effects of infarct expansion and extension give rise to the feed-forward cycle of remodelling process, resulting in continuous cardiomyocyte apoptotic and necrotic death, ventricular thinning and dilation (Diwan et al., 2007). Despite carrying a high risk, the cause of infarct extension, to date, still remains unanswered.

From a mechanical perspective, elevated stress and strain in the BZ and neighbouring RZ are believed to be the key to induce infarct extension. This is because early infarct thinning following infarct expansion results in an increase in the radius of curvature of the BZ, thereby augmenting wall stress in the BZ (Jackson et al., 2002). Besides, the high stress is also a result of juxtaposition of the BZ between the non-contractile IZ and the contractile RZ, thereby creating a "tethering" effect in the BZ (Ashikaga et al., 2005). Such tethering effect is though bidirectional, it amortises over some distance, causing the BZ to experience the greatest stress (French & Kramer, 2007). Earlier experimental studies have demonstrated a rise in the myocyte volume at the BZ

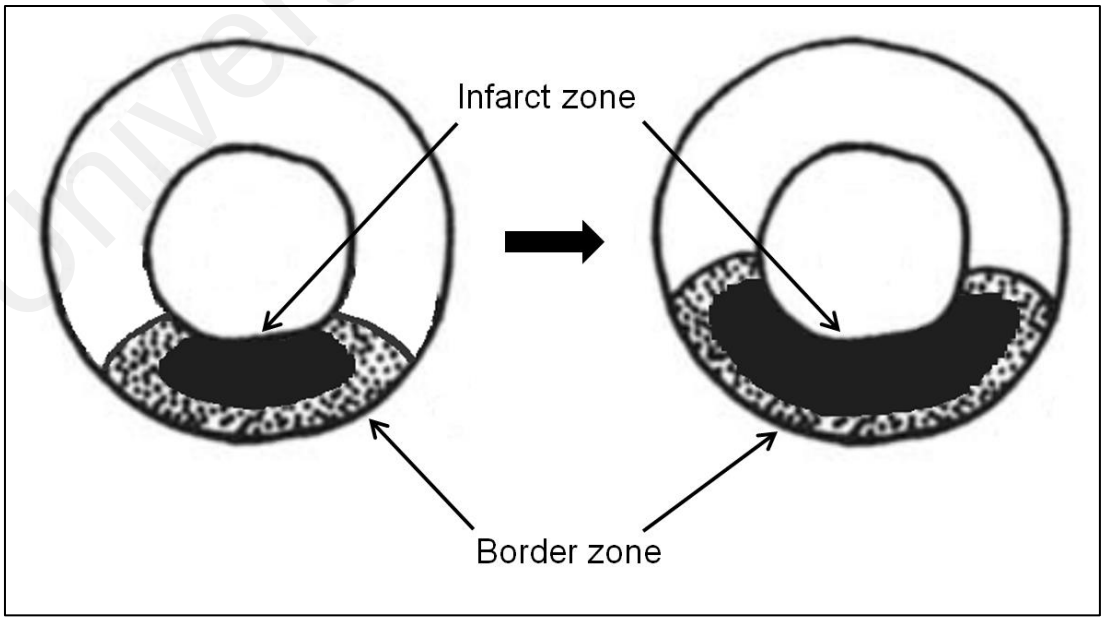

Figure 2.9: Ventricular changes with infarct extension. Border zone (BZ) extends and recruits adjacent myocardium, whilst the functional profile of the BZ becomes closer or even identical to that of the infarct zone (IZ).

compared to the RZ, as a result of increased myosin production at the BZ (Kozlovskis et al., 1984). More importantly, these regional differences in cell volume, shape and metabolism are correlated with the tethering effect, further strengthening the significance of stress and strain distribution in LV remodelling (Kramer et al., 1993). Furthermore, the tethering effect is also believed to be responsible for the observed reduction in BZ contractility (French & Kramer, 2007).

From a biological perspective, mechanical stress imposed on the BZ cardiomyocytes induces oxidative stress and activate proinflammatory pathways within the cells. This is supported by the presence of both tumour necrosis factor (TNF) alpha (Akasaka et al., 2006) and inducible nitric oxide synthase protein (Gilson et al., 2007) in the BZ cardiomyocytes. The combination of both the oxidative and nitrosative stresses gives rise to apoptosis, which replaces the BZ cardiomyocytes with fibrous tissue and extends the IZ (French & Kramer, 2007). The presence of vacuolated myocytes in the BZ supports this hypothesis and suggests a mechanism responsible for the BZ depressed contractility. The majority of the vacuolated myocytes are apoptotic. This finding also suggests that progressive myopathic process occurs in normally perfused myocardium, extending the impaired region, ultimately leading to global ventricular dysfunction by nonischemic myocyte loss secondary to stretch-induced myocyte apoptosis (Jackson et al., 2002).

It has also been proposed that increased oxygen demand of thickened myocardium, exceeding that of coronary supply, can contribute to ischemia (Erlebacher et al., 1982; Gaasch, Zile, Hoshino, Apstein, & Blaustein, 1989; Hutchins & Bulkley, 1978; Shiojima et al., 2005). However, a previous study has shown that coronary flow reserve is maintained in the BZ. This study demonstrated that the balance between oxygen demand and supply is not violated, thereby ruling out the increased myocardial demand

hypothesis (Lima et al., 1985). Other biological pathways that may contribute to infarct extension include alteration of contractile proteins (Nakao, Minobe, Roden, Bristow, & Leinwand, 1997), remodelling of ECM with consequent fibrosis (Weber, 1997), and autophagy, a process of protein and organelle recycling in the response of the cardiomyocytes to stress (Hill & Olson, 2008; Matsui et al., 2007; Zhu et al., 2007).

2.4 Transduction of Ventricular Remodelling

2.4.1 Volume Overload

Grossman et al. (1975) proposed that volume overload results in addition of sarcomeres in series, causing individual cardiomyocytes to grow longitudinally to increase ventricular diameter, and ultimately leading to eccentric hypertrophy, as illustrated in Figure 2.10. In eccentric hypertrophy, LV increases in its cavity volume and mass, with an increase, no change or reduction in its wall thickness (Dorn, Robbins, & Sugden, 2003).

Eccentric hypertrophy is commonly seen in post-MI LV. In the following weeks to months after MI, cardiomyocytes in the non-infarcted region undergo slippage (sliding side-by-side) due to the loss of intercellular connections, causing wall thinning and dilation of the non-infarcted region (Olivetti, Capasso, Sonnenblick, & Anversa, 1990; Weisman et al., 1988). With such dilation, the LV EDV and ESV increase, whilst the LV filling pressure decreases (Mckay et al., 1986). The hypertrophy initially appears to be beneficial, compensating the functional loss of the infarcted myocardium and restoring the CO at the expense of increased LV volume. However, in long-term, the hypertrophy becomes maladaptive (J. M. Pfeffer, Pfeffer, Fletcher, & Braunwald, 1991). As the ventricular wall continues to undergo dilation, the LV cavity enlarges at a rate faster than that of the increase in myocardial mass. Such mismatch between the LV volume and wall thickness elevates wall stress, which may eventually result in infarct

expansion and extension. Besides, eccentric hypertrophy also depresses the LV EF (Anand & Florea, 2011).

2.4.2 Pressure Overload

According to Grossman's systolic-stress-correction hypothesis, pressure overload results in addition of sarcomeres in parallel, causing individual cardiomyocytes to grow laterally to increase wall thickness, and ultimately leading to concentric hypertrophy (Grossman et al., 1975), as shown in Figure 2.10. In concentric hypertrophy, LV increases in its wall thickness and mass, with little or no change in its cavity volume (Dorn et al., 2003). According to the Laplace's law, an increase in wall thickness depresses systolic wall stress. If the increase in wall thickness due to concentric hypertrophy is adequate, an elevated wall stress can be restored to normal. Therefore,

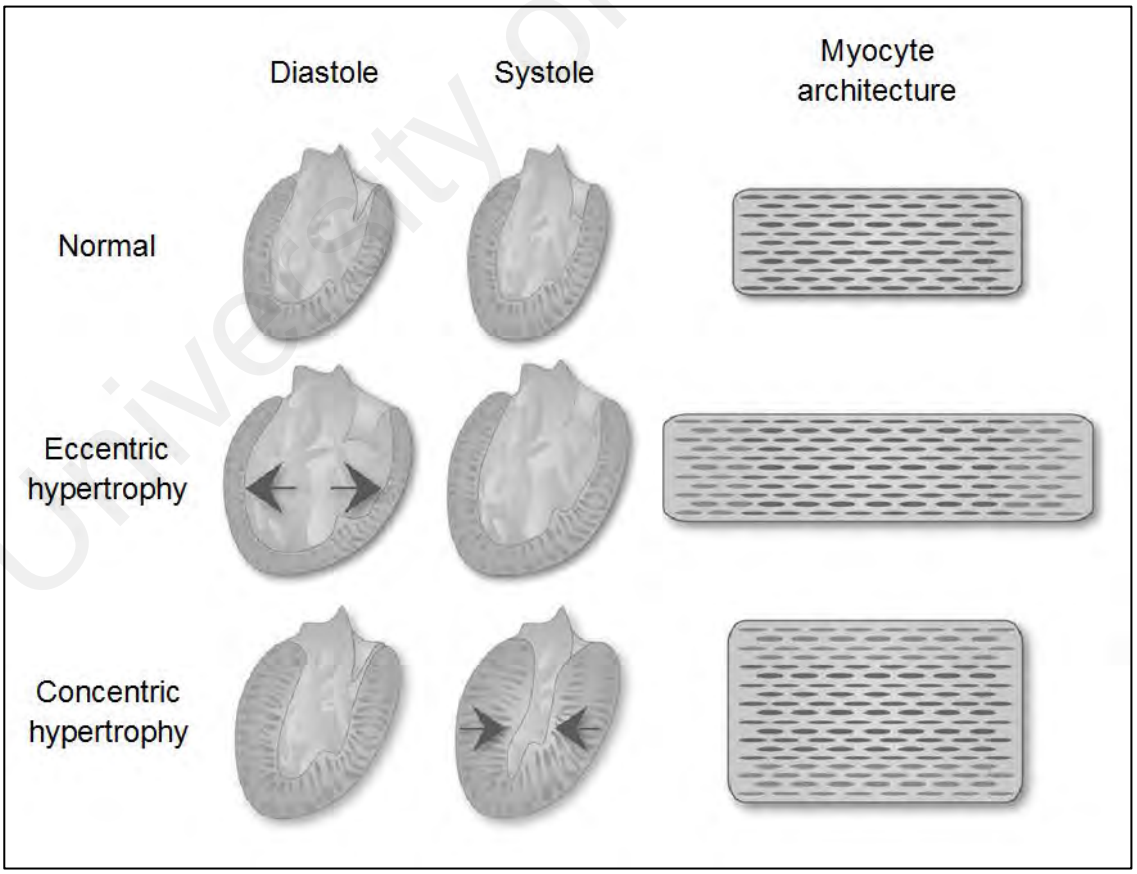

Figure 2.10: Eccentric and concentric hypertrophies, with the arrows showing the addition of sarcomeres in series (eccentric hypertrophy) and parallel (concentric hypertrophy), causing dilation and thickening of myocardial wall respectively (Katz & Rolett, 2015).

concentric hypertrophy of LV was perceived as adaptive and beneficial (Grossman et al., 1975).

However, extensive studies in the past decades have questioned the wall-stress hypothesis. According to the nature of signalling stimulus, the LV can either undergo adaptive hypertrophy and recover (Sugden, 2001), or maladaptive hypertrophy, which leads to ventricular dilation and eventually failure (Baines & Molkentin, 2005). Moreover, experimental studies have shown that attenuation or elimination of pressure overload-induced concentric hypertrophy, by interrupting myocardial signalling pathways, is beneficial, in which ventricular dilatation does not develop (Frey, Katus, Olson, & Hill, 2004). Therefore, concentric hypertrophy can be both adaptive and maladaptive.

2.4.3 Transduction of Biomechanical Stress

It is though well recognised that biomechanical stress induces cardiac hypertrophy and remodelling, its underlying mechanisms are still not established. The transduction of mechanical signals probably involves stretch-sensitive ion channels, integrins, and other structural proteins in a complex network that links the ECM, cytoskeleton, sarcomeres, Ca^{2+}-handling proteins and nucleus (Sadoshima & Izumo, 1997).

Mechanical stress induces synthesis and secretion of potent growth factors, which include insulin-like growth factor I, angiotensin II and endothelin-1, in both cultured cells (Sadoshima & Izumo, 1997) and in patients with aortic stenosis (Serneri et al., 1999). Besides, mechanical stretch is capable of activating angiotensin II receptors directly, even without angiotensin II (Zou et al., 2004). Cytokines such as TNF, interleukin-1, and interleukin-6 family, which are activated in response to environmental injury, have also been shown to influence LV remodelling (Mann, 2003).

Cyclic mechanical stretch has been demonstrated to result in hypertrophic growth and apoptosis of cardiomyocytes, by inducing membrane type matrix metalloproteinase (MT-MMP) and reactive oxygen species (ROS) productions. MT-MMPs activate the latent MMPs in myocardium, which produces active interstitial collagenases (MMP-1). MMP-1 degrade ECM proteins and give rise to ECM remodelling. The MT-MMPs may also induce ECM remodelling by directly degrading the ECM components (Tyagi et al., 1998). It is well established that ROS can induce apoptosis, and its production has been found to be stretch amplitude-dependent. The mechanism of ROS production by mechanical stretch is unclear, perhaps due to increased myocardial oxygen consumption following mechanical stretch. At low levels of stretch (low levels of ROS), the cardiomyocytes undergo hypertrophy, whilst at high levels of stretch (high levels of ROS), the cardiomyocytes undergo apoptosis (Pimentel et al., 2001). Therefore, mechanical stretch plays an important role in modulating ventricular remodelling process.

2.4.4 Calcium Homeostasis

Although different signalling pathways have been implicated in the biomechanical stress induced-remodelling process, they have one common outcome, which is to alter intracellular Ca^{2+} homeostasis (Chien, 2000). Heart failure is accompanied by elevated resting intracellular Ca^{2+} concentration, depressed Ca^{2+} release by SR upon activation, and depressed uptake of Ca^{2+} by SR during relaxation. These alterations in Ca^{2+} homeostasis are correlated with depressed cardiac function, and are believed to contribute to heart failure (Lim & Molkentin, 1999). Two independent studies have shown that increasing peak intracellular Ca^{2+} transient can inhibit heat failure progression in both genetic and acquired forms of cardiomyopathy (Minamisawa et al., 1999; Miyamoto et al., 2000). Phosphorylation of phospholamban (an endogenous inhibitor of SR Ca^{2+}-ATPase) enhances Ca^{2+} uptake by SR, and has been shown to be

able to inhibit the hypertrophy progression (Minamisawa et al., 1999), further strengthening the altered Ca^{2+}-handling hypothesis.

Apart from its correlation with heart failure, intracellular Ca^{2+}-mishandling is also potent in activating Ca^{2+}-sensitive intracellular signalling factors. Calcium–calmodulin–dependent phosphatase calcineurin is a strong signalling molecule for hypertrophy. Unlike skeletal muscle, calcineurin signalling in cardiomyocytes happens to be pathological (Hill & Olson, 2008). It is sufficient, and in many cases necessary, for pathologic cardiac growth (Molkentin et al., 1998). Increased calcineurin activity has been reported in MI (Wilkins et al., 2004), aortic stenosis (Ritter et al., 2002) and heart failure (Lim & Molkentin, 1999) cases. Other Ca^{2+}-dependent signalling molecules that are involved in the transduction of hypertrophic stimuli include Ca^{2+}-dependent protein kinases (Passier et al., 2000; Ramirez, Zhao, Schulman, & Brown, 1997) and mitogen-activated protein kinases (Hill & Olson, 2008).

The processes associated with the transduction of biomechanical stress to ventricular remodelling are summarised in Figure 2.11.

2.5 Heart Models

Over the few decades, modelling has been an alternative approach in research pertaining to biological sciences, including heart. Cardiac models not only help in interpreting experimental and clinical data, but also in analysing important mechanisms and interrelationships (N. A. Trayanova, 2011). The advancement of imaging modalities in the recent years has facilitated heart modelling research to grow rapidly, extending its capability in cardiac research. In this section, the existing heart models will be discussed from different perspectives, including geometry, electrophysiological and material models.

2.5.1 Left Ventricular Model Geometries and Anatomic Structure

LV geometry can be divided into two categories, which are idealised and subject-specific geometries. In an LV model based on idealised geometry, truncated ellipsoid is used to represent LV geometry for simplification (Choi et al., 2011; Kroon et al., 2009), as shown in Figure 2.12a. On the other hand, subject-specific geometry is normally obtained via CMR images (Wall, Guccione, Ratcliffe, & Sundnes, 2011; Wenk et al., 2012). Subject-specific geometry allows better capture of LV shape irregularity, but at a cost of computational time and model robustness, owing to its relatively unsmoothed surfaces. Besides, subject-specific geometry also allows for representation of structural difference of individual heart, such as infarction (Wall et al., 2011; Wenk et al., 2012) and aneurysm formation (J. M. Guccione et al., 2001), as illustrated in Figures 2.12b and 2.12c respectively.

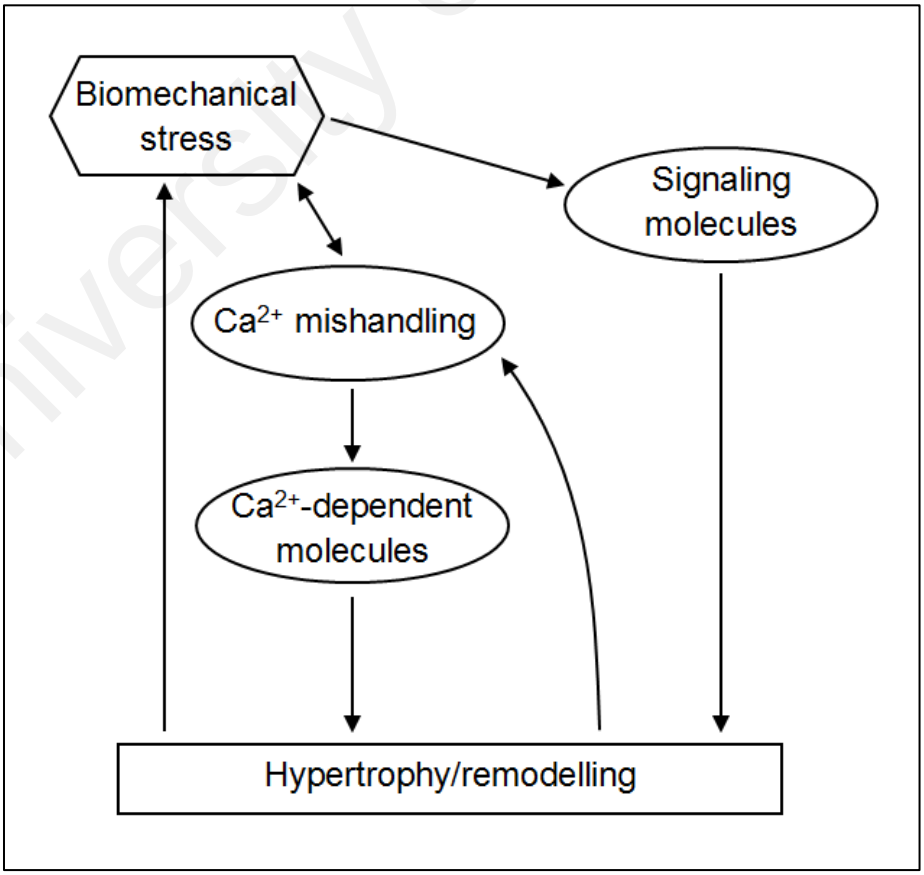

Figure 2.11: A summary of the processes associated with the transduction of biomechanical stress to LV remodelling.

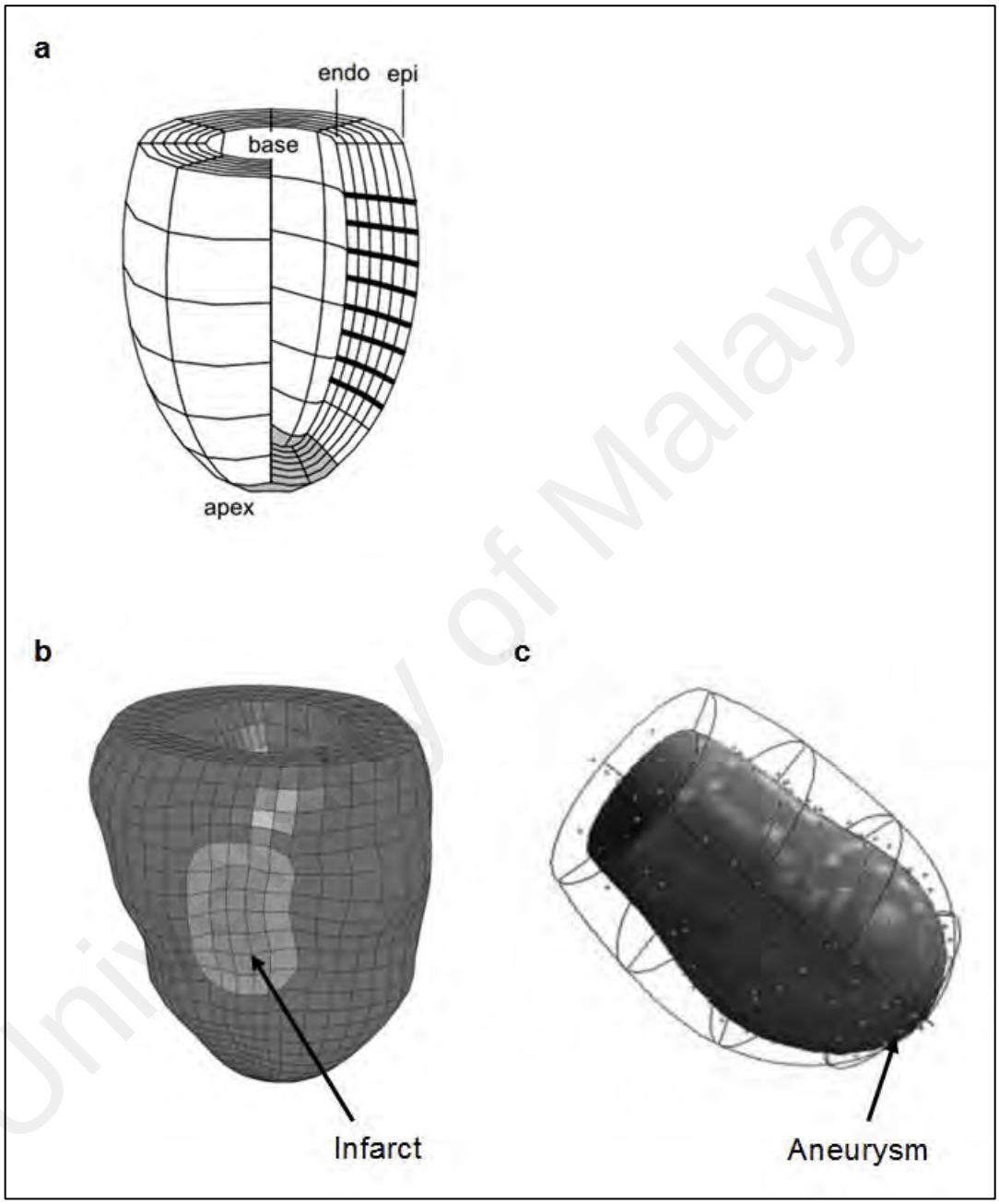

Figure 2.12: (a) Idealised LV geometry (Kroon, Delhaas, Bovendeerd, & Arts, 2009). (b) LV geometry with an infarct (Wenk et al., 2012). (c) LV geometry with aneurysm formation (J. M. Guccione et al., 2001).

Histologically, myocardium is orthotropic with three characteristic directions, which are fibre, sheet and radial directions. The fibre direction corresponds to the muscle fibre direction; the sheet direction is defined to be in the plane of muscle layer perpendicular to the fibre direction; whilst the radial direction is perpendicular to the other two (Holzapfel & Ogden, 2009), as shown in Figure 2.13. The fibre direction can be implemented into models based on DT CMR data (Wall et al., 2011; V. Y. Wang et al., 2009), as demonstrated in Figure 2.14a. In case DT CMR data is out of reach, fibre direction can be implemented via rule-based method, by referring to the fibre direction information readily available from previous studies. In rule-based method, fibre orientation is defined at the endocardial and epicardial surfaces, whilst the fibre orientation in between is defined by an interpolation function, based on local relative distance to the endocardial and epicardial surfaces (Chabiniok et al., 2012; Choi et al., 2011), as demonstrated in Figure 2.14b.

2.5.2 Electrophysiological Models

Electrophysiological models can be classified into two types, namely biophysically-based and phenomenological models. Biophysically-based models are formularised based on individual electrophysiological behaviours, such as ion channel, pump and exchanger physiologies. Therefore, biophysically-based models consist of a system of

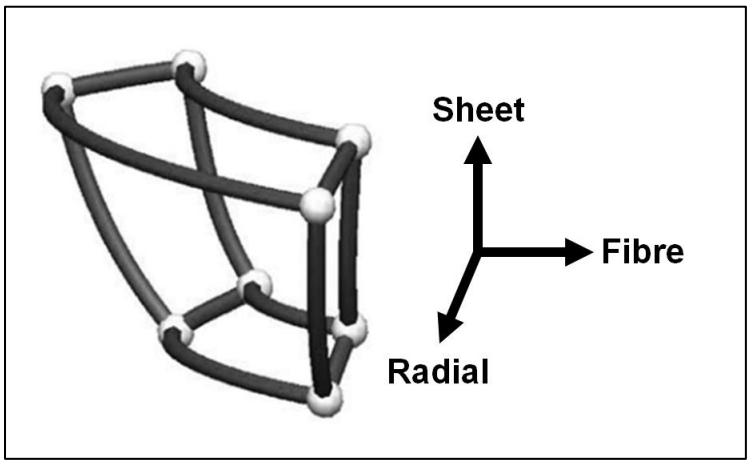

Figure 2.13: Fibre, sheet (perpendicular to fibre direction but tangential to myocardial surface) and radial (normal to myocardial surface) directions.

non-linear first order ordinary differential equations (ODEs), describing the electrophysiological behaviours (Lopez-Perez, Sebastian, & Ferrero, 2015). The Hodgkin and Huxley (1952) formalism, which models the electrophysiological dynamics at cellular level, is one of the earliest and most popular biophysically-based models. Over the past decades, as more myocardial electrophysiological behaviours are identified, the biophysically-based models become more complicated. From the Beeler and Reuter (1977) model, which consists of only 8 ODEs, the biophysically-based models have evolved into more complicated models, such as the recent O'Hara, Virág, Varró, and Rudy (2011) model, which consists of more than 40 ODEs.

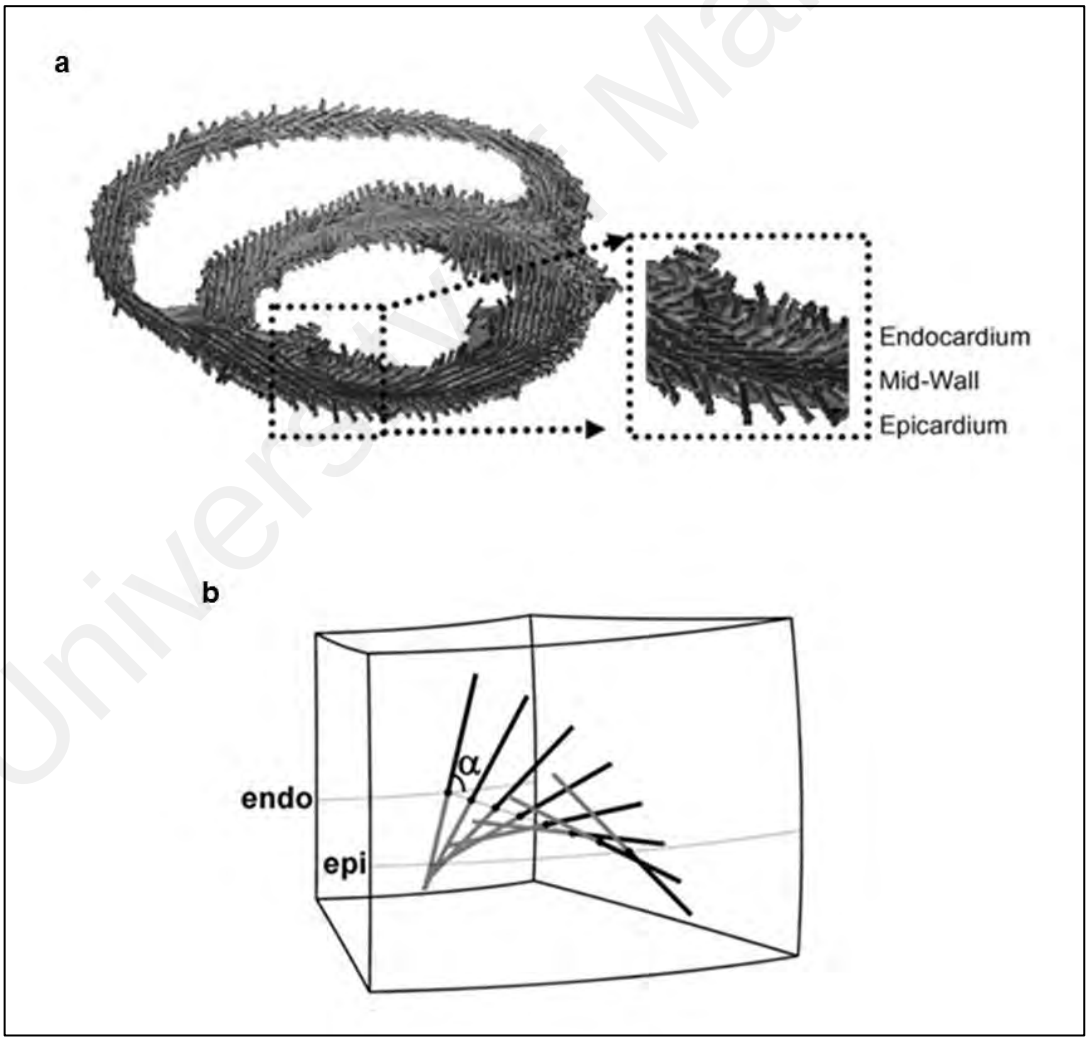

Figure 2.14: (a) Implementation of fibre direction based on diffusion tensor (DT) cardiac magnetic resonance imaging (CMR) data (V. Y. Wang et al., 2009). (b) Implementation of fibre direction using rule-based method (Choi, Rademakers, & Claus, 2011).

To simulate the propagation of AP, cellular-level models are modified to tissue-level models, incorporating partial differential equations (PDEs). In the models, the PDEs are coupled to the cellular-level model ODEs, corresponding to the dependency of AP on cellular electrophysiology (Geselowitz & Miller, 1983; Roth, 1988). Since myocardium is made up of two electrophysiologically nonhomogeneous domains, which are intracellular and extracellular domains, the so-called bidomain models have been developed to simulate current flows in the extracellular domain, such as simulating extracellular potentials (Potse, Dubé, Richer, Vinet, & Gulrajani, 2006; Whiteley, 2006).

Although biophysically-based models are considerably accurate and capable of capturing complex electrophysiological events, such as arrhythmias and current re-entry, they are computationally expensive. As such, phenomenological models are introduced. Unlike biophysically-based models, which capture the actual electrophysiological behaviours, phenomenological model mathematical descriptions are non-physiologic. Therefore, phenomenological models, at a reduced complexity, generate only a resemblance of the electrophysiological morphology (Lopez-Perez et al., 2015). The FitzHugh (1961) model, which was then modified and adapted to cardiac AP by latter studies (Aliev & Panfilov, 1996; Mitchell & Schaeffer, 2003), is one of the earliest phenomenological models. A commonly used example of phenomenological cardiac models is the Aliev and Panfilov (1996) two-variable model, which adequately demonstrates the pulse shape and restitution property of myocardium. The coefficients of the model, though nonphysiologic and have no direct relation to the electrophysiological behaviours, can be adjusted to fit the experimental AP curves under given conditions. Another type of simplified phenomenological model is the Eikonal diffusion equation, which has been used to simulate the depolarisation time of myocardium (Sermesant et al., 2012).

2.5.3 Passive Material Models

Myocardium has a highly non-linear passive stress-strain relationship, and has generally been modelled as a hyperelastic material, in which its stress-strain behaviour is defined in terms of a strain energy density function. To take into account the significance of fibre structure, a number of transversely isotropic models have been developed (Costa et al., 1996; J. M. Guccione, McCulloch, & Waldman, 1991; Humphrey, Strumpf, & Yin, 1990). In these models, the material properties differ in only two directions, which are fibre and cross-fibre directions.

Ideally, myocardial material model should be orthotropic, since myocardium is orthotropic with three characteristic directions: fibre, sheet and radial directions. As such, a number of orthotropic models have been proposed by latter studies (Costa, Holmes, & McCulloch, 2001; Holzapfel & Ogden, 2009; Usyk, Mazhari, & McCulloch, 2000). In these models, material properties differ in the fibre, sheet and radial directions. An orthotropic model, though improves the model behaviours during diastole, has little effect on model behaviours during systole. Moreover, it still remains to be explored whether the active stress generated by myocardium is also orthotropic (Usyk et al., 2000).

To characterise the passive viscoelastic response of myocardium, viscoelastic models have also been proposed. The Cansız, Dal, and Kaliske (2015) model, which is one of the few orthotropic viscoelastic models, is developed by extending the Holzapfel and Ogden (2009) hyperelastic model. This is done by adding decomposition of the viscous part of the free energy function into the fibre, sheet and radial directions. Although the model shows excellent agreement with available experimental data, more experimental data are needed for further validation, particularly the distinct relaxation and creep curves at different stretch amplitudes in the fibre, sheet and radial directions. In the

study of Land et al. (2017), it was found that viscous component though represents 44 ± 5% of total passive force, 75% of it decays within 92 ± 24 ms. Furthermore, the viscous component is dominated in the active phase, has insubstantial effect on ejection fraction (Land et al., 2017). Moreover, the addition of viscoelastic dynamics into the model considerably extends the computational time.

2.5.4 Active Material Models

Myocardial contractile mechanics basically involves two major mechanisms, namely cardiac EC coupling and mechano-feedback coupling, in which myocardial deformation affects its own properties. Over the past decades, point models have been developed to simulate various myocyte activation kinetics, including AP transient, Ca^{2+} transient, CICR phenomenon, actin-myosin crossbridging kinetics and actin-myosin Ca^{2+} sensitivity. Various experimental myocyte characterisations have been replicated, such as force-sarcomere length relations, force-Ca^{2+} relations and force-velocity relations. Due to the complexity of myocyte activation mechanics, the previously developed point models contain tens of ODEs (Mullins & Bondarenko, 2013; Rice et al., 2008). Such complicated systems, though capable of approximating myocyte contractile mechanics reasonably well under various given conditions, impose a computational challenge when implemented in organ-level.

Therefore, phenomenological models have been proposed. As in the electrophysiological field, the purpose of phenomenological models is to generate only a resemblance of myocardial active contraction morphology at a reduced complexity. Therefore, phenomenological models do not capture the subcellular kinetics, and their coefficients are non-physiologic. Nash and Panfilov (2004) developed a relatively simple model, in which the active contraction stress is modulated by a single AP-dependent differential equation. However, this model does not take into account the

mechano-feedback properties, such as the force-sarcomere length relations. In some latter studies, the force-sarcomere length relations and force-velocity relations are taken into consideration, by incorporating sarcomere strain and strain rate into their formulism (Choi et al., 2011; Kerckhoffs, Omens, McCulloch, & Mulligan, 2010; Sermesant et al., 2012). One notable active stress formulism, which was used in many latter studies (Wall et al., 2011; Wenk et al., 2012; Zhang et al., 2012), is the J. Guccione, Waldman, and McCulloch (1993) model. In the model, the sarcomere length-dependent isometric twitch duration and calcium sensitivity (force-sarcomere length relations) are taken into account and modulated by two separate variables. In Land et al. (2017) model, a three-state crossbridge model was utilised to capture the skinned myocyte crossbridge kinetics at body temperature. However, the skinned myocyte data-based model failed to capture physiological measurements in whole-heart simulations. To date, it is still unanswered why skinned myocyte data is not compatible with intact myocyte, possibly due to difference in crossbridge kinetics between the two (Land et al., 2017).

The active stress computed from the active contraction formulism was then added to the second Piola-Kirchhoff stress tensor along the fibre direction to resemble fibre contraction. However, in a latter study, it has been demonstrated that myocardial strain improves significantly with 40% of active stress added to the cross-fibre directions (Walker et al., 2005). Apart from active stress, active strain can also be an alternative in simulating myocardial contraction, as proposed by Ambrosi and Pezzuto (2012). The active strain approach, though mathematically more robust, remains to be validated in regards to its physiological effectiveness.

Although there are many existing phenomenological active contraction formulism available, none can precisely capture the myocardial active contraction morphology,

especially the one of human, due to limitation in the myocardial contraction kinetic understanding.

2.6 Left Ventricular Computational Mechanics Studies

Although advanced imaging techniques allow the quantification of myocardial strain, another significant component of myocardial mechanics, myocardial stress, is unreachable via imaging modalities. Therefore, the use of computational finite element (FE) method is essential in comprehending the mechanical function of infarcted LV, since it offers a more complete visualisation of LV regional mechanics, including myocardial stress. Over the past decades, FE method has been used by researchers to study different factors that possibly affect the LV mechanical function.

Kerckhoffs, McCulloch, Omens, and Mulligan (2009), and Fomovsky, Macadangdang, Ailawadi, and Holmes (2011), both utilised canine heart models, investigated the effects of IZ properties on LV function. It was found that LV global function and averaged LV regional function dropped with larger infarct size. Nonetheless, the regional function in the RZ was unaffected by infarct size (Kerckhoffs et al., 2009). In the study of Fomovsky et al. (2011), isotropic stiffening of the infarct was though shown to increase contractility, diastolic function was compensated and had insignificant improvement on SV. It was demonstrated that the greatest SV, with enhanced filling and uncompensated contractility, was achieved with high longitudinal but low circumferential infarct stiffness (Fomovsky et al., 2011).

In regards to BZ, it was evident that the myocardial contractility of BZ was reduced following MI, which is believed to be capable of causing LV remodelling (Shimkunas et al., 2013; Wenk et al., 2012). Furthermore, elevated BZ contractility has been shown to improve LV function, including greater SV and leftward shift in the ESPVR (Zhang et al., 2012).

In the study of Gao et al. (2017), in which personalised models were generated from 11 ST-elevation MI (STEMI) patients and 27 healthy volunteers, the LV wall active tension (normalised by systolic blood pressure) was found to be greater among the STEMI patients, compared to the healthy volunteers. This observation suggests STEMI patients experienced increased demand on the contractile reserve of remote functional myocardium. On top of that, the normalised active tension, patient-specific contractility and systolic myofilament kinematics were demonstrated to have the strongest explanatory power for identifying the myocardial function changes post-MI (Gao et al., 2017).

On the other hand, Choi et al. (2011) studied the role of LV shape on LV regional mechanics, using an idealised LV model. In the study, the intramyocardial distributions of fibre stress, strain and stroke work density were found to be shape dependent. The ejection was reduced with an increase in LV sphericity, owing to diminished fibre stress development, fibre shortening and stroke work in the midwall and subepicardium at the mid ventricle (Choi et al., 2011). In another cardiomechanics study, contractility parameters were quantified for different LV regions. Subsequently, the location of MI can be identified referring to the regional contractility parameters (Chabiniok et al., 2012).

2.7 Research Gap Summary

Although LV remodelling following MI can give rise to heart failure and contribute to high mortality and morbidity rate of MI patients, to date, there are still a lot of questions remain to be answered in regards to its causal factors, especially from mechanical perspectives.

Since LV remodelling is a maladaptation in response to changes in loading conditions following the presence of infarct, the properties of an infarct play significant

roles in manipulating remodelling process. The state of infarct is one of the most important infarct properties that determines remodelling, with larger and more transmural infarct imposing greater risk of remodelling. However, it is arguable whether infarct size or infarct transmural extent (TME) is more important in contributing LV remodelling. Infarct TME refers to the volumetric penetration of infarct from endocardium towards epicardium. A number of earlier studies, using multivariate linear regression analysis, found that infarct size is the primary indicator of LV remodelling (Masci et al., 2011; Ørn et al., 2007; Wu et al., 2008). On the contrary, others suggested that infarct TME is the strongest predictor of LV remodelling (Ahn et al., 2013; Berti et al., 2011; O'Regan et al., 2012). The contradiction in findings may be due to proportional relationship between infarct size and TME. This is because a larger infarct tends to have greater TME, making clinical studies facing challenges in examining these two factors separately. Furthermore, discussion on how the infarct states influence LV regional mechanics, which subsequently controls LV remodelling, is lacking.

As mentioned in Section 2.3, infarct expansion and extension are two essential remodelling processes. Briefly, in infarct expansion, infarct becomes dilated and thinner as of myocyte slippage (Schuster & Bulkley, 1979), and can lead to complications such as aneurysm formation, congestive heart failure (Erlebacher et al., 1982) and myocardial rupture. On the other hand, infarct extension involves reinfarction of normally perfused BZ adjacent to the infarct, which subsequently extends the IZ progressively, and at the same time drags the neighbouring myocardium into the BZ (Jackson et al., 2002). Infarct expansion is caused by overdistension of infarct (Whittaker et al., 1991). Since infarct is incapable of contracting, it cannot withstand the high LV systolic pressure and undergoes systolic bulging, causing myocyte slippage, dilation and eventually, expansion of the infarct (Gajarsa & Kloner, 2011). Although the mechanical causal factor of infarct expansion is well established, little is known for infarct extension.

It has been proposed that infarct extension is caused by the presence of abnormally high stress at the BZ owing to the mechanical "tethering" between the normal and ischemic myocardium (Lima et al., 1985; Sakai, Watanabe, & Millard, 1985; Walker et al., 2008). Nevertheless, detailed exploration of the mechanisms underlying infarct extension, which involve the interaction between the RZ and IZ, as well as the resultant high stress at the BZ, is still lacking, including the role of infarct state in such interaction. Wenk et al. (2012) and Shimkunas et al. (2013) demonstrated depressed BZ contractility after MI using their LV mechanics models, but did not elucidate how this results in abnormally high stress in the BZ. Ratcliffe (2002) proposed that an increase in systolic BZ stress causes isovolumic stretching, which then initiates apoptosis and reduces contractility. In a study by Walker et al. (2005), which utilised a sheep-specific computational FE model, simulation results showed that the BZ presented 24% and 115% elevation in midwall fibre and cross-fibre stresses respectively, as compared to the RZ. However, contradictory findings were revealed in another FE modelling study (J. M. Guccione et al., 2001), which demonstrated that experimentally observed isovolumic stretching at the BZ was caused by impaired intrinsic contractility and not elevated wall stress, suggesting that impaired intrinsic contractility is the culprit responsible for infarct extension, instead of overloading stress. Nevertheless, this study cannot explain the phenomenon of nonischemic infarct extension, which involves infarct extension at the RZ with normal intrinsic contractility, during post-infarct ventricular remodelling as observed by Jackson et al. (2002). Therefore, studies on the possible causal factors of infarct extension are highly appreciated, including the correlation between infarct extension and LV regional mechanics variables.

CHAPTER 3: ELECTROMECHANICS MODELLING OF THE EFFECTS OF INFARCT STATE ON LEFT VENTRICULAR REGIONAL MECHANICS

3.1 Introduction

In this chapter, a generic electromechanical left ventricle (LV) model, incorporating realistic fibre orientation, excitable contracting myocardium and LV cycle dynamics, was developed. The performances of the model were then compared with physiological LV functions, including action potential (AP) propagation, end-diastolic volume (EDV), end-systolic volume (ESV), LV twisting and LV wall thickening. Subsequently, LV models with different infarct sizes and transmural extents (TMEs) were simulated, using the generated LV model, to investigate the impacts of infarct size and TME on LV regional mechanics, which is believed to be the primary determinant of LV remodelling.

3.2 Literature Review

Myocardial infarction (MI) occurs when there is inadequate blood flow to the heart, and can cause irreversible damage to a part of heart muscle, forming an infarct. Following MI, the LV undergoes changes in response to alterations in myocardial load due to the presence of infarct, to maintain cardiac homeostasis (Choi et al., 2011). However, these changes can be pathological, resulting in degeneration of myocardial function and adverse remodelling of LV over time, eventually giving rise to heart failure. Furthermore, heart failure following MI is the main cause of late mortality and morbidity (Cahill & Kharbanda, 2017). Therefore, understanding the driving forces underlying remodelling process is important in reducing the rates of MI patient morbidity and mortality.

Although it has been found that there is a correlation between infarct state and LV remodelling, it is still debatable whether infarct size or infarct TME is more important in determining the possibility of LV remodelling. A number of earlier studies, using

multivariate linear regression analysis, found that infarct size is the primary indicator of LV remodelling (Masci et al., 2011; Ørn et al., 2007; Wu et al., 2008). On the contrary, others suggested that infarct TME is the strongest predictor of LV remodelling (Ahn et al., 2013; Berti et al., 2011; O'Regan et al., 2012). Nonetheless, the effects of infarct state (i.e. infarct size and TME) on LV regional mechanics were not investigated in these clinical studies.

Although advanced imaging techniques allow quantification of myocardial strain, myocardial stress, another significant variable related to myocardial mechanics, is unreachable via imaging techniques. To overcome this limitation, the Laplace's law has been used to quantify myocardial wall stress. However, it does not take into account the varying LV tissue properties and fibre orientation, leading to inaccurate wall stress calculation (Zhang et al., 2011).

Therefore, the use of computational finite element (FE) method is essential in comprehending the mechanical function of infarcted LV, since it offers a more complete visualisation of LV regional mechanics, including myocardial stress. Furthermore, it allows the manipulation of individual physiological variables, making it easier and more accurate to investigate the effects of each physiological variable (e.g. infarct size and TME) on functional aspects of interest. For examples, Fomovsky et al. (2011) investigated the effects of myocardial properties and infarct location on LV function, Kerckhoffs et al. (2009) examined the effects of infarct size on LV global function and averaged LV regional function, with both utilising canine FE heart models, whilst Choi et al. (2011), using idealised LV model, studied the effects of LV shape on LV regional mechanics. Nevertheless, FE computational study on the effects of infarct state, particularly the infarct size and TME, on LV regional mechanics is still lacking.

3.3 Methods

3.3.1 Geometry

The LV geometry was modelled as a truncated 3D ellipsoid. Its inner cavity had a volume of 65 ml, a short-to-long axis length ratio of 0.5, and a truncated base opening of 3 cm in diameter, representing the valve annuli (Choi et al., 2011). Wall thicknesses at the LV mid and apex were assigned such that their values at end-diastole agreed with those reported in a previous study (Lee et al., 2013). All model dimensions at zero-strain state are given in Table 3.1, whilst the generated LV geometry, along with its basal, endocardial and epicardial surfaces, is shown in Figure 3.1.

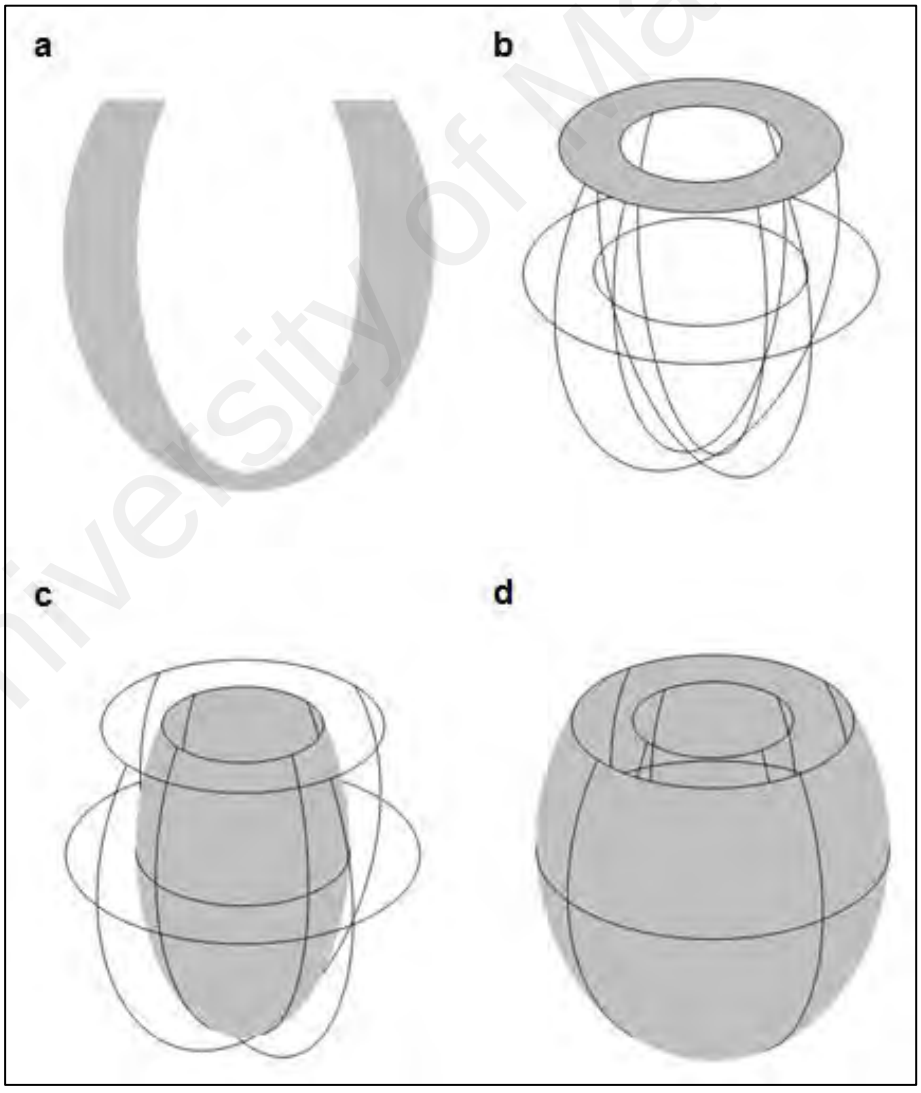

Figure 3.1: LV geometry (a), along with its basal (b), endocardial (c) and epicardial (d) surfaces.

Table 3.1: Dimensions of the LV geometry at zero-strain state.

Dimension	Value
Semi-minor axis length of the inner ellipsoid	20.29 mm
Semi-major axis length of the inner ellipsoid	40.58 mm
Truncated length of the inner ellipsoid	13.25 mm
Mid ventricle wall thickness	13.33 mm
Apex wall thickness	3.22 mm

3.3.2 Myocardial Fibre Orientation

Myocardial fibre orientation was assumed to vary transmurally from +60° at the endocardium to -60° at the epicardium, with respect to the circumferential direction (Pravdin et al., 2013).

In the COMSOL FE software package (COMSOL AB, Sweden), the tangent basis vectors: $\hat{\mathbf{e}}_1$, $\hat{\mathbf{e}}_2$ and $\hat{\mathbf{e}}_3$ are defined only at boundaries, as shown in Figure 3.2; with $\hat{\mathbf{e}}_3$ is normal to each boundary, whilst $\hat{\mathbf{e}}_1$ and $\hat{\mathbf{e}}_2$ are tangential to each boundary, with $\hat{\mathbf{e}}_1$ lying fully in the *x*-*y* plane, whilst $\hat{\mathbf{e}}_2$ is perpendicular to $\hat{\mathbf{e}}_1$. These tangent basis vectors at both the endocardial and epicardial surfaces were then made available for the entire LV geometry, using COMSOL identity mapping tool. By applying this tool, the local tangent basis vectors in the LV geometry were replicated from those defined at its corresponding closest points located at the endocardial and epicardial surfaces. In order to ensure that they vary smoothly across the LV wall, weighting was done on the local tangent basis vectors throughout the whole LV geometry:

$$\vec{\mathbf{u}} = (1-\beta)\hat{\mathbf{e}}_{endo} + \beta\hat{\mathbf{e}}_{epi} \tag{3.1}$$

where $\hat{\mathbf{e}}_{endo}$ and $\hat{\mathbf{e}}_{epi}$ are tangent basis vectors at the corresponding closest points at the endocardial and epicardial surfaces respectively, whilst β denotes the transmurality index:

$$\beta = \frac{d_{endo}}{d_{endo} + d_{epi}} \tag{3.2}$$

with d_{endo} (mm) and d_{epi} (mm) representing the distance from the local point to its corresponding closest points at the endocardial and epicardial surfaces respectively, computed using the in-built wall distance module in COMSOL. The wall distance module computes the distance of each point in the defined geometry (i.e. the LV geometry) to the closest defined wall (i.e. endocardium and epicardium), using modified Eikonal equations (Fares & Schröder, 2002):

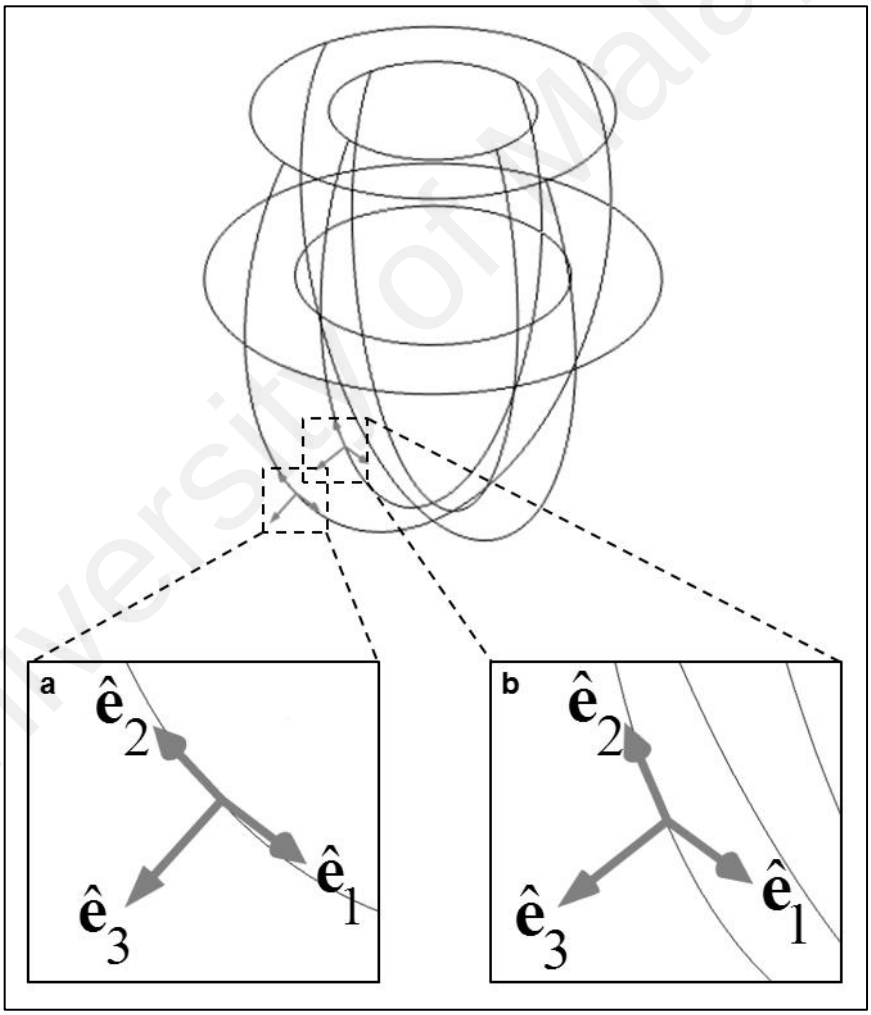

Figure 3.2: Tangent basis vectors ($\hat{e}_1$,$\hat{e}_2$ and $\hat{e}_3$) defined at the epicardial (a) and endocardial (b) surfaces, with $\hat{e}_3$ is normal to each boundary, whilst $\hat{e}_1$ and $\hat{e}_2$ are tangential to each boundary, with $\hat{e}_1$ lying fully in the x-y plane, whilst $\hat{e}_2$ is perpendicular to $\hat{e}_1$.

$$\nabla G \cdot \nabla G + \sigma_W G(\nabla \cdot \nabla G) = (1 + 2\sigma_W) G^4 \tag{3.3}$$

$$d = \frac{1}{G} - \frac{l_{ref}}{2} \tag{3.4}$$

where G (mm^{-1}) is the reciprocal of distance, d (mm), to the defined wall, whilst smoothing parameter, σ_W, was set to 0.2 by default in COMSOL for the LV geometry. At the defined wall, G is equivalent to $\frac{2}{l_{ref}}$, with the reference length, l_{ref} (mm), set by default in COMSOL to 6.72 mm for the LV geometry (COMSOL, 2012). The transmurality index, β, of the LV geometry is illustrated in Figure 3.3, for which 0 and 1 indicate the endocardium and epicardium respectively.

The circumferential ($\mathbf{u}_c$), longitudinal ($\mathbf{u}_l$) and radial ($\mathbf{u}_r$) base unit vectors of the LV geometry were then computed by:

$$\hat{\mathbf{u}}_h = \left. \frac{\vec{\mathbf{u}}_h}{|\vec{\mathbf{u}}_h|} \right|_{h=c,l,r} \tag{3.5}$$

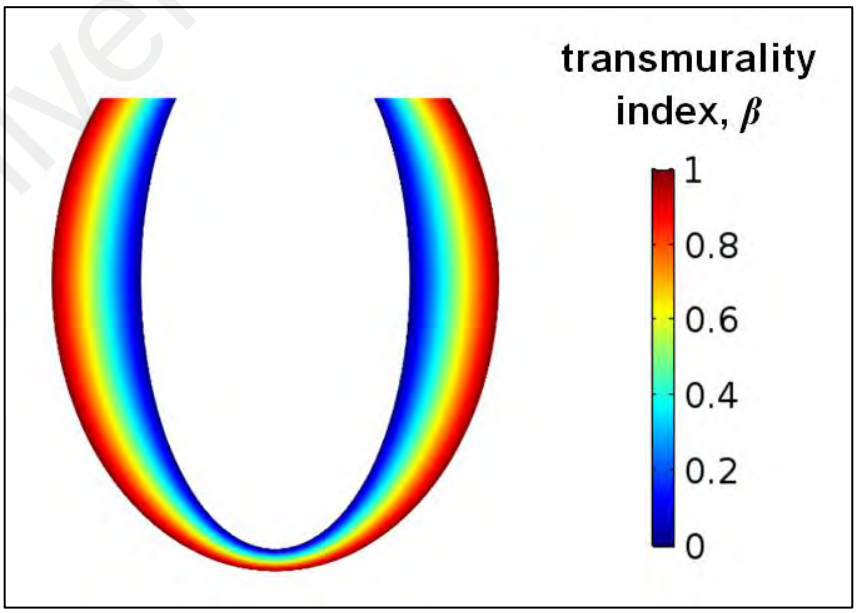

Figure 3.3: Transmurality index, β, of the LV geometry, in which 0 and 1 indicate the endocardium and epicardium respectively.

in which the subscript, $h = c, l, r$ represents the individual base vectors. The resultant $\mathbf{u}_c$, $\mathbf{u}_l$ and $\mathbf{u}_r$ base vectors are shown in Figure 3.4a. The $\mathbf{u}_c$ and $\mathbf{u}_l$ base vectors were then rotated with respect to the $\mathbf{u}_r$ base vector (r):

$$\hat{\mathbf{u}}_h' = \mathbf{R}\hat{\mathbf{u}}_h\big|_{h=c,l} \tag{3.6}$$

with $\hat{\mathbf{u}}_c'$, $\mathbf{u}_c$, $\hat{\mathbf{u}}_l'$ and $\mathbf{u}_l$ denoting the fibre (f), circumferential, sheet (s) and longitudinal base vectors respectively, whilst $\mathbf{R}$ is a rotational matrix defined as:

$$\mathbf{R} = \begin{bmatrix} \cos\theta + r_i^2(1-\cos\theta) & r_i r_j(1-\cos\theta) - r_k\sin\theta & r_i r_k(1-\cos\theta) + r_j\sin\theta \\ r_j r_i(1-\cos\theta) + r_k\sin\theta & \cos\theta + r_j^2(1-\cos\theta) & r_j r_k(1-\cos\theta) - r_i\sin\theta \\ r_k r_i(1-\cos\theta) - r_j\sin\theta & r_k r_j(1-\cos\theta) + r_i\sin\theta & \cos\theta + r_k^2(1-\cos\theta) \end{bmatrix} \tag{3.7}$$

where coefficients r_i, r_j and r_k represent the projections of the $\mathbf{u}_r$ base vector onto the local orthogonal coordinate system axes, i.e. i, j and k axes respectively, whilst θ (°) is the myocardial fibre angle, given by:

$$\theta = 60° - 120°\beta \tag{3.8}$$

The generated f, s and r directional base vectors are illustrated in Figure 3.4b, with the f direction changing transmurally across the LV wall (+60° at the endocardium to -60° at the epicardium, with respect to the $\mathbf{u}_c$ direction).

3.3.3 Electrophysiology Formulations

AP propagation from the apex to the base of the LV was simulated using the modified FitzHugh-Nagumo equations adopted from Aliev and Panfilov (1996):

$$\frac{\partial V}{\partial t} = \left(\sum_{i=1}^{3}\sum_{j=1}^{3}\frac{\partial D_{ij}}{\partial x_i}\frac{\partial V}{\partial x_j}\right) - kV(V-a)(V-1) - cIV + cI_s \tag{3.9}$$

$$\frac{\partial I}{\partial t} = (\varepsilon + \frac{\mu_1 I}{\mu_2 + V})[-cI - kV(V - b - 1)] \tag{3.10}$$

in which V refers to the dimensionless transmembrane potential with normalised amplitude between 0 and 1, and I represents the dimensionless conductance of a slow inward current, influencing the recovery of V and serving to activate the onset of t_s (s), a variable representing the total time after AP activation, which varies throughout the myocardium:

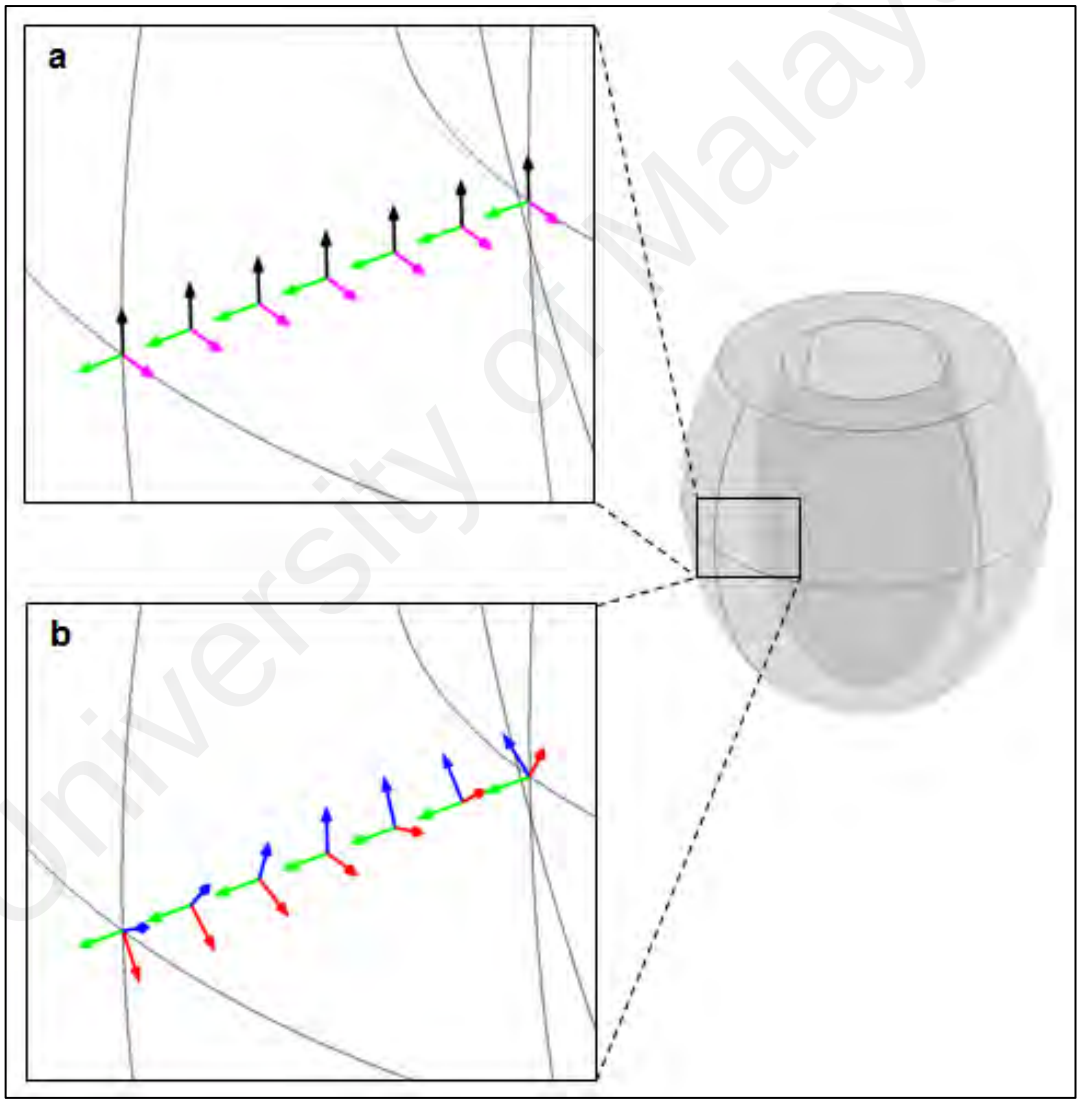

Figure 3.4: (a) Circumferential (u_c, pink), longitudinal (u_l, black) and radial (u_r, green) base vectors of the LV geometry. (b) Transmurally changing fibre (*f*, red), sheet (*s*, blue) and radial (*r*, green) directions across the LV wall.

$$\frac{\partial t_s}{\partial t} = \begin{cases} 1 & I > 0.002, \\ 0 & otherwise \end{cases} \tag{3.11}$$

Parameters a, b, c (s^{-1}), k (s^{-1}), ε, μ_1 and μ_2 regulate the shape and restitution properties of the AP, and I_s is a dimensionless external stimulus current, which was applied at the LV apex to initiate active contraction. x_i and x_j denote the unit vectors of the local orthogonal coordinate system axes, whilst D_{ij} (m^2/s) is the electrical conductivity tensor components for myocardium, as given by:

$$D_{ij} = f_i f_j D_f + s_i s_j D_t + r_i r_j D_t \tag{3.12}$$

where D_f (m^2/s) and D_t (m^2/s) are the fibre and cross-fibre conductivities respectively. The components f, s and r represent the projections of fibre, sheet and radial base vectors respectively, onto the global orthogonal coordinate system axes denoted by their subscripts i and j.

3.3.4 Passive Material Model Formulations

The passive mechanical properties of myocardium were modelled as a quasi-static, nearly-incompressible hyperelastic material by using a non-linear strain energy function, W (kPa). Transversely isotropic behaviour was assumed, aligned with the local defined fibre direction. Nearly-incompressible behaviour was imposed by using a Lagrangian multiplier, p (MPa) (Choi et al., 2011):

$$W = \frac{1}{2} C_0 (e^Q - 1) + p(J - 1) \tag{3.13}$$

where C_0 (kPa) represents the overall stiffness of myocardium, whilst J is the volumetric strain, defined as the fractional volume change of a local infinitesimal region under deformation. J is equal to 1 for volume-preserving strains, and is given by the

determinant of the deformation gradient tensor. Q was expressed in terms of the local strain components as:

$$Q = b_f E_{ff}^{\ 2} + b_t (E_{ss}^{\ 2} + E_{rr}^{\ 2} + 2E_{sr}^{\ 2}) + 2b_{fa}(E_{fs}^{\ 2} + E_{fr}^{\ 2}) \tag{3.14}$$

with parameters b_f, b_t and b_{fa} describing the exponential stress-strain relation of the material (J. M. Guccione, Costa, & McCulloch, 1995). E_{pq} represents components of the Green-Lagrange strain tensor, with the f, s and r subscripts denoting the local fibre, sheet and radial directions respectively:

$$\begin{bmatrix} E_{ff} & E_{fs} & E_{fr} \\ E_{sf} & E_{ss} & E_{sr} \\ E_{rf} & E_{rs} & E_{rr} \end{bmatrix} = \begin{bmatrix} f_i & f_j & f_k \\ s_i & s_j & s_k \\ r_i & r_j & r_k \end{bmatrix} \begin{bmatrix} E_{ii} & E_{ij} & E_{ik} \\ E_{ji} & E_{jj} & E_{jk} \\ E_{ki} & E_{kj} & E_{kk} \end{bmatrix} \begin{bmatrix} f_i & s_i & r_i \\ f_j & s_j & r_j \\ f_k & s_k & r_k \end{bmatrix} \tag{3.15}$$

in which subscripts i, j and k represent the global orthogonal coordinate system axis components of the Green-Lagrange strain tensor, as well as the f, s and r base vectors.

3.3.5 Active Contraction Formulations

In a previous study, Rice et al. (2008) developed a point model of cardiac myofilament dynamics based on experimental studies performed on rats, to characterise myofilament properties, including characterising isometric twitch force as a function of sarcomere length. To replicate the isometric twitch force, an equation for the active tension, T_a (kPa), was formulated:

$$T_a = A \frac{t_s^{\ 2}}{\tau} e^{-\frac{t_s^{\ \eta}}{\tau}} \tag{3.16}$$

where t_s (s) denotes the local time of active contraction, as described in Equation 3.11. A defines the amplitude of T_a, whilst τ and η determine the onset and offset rates:

$$A = T_0(A_3\lambda^3 + A_2\lambda^2 + A_1\lambda + A_0) \tag{3.17}$$

$$\tau = \tau_0(m_\tau \lambda + c_\tau) \tag{3.18}$$

$$\eta = \eta_0(m_\eta \lambda + c_\eta) \tag{3.19}$$

Parameters T_0 (kPa), A_3 (μm^{-3}), A_2 (μm^{-2}), A_1 (μm^{-1}), A_0, τ_0, m_τ (μm^{-1}), c_τ, η_0, m_η (μm^{-1}) and c_η are coefficients for the polynomial functions of A (kPa), τ and η, with λ (μm) denoting the local sarcomere length, as defined by:

$$\lambda = \lambda_0 \sqrt{2E_{ff} + 1} \tag{3.20}$$

with λ_0 (μm) representing the reference sarcomere length at zero strain.

LV active contraction was modelled by adding T_a to the passive stress in the myocardial fibre direction, whilst 40% of T_a was added to the stress in the cross-fibre directions (Walker et al., 2005):

$$S_{pq} = \frac{\partial W}{\partial E_{pq}} + (0.6\delta_{pf}\delta_{fq} + 0.4\delta_{pq})T_a \tag{3.21}$$

in which S_{pq} denotes the p, q^{th} components of the second Piola-Kirchhoff stress tensor (p, $q = f$, s, r), whilst δ is the Kronecker delta.

3.3.6 Boundary Conditions

The basal LV surface was held fixed to account for the effect of the left atrium (LA) and valve annuli. For simplicity, no pressure was applied on the epicardium, similar to previous FE studies (Choi et al., 2011; Wenk et al., 2012). A complete LV cycle was simulated according to the following steps:

i. During diastole, an LV pressure, P_{LV} (mmHg), value of 8 mmHg was imposed on the LV endocardium (Choi et al., 2011).

ii. To simulate isovolumic contraction (IVC), the LV cavity volume, V_{LV} (ml), was held constant, whilst P_{LV} was solved concurrently as an additional variable associated with this constant-volume constraint. The end of IVC was assumed to be reached when P_{LV} achieved 80 mmHg, at which instant the aortic valve was deemed to open.

iii. In simulating the subsequent ejection phase, the isovolumic constraint boundary condition was replaced by a 3-element Windkessel model to compute the P_{LV} associated with the effect of blood ejection:

$$P_{LV} = P_A + Q_A R_c \tag{3.22}$$

$$C_p \frac{dP_A}{dt} + \frac{P_A}{R_p} - Q_A = 0 \tag{3.23}$$

where P_A (mmHg) represents the distal arterial blood pressure and Q_A (ml/s) denotes the rate of blood flow being ejected from the LV. In the Windkessel model, R_c (mmHg•s/ml), R_p (mmHg•s/ml) and C_p (ml/mmHg) are the aortic root impedance, peripheral impedance and peripheral capacitance respectively. The ejection phase ended when P_A was greater than P_{LV}, at which point the aortic valve was deemed to close.

iv. In the subsequent isovolumic relaxation (IVR) phase, an isovolumic constraint boundary condition similar to the IVC phase was used to replace the Windkessel model. The IVR phase was assumed to be complete when P_{LV} reached 0 mmHg, at which instant the mitral valve opened.

v. Finally, early diastole was simulated by applying a P_{LV} of 0 mmHg to the LV endocardium, such that the LV returned to its reference (i.e. zero-strain) state.

3.3.7 Optimisation of Parameter Values

The parameter values of a, b, ε, μ_1 and μ_2 were adopted from Nash and Panfilov (2004). Constants c and k were adjusted to reproduce the physiological shape and restitution duration of the cardiac AP. D_f and D_t were tuned to reproduce the ratio of fibre to cross-fibre conduction speed reported in a previous study (Potse et al., 2006), as well as the reported physiological activation time of the whole LV (Ramanathan, Jia, Ghanem, Ryu, & Rudy, 2006).

C_0 was set such that LV EDV equalled 118.7 ml, as reported by Schlosser et al. (2005). The values of the stress-strain parameters, b_f, b_t and b_{fa}, were adopted from Wenk et al. (2012). λ_0 was set to 1.9 μm, following the value reported by Rice et al. (2008). The parameters used in the formulation of T_a (i.e. A_3, A_2, A_1, A_0, τ_0, m_τ, c_τ, η_0, m_η and c_η) were first optimised to reproduce the isometric twitch force reported by Rice et al. (2008). Parameters τ_0 and η_0 were then further tuned to regulate the onset and offset rates of T_a, together with the optimisation of the Windkessel model input parameters (R_c, R_p and C_p), to produce physiological P_{LV} and V_{LV} values comparable to a standard Wiggers diagram (Guyton & Hall, 2006). Subsequently, T_0 was regulated to reproduce previously reported ESV (Schlosser et al., 2005).

3.3.8 Infarct Models

To compare the effects of infarct size and TME, four models were simulated:

i. healthy LV model (NORMAL),

ii. large but nontransmural infarct model (L-XTR),

iii. small but transmural infarct model (S-TR),

iv. large and transmural infarct model (L-TR).

While infarct was introduced, its shape was kept rounded (to avoid sharp edges, which can affect stress distribution), and at the same time, it was kept some distance away from the basal surface and apex (to avoid boundary effects). The volume, area (measured at the endocardium) and TME of the generated infarcts are given in Table 3.2. Infarct TME was calculated by:

$$\text{TME} = \frac{\text{Infarct Volume}}{\text{Endocardial Area Covered} \times \text{Mid Ventricle Wall Thickness}} \times 100\% \quad (3.24)$$

The infarcts were considered as transmural if TME exceeded 50%, and nontransmural otherwise (Becker et al., 2009). Infarct zone (IZ) was approximated as having a threefold passive stiffness to that of the remote zone (RZ), in accordance with its reportedly higher stiffness at 6 weeks (Gupta, Ratcliffe, Fallert, Edmunds, & Bogen, 1994; Hiesinger et al., 2012), the timeframe at which remodelling is believed to take place. To account for the lower electrical conductivity of IZ, the conductivity parameters, D_f and D_t, were manually tuned such that the ratio of conduction velocity of RZ to IZ matched the ratio reported in Abd-Elmoniem et al. (2012). In regards to its active contractile property, the IZ was assumed to have zero contractility (T_0 = 0 kPa), corresponding to its non-contractile property (Wenk et al., 2012).

To ensure smooth transition of material properties across the RZ and IZ, a border zone (BZ) was introduced between the RZ and IZ. The BZ properties (C_0, D_f, D_t and T_0) were modelled as gradually transitioning from the RZ to the IZ following the pattern illustrated in Figure 3.5, with blue and red colours representing the RZ and IZ respectively, whilst in-between colours describe the BZ transition from the RZ to the IZ.

3.3.9 Mesh Independence Test

The LV geometry was meshed with quadratic tetrahedral elements. The mesh size was then adjusted until the average end-systolic fibre strain (i.e. engineering strain along

Table 3.2: Infarct volume, area at the endocardium, and TME for each model.

Model	Infarct volume (cm^3)	Infarct area at the endocardium (cm^3)	Infarct TME (%)
L-XTR	9.31	16.50	42.3
S-TR	9.11	7.38	92.6
L-TR	22.72	16.39	104.0

TME: transmural extent; L-XTR, S-TR and L-TR: infarct models with varying infarct sizes and TMEs.

the local myocardial fibre direction) at the IZ of the L-TR model changed by less than 1%. It was found that the physics-controlled automated fine mesh size setting, which had a total number of 10833 tetrahedral elements, and a maximum element size of 5.69 mm, was sufficient for this study. The total number of elements, maximum element size, and average end-systolic fibre strain at the IZ using different mesh options are given in Table 3.3. The meshes generated from the physics-controlled fine and finer mesh options, along with the deformed meshes of the NORMAL model (meshed with the physics-controlled fine mesh option) at both end-diastole and end-systole are shown in Figure 3.6.

The resulting non-linear equations were solved monolithically using the PARDISO solver with generalised alpha time stepping method in COMSOL (v4.4, COMSOL AB, Sweden). An absolute tolerance of 1.0×10^{-3} and a time step of 5 ms were used for the LV cycle simulations. The models were solved using an Intel Xeon E5-2620 6-core 2.00 GHz processor with 64 GB of RAM. It took nearly seven hours to compute a full LV cycle.

To ensure the physiological relevance of the generated NORMAL model, its performance was compared with previously reported LV studies. Subsequently, preliminary analysis was performed on the regional mechanics of the infarct LV models, to determine the role of infarct size and TME on LV regional mechanics.

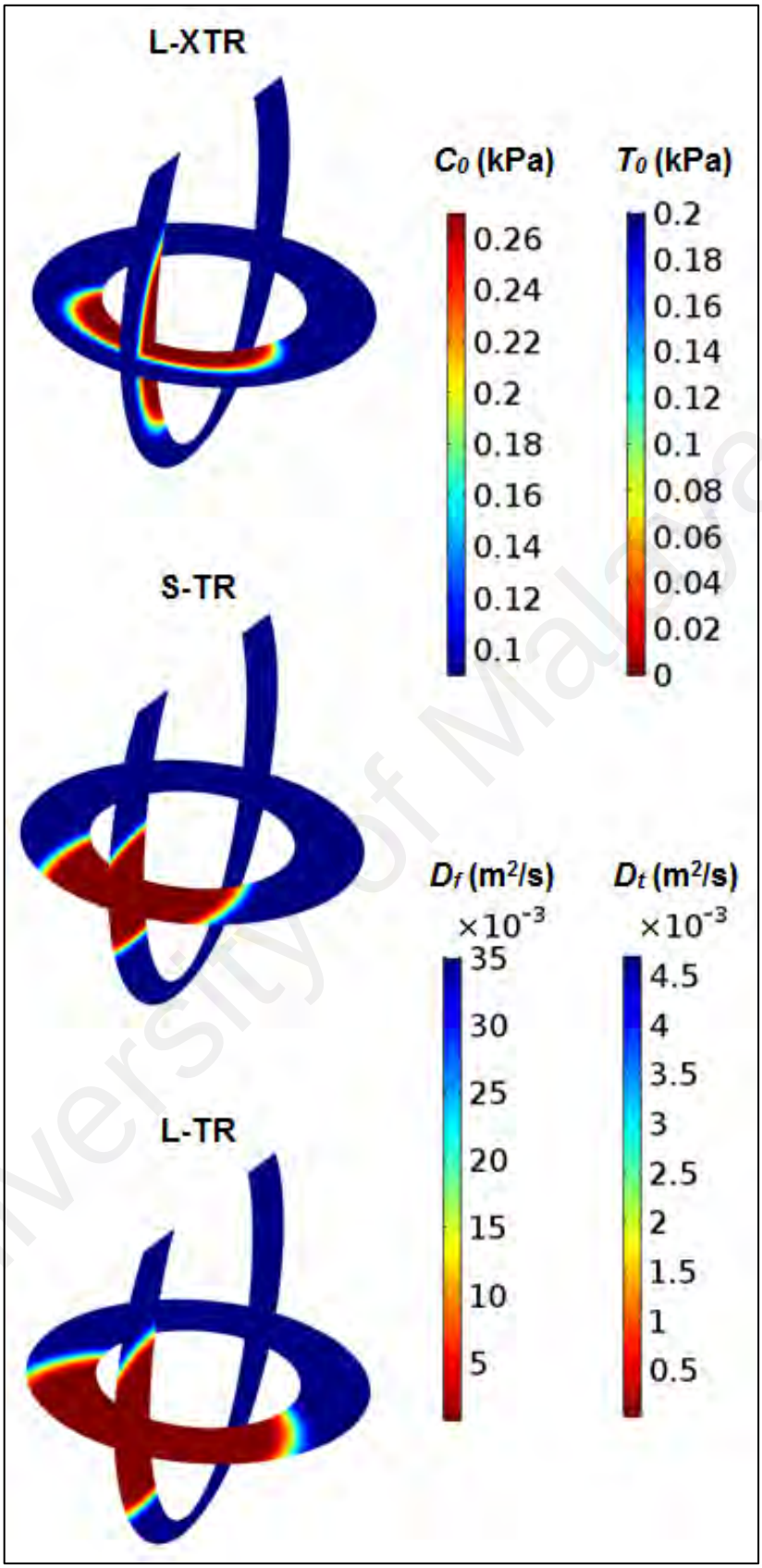

Figure 3.5: Generated infarct models with varying infarct size and transmural extents (TMEs). The scales show the myocardial properties (C_0, D_f, D_t and T_0), with blue and red colours representing remote zone (RZ) and infarct zone (IZ) respectively, whilst in-between colours describe the border zone (BZ) transition from the RZ to the IZ.

Table 3.3: Comparison of the total number of elements, maximum element size, and average end-systolic fibre strain (engineering strain along the local myocardial fibre direction) at the IZ using two different mesh settings for the L-TR model.

Physics-controlled mesh option	Fine	Finer
Total number of elements	10833	31574
Maximum element size (mm)	5.69	3.91
Average IZ fibre strain	0.1701	0.1699
Percentage change in IZ fibre strain		0.12%

IZ: infarct zone.

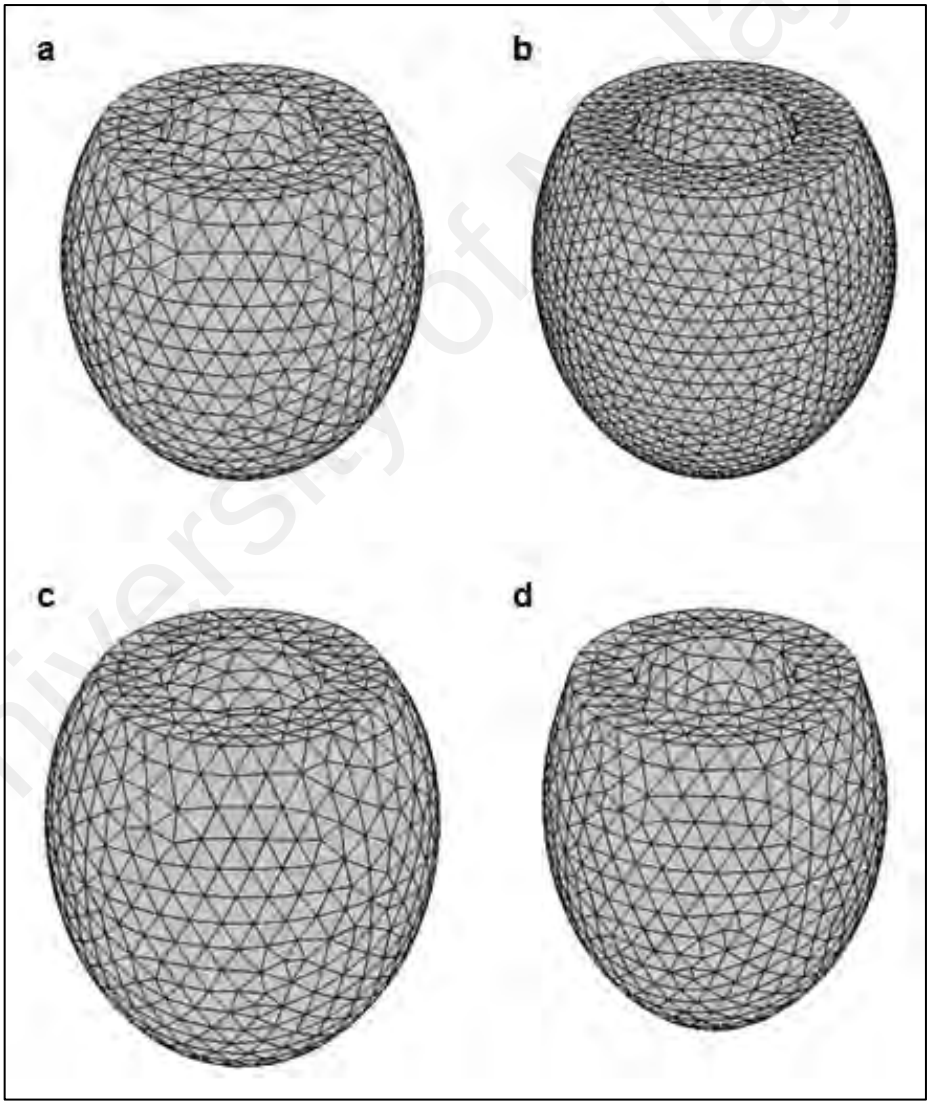

Figure 3.6: Undeformed meshes generated from the physics-controlled (a) fine and (b) finer mesh options. Deformed meshes of the NORMAL model (meshed with the physics-controlled fine mesh option) at (c) end-diastole and (d) end-systole.

3.4 Results

Estimated parameter values of the LV models are listed in Table 3.4.

3.4.1 Electrophysiological Functions

Figure 3.7 shows the AP profiles of two selected points in a simple 3D block (15×15×100 mm, with points 50 mm apart as shown in Figure 3.7a), using the conductivity settings of RZ fibre (D_f at the RZ), RZ cross-fibre (D_t at the RZ), IZ fibre (D_f at the IZ) and IZ cross-fibre (D_t at the IZ) directions. The AP duration was approximately 200 ms, regardless of the conductivity and location.

Conduction velocity obtained in the present study for the different conductivity settings was compared to values recorded in previous studies (Table 3.5) (Abd-Elmoniem et al., 2012; Potse et al., 2006). In the present study, the AP propagation was the fastest for the RZ fibre conductivity setting, followed by RZ cross-fibre, IZ fibre and lastly IZ cross-fibre conductivity settings, with recorded values of 4176 mm/s, 1543 mm/s, 627 mm/s and 231 mm/s respectively. This yielded a ratio of 2.71 for fibre to cross-fibre conduction velocity, at both the RZ and IZ; and a ratio of 6.66 and 6.68 for RZ to IZ conduction velocity along the fibre and cross-fibre directions respectively.

Figure 3.8 presents the activation times for the endocardium and epicardium of the NORMAL model. It took approximately 30 ms for the AP to travel from the apex to the base of the NORMAL model, for both the endocardium and epicardium.

3.4.2 Mechanical Functions

Figure 3.9 illustrates the isometric twitch force-time profiles as a function of sarcomere length, λ, recorded in Rice et al. (2008) and replicated in the present study. The isometric twitch force-time waveforms exhibited a right-skewed, bell-shaped

profile regardless of the λ value. The amplitude, duration and time to reach the maximum twitch force amplitude, were observed to increase with increasing λ.

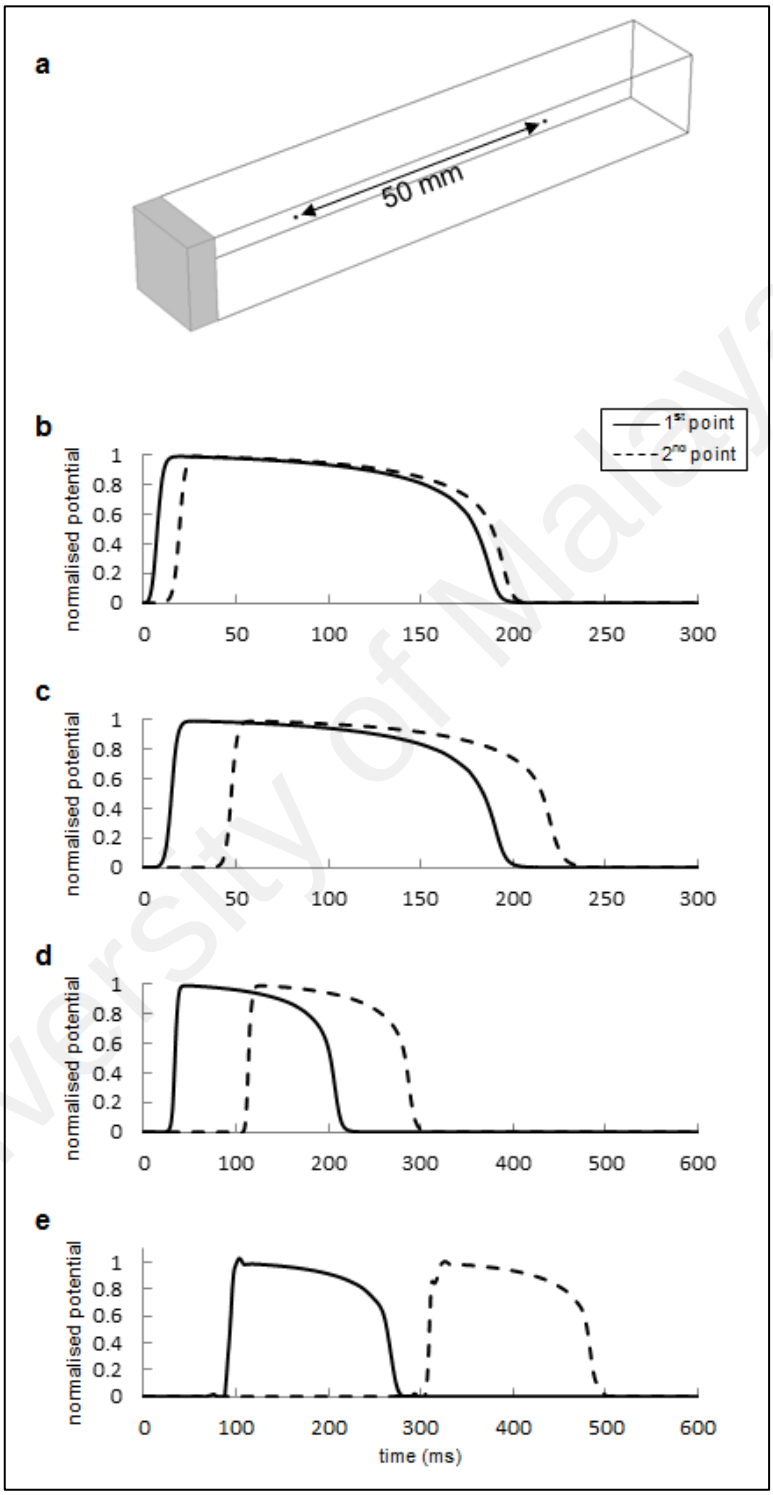

Figure 3.7: (a) Simple 3D block (15×15×100 mm) used for determining the action potential (AP) conduction velocity, with the stimulus current, I_s, applied at the shaded region (5 mm long). AP profiles of the two selected points in Figure 3.7a (50 mm apart), using the conductivity settings of (b) RZ fibre, (c) RZ cross-fibre, (d) IZ fibre and (e) IZ cross-fibre.

Table 3.4: LV model parameter values.

Parameter	Value
Electrophysiology formulations	
a	0.1
b	0.1
c	200 s^{-1}
k	1600 s^{-1}
ε	0.01
μ_1	0.12
μ_2	0.3
I_s	2
D_f	35e-3 m^2/s
D_t	4.7e-3 m^2/s
Passive material model formulations	
C_0	0.090 kPa
b_f	24.63
b_t	9.63
b_{fa}	8.92
p	1 MPa
Active contraction formulations	
λ_0	1.9 μm
T_0	0.2 kPa
A_3	309.5 μm^{-3}
A_2	-1497.3 μm^{-2}
A_1	2428.6 μm^{-1}
A_0	-1320.2
τ_0	0.01
m_τ	0.0604 μm^{-1}
c_τ	-0.0719
η_0	6.5
m_η	-0.5257 μm^{-1}
c_η	1.9744
Windkessel properties	
R_c	0.04 mmHg*s/ml
R_p	1.18 mmHg*s/ml
C_p	0.39 ml/mmHg
Infarct properties	
C_0	0.270 kPa
D_f	75e-5 m^2/s
D_t	3.5e-5 m^2/s
T_0	0 kPa

Table 3.5: AP propagation velocity as recorded in previous and present studies.

Conduction velocity (mm/s)				
	Fibre (RZ)	**Cross-fibre (RZ)**	**Fibre (IZ)**	**Cross-fibre (IZ)**
Potse et al. (2006)	770	278		
Abd-Elmoniem et al. (2012)	390±205		57±24	
This study	4176	1543	627	231
Ratio				
	Fibre/cross-fibre (RZ)	**Fibre/cross-fibre (IZ)**	**RZ/IZ (fibre)**	**RZ/IZ (cross-fibre)**
Potse et al. (2006)	2.77			
Abd-Elmoniem et al. (2012)			6.84	
This study	2.71	2.71	6.66	6.68

RZ: remote zone; IZ: infarct zone.

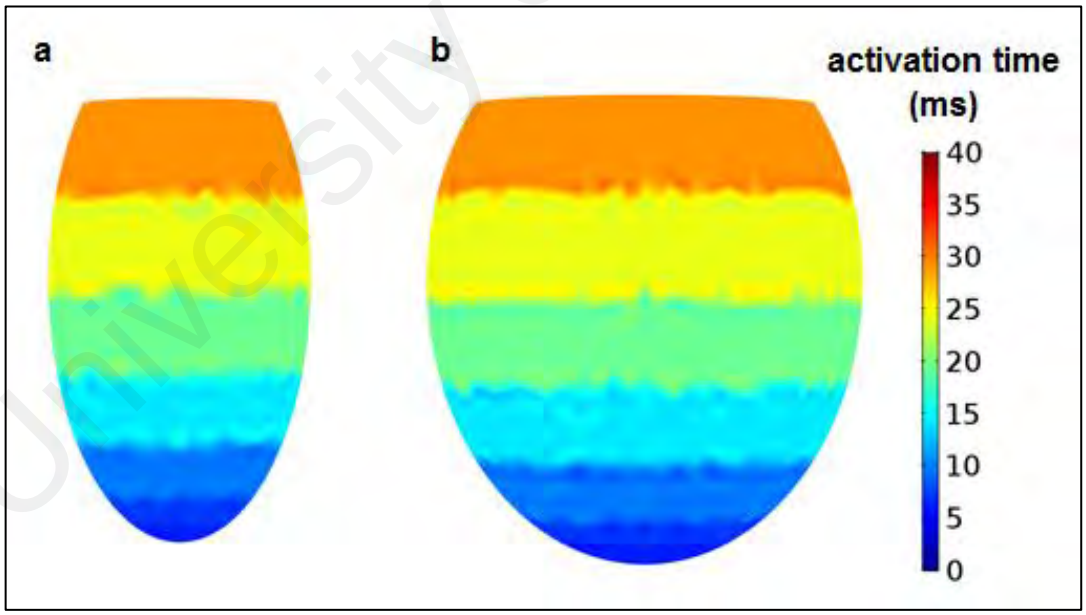

Figure 3.8: Activation times for the (a) endocardium and (b) epicardium of the NORMAL model.

The full cycle trajectories of P_{LV} and V_{LV} of the NORMAL model are shown in Figure 3.10. During diastole (t = 0-0.5 s), both the P_{LV} and V_{LV} increased with time, reaching 8 mmHg and 118.7 ml respectively, at end-diastole. During systole (t = 0.5-0.787 s), the LV contracted, elevating the P_{LV} to a systolic pressure of 120.5 mmHg, and reducing the V_{LV} to an ESV of 49.9 ml.

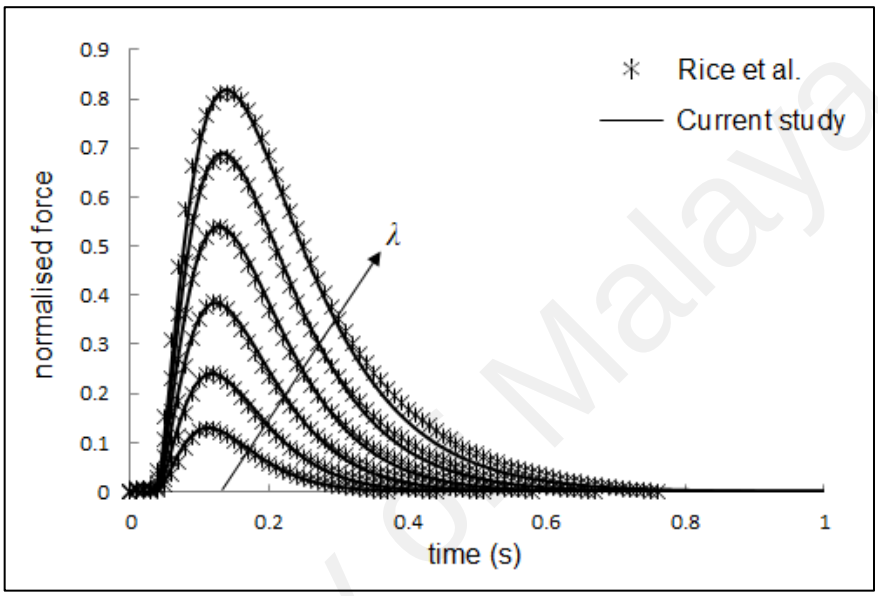

Figure 3.9: Isometric twitch force-time profiles as a function of sarcomere length, λ (from 1.8 to 2.3 µm with an increment of 0.1 µm), reported in Rice et al. (2008) (*) (Rice, Wang, Bers, & De Tombe, 2008) and replicated in the present study (—).

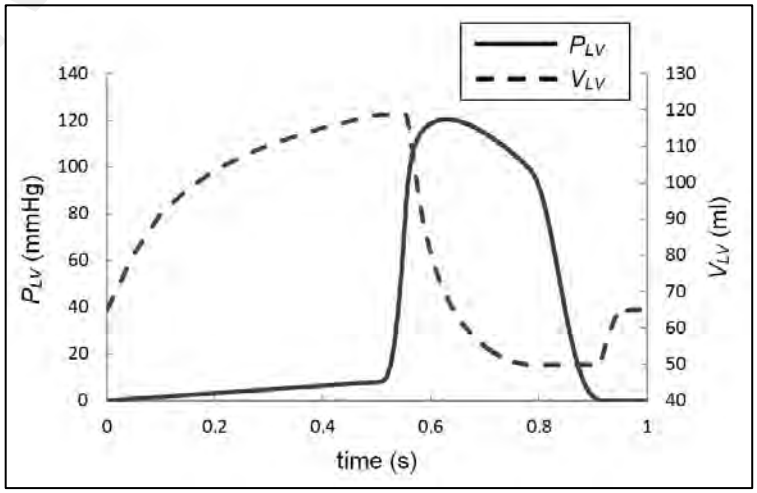

Figure 3.10: Simulated time course of P_{LV} and V_{LV} for the NORMAL model. P_{LV}: left ventricular pressure; V_{LV}: left ventricular cavity volume.

Figure 3.11 presents the twist angle (counterclockwise as viewed from the apical end) of apical mid wall myocardium over the entire LV cycle of the NORMAL model, starting from the ejection phase. LV twisting increased with ejection and reached a maximum twist angle of 17.9° at the IVR phase. The LV untwisted at the latter stage of IVR and during early diastole, before twisting again during late diastole. In regards to wall thickness, the mid ventricle kept thickening during systole, reaching a maximum wall thickening of 45.0% at end-systole, with respect to the end-diastolic wall thickness, as shown in Figure 3.12.

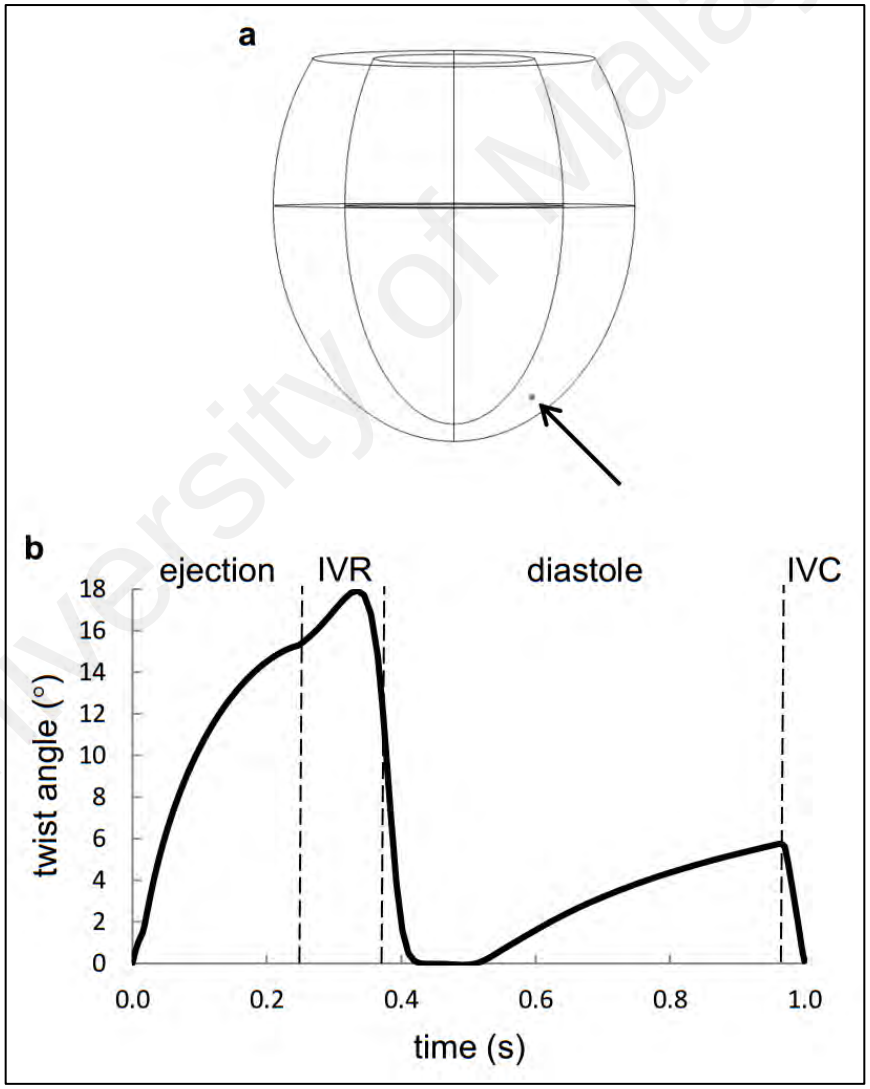

Figure 3.11: (b) Twist angle (counterclockwise as viewed from the apical end) over the entire LV cycle of the NORMAL model, starting from the ejection phase, generated from (a) a point located at the apical mid wall, as shown by the arrow. IVR: isovolumic relaxation; IVC: isovolumic contraction.

3.4.3 Regional Mechanics of the Generated Models

Figure 3.13 shows the short axis transmural distributions of circumferential, longitudinal and fibre strains (engineering strain along the circumferential, longitudinal and local myocardial fibre directions respectively) for the NORMAL model at end-systole (referenced to zero-strain state). Meanwhile, Figures 3.14 and 3.15 illustrate the fibre strain distributions at the subendocardium ($\beta = 0.17$) and subepicardium ($\beta = 0.83$) respectively, of the simulated LV models at end-systole. At the subendocardium, the fibre strain appeared to be the highest at the IZ for the S-TR and L-TR models, whilst the IZ of the L-XTR model exhibited moderately high fibre strain. However, abnormal fibre strain distribution was seen only at the subepicardium of the S-TR and L-TR models, but not for the L-XTR model. Overall, the average IZ fibre strain exhibited by the S-TR and L-TR models was lower at end-diastole, but higher at end-systole, compared to that of the L-XTR model, as given in Table 3.6.

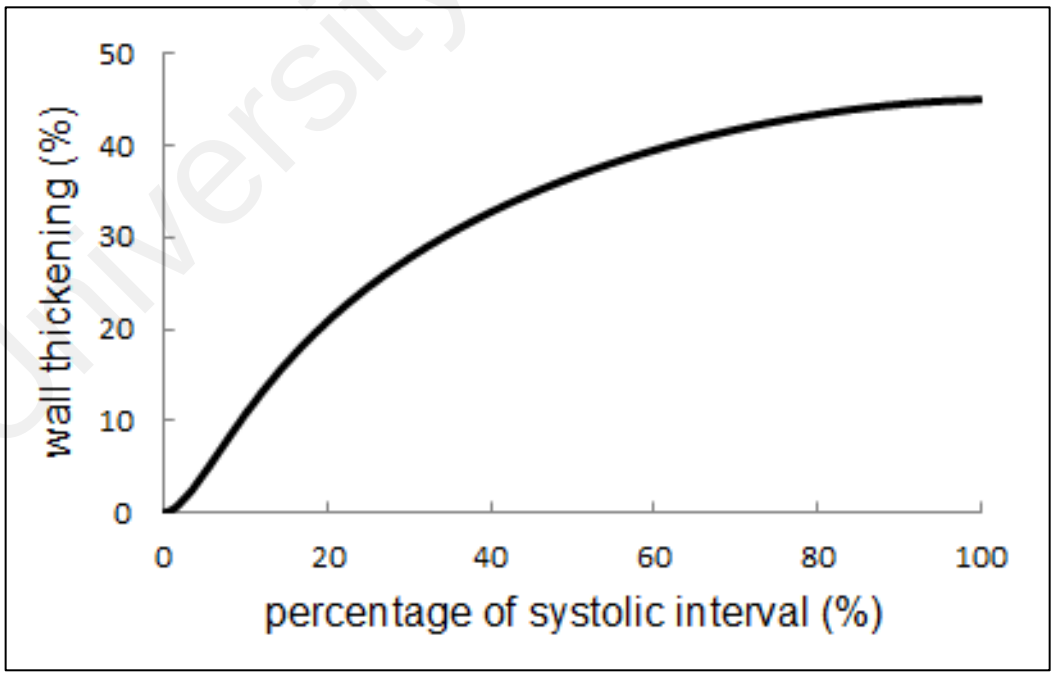

Figure 3.12: Wall thickening percentage of the NORMAL model mid ventricle during systole, with respect to its end-diastolic wall thickness.

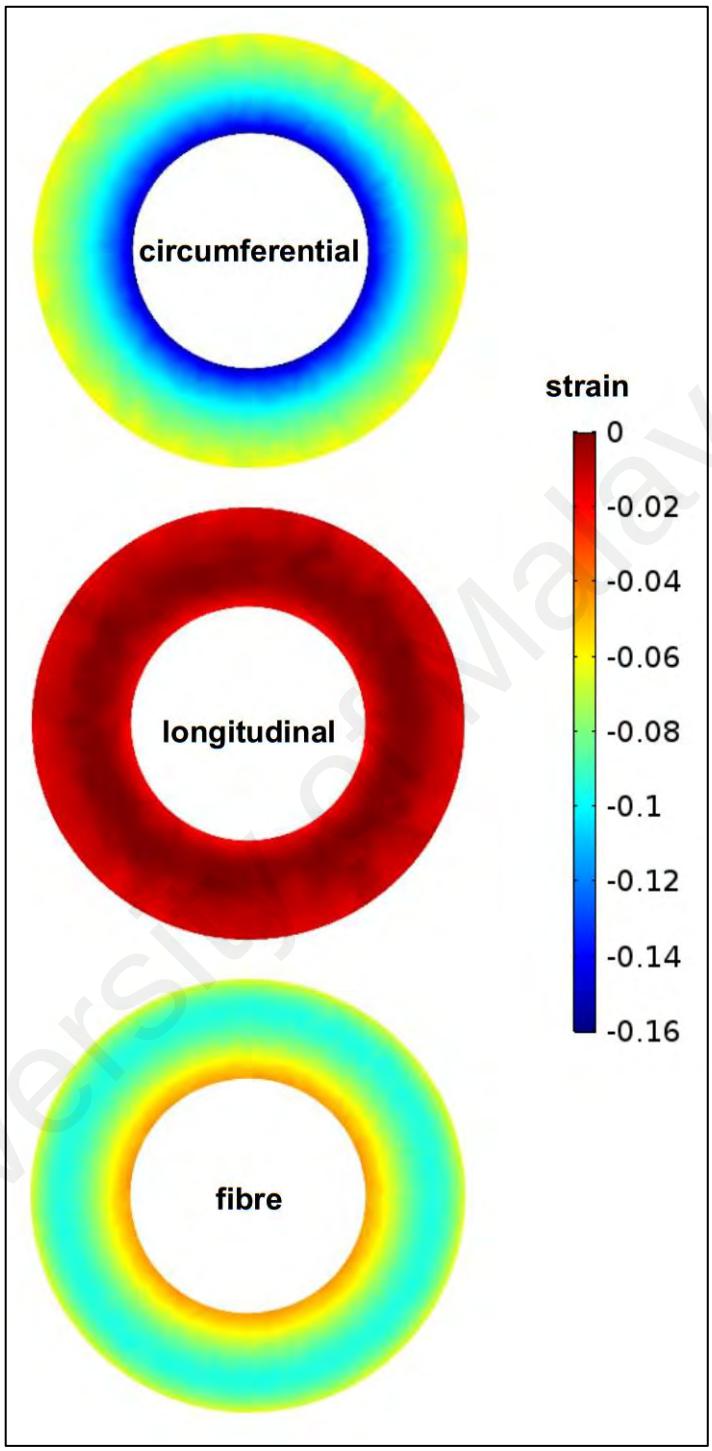

Figure 3.13: Transmural distributions of circumferential, longitudinal and fibre strains for the NORMAL model in short axis view (referenced to zero-strain state).

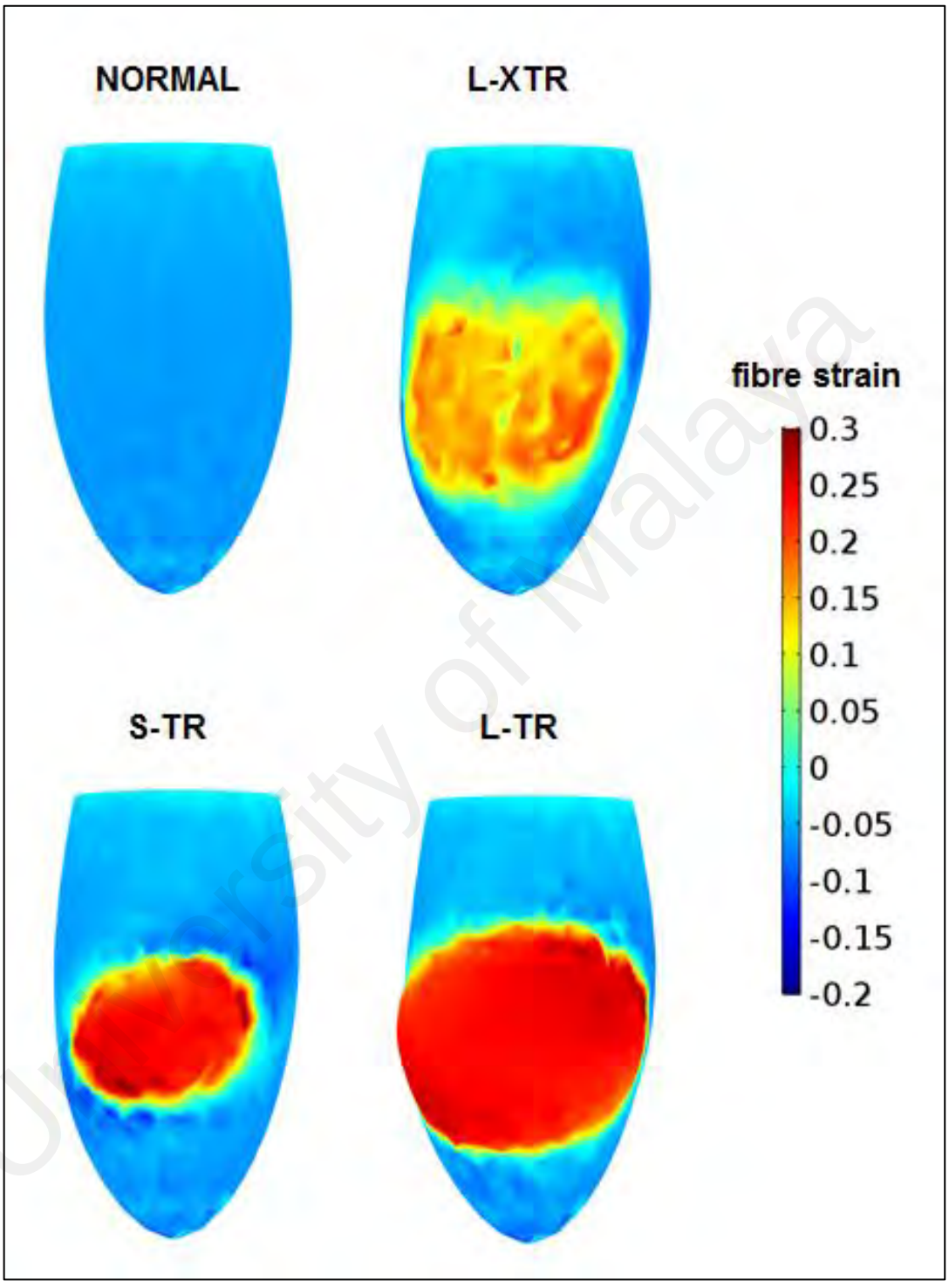

Figure 3.14: Fibre strain (engineering strain along the local myocardial fibre direction) distributions at the subendocardium (transmurality index, $\beta = 0.17$) of the simulated LV models at end-systole (referenced to zero-strain state).

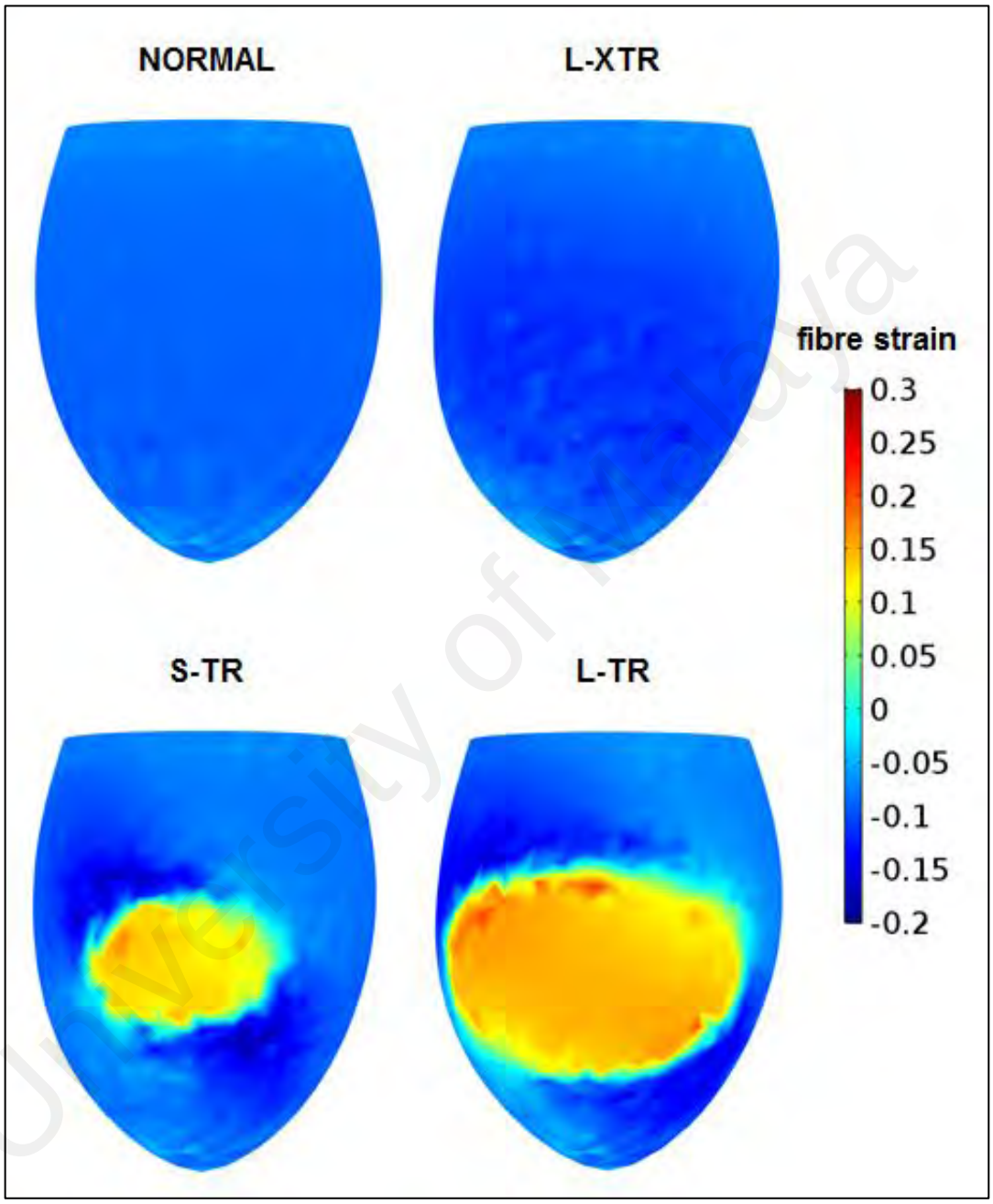

Figure 3.15: Fibre strain distributions at the subepicardium (β = 0.83) of the simulated LV models at end-systole (referenced to zero-strain state).

Table 3.6: Average IZ fibre strain of the simulated infarct models at end-diastole and end-systole.

Model	End-diastole	End-systole
L-XTR	0.118	0.135
S-TR	0.104	0.150
L-TR	0.101	0.170

L-XTR, S-TR and L-TR: infarct models with varying infarct sizes and TMEs.

The fibre stress (Cauchy stress along the local myocardial fibre direction) distributions at the subendocardium and subepicardium of the simulated models at end-systole are shown in Figures 3.16 and 3.17 respectively. For the subendocardium, relatively high fibre stress was evident at the upper-left and lower-right corners of the IZ. Higher fibre stress was recorded for the S-TR and L-TR models, which had peak magnitudes of 146.9 kPa and 148.6 kPa respectively, compared to the L-XTR model, which had a peak magnitude of only 117.1 kPa. The high stress observed at the base of the simulated models was a consequence of the fixed base boundary condition, and therefore can be ignored. For the subepicardium, the upper-right and lower-left corners of the IZ demonstrated comparatively higher stress than other regions for the S-TR and L-TR models, but not for the L-XTR model.

Figures 3.18 and 3.19 present the shear stress (Cauchy stress transverse to the local myocardial fibre direction) distributions at the subendocardium and subepicardium respectively, of the simulated models at end-systole. At the subendocardium, moderately high shear stress was seen at the apical region for the L-XTR model (42.3 kPa) and at the superior of the IZ of the L-TR model (42.4 kPa). Meanwhile, extremely high shear stress was displayed at the inferior and right side of the IZ of the S-TR model (80.9 kPa). However, no augmented shear stress region was observed at the subepicardium in the simulated infarct models. Overall, the strain and stress

distributions at the subendocardium appeared to be more abnormal than that of the subepicardium.

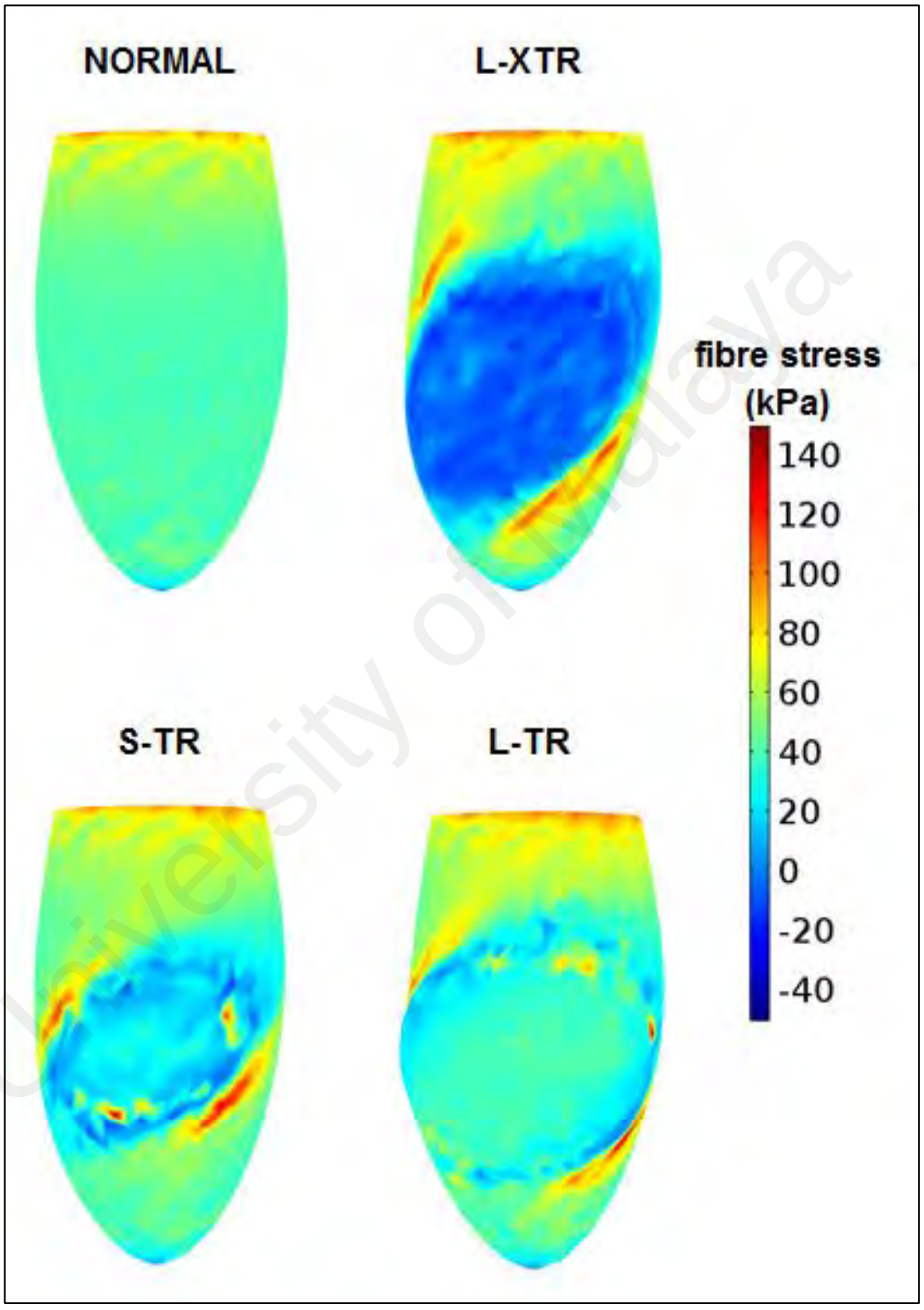

Figure 3.16: Fibre stress (Cauchy stress along the local myocardial fibre direction) distributions at the subendocardium of the simulated LV models at end-systole.

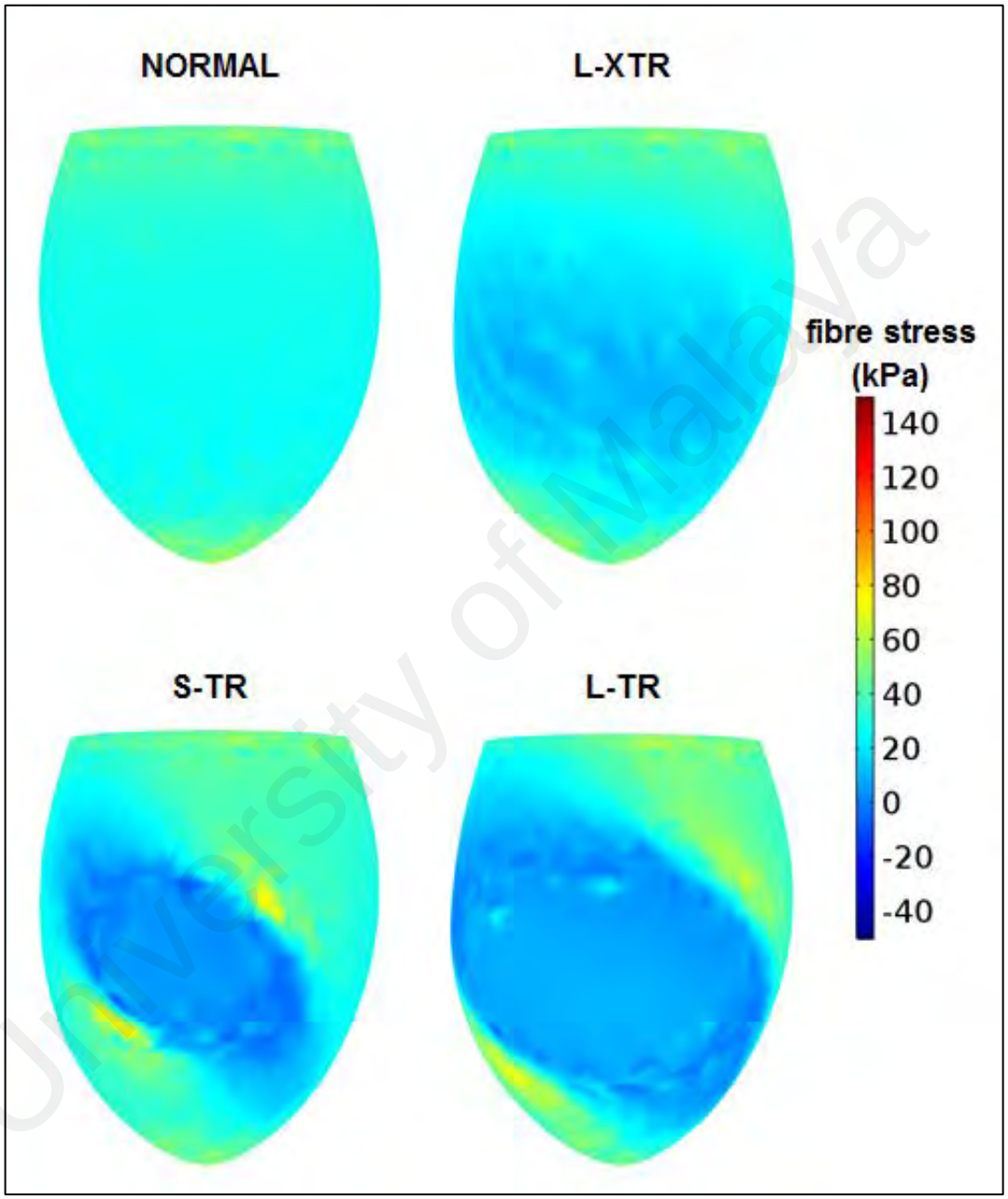

Figure 3.17: Fibre stress distributions at the subepicardium of the simulated LV models at end-systole.

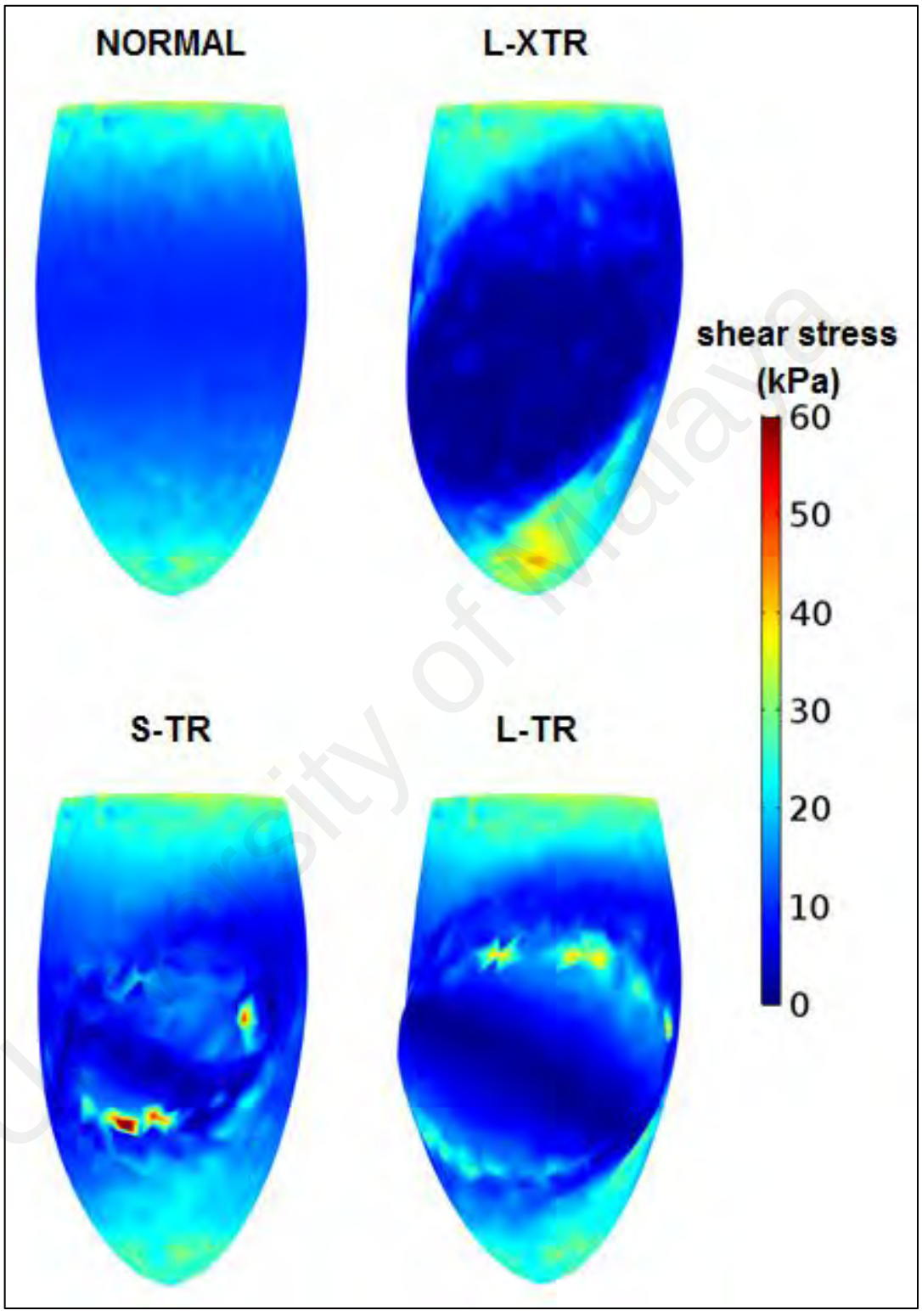

Figure 3.18: Shear stress (Cauchy stress transverse to the local myocardial fibre direction) distributions at the subendocardium of the simulated LV models at end-systole.

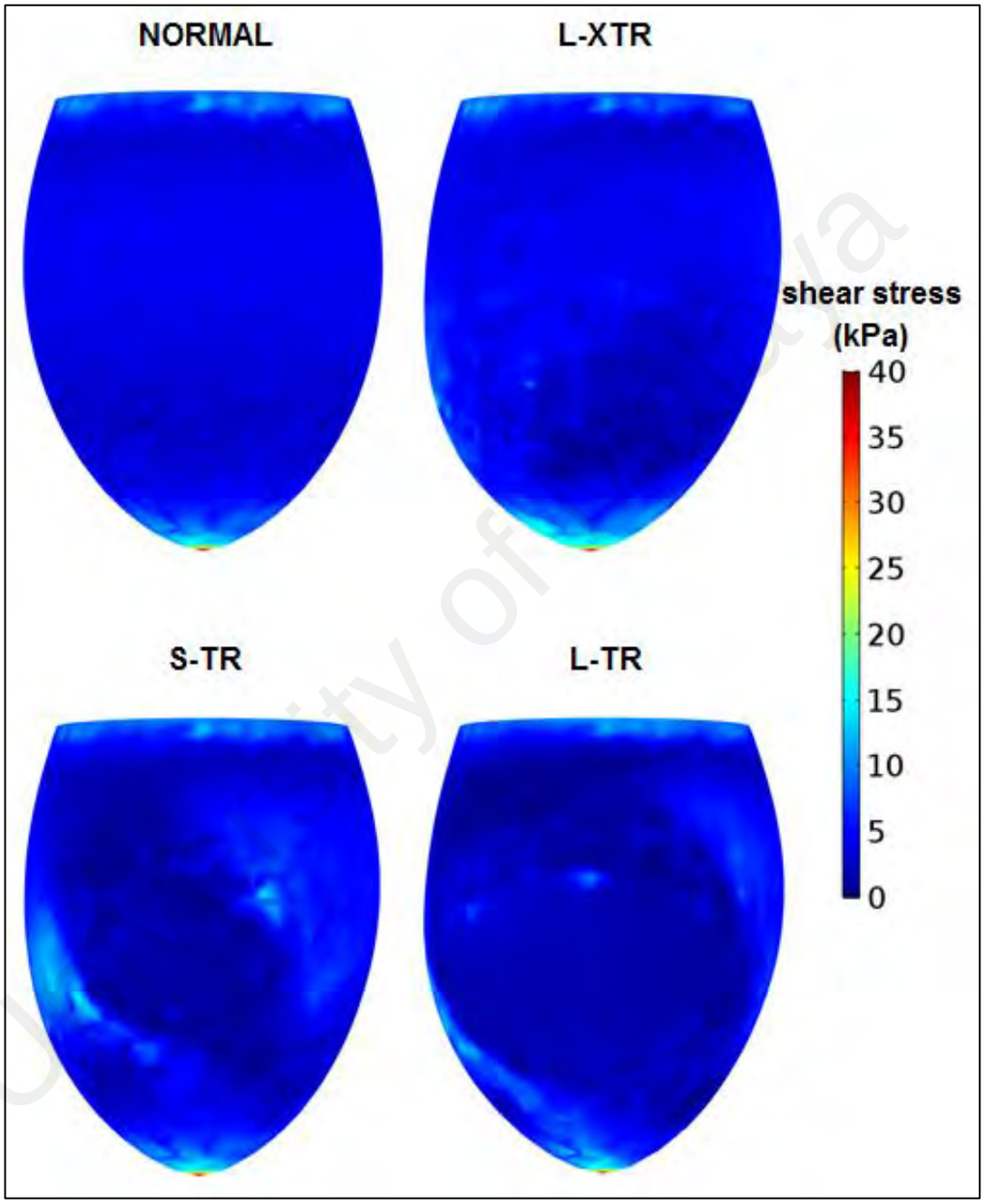

Figure 3.19: Shear stress distributions at the subepicardium of the simulated LV models at end-systole.

3.5 Discussion

In this section, the physiological relevance of the generated NORMAL model will be discussed, comparing to findings reported in previous LV studies. Subsequently, the significance of infarct size and TME on LV remodelling will be analysed based on the preliminary results obtained.

3.5.1 Electrophysiological Functions

The AP physiological shape and restitution duration reported in previous studies (Aliev & Panfilov, 1996; Nash & Panfilov, 2004) were successfully reproduced (Figure 3.7). Although the obtained AP propagation velocity in the present study was not in good agreement with previous studies, the ratios of fibre to cross-fibre, and RZ to IZ conduction velocities (Table 3.5), however, matched well with previously reported values of 2.77 (Potse et al., 2006) and 6.84 (Abd-Elmoniem et al., 2012) respectively. More importantly, the time required for the AP to travel from the apex to the base of LV model (Figure 3.8) agreed well with an earlier study (Ramanathan et al., 2006).

3.5.2 Mechanical Functions

The isometric twitch force-time profile as a function of λ, reported in a previous study (Rice et al., 2008), had been successfully replicated in the current study. Despite utilising a set of much simpler equations (Equations 3.16 - 3.20), the key characteristics, including its shape, amplitude, duration and time to reach maximum amplitude (Figure 3.9), were in close agreement with the results of Rice et al. (2008). However, since the isometric twitch force reported in [Rice 2008] was from a rat myocyte, parameters τ_0 and η_0 were tuned in the present study to adjust the isometric twitch force onset and offset rates, such that the resultant isometric twitch force could more accurately reflect that of human myocardium. The full cycle trajectories of P_{LV} and V_{LV} as in the Wiggers diagram (Guyton & Hall, 2006) were successfully produced (Figure 3.10), with

physiologically relevant EDV and ESV values (i.e. 118.7 ml and 50.1 ml respectively (Schlosser et al., 2005)).

During ejection, the apex rotated counterclockwise with respect to the base, as viewed from the LV apical end (Figure 3.11). Overall LV rotation is determined by torque generated by the myocardium, and therefore by the radius and volume of the LV tissue. The subepicardium, which has a larger radius and volume than the subendocardium, becomes the dominant force, and its shortening causes the apex to rotate counterclockwise when viewed from the apical end (J. Wang, Khoury, Yue, Torre-Amione, & Nagueh, 2008). The maximum twist angle recorded in the current study (17.9°), although higher than the reported value (14 ± 5°) by J. Wang et al. (2008), stayed within the standard deviation range. Furthermore, the overall twist angle profile obtained was also reasonably similar to that reported by J. Wang et al. (2008). The discrepancy in the magnitude of twisting could be due to the difference in LV location used to measure the LV twisting, which directly and significantly affects the amount of twisting obtained. In regards to the LV wall thickening, the recorded maximum value (45.0%) in the present model (Figure 3.12) was though not as high as the average value of 54.0% measured in an earlier study (Pandian et al., 1983), it was well within the standard deviation range of greater than 20%.

3.5.3 The Effects of the Infarct State on Left Ventricular Regional Mechanics

Based on the results (Figures 3.14 and 3.15, and Table 3.6), the fibre stain distributions at end-systole (both the subendocardium and subepicardium), as well as the average IZ fibre strain (both at end-diastole and end-systole), of the transmural infarct models (S-TR and L-TR) were more abnormal than that of the nontransmural infarct model (L-XTR). This suggested that infarct TME plays a more significant role in the deterioration of LV regional strain, as compared to infarct size. If the transmural

infarct were overstretched to the point of systolic bulging, it very likely gives rise to infarct expansion, in which the infarct becomes thinner and dilates (French & Kramer, 2007).

Moreover, the local bulging experienced by the infarcts during systole can increase myofibre strain and stress (Opie, Commerford, Gersh, & Pfeffer, 2006), which explains the relatively high fibre stress observed at certain regions surrounding the IZ, particularly for transmural infarct models S-TR and L-TR (Figures 3.16 and 3.17). Such high stress is believed to induce ventricular remodelling. In a study by Aikawa et al. (2001), it was found that chronic LV volume changes were associated with an augmented regional wall stress, which could be attenuated with the administration of LV pressure reducing angiotensin converting enzyme (ACE) inhibitors (Aikawa et al., 2001; M. A. Pfeffer, Lamas, Vaughan, Parisi, & Braunwald, 1988).

Surprisingly, shear stress recorded from the subendocardium of the S-TR model was higher than that of the L-TR model (Figure 3.18). Clinically, a smaller infarct poses lower threat. Moreover, no augmented shear stress was seen at the subepicardium for all the infarct models (Figure 3.19). Based on the results, shear stress may not be as reliable as fibre strain and stress in determining the impairment of LV regional mechanics following an MI event.

In summary, it was found that a transmural infarct is more likely to experience volume overload at end-systole. The occurrence of volume overload at the IZ is transformed into pressure loading at its surrounding myocardium, causing the LV to be more susceptible to ventricular remodelling. Therefore, TME, rather than infarct size, is more predictive of the likelihood of remodelling. This finding contradicts earlier studies (Masci et al., 2011; Ørn et al., 2007; Wu et al., 2008), which suggested infarct size as a strong predictor of remodelling events. However, these studies did not take into account

the role of infarct TME. More recent clinical studies (Ahn et al., 2013; Berti et al., 2011; O'Regan et al., 2012), which took into account both the infarct size and TME, found that infarct TME was the only significant predictor of remodelling through multivariate analysis, in agreement with the finding of the present study. Differences in findings of the clinical studies may be due to difficulties in separating infarct TME and size. This is because a larger infarct tends to have greater TME. Furthermore, limitations in the spatial resolution, as well as the presence of noise and artefacts in existing imaging techniques, presents a challenge to clinicians in determining infarct TME and size accurately.

3.5.4 Model Limitations

Although simplified generic LV geometries may not give similar strain and stress results as patient-specific geometries, the effects of infarct state on LV function should still follow the same trend for both types of geometry. In addition, to date, the actual threshold values of strain and stress to initiate remodelling events remain unknown. Therefore, the focus of this preliminary study was on the qualitative instead of quantitative effects of the infarct state, and it was assumed that the simplified generic geometry was sufficient for such a qualitative purpose.

Simulated stress results at the LV base were unphysiologically high, due to the fixed basal surface boundary condition applied in the model. Similar behaviour was also reported in an earlier FE modelling study (Choi et al., 2011), which can be addressed by replacing the fixed constraint with an elastic boundary condition to allow minimal basal surface motion.

The dynamics of myocyte twitch tension in the models was modulated by myocyte sarcomere length throughout the systolic phase, without incorporation of a force-velocity relationship. The main reason was that LV myocyte force-velocity relationship

for humans, or species with similar LV physiology to humans, is still lacking to date (McDonald, Hanft, Domeier, & Emter, 2012). The decrease of sarcomere length and corresponding decrease in twitch tension during contraction were assumed to be adequate in representing the force-velocity relationship of the myocyte. Moreover, it has been shown that the isometric twitch force-time profiles as a function of sarcomere length (Figure 3.9) obtained in this study prior to adjustment was similar to the ones reported in Rice et al. (2008).

3.6 Conclusions

In this chapter, a simplified generic electromechanical LV model, which incorporated realistic fibre orientation, excitable contracting myocardium and LV cycle dynamics, was developed. This model had been shown to be capable of reproducing physiological LV functions, including AP propagation, LV pressure and cavity volume, LV twisting and wall thickening. By resimulating the LV model with different infarct sizes and TMEs, it was found that infarct TME, rather than size, is the determinant of LV regional mechanics. Among the LV regional mechanics studied, it appeared that fibre strain and stress are more likely to be correlated with LV remodelling, as compared to shear stress.

In the next chapter, an LV model with different levels of infarct TME is simulated, to examine in a more detailed manner the role of infarct TME on LV regional mechanics, including the interaction between contractile myocardium and non-contractile infarct.

CHAPTER 4: THE ROLE OF INFARCT TRANSMURAL EXTENT IN INFARCT EXTENSION

4.1 Introduction

In the last chapter, it was found that infarct transmural extent (TME), rather than size, is the determinant of left ventricular (LV) regional mechanics impairments, and such impairments are believed to be the primary determinants of LV remodelling. In the present chapter, infarcts with different levels of TME were implemented in the LV model to examine the effects of infarct TME on localised stress at the border zone (BZ), which is believed to be a causal factor of infarct extension. The mechanisms underlying highly abnormal stress distribution were investigated from a mechanical viewpoint. In particular, the mechanism on how mechanical interaction between normal and ischemic myocardium can contribute to impaired BZ mechanics was studied, taking into account the importance of local fibre orientation.

4.2 Literature Review

Infarct expansion and extension have been recognised as the main processes leading to LV remodelling. Infarct expansion, which occurs during a timeframe of days to weeks after an acute myocardial infarction (MI), involves radial thinning, circumferential lengthening and dilation of non-contractile infarct region. It has adverse effects on LV function and contractility of residual myocardium, possibly resulting in ventricular dilation, aneurysm formation and infarct rupture (French & Kramer, 2007). Infarct extension, on the other hand, takes place over a timeframe of weeks to months following MI. It involves reinfarction of normally perfused BZ adjacent to the infarct, which subsequently extends the infarct zone (IZ) progressively, and at the same time drags the neighbouring myocardium into the BZ (Jackson et al., 2002). Patients with infarct extension have an in-hospital mortality more than four times higher than those without extension (Muller et al., 1988). Furthermore, increasing amount of transmural

necrosis following infarct extension can cause infarct expansion and its related complications. The combined effects of infarct expansion and extension give rise to the feed-forward cycle of remodelling, resulting in continuous cardiomyocyte apoptotic and necrotic death, ventricular thinning and dilation (Diwan et al., 2007).

Infarct expansion is caused by overdistension and systolic bulging of the non-contractile infarct (Whittaker et al., 1991). Under high distending pressure, myocytes undergo slippage, giving rise to the dilation, and eventually expansion of the infarct (Gajarsa & Kloner, 2011). In an earlier study, Kaul (1995) elucidated the pivotal role of viable subepicardium in preventing dilation and thinning of infarct, which subsequently preserved LV shape, as well as inhibited infarct expansion. Although the influence of infarct TME towards infarct expansion is well known, the correlation between infarct TME and events underlying infarct extension at the BZ remains unanswered. It has been proposed that infarct extension is caused by the presence of abnormally high stress at the BZ owing to the mechanical "tethering" between the normal and ischemic myocardium (Lima et al., 1985; Sakai et al., 1985; Walker et al., 2008). Nevertheless, unlike infarct expansion, detailed exploration of the mechanisms underlying infarct extension, which involve the interaction between the remote zone (RZ) and IZ, as well as the resultant high stress at the BZ, is still lacking. Wenk et al. (2012) and Shimkunas et al. (2013) demonstrated depressed BZ contractility after MI using their patient-specific and sheep LV models respectively, but did not elucidate how this give rises to abnormally high stress in the BZ. Furthermore, the role of infarct TME in such interaction remains unclear. Likewise, the importance of local fibre orientation on the presence of high stress at the BZ has not been explored.

4.3 Methods

Five infarct models with different levels of infarct TME were built from the NORMAL model developed in Chapter 3: 10% (TR10), 24% (TR24), 51% (TR51), 75% (TR75) and 100% (TR100) infarct TMEs. To exclude the impact of infarct size on LV regional mechanics, the infarct size was equal in all models. As mentioned earlier in Chapter 3, infarct shape was kept rounded (to avoid sharp edges which could affect stress distribution), and at the same time they were kept some distance away from the basal surface and the apex (to avoid boundary effects). With these criteria, a relative infarct size of 14.3% was obtained (calculated from infarct area at the endocardium divided by total endocardial area), which is within the normal range of infarct size (Ahn et al., 2013). Infarct volume, area (measured at the endocardium) and TME are given in Table 4.1, with infarct TME calculated using Equation 3.24. The infarcts were considered as transmural (models TR51, TR75 and TR100) if their TME exceeded 50%, and non-transmural (models TR10 and TR24) otherwise (Becker et al., 2009). To ensure smooth transition of material properties across the RZ and IZ, a BZ was introduced between the RZ and IZ, as described in the previous chapter. The generated infarct models, together with their myocardial properties (C_0, T_0, D_f, and D_t), are shown in Figure 4.1, with red and blue colours representing the IZ and RZ respectively, with in-between colours denoting BZ transition from the IZ to the RZ.

To ascertain the physiological relevance of the generated models, their performance was evaluated by comparing the resultant circumferential strain trajectories of various myocardial layers against those obtained from a past clinical study (Becker et al., 2009). In order to elucidate the impairment of BZ myocardial mechanics as a function of infarct TME, mechanical interaction between the IZ, BZ and RZ was analysed. The effect of fibre orientation on this interaction was studied by comparing fibre stress against the difference in angle between the myocardial fibre and the BZ-RZ boundary.

Table 4.1: Infarct volume, area (measured at the endocardium) and TME of the simulated models.

Model	Volume (cm^3)	Area (cm^2)	TME (%)
TR10	1.46	11.17	10
TR24	3.58	11.10	24
TR51	7.52	11.10	51
TR75	11.22	11.15	75
TR100	14.92	11.15	100

TME: transmural extent; TR10, TR24, TR51, TR75 and TR100: Infarct LV models with varying infarct TMEs.

Subsequently, stress-strain loops were used to indicate BZ myocardial work density, which reveal the energy expenditure and efficiency of the myocardium at the BZ. Such myocardial energy expenditure and efficiency can infer possible long-term deterioration of LV function (Watanabe, Sugano, Sugiura, & Hisada, 2004).

4.4 Results

4.4.1 Left Ventricular Activation and Global Function

Figure 4.2 illustrates the activation times for the subendocardium (transmurality index, $\beta = 0.17$) and subepicardium ($\beta = 0.83$) for the NORMAL and TR100 models. In both the subendocardium and subepicardium, an approximate 10 ms delay was observed at the BZ and RZ at the basal and mid regions for the TR100 model. The greatest delay of up to nearly 35 ms was observed at the upper part of the IZ relative to the NORMAL model.

Simulated end-diastolic volume (EDV), end-systolic volume (ESV), stroke volume (SV) and ejection fraction (EF) of the models are listed in Table 4.2. The infarct TME affected the ESV more than the EDV, resulting in an increase of 9.1 ml in the ESV and a decrease of 3.9 ml in the EDV from NORMAL to TR100. The SV, EF and peak systolic pressure (P_{SYS}) declined as infarct TME increased, with 13.0 ml, 9% and 14.4 mmHg reductions in the TR100 model relative to the NORMAL model respectively.

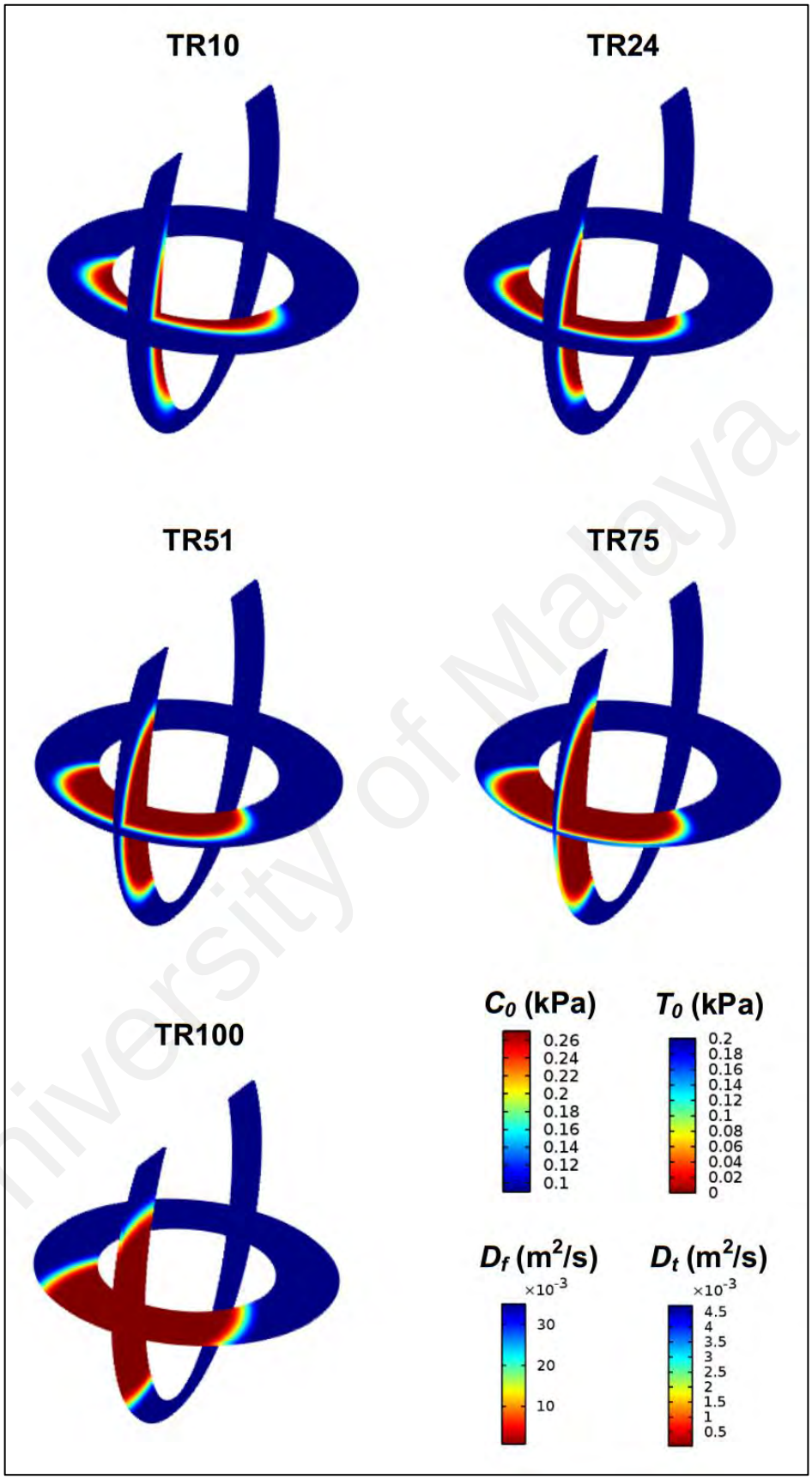

Figure 4.1: Generated infarct models with varying infarct TMEs. The scales show the myocardium properties (C_0, T_0, D_f, and D_t), with red and blue colours representing the IZ and RZ respectively, whilst in-between colours denoting BZ transition from the IZ to the RZ.

Table 4.2: Simulated hemodynamic values.

Model	EDV (ml)	ESV (ml)	SV (ml)	EF (%)	P_{SYS} (mmHg)
NORMAL	118.7	49.9	68.8	58	120.5
TR10	115.6	51.0	64.6	56	117.0
TR24	115.6	52.0	63.6	55	115.2
TR51	115.2	54.6	60.6	53	110.6
TR75	114.9	57.2	57.7	50	107.0
TR100	114.8	59.0	55.8	49	106.1

EDV: end-diastolic volume; ESV: end-systolic volume; SV: stroke volume; EF: ejection fraction; P_{SYS}: peak systolic pressure; NORMAL: non-infarct LV model; TR10, TR24, TR51, TR75 and TR100: Infarct LV models with varying infarct transmural extents.

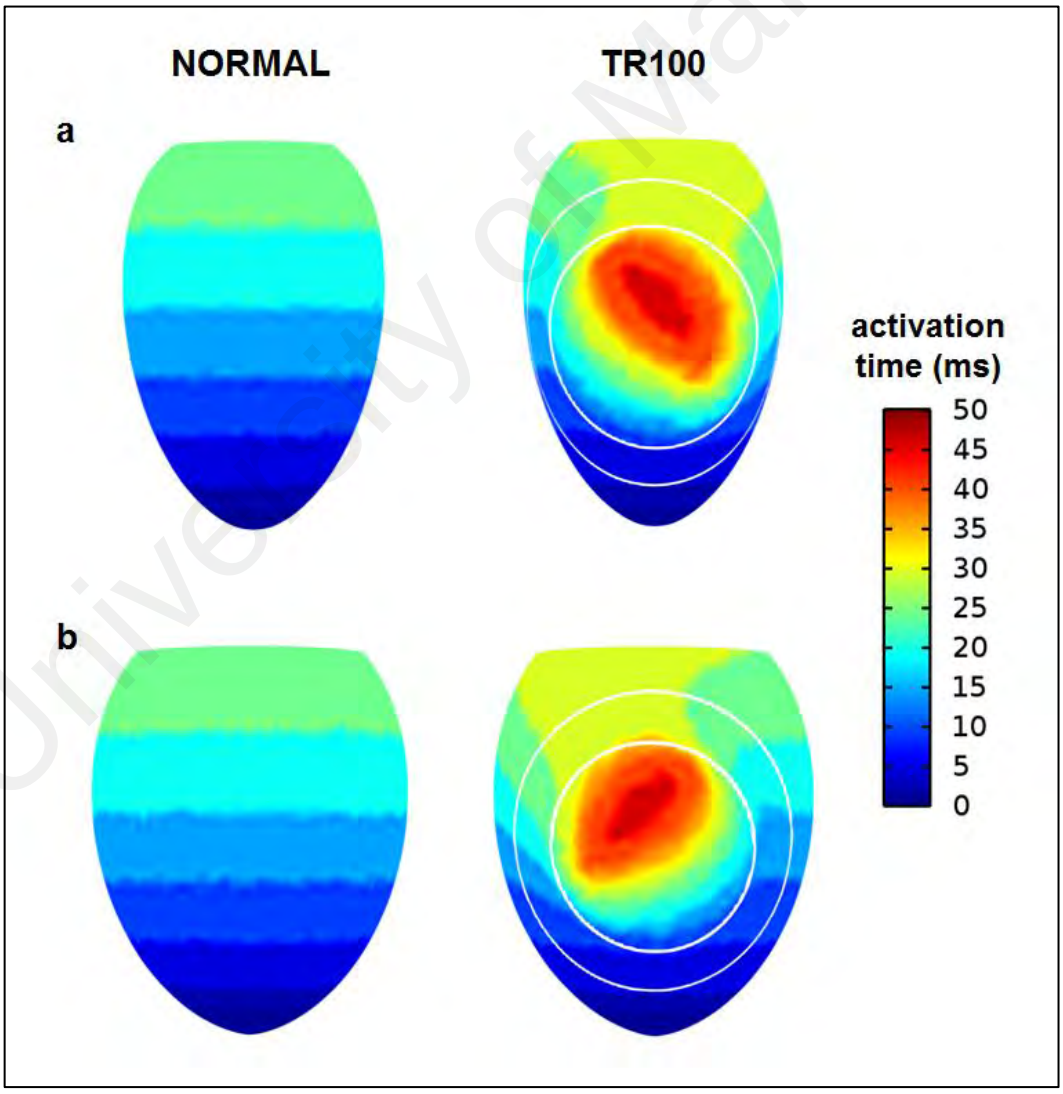

Figure 4.2: Simulated activation times of the (a) subendocardium and (b) subepicardium for the NORMAL and TR100 models.

4.4.2 Circumferential, Longitudinal and Fibre Strains

To illustrate the time course of strains for various myocardial layers (subendocardium, middle myocardium and subepicardium), a point from each layer of the infarct segment was selected as shown in Figure 4.3a. For better presentation of the myocardial strains during contraction, the early ejection phase was chosen as the starting point for the time course plots. Figure 4.3b shows the simulated time course of circumferential, longitudinal and fibre strains in the three myocardial layers of the NORMAL model, whilst Figure 4.3c demonstrates the circumferential strain of the simulated models.

From Figure 4.3b, systolic longitudinal strain was the lowest for all three myocardial layers of the NORMAL model. Systolic circumferential strain was greater than that of fibre strain at the subendocardium, but lower at the subepicardium. At the middle myocardium, fibre strain equalled circumferential strain since the fibre orientation was circumferential at the middle myocardium. As can be seen in Figure 4.3c, the absolute magnitude of systolic strain declined when moving from the subendocardium to the subepicardium. At the subendocardium, systolic strain was impaired in all infarct models, with a greater impairment with increasing level of infarct TME. Conversely, in the middle myocardium and subepicardium, impairment of systolic strain was only pronounced in the transmural infarct models. In these transmural infarct models, the systolic strain at all the three myocardial layers was depressed with increasing infarct TME.

4.4.3 Mechanical Interaction between Infarct, Border and Remote Zones

The progression of the end-systolic fibre strain (engineering strain along the myocardial fibre direction) and fibre stress (Cauchy stress along the myocardial fibre direction) distributions from IZ to BZ and RZ were generated to visualise the

mechanical interaction among the three zones. To do this, the fibre strain and stress distributions were plotted along rings spanning around the subendocardium and subepicardium, as shown in Figures 4.4a and 4.4b respectively. As the subendocardium of both the nontransmural and transmural models (presented by the TR24 and TR100 models respectively) was infarcted, the fibre strain was highly elevated at the IZ of both models. Meanwhile, the myocardium progressed from being non-contractile at the IZ-BZ boundary to contractile at the BZ-RZ boundary, as shown in Figure 4.4c. Unlike the

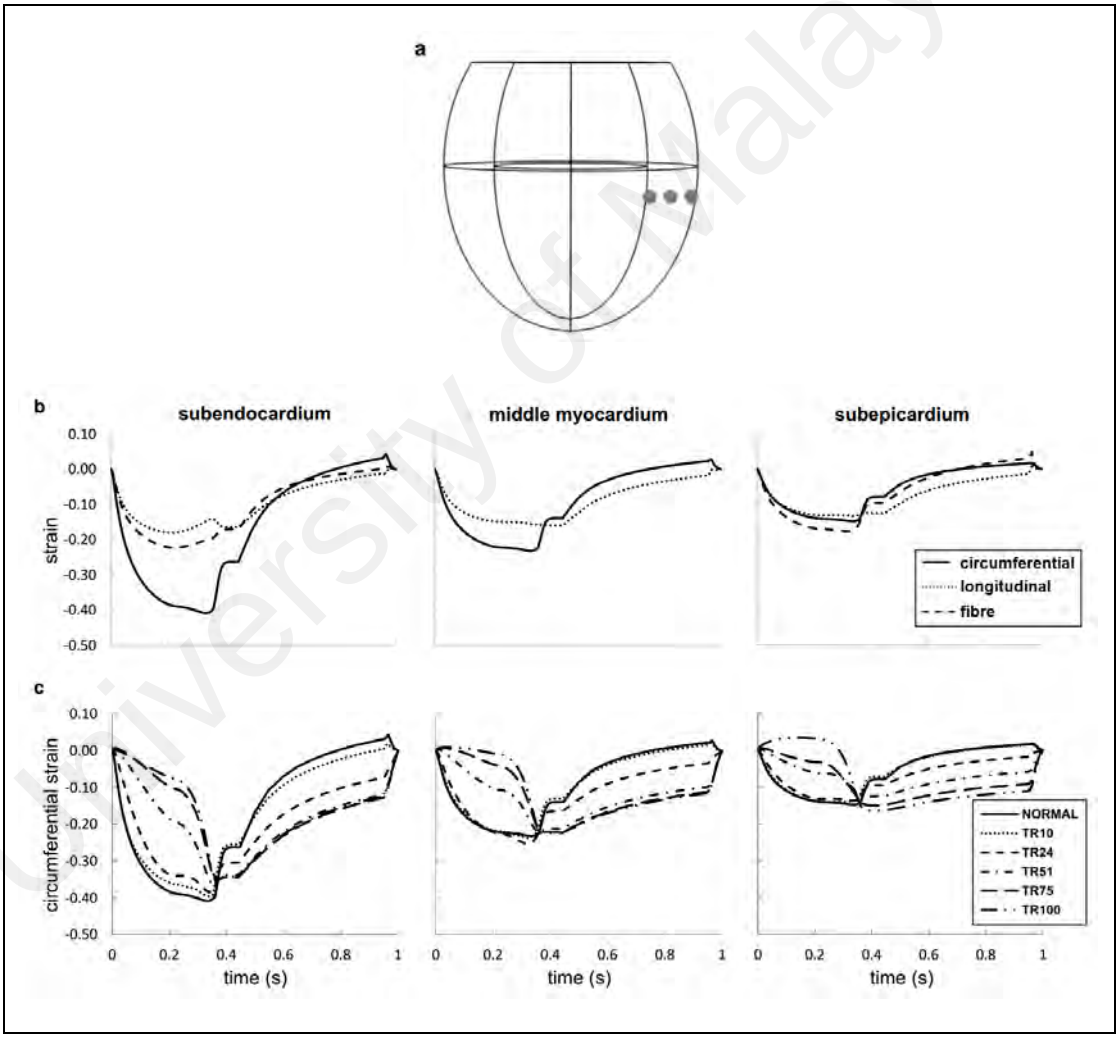

Figure 4.3: (a) Selected point in each layer of the myocardium for generating time course of strains. (b) Simulated time course of circumferential, longitudinal and fibre strains in the subendocardium, middle myocardium and subepicardium of the NORMAL model. (c) Simulated time course of circumferential strain in the subendocardium, middle myocardium and subepicardium of simulated models.

subendocardium, the infarct extended to the subepicardium only in the transmural model. Abnormally high strain was thus observed only at the subepicardium of the TR100 model, as illustrated in Figure 4.4d, with the transition from non-contractile to contractile occurring at the BZ. Consequently, high stress was observed at the subendocardium of both the TR24 and TR100 models, and at the subepicardium of the TR100 model only.

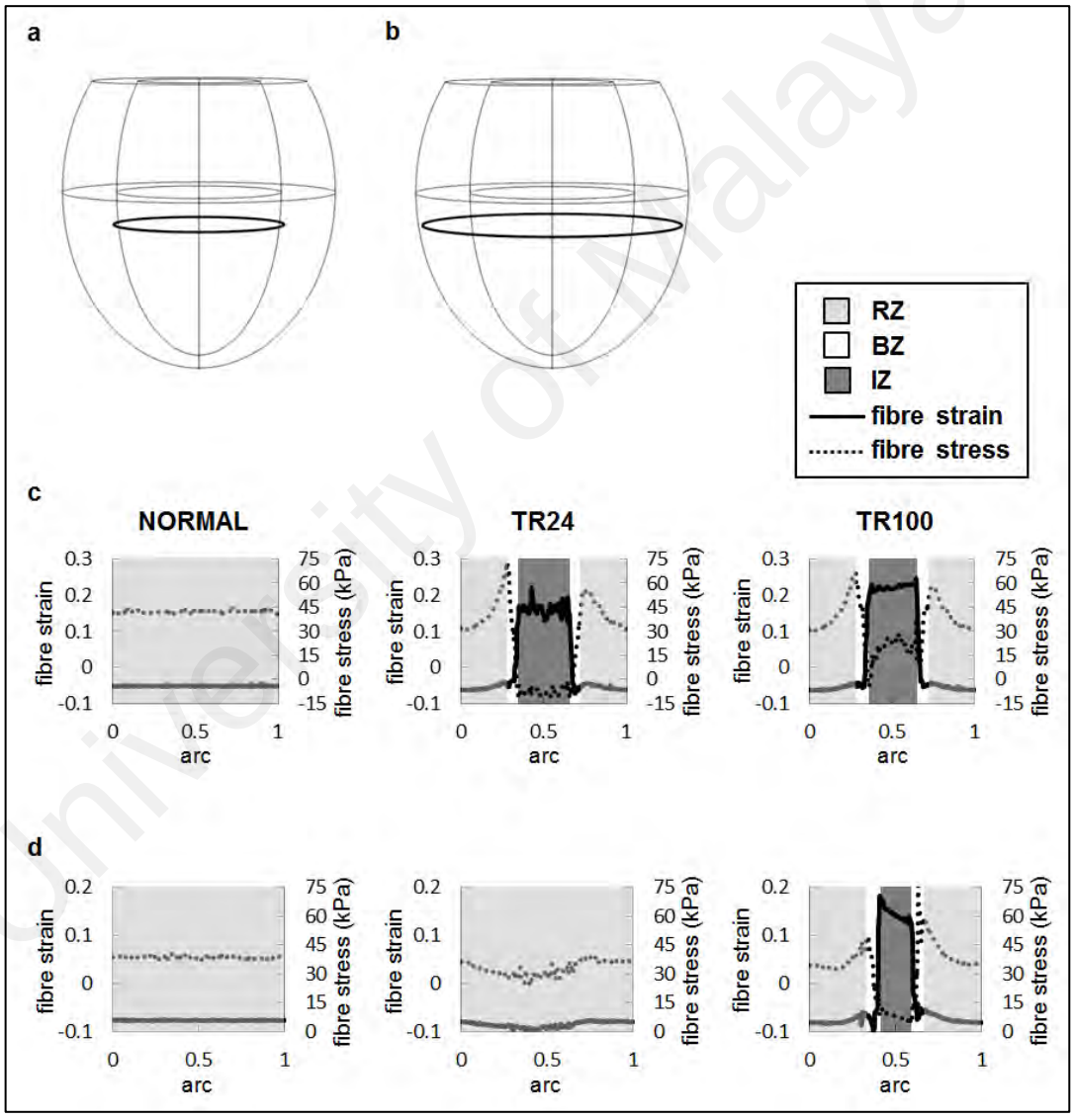

Figure 4.4: Circumferential rings spanning around the (a) subendocardium and (b) subepicardium used to generate Figures 4.4c and 4.4d respectively. End-systolic fibre strain and stress distributions across the (c) subendocardium and (d) subepicardium of the NORMAL, TR24 and TR100 models.

To study the effect of fibre orientation on stress distribution, end-systolic fibre stress for the subendocardium and subepicardium of the TR100 model was plotted, as shown in Figures 4.5a and 4.5b respectively, with arrows representing the local fibre orientation. As can be seen, the fibre stress distributions for both myocardial layers were nonhomogeneous, particularly at the BZ. Figure 4.5c presents the correlation between the fibre stress, and the angle difference between the myocardial fibre and the BZ-RZ boundary. As shown in the figure, the fibre stress was highest at regions where the myocardial fibre was tangential to the BZ-RZ boundary (indicated by 0º angle difference). In contrast, much lower stress was obtained at areas with fibre orientation perpendicular to the BZ-RZ boundary. To examine whether the high stresses were due to an improper enforcement of material incompressibility (since a nearly-incompressible framework was used), the resulting volumetric strain throughout the myocardium was inspected. Most regions exhibited a volumetric strain of 1 (i.e. incompressibility), with the exception of only small localised regions near some parts of the IZ-BZ boundary, with the volumetric strain ranging from 0.7-1.4, likely due to errors in mesh discretisation. These regions, however, were small and did not systematically correspond to the regions of high fibre stress shown in Figure 4.5. Based on this analysis, it can be concluded that the high fibre stresses were not caused by variation in the volumetric strain.

4.4.4 Myocardial Mechanics as a Function of Infarct Transmural Extent

Figures 4.6a and 4.6b illustrate the fibre stress-strain loops (FSSLs) (i.e. fibre directional Cauchy stress against fibre directional engineering strain) of the simulated models, taken from the maximum fibre stress points at the subendocardium and subepicardium respectively. It can be seen that as infarct TME increased, the FSSLs became less rectangular with greater maximum stress, in both myocardial layers. The

FSSL for the subendocardium of the TR100 model was the only exception, which appeared to fall between those for the TR24 and TR51 models.

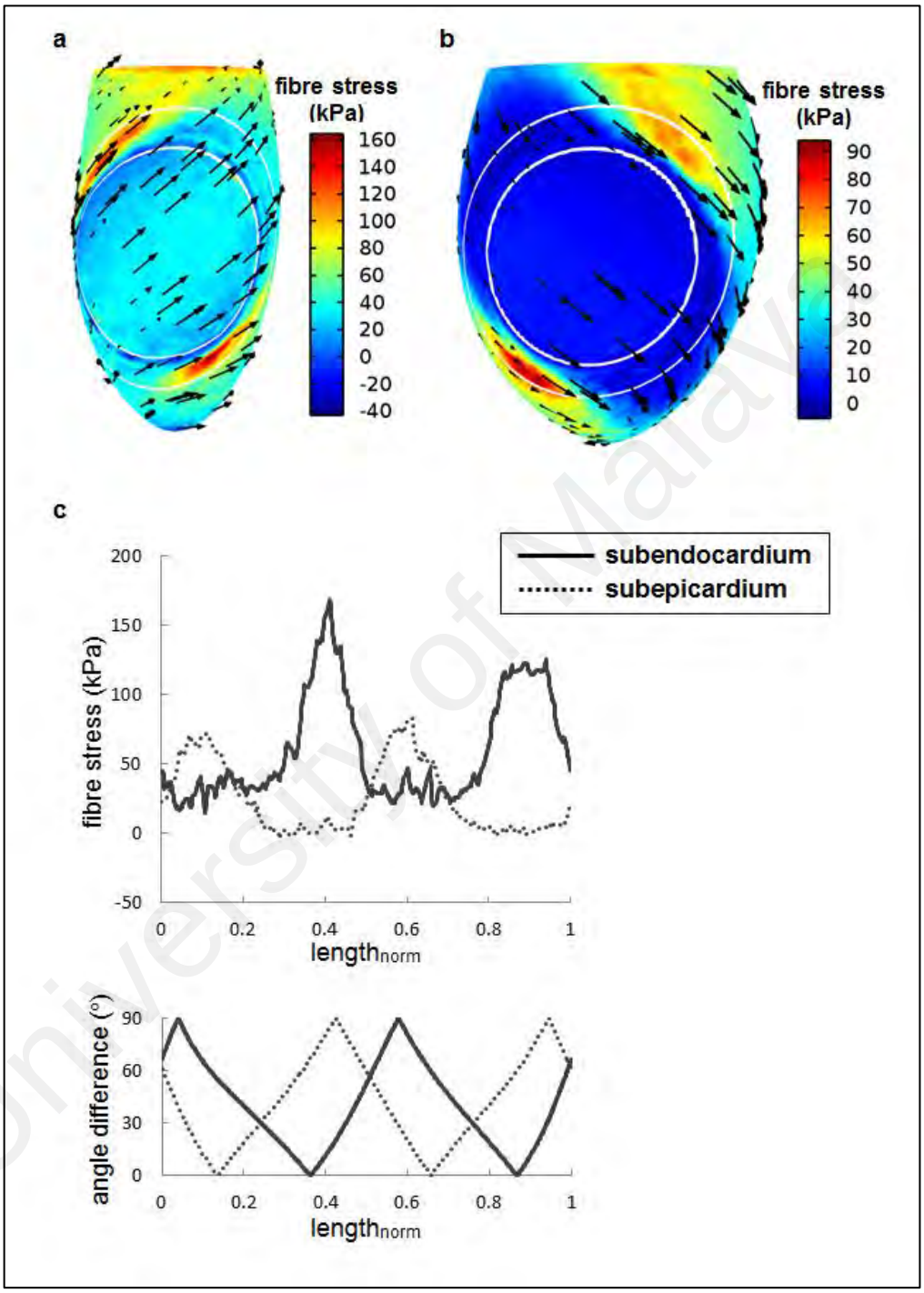

Figure 4.5: Fibre stress distributions for the (a) subendocardium and (b) subepicardium of the TR100 model at end-systole, with the IZ, BZ and RZ separated by white circles, whilst the fibre orientation is indicated by black arrows. (c) Fibre stress (top panel) versus angle difference between myocardial fibre and BZ-RZ boundary (bottom panel) plotted along the BZ-RZ boundary of the subendocardium and subepicardium. $length_{norm}$: normalised length along the BZ-RZ boundary.

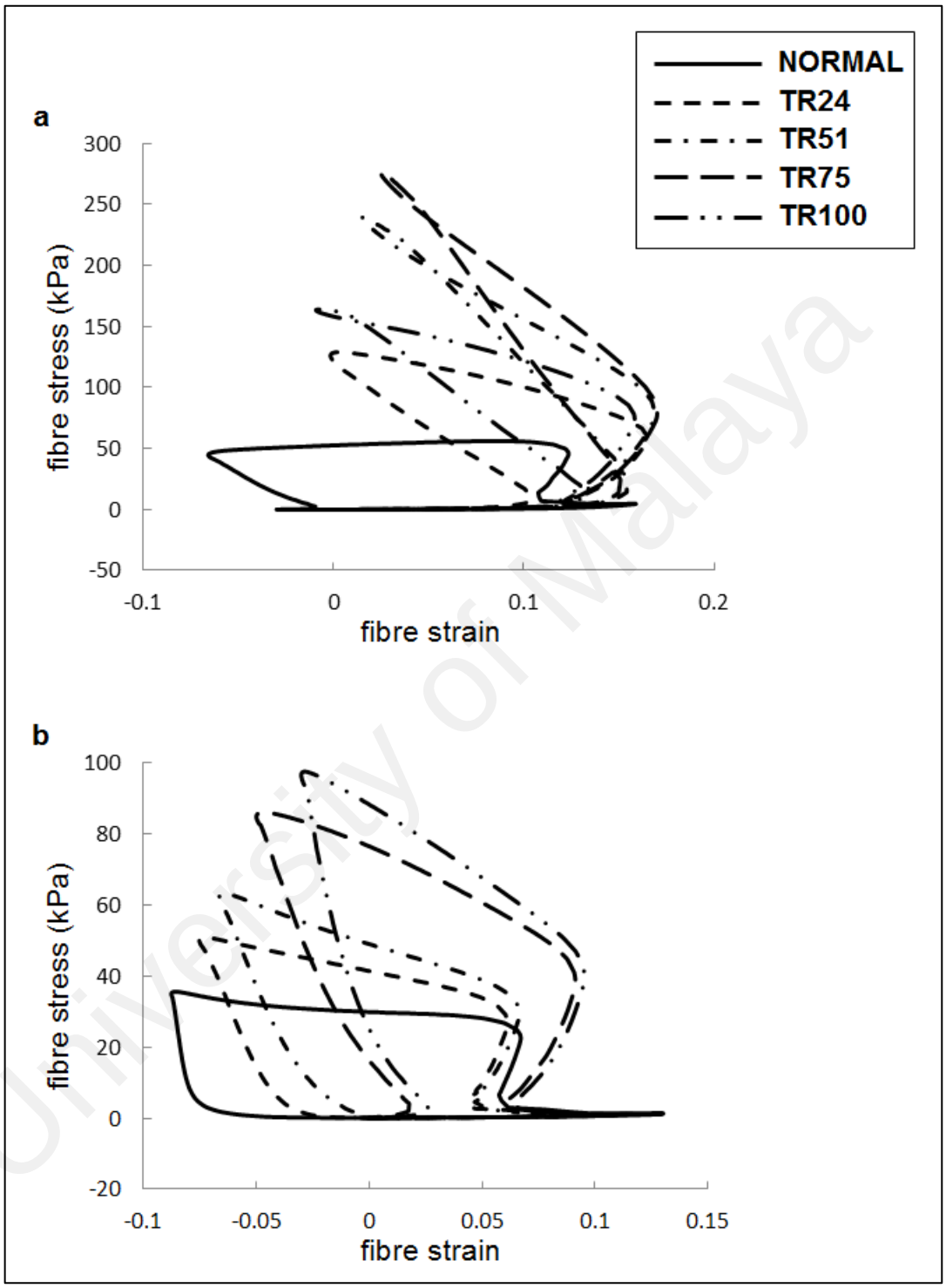

Figure 4.6: Fibre stress-strain loops (FSSLs) of the simulated models with varying infarct TMEs, taken from the maximum stress points at the (a) subendocardium and (b) subepicardium.

To demonstrate the importance of viable subepicardium in preserving LV shape, end-systolic fibre strain and stress in both short and long axis views were plotted for each model (Figure 4.7 - 4.10). The fibre strain at the IZ was generally elevated, and the fibre stress distribution at the BZ became more abnormal, with increasing infarct TME. Dilation of the IZ can be seen in the transmural infarct models, as indicated by the eccentricity of the model cavities.

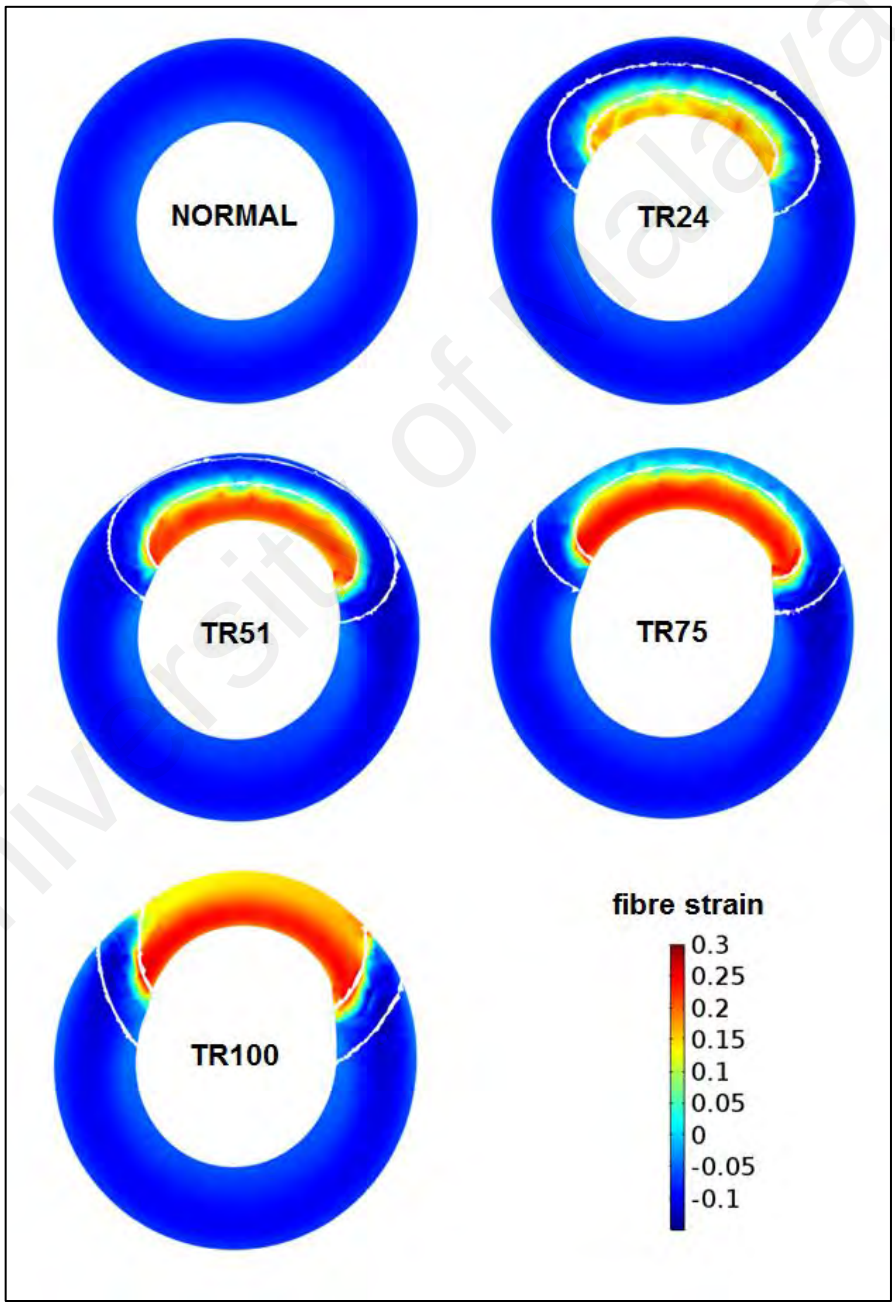

Figure 4.7: End-systolic fibre strain distributions of the simulated models in short axis view.

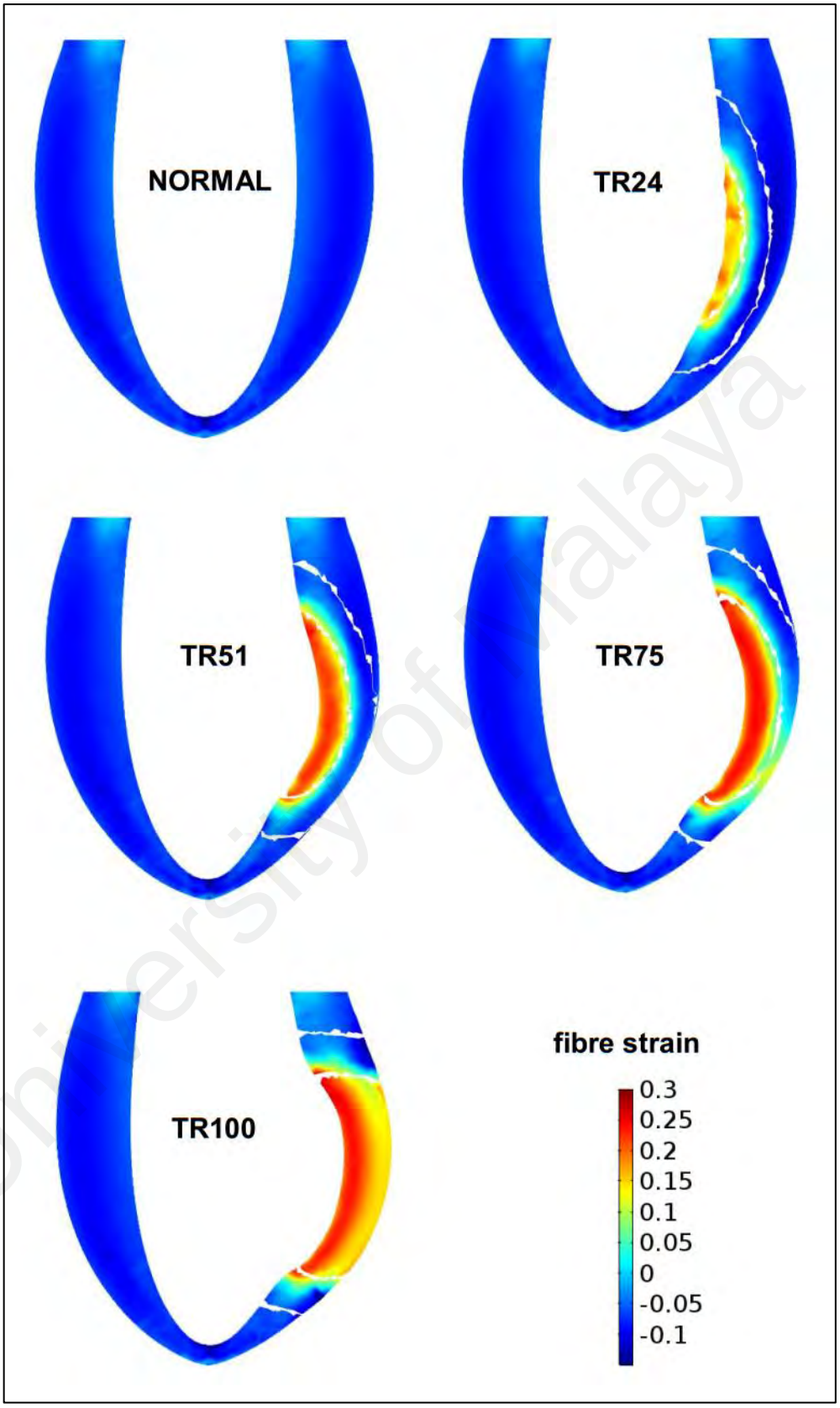

Figure 4.8: End-systolic fibre strain distributions of the simulated models in long axis view.

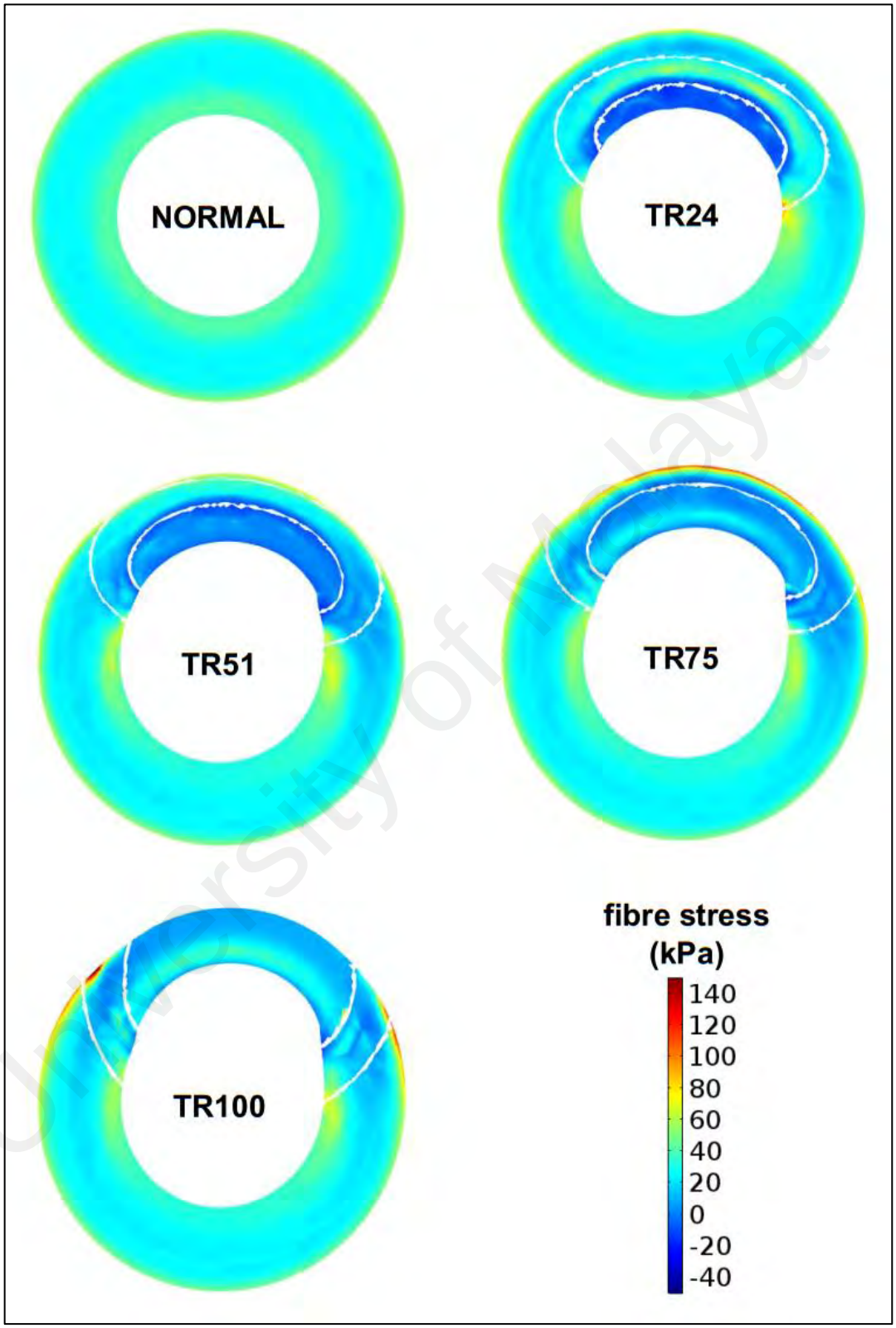

Figure 4.9: End-systolic fibre stress distributions of the simulated models in short axis view.

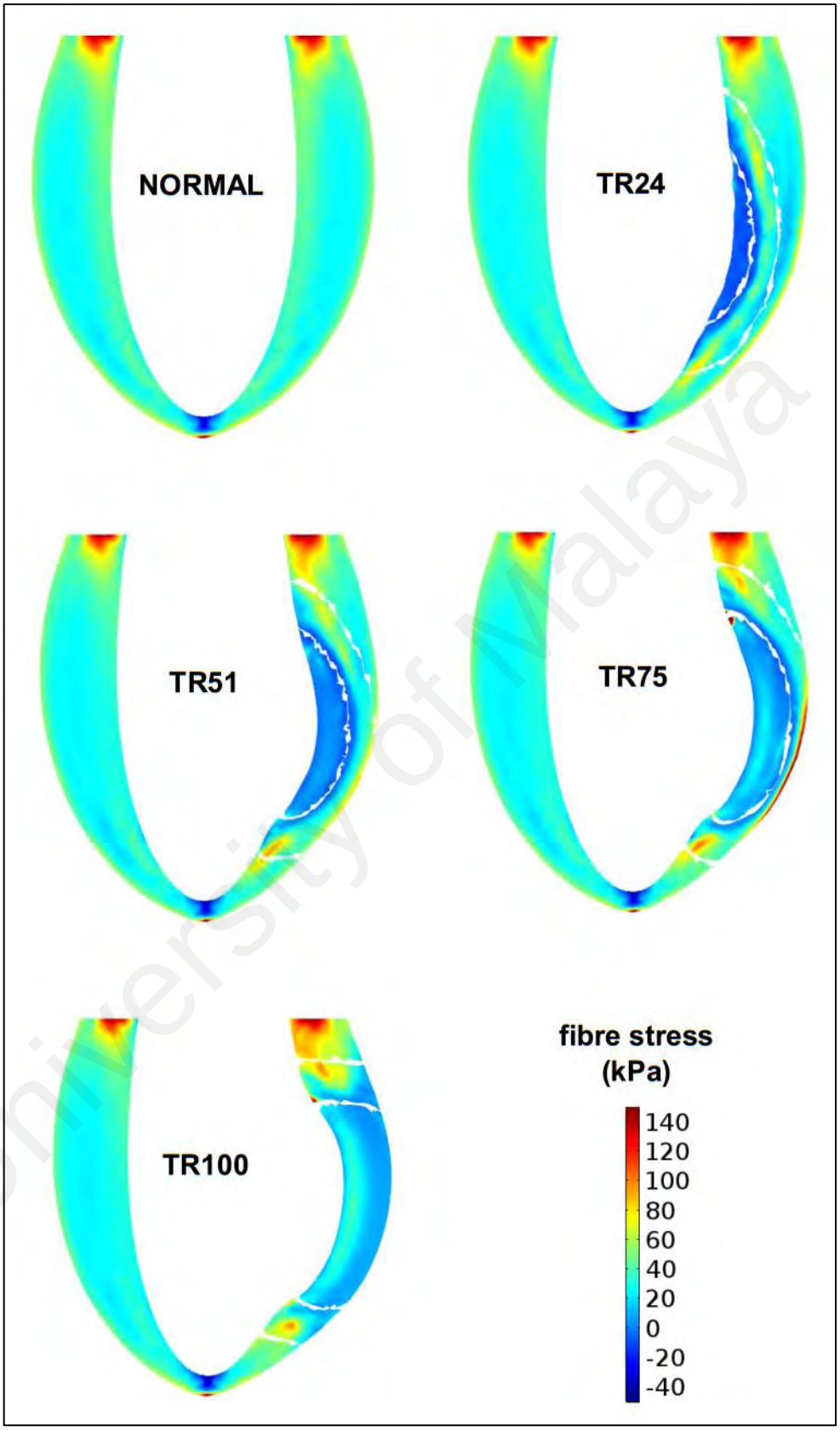

Figure 4.10: End-systolic fibre stress distributions of the simulated models in long axis view.

Average IZ fibre strain, along with the maximum fibre stresses in the subendocardium and subepicardium, with increasing infarct TME is illustrated in Figure 4.11a. The average IZ fibre strain increased by 0.078 from 10% to 51% infarct TME and began to saturate beyond that, with an increase of only 0.011 from 51% to 100% TME. With regards to the maximum stress in the subendocardium, its magnitude increased by 196 kPa from 10% to 51% infarct TME, followed by a rise of 37 kPa from 51% to 75% infarct TME, and dropped by 113 kPa at 100% TME. Meanwhile, the maximum fibre stress in the subepicardium increased linearly with increasing infarct TME, and its magnitude was generally lower relative to that of the subendocardium at all levels of infarct TME. The rotation gradient of the myocardium (with maximum fibre stress) was generated along the dashed line illustrated in Figure 4.11b. It was observed that the subendocardial maximum stress followed the trend of myocardial rotation gradient with increasing infarct TME, as depicted in Figure 4.11c.

4.5 Discussion

The results from this chapter showed that infarct TME contributed substantially to the highly abnormal stress distribution and impaired mechanics at the BZ, which are believed to contribute to infarct extension and remodelling. New findings included the importance of mechanical interaction between ischemic and viable myocardium, as well as the contribution of fibre orientation in such interaction.

4.5.1 Comparison of Model Performance

From the results, the impairment of circumferential strain was only pronounced in the subendocardium, with minor impairment observed in the middle myocardium and subepicardium of non-transmural infarct LV models. With regards to the transmural infarct LV models, the circumferential strain was reduced in all three layers of myocardium. The same findings were also observed in a clinical study using

echocardiography on fifty-six patients (Becker et al., 2009). Furthermore, the time course of circumferential strain, as well as its regression of magnitude change from the subendocardium to the middle myocardium and subepicardium (Figure 4.3), showed good agreement with the circumferential strain tracings reported in the study of Becker et al. (2009), thus supporting the physiological relevance of the presented models.

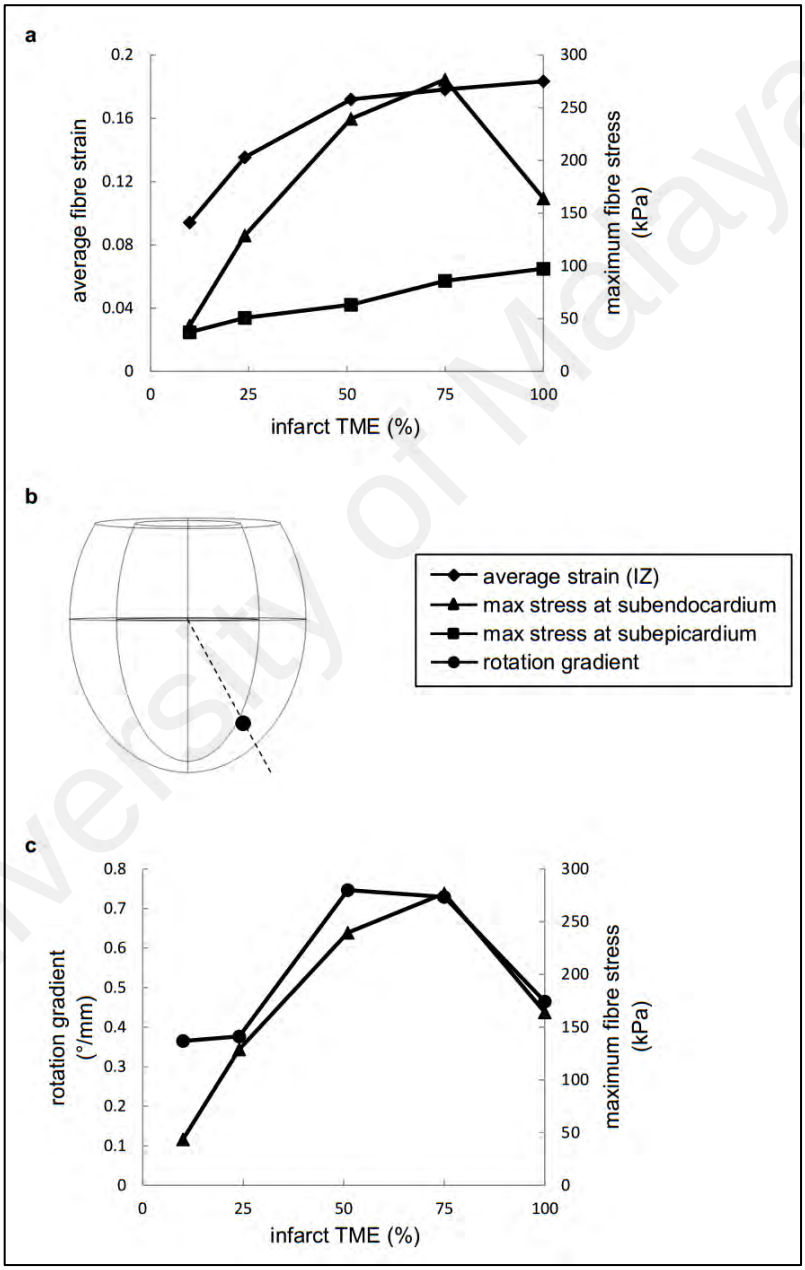

Figure 4.11: (a) Average end-systolic fibre strain in the IZ, the maximum fibre stresses in the subendocardium and subepicardium with increasing TME of the infarct, and (c) the correlation between the maximum fibre stress in the subendocardium and its rotation gradient, generated along the dashed line shown in (b).

4.5.2 Mechanical Interaction between Infarct, Border and Remote Zones

It is believed that the juxtaposition of BZ in between the non-contractile IZ and contractile RZ creates a "tethering" effect and gives rise to abnormally high stress in the BZ, which possibly can lead to infarct extension (Ashikaga et al., 2005). Since mechanical interaction operates in both directions, mechanical tethering is imposed on all the IZ, BZ and RZ. However, high stress has been observed only in the BZ but not in the IZ and RZ. Based on the results (Figure 4.4), the BZ and its surrounding myocardium were the only regions with elevated fibre stress, with strain levels lying between that of the other two zones. Mechanically, high fibre stress is present only when a large fibre strain is applied to a stiff myocardium. The presence of high BZ strain and contractility ("stiffness" during active contraction) explains the abnormally high stress observed in this region. On the contrary, this phenomenon was not observed in either the IZ or the RZ, owing to the low stiffness of the IZ and the diminished strain at the RZ.

Another important finding of the present study is the role played by fibre orientation on the non-homogeneous distribution of end-systolic fibre stress, with the greatest stress recorded in regions with fibre orientation tangential to the BZ-RZ boundary (Figure 4.5). This can be explained by the difference in stiffness between the fibre and cross-fibre directions. Since the myocardial wall was stiffer in the fibre direction ($b_f > b_t$), the IZ was stretched unevenly, with greater stretching occurring in the cross-fibre direction. As a result, BZ regions with fibre direction tangential to the BZ-RZ boundary bore the greatest tethering effect, thus yielding the highest stress. In short, it was the mechanical tethering or interaction among the three zones, together with the simultaneous presence of moderately high strain and contractility at the BZ, as well as the fibre orientation at the IZ, that gave rise to the localised abnormally high stress pattern at the BZ.

4.5.3 Correlation between Infarct Transmural Extent and Impaired Border Zone Regional Mechanics

Kaul (1995) elucidated the crucial role played by the viable subepicardium in preventing the IZ from dilating and thus maintaining the shape of LV. In transmurally infarcted LVs, the surviving contractile subepicardium was no longer adequate to withstand the outward pressure imposed by the IZ. As a result, the IZ began to dilate and exhibit an elevated fibre strain (Figures 4.7, 4.8 and 4.11). This explains the observations from recent studies (Ahn et al., 2013; Berti et al., 2011; O'Regan et al., 2012), which found a higher risk of remodelling events in transmurally infarcted LVs. As the results demonstrated, localised high stress at the BZ was a result of mechanical tethering following an overstretched IZ (Figures 4.4, 4.9 and 4.10), with the magnitude of the maximum fibre stress recorded at both the subendocardium and subepicardium was also found to have a positive correlation with average IZ fibre strain (Figure 4.11). One exceptional case was found at the subendocardium of the TR100 model, where the maximum stress dropped, despite an increase in average infarct strain with increasing infarct TME.

Further analysis showed that the rotation gradient was closely correlated with maximum stress observed at the subendocardium, and may explain the unexpected decline of maximum stress for the TR100 model. The rotation gradient measures the sliding of the neighbouring myocardial sheets against each other, and is responsible for the shear stress imposed on the myocardium. Due to a gradual change in the fibre orientation from +60° at the endocardium to -60° at the epicardium, the rotation of the subepicardium is counteracted by the subendocardium, increasing the rotation gradient across the myocardial wall and so the wall stress. However, since the subepicardium exhibits a larger radius and volume, it determines the overall rotation of the LV wall (J. Wang et al., 2008). In the TR100 model with infarction spanning across the entire wall

thickness (no counteract motion from the subendocardium and subepicardium), the resultant rotation gradient was depressed, and thus a reduction in the maximum stress was recorded at the subendocardium. Nevertheless, a fully transmural infarcted LV (as represented by the TR100 model) can still be a major concern because its infarct expansion can chronically augment the mechanical tethering and thus the stress imposed on the BZ.

FSSL has been used to indicate myocardial work density, which reveals the energy expenditure and efficiency of myocardium (Watanabe et al., 2004). A less rectangular loop represents lower myocardial energy efficiency, whilst a greater loop area signifies higher myocardial energy expenditure. Although Wenk et al. (2012) and Shimkunas et al. (2013) successfully demonstrated a depressed contractility in the BZ after the occurrence of MI, subsequent complications associated with depressed contractility were not discussed. Based on the simulation results (Figure 4.6), the myocardial energy efficiency was shown to decline while the energy expenditure increased with increasing infarct TME. Therefore, apart from the depressed contractility and high stress at the BZ, it is believed that impaired energy efficiency and elevated energy expenditure are also accountable for the higher risk of infarct extension in transmurally infarcted LVs.

4.5.4 Left Ventricular Activation and Global Function

In spite of delayed activation at the LV base and mid region of the TR100 model, activation at the BZ was not delayed compared to the RZ, whilst a pronounced activation delay was observed at the IZ. In contrast, systolic function of the BZ was found to be depressed compared to that of the RZ. From the mismatch between regions with depressed systolic function and delayed activation (Figures 4.2 and 4.5), it is suggested that impaired regional mechanics at the BZ is most likely contributed solely by altered LV mechanical function instead of electrophysiological factors. The same

finding was also reported in a recent study by Ashikaga et al. (2005) using a high resolution CMR technique.

LV global functions, though depressed with increasing infarct TME, fell within the normal or mildly abnormal range (Lang et al., 2006) for all models simulated in the present study (Table 4.2). This observation suggested that the regional impairment of LV, including the myocardial strain and stress overloads, can be masked by global indices of LV function. LV remodelling can still occur in spite of normal global LV function (Anversa, Loud, Levicky, & Guideri, 1985). Therefore, global indices should not be the only determinants for prediction of remodelling events following MI.

4.5.5 Clinical Significance

As discussed above, following an acute MI, particularly in the transmurally infarcted LV, the interaction between the IZ, BZ and RZ can give rise to the concentration of BZ high stress, impaired efficiency and elevated energy expenditure. Prolonged, severe stress overload can lead to excessive forms of collagen deposition or fibrosis, which diminishes the capillary density and amplifies the oxygen diffusion distance (Sabbah, Sharov, Lesch, & Goldstein, 1995). These, together with increased energy expenditure and reduced energy efficiency (increased oxygen demand), place the BZ myocardium at further risk of hypoxia (Gaasch et al., 1989; Shiojima et al., 2005). Although a previous study has shown that the balance between oxygen demand and supply is not violated in the BZ (Lima et al., 1985), severely affected myocardial metabolism may induce reactive oxygen species (ROS) production, making the BZ more susceptible to apoptosis and infarct extension (Pimentel et al., 2001), a process in which the BZ turns into ischemic myocardium and becomes part of the IZ (Creemers & Pinto, 2010; Di Napoli et al., 2003; Walker et al., 2008). Meanwhile, the BZ extends to its neighbouring RZ (Jackson et al., 2002; Walker et al., 2008). Infarct extension, combined with infarct

expansion, contributes to the feed-forward cycle of LV remodelling, which involves slippage, apoptotic and necrotic cell death, changes in the myocardial interstitium, a diminished wall thickness and LV dilation (Diwan et al., 2007), and eventually leads to heart failure.

From a mechanical perspective, overstretching of infarct is accountable for both infarct expansion and extension. Thus, any interventions that aim to inhibit bulging and dilation of infarct, such as a cardiac support device (Blom et al., 2005), biomaterial injection (Nelson, Ma, Fujimoto, Hashizume, & Wagner, 2011) and patching (Dor, 2001), are believed to help prevent or delay LV remodelling. These interventions should not focus only on inhibiting infarct expansion, but should also consider preventing infarct extension. To ensure long-term successful outcomes, these interventions should take into account the relative stiffness of the fibre to cross-fibre direction at the IZ and seek ways to obtain a more homogenous stress distribution at the BZ, as the simulation results showed that fibre orientation plays an important role in producing high stress at the BZ, which is believed to cause infarct extension.

4.5.6 Model Limitations

As mentioned in chapter 3, a simple truncated ellipsoid LV model, which lacks patient-specific validation, is subject to inaccuracies in geometry and material properties. Such inaccuracies, especially for the relative IZ stiffness (with respect to the RZ stiffness), might affect the extent of connectivity between the ischemic and viable myocardium, and subsequently the quantitative results for stress and strain. However, the major qualitative findings would not be affected, since the mechanical tethering mechanism between the ischemic and viable myocardium, the bulging of the IZ and the impaired mechanical energy efficiency of the myocardium with increasing infarct TME, and the effect of fibre directionality would all still be exhibited, regardless of

inaccuracies in the geometry and material properties. Therefore, despite these inaccuracies, the generic model was sufficient to meet the purpose of this study, namely to investigate the qualitative impact of infarct TME on LV regional mechanics. Furthermore, the quantitative comparison between the simulation results with published findings was not the focus of this study, since to date, threshold values of strain and stress for the initiation of infarct expansion and extension remain unclear.

Residual stresses, which are present in the myocardium, were not included in the models. However, as shown in the results, myocardial mechanics was most impaired during end-systole, at which instant the LV pressure was much greater than the residual stresses imposed on the myocardium. Thus, the effects of residual stresses are minimal, particularly during end-systole, and are unlikely to alter the major findings.

As mentioned in the previous chapter, the dynamics of myocyte twitch tension in the models was modulated by myocyte sarcomere length throughout the systolic phase, without incorporation of a force-velocity relationship. The main reason was that LV myocyte force-velocity relationship for humans, or species with similar LV physiology to humans, is still lacking to date (McDonald et al., 2012). The decrease of sarcomere length and corresponding decrease in twitch tension during contraction were assumed to be adequate in representing the force-velocity relationship of the myocyte. In addition, the time course of myocardial circumferential strain in the present models was shown to match well with observations in a previous study (Becker et al., 2009).

In this study, LV electrophysiology simulation was simplified and the activation time result obtained in the present study does not reflect the actual AP conduction. Physiologically, AP first propagates from interventricular septum to LV apex via the bundle of His. Then, the AP enters the Purkinje fibres, propagates upwards and spreads across the endocardial surface of LV free wall. Finally, the AP spreads throughout the

LV wall with fibre and cross-fibre conduction velocities (Tortora & Derrickson, 2012). Modelling of physiological AP conduction system would require multi-domain geometry, sizably amplifying the computational time and complicating the simulations. As such, the AP conduction was simplified in this study by simulating the AP propagated towards the base with fibre and cross-fibre conduction velocities, which were greater than values reported in the previous study (Potse et al., 2006). More importantly, since the regions with abnormal mechanics did not systematically correspond to the regions of delayed activation, electrophysiological function was not responsible for the impaired mechanics observed. Therefore, the findings of this study are not affected by such simplification.

Simulating the AP conduction using FitzHugh-Nagumo equations ignored also the mechano-electric feedback. It has been shown in previous modelling studies that mechano-electric feedback can alter the effective refractory period (N. Trayanova, Li, Eason, & Kohl, 2004) and cause dispersion of action potential (AP) duration (Wall et al., 2011). The presence of infarct, which alters the activity of mechano-electric feedback, can lead to electrophysiology-related complications such as current reentry, arrhythmias and tachycardia (Jie, Gurev, & Trayanova, 2010). However, since the focus of the present work was on the impairment of LV mechanical function following MI, incorporating variations in myocyte electrophysiological properties within the infarct as well as mechano-electric feedback, along with their corresponding complications, were beyond the scope of this study. Therefore, the modified FitzHugh-Nagumo model was assumed sufficient in simulating AP propagation. Other diseases, such as mitral regurgitation and LV outflow tract obstruction, which may occur following an MI event, were also beyond the scope of this study.

4.6 Conclusions

In the present study, it has been demonstrated that infarct TME is an important determinant for the presence of impaired LV regional mechanics, which is believed to place the LV at a higher risk of infarct extension. The LV regional mechanics that is impaired with an increase in infarct TME includes highly abnormal stress distribution, elevated myocardial energy expenditure and impaired myocardial energy efficiency at the BZ. In addition, the simulation results suggested that the impaired myocardial mechanics at the BZ is a consequence of the combined effects of mechanical tethering, simultaneous presence of moderately high strain and contractility at this region, and also fibre orientation at the IZ, but not of electrophysiological factors. Furthermore, it was also found that LV global indices are inadequate in determining the regional impairments of LV mechanics.

In the next chapter, the developed generic LV model will be modified into a patient-specific model, incorporating patient-specific infarcted LV geometry and optimised regional material properties, to allow a more accurate quantification of the simulated variables. Subsequently, the patient-specific model will be used to examine the correlation of myocardial mechanics impairments with infarct extension.

CHAPTER 5: THE ROLE OF END-DIASTOLIC STRETCH ON INFARCT EXTENSION

5.1 Introduction

In the last chapter, it was found that a transmural infarct substantially impairs the left ventricular (LV) regional mechanics, including the presence of abnormally high stress, elevated myocardial energy expenditure and reduced myocardial energy efficiency. In this chapter, the correlation of the impaired regional myocardial mechanics with infarct extension was examined.

The occurrence of infarct extension was assessed by comparing infarct size obtained from late gadolinium enhancement (LGE) cardiovascular magnetic resonance imaging (CMR) between two time points, i.e. (i) within one week after a myocardial infarction (MI) and (ii) four to five months after the first scan. Based on the cine and LGE CMR images from the first scan, patient-specific LV models were reconstructed for three MI patients, and parameter optimisation was performed to estimate active and passive material parameters. Thereafter, full cycle simulations were performed on each patient-specific model to investigate the correlation between impaired myocardial mechanics and infarct extension. Subsequently, a sensitivity study was carried out to ascertain the causal factors behind impaired myocardial mechanics at the remote zone (RZ) surrounding the border zone (BZ) and infarct zone (IZ).

5.2 Literature Review

As mentioned in the previous chapter, infarct extension, unlike infarct expansion, is unknown in its causation and is a subject of much speculation. Depressed BZ contractile function (Kramer et al., 1993), and BZ stretching during the isovolumic contraction (IVC) phase (Moulton et al., 1995), have been observed in previous studies; and these have been hypothesised to cause ventricular remodelling. Tyagi et al. (1998)

demonstrated through their experimental work that abnormal mechanical cyclic stretching could induce membrane type matrix metalloproteinases (MT-MMPs) and tissue plasminogen activators in cardiac fibroblasts, thereby activating latent matrix metalloproteinases (MMPs). Stretch-induced apoptosis had been shown by Pimentel et al. (2001) to be manipulated by stretch amplitude-dependent production of reactive oxygen species (ROS), with low levels of stretch inducing hypertrophy, and high levels inducing apoptosis. Although depressed contractile function and isovolumic stretching phenomena have been observed in BZ in several experimental studies, the causal factors contributing to these observations remain unclear.

Ratcliffe (2002) proposed that an increase in systolic BZ stress causes isovolumic stretching, which then initiates apoptosis and reduces contractility. In a study by Walker et al. (2005), which utilised a sheep-specific computational finite element (FE) model, simulation results showed that the BZ presented 24% and 115% elevation in midwall fibre and cross-fibre stresses respectively, as compared to the RZ. However, contradictory findings were revealed in another FE modelling study (J. M. Guccione et al., 2001), which demonstrated that experimentally observed isovolumic stretching at the BZ was caused by impaired intrinsic contractility and not elevated wall stress. However, this cannot explain the phenomenon of nonischemic infarct extension, which involves infarct extension at the RZ with normal intrinsic contractility, during post-infarct ventricular remodelling as observed by Jackson et al. (2002).

Therefore, it still remains speculative on the possible causal factors that are responsible for infarct extension, particularly on how they contribute to isovolumic stretching and depressed contractility of neighbouring myocardium.

5.3 Methods

5.3.1 Image Acquisition

This study was approved by the University Malaya Medical Centre Medical Ethics Committee (reference number: MEC989.75 and MEC1190.44) and carried out in compliance with the guideline document "International Conference on Harmonization - Guidelines for Good Clinical Practice (ICH-GCP) and the Declaration of Helsinki". The selection of MI patients was based on the following four criteria:

i. above eighteen years old,

ii. first time MI of type ST elevation,

iii. received percutaneous coronary intervention treatment within 24 hours following MI,

iv. did not have aortic stenosis, mitral regurgitation or arrhythmia.

Each of the selected patients underwent a CMR scan to obtain cine and LGE images within a week after the reperfusion treatment and a subsequent follow-up scan (second scan) four to five months after the first scan.

The cine and LGE images were acquired with a 1.5T MRI system (SignaHDxt 1.5T, GE Healthcare, WI, U.S.A.) using Array Spatial Sensitivity Encoding (ASSET) and multi-breath-hold steady-state free precession techniques (FOV: 350 × 350 mm, image matrix: 256 × 256, pixel size: 1.37 × 1.37 mm, flip angle: 55°, TE/TR: 1.58/3.67 ms, imaging frequency 63.94 MHz, breath-hold time: 15 s). The cine images consisted of a stack of short-axis (SX) slices (number of slices: 10 - 17, slice thickness: 8 mm, gap: 0 mm), covering from the LV base to the LV apex, as well as a set of six long-axis (LX) slices rotated radially around the LV chamber centre (with 30° between slices), as shown in Figure 5.1. The images were acquired at 20 time frames per LV cycle.

Meanwhile, the LGE images comprised of a stack of SX slices as in cine, but with only two LX slices (i.e. the 2- and 4-chamber views), and were acquired at end-systolic cardiac phase.

5.3.2 Image Registration for Motion Correction

Since the cine images were acquired from multiple breath-holds, patient motion between each breath-hold, for example that caused by respiratory motion, gave rise to the misalignment of SX and LX slices. In order to ensure accurate 3D LV geometry reconstruction, an in-house multi-slice image registration framework (Liew et al., 2015) was applied on the cine images.

Specifically, all the SX and LX slices were initially transformed to the reference coordinate system of the heart, based on the position and orientation information provided by the DICOM header file, before these slices were subject to misalignment correction using an in-house multi-slice rigid registration algorithm. Theoretically, pixel intensity profiles along the intersecting lines of the SX and LX slices should coincide or be similar when the slices are properly aligned to each other. To accomplish this

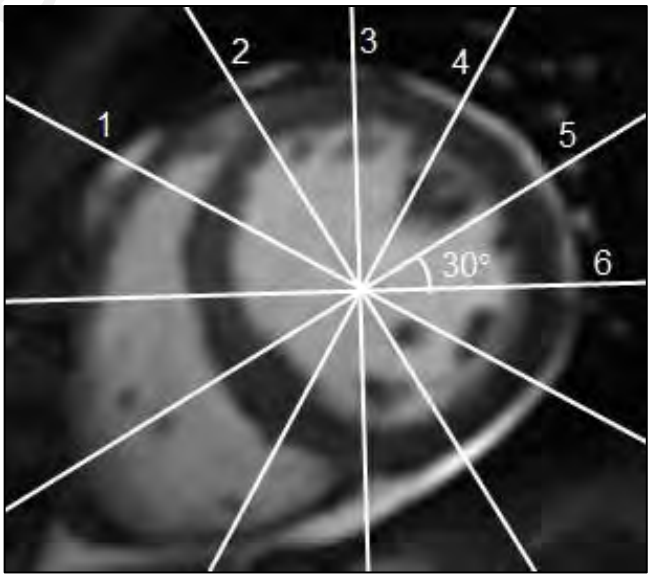

Figure 5.1: Long-axis (LX) image slices rotated radially around the left ventricular (LV) chamber centre, with 30° between subsequent slices.

registration, rigid transformation was applied on the SX and LX slices such that the similarity of their intersecting pixel intensity profiles yielded maximum normalised cross-correlation value. The rigid transformation matrix, **r** used in the current study accounted for 6 degrees of freedom misalignment, and consisted of three translational (i.e. t_x, t_y and t_z along x, y and z axes respectively) and three rotational parameters (i.e. ϕ_x, ϕ_y and ϕ_z about x, y and z axes respectively):

$$\mathbf{r}(\mathbf{v}) = \mathbf{R}\mathbf{v} + \mathbf{t} \tag{5.1}$$

where **v** represents an image voxel to be transformed, whilst **t** is the 3D translation vector:

$$\mathbf{t} = (t_x, t_y, t_z)^T \tag{5.2}$$

and **R** represents a 3D rotation matrix:

$$\mathbf{R} = \begin{pmatrix} \cos\phi_y \cdot \cos\phi_z & \cos\phi_x \cdot \sin\phi_z + \sin\phi_x \cdot \sin\phi_y \cdot \cos\phi_z & \cdots \\ -\cos\phi_y \cdot \sin\phi_z & \cos\phi_x \cdot \cos\phi_z - \sin\phi_x \cdot \sin\phi_y \cdot \sin\phi_z & \cdots \\ \sin\phi_y & -\sin\phi_x \cdot \cos\phi_y & \end{pmatrix}$$

$$\begin{pmatrix} \sin\phi_x \cdot \sin\phi_z - \cos\phi_x \cdot \sin\phi_y \cdot \cos\phi_z \\ \sin\phi_x \cdot \cos\phi_z + \cos\phi_x \cdot \sin\phi_y \cdot \sin\phi_z \\ \cos\phi_x \cdot \cos\phi_y \end{pmatrix} \tag{5.3}$$

The centre of rotation for each SX slice was placed at its intersecting point with all the LX slices. On the other hand, the centre of rotation for each LX slice was positioned at the intersecting point of the middle SX slice with all the LX slices.

Ideally, the heart should be the only organ focused on in the images for motion correction. However, surrounding structures, such as the liver, lung and thoracic cage, confound the correction process, as the locations of these tissues vary spatially with respiration during image acquisition. As such, a region of interest (ROI) mask was

introduced to exclude the surrounding structures during the motion correction process. For each slice, the ROI mask was computed from a 2D + time image sequence at that slice location based on the temporal variance of the pixel intensity across the entire cardiac cycle, i.e. by taking the variance of pixels along the temporal dimension to yield a single, compressed variance image. In the variance image, an area with moving structures, predominantly the heart, would have a high variance value, whilst the surrounding area, which was relatively static, would return a negligible or low variance value. The ROI was then thresholded and morphologically processed to form an ellipse binary mask enclosing the heart. Subsequently, a secondary larger ellipse was drawn by dilating this primary ellipse mask. The pixels enclosed by the primary ellipse were assigned a weight of 1, whilst the pixels outside of the secondary ellipse were assigned a weight of 0. The pixels in between these two ellipses were assigned a weight of 1 to 0 by linearly interpolating from the primary ellipse to the secondary ellipse. This weight assignment helped improve the robustness of the registration algorithm by allowing different pixels to have different levels of impact on the registration process, i.e. the heart pixels affected the registration more compared to the surrounding non-heart pixels. An example of primary and secondary ellipses, ROI weighting mask and variance image computed for both the SX and LX slices is shown in Figure 5.2. The ROI mask defined for each slice encompassed both the RV and LV in order to reduce ambiguous optimal registration arising from subtle changes in their shape along the LX direction, especially at the basal and mid ventricular positions.

The registration process was driven by a similarity measure utilising the ROI weighting mask. Since the magnetic field could be fluctuating and inhomogeneous throughout the image acquisition procedure, the pixel intensity of the same anatomical structure could vary between slices. The similarity measure, which was the cross-

correlation, was therefore zero-normalised, in order to account for the linear fluctuation of intensity profiles across slices (Makela et al., 2002):

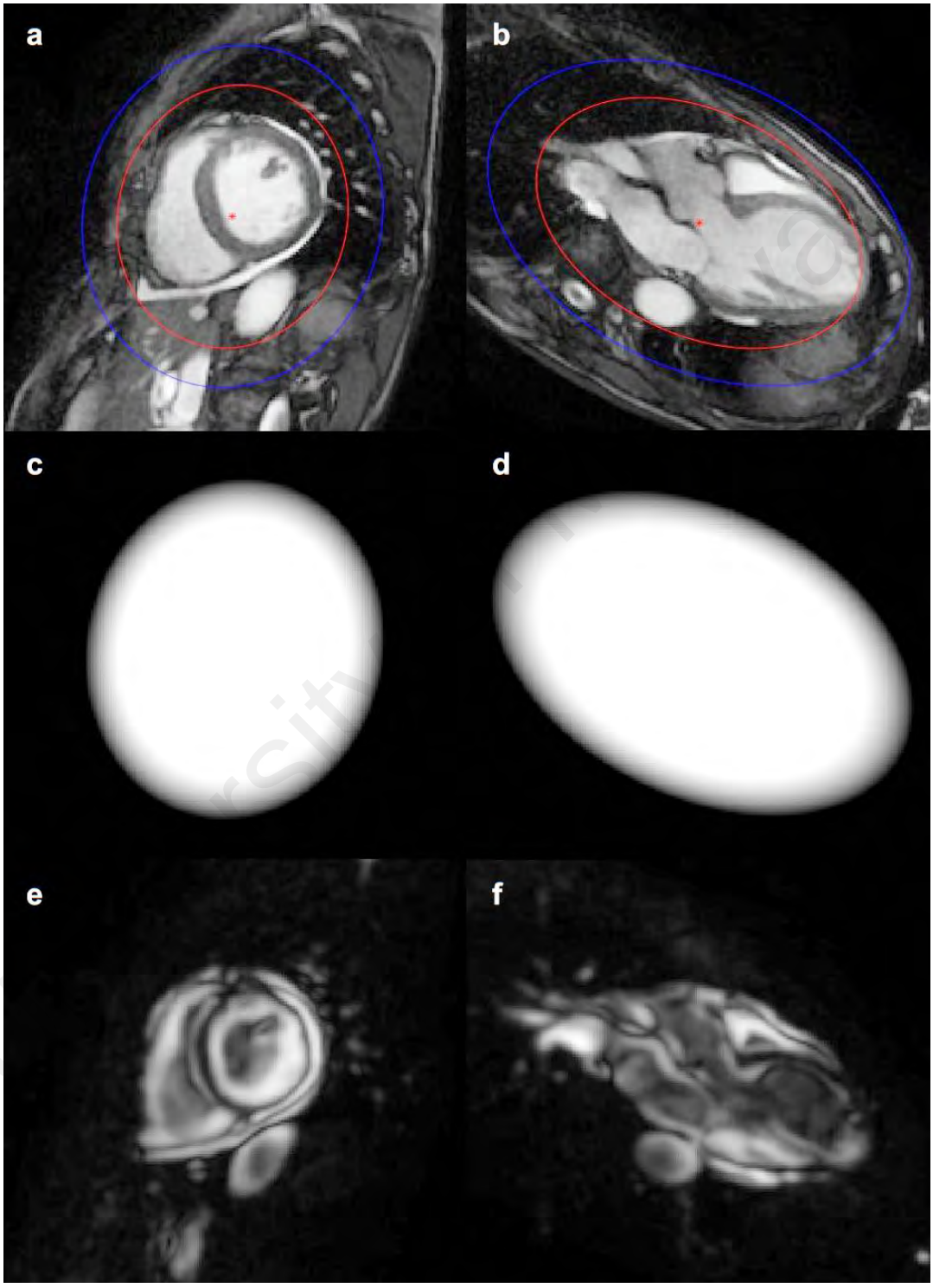

Figure 5.2: Primary and secondary ellipse definitions for the (a) short-axis (SX) and (b) long-axis (LX) images. Region of interest (ROI) weighting masks of the SX and LX images are shown in (c) and (d) respectively, whilst variance images of the SX and LX images are shown in (e) and (f) respectively.

$$\mathrm{ZNCC} = \frac{\sum_{k=1}^{K} W_{m\cap n}(k)\cdot\left(S^{m}_{m\cap n}(k)-\mu S^{m}_{m\cap n}\right)\cdot\left(S^{n}_{m\cap n}(k)-\mu S^{n}_{m\cap n}\right)}{\sqrt{\sum_{k=1}^{K} W_{m\cap n}(k)\cdot\left(S^{m}_{m\cap n}(k)-\mu S^{m}_{m\cap n}\right)^{2}}\cdot\sqrt{\sum_{k=1}^{K} W_{m\cap n}(k)\cdot\left(S^{n}_{m\cap n}(k)-\mu S^{n}_{m\cap n}\right)^{2}}} \quad (5.4)$$

where ZNCC denotes the zero-normalised cross-correlation similarity measure, with $W_{m\cap n}$ denoting the intensity of the ROI mask at the intersection line of slices *m* and *n*. *K* is the number of samples along the intersection line, $S^{m}_{m\cap n}$ and $S^{n}_{m\cap n}$ denote the intensity profiles of the intersection line on slices *m* and *n* respectively, whilst $\mu S^{m}_{m\cap n}$ and $\mu S^{n}_{m\cap n}$ denotes the means of $S^{m}_{m\cap n}$ and $S^{n}_{m\cap n}$ respectively. During the computation of ZNCC for each pair of the intersecting slices, the ROI weighting mask was applied on one slice, while a uniform mask with all weights set to 1 was applied on another slice.

The multi-slice registration algorithm was optimised by minimizing the cost function:

$$\mathrm{cost} = 1 - \mathrm{ZNCC} \quad (5.5)$$

which measures the dissimilarity of intersecting line intensity profiles. All the SX and LX slices were simultaneously registered relative to a static reference LX slice, which was the 4-chamber view slice. The total cost function to be minimized was equal to the sum of cost functions from all pairs of intersecting slices (including both the SX and LX slices), with 6 independent parameters (t_x, t_y, t_z, ϕ_x, ϕ_y and ϕ_z) per slice to be estimated. The optimisation procedure was performed using a Quasi-Newton optimiser, with its optimising step size calculated using a line search method. In each iteration, the gradient and Hessian matrices were computed and updated using a finite-differencing method.

For more detailed description of this multi-slice registration algorithm, please refer to Liew et al. (2015).

5.3.3 Left Ventricular Geometry Reconstruction

The LV epicardial and endocardial contours on both the SX and LX slices were manually delineated using the Segment software (free version 1.9 R3136, Medviso, AB). Subsequently, the contours were transformed into the MRI coordinate system according to the multi-slice registration results for motion correction. Patient-specific LV geometry was reconstructed by fitting closed and open cubic B-spline curves along the circumferential and longitudinal directions respectively, as shown in Figure 5.3. The LV region within the SX slices was reconstructed based on the contours obtained from the SX slices, whilst the base and apex regions, which were beyond the SX slices, were reconstructed based on the contours from the LX slices (Liew et al., 2015). For each patient, the LV geometries for three cardiac time points were reconstructed: early diastole (i.e. the second cardiac time point after mitral opening), end-diastole and end-systole. LV geometry reconstructed from early diastole was used as the reference geometry for FE modelling simulations, because the LV is believed to be under minimum stress condition at this cardiac time point. Meanwhile, the end-diastolic and end-systolic LV geometries were used for model parameter optimisation.

The delineation of the non-perfused region (NPR) was performed on the SX cine images obtained at early diastole by referring to the contrast observed from the SX LGE images, as shown in Figure 5.4. The delineated NPR curves were then transformed into the MRI coordinate system, circumferentially and longitudinally fitted with B-spline curves, to reconstruct the NPR geometry. The united geometry of the reference LV and the NPR was then imported into COMSOL multi-physics modelling software. The LV geometry was then rotated such that its major axis (line passing from the LV apex to the mitral aspect of the left aortic valve commissure) was aligned with the z-axis of the COMSOL coordinate system (Streeter et al., 1969). An example of reference LV geometry is shown in Figure 5.5, with cyan and yellow colours indicating the perfused

region (PR) and NPR respectively. To avoid convergence errors during simulations, 20% (by volume) of the reference LV geometry was removed, starting from the base. The reconstructed end-diastolic and end-systolic geometries, as for the reference geometry, were imported into COMSOL and rotated following the reference LV geometry rotation.

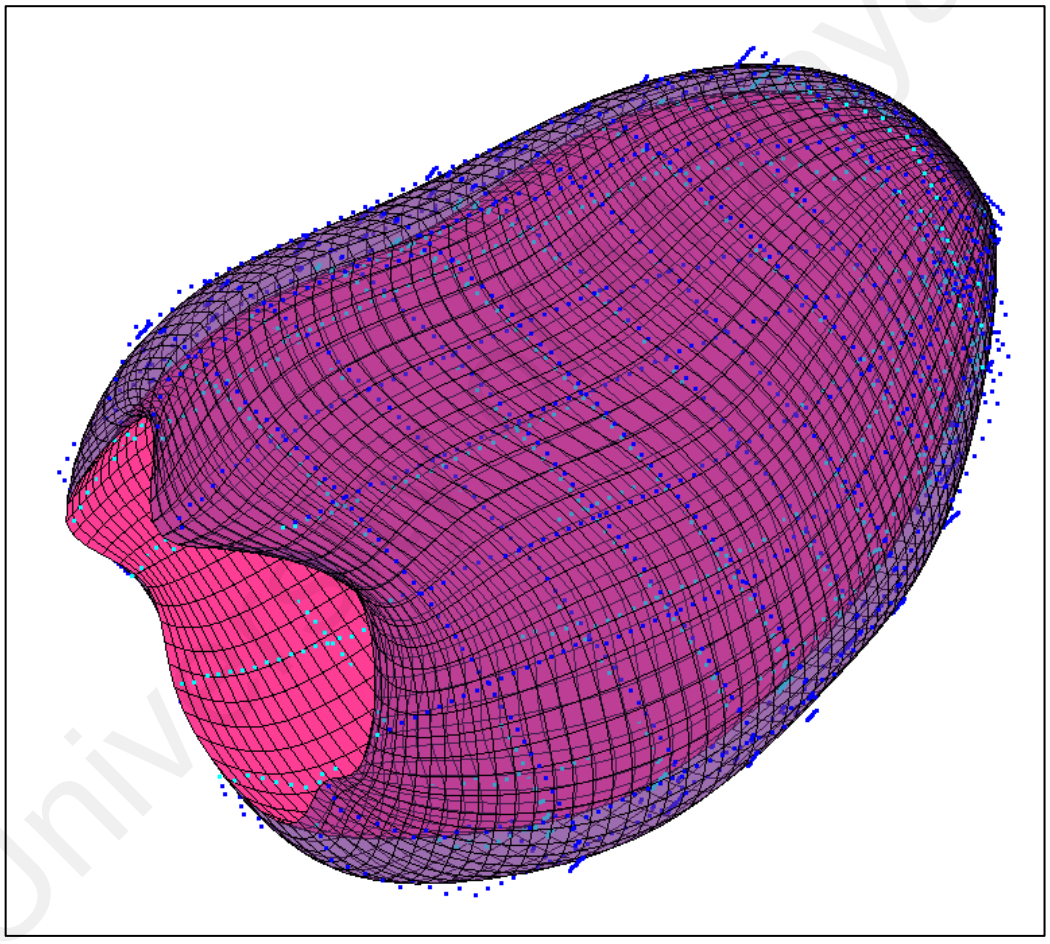

Figure 5.3: Reconstruction of patient-specific LV geometry by fitting closed and open cubic B-spline curves along the circumferential and longitudinal directions respectively, referring to the delineated epicardial and endocardial contours. These epicardial and endocardial contours are represented by the blue and cyan dots respectively.

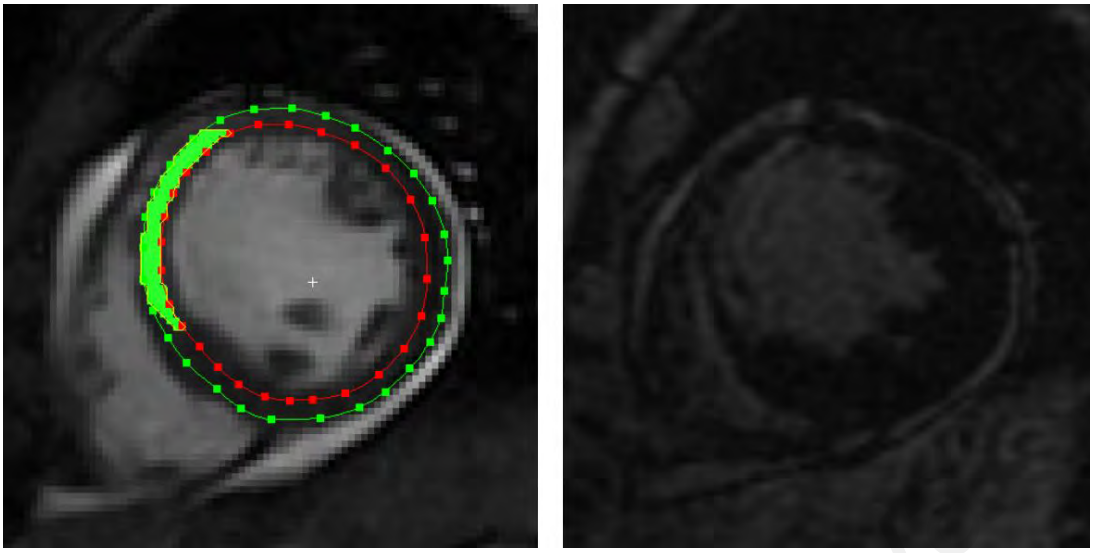

Figure 5.4: Delineation of the non-perfused region was performed on the short axis cine image obtained at early diastole (left) by referring to the contrast observed from the short axis LGE image (right).

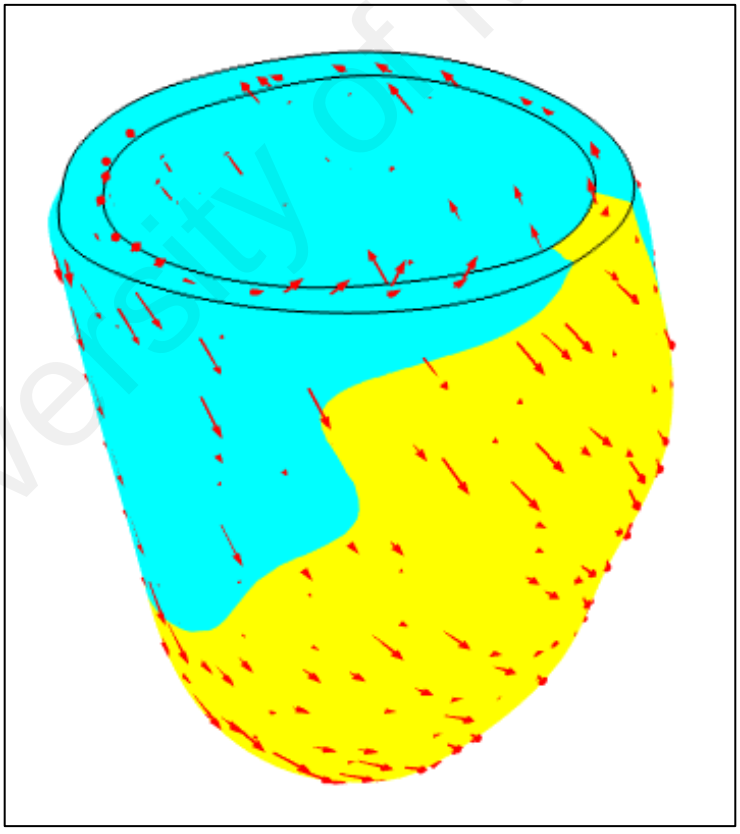

Figure 5.5: Patient-specific reference LV geometry, with cyan and yellow colours indicating perfused (PR) and non-perfused (NPR) regions respectively. The red arrows represent the local fibre orientation, which varies transmurally from +60° at the endocardium to -60° at the epicardium.

5.3.4 Mechanics Formulations

As described in Section 3.2, the LV was modelled as a quasi-static and nearly incompressible hyperelastic material with transversely isotopic behaviour aligned with the local fibre direction. This local fibre direction was assumed to vary transmurally from +60° at the endocardium to -60° at the epicardium, as shown in Figure 5.5. The overall passive stiffness of the myocardium was manipulated by the parameter C_0 (kPa), whilst the active contractile ability of the myocardium was controlled by the active twitch stress parameter, T_0 (kPa), which reflects the myocardial intrinsic contractility, the local time of active contraction, t_s (s), and the sarcomere length profile, λ (μm). Since the action potential (AP) propagation was shown in Chapter 4 to play a negligible contribution on the impairments of regional mechanics, electrophysiology formulations were not incorporated into the present patient-specific LV model. Instead, active contraction of the myocardium was initiated simultaneously throughout the entire LV.

5.3.5 Parameter Optimisation of the Patient-Specific Left Ventricular Model

The model parameter optimisation process was performed in two stages, i.e. end-diastolic optimisation followed by end-systolic optimisation. During the end-diastolic optimisation process, an end-diastolic pressure of 8 mmHg was assumed based on the published literature (Choi et al., 2011) and applied to the LV endocardium. The basal surface of the LV was constrained from moving vertically. To account for the effect of valve annuli, a spring constant per unit area, k_0 (N/m^3), was applied on the basal surface. The objective function of the optimisation was defined as:

$$\mathrm{OBJ} = \iint_{epi} \zeta_{epi}^{ED} + \iint_{endo} \zeta_{endo}^{ED} \tag{5.6}$$

with ζ_{epi}^{ED} and ζ_{endo}^{ED} representing the distance from the simulated (reference LV geometry with end-diastolic pressure applied) epicardial and endocardial walls to the

actual (LV geometry at end-diastolic time point) epicardial and endocardial walls, respectively, as illustrated in Figure 5.6. $\iint_{epi}$ and $\iint_{endo}$ denote the surface integrals for the simulated epicardial and endocardial walls respectively. The C_0 and k_0 values were estimated by minimising the objective function (OBJ). During simulation, the basal surface of the LV geometry was constrained from moving vertically while other regions were allowed to move freely. In reality, however, the LV sits in the thoracic cavity, causing the LV apex to be relatively immobile, with other LV regions moving freely. Such a discrepancy led to misalignment between the simulated and actual geometries. To overcome this misalignment problem, the actual geometry was realigned by referring to the apex and mid ventricle of the simulated geometry, as demonstrated in Figure 5.7. Subsequently, the optimisation and realignment procedures were repeated until both the estimated C_0 and k_0 values changed by less than 5%.

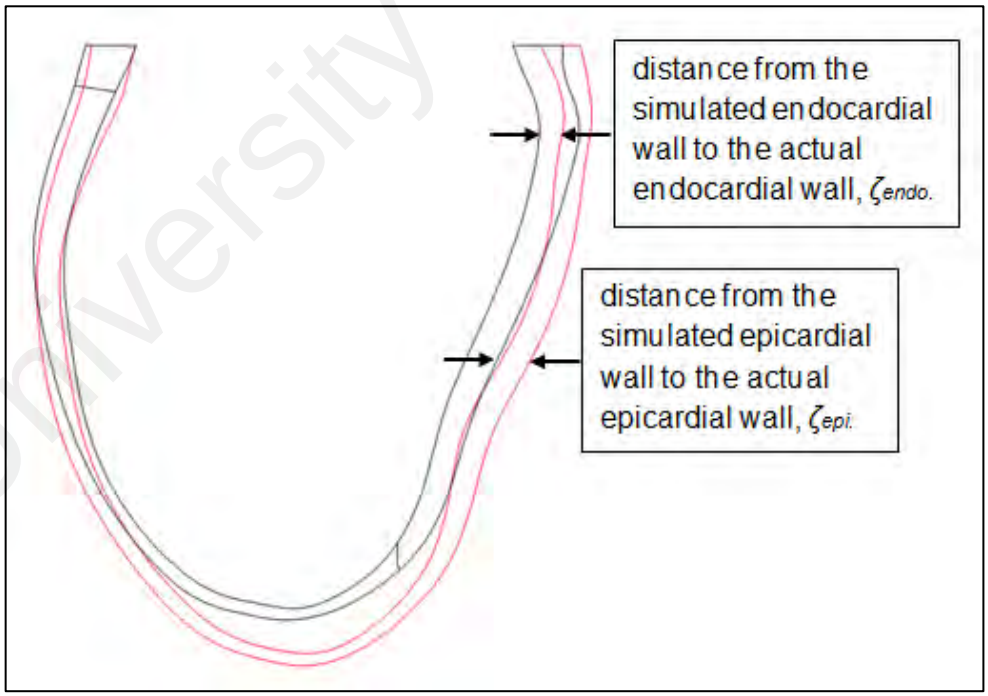

Figure 5.6: Distance from the simulated (reference LV geometry with end-diastolic pressure applied) epicardial and endocardial walls to the actual (LV geometry at end-diastolic or end-systolic time point) epicardial (ζ_{epi}) and endocardial (ζ_{endo}) walls respectively, with black and red lines representing the simulated and actual LV geometries respectively.

During the end-systolic optimisation process, an end-systolic pressure of 100 mmHg was utilised, based on the Wiggers diagram (Guyton & Hall, 2006), and applied to the LV endocardium. Similar to end-diastolic optimisation, the basal surface of the LV was constrained from moving vertically during simulation. Variable t_s was set to be 0.272 s, the time point at which the generic LV model NORMAL described in Chapter 4 reached its end-systole, with simultaneous initiation of active contraction throughout the entire LV. The same objective function for parameter optimisation defined in Equation 5.6 was used, except that the end-diastolic expressions ($\zeta_{epi}^{ED}$and ζ_{endo}^{ED}) were replaced with that of end-systolic expressions (ζ_{endo}^{ES} and ζ_{endo}^{ES}). The parameter values of C_0 and k_0 estimated during the end-diastolic optimisation process were maintained in the end-systolic optimisation (note: the optimised C_0 value from the end-diastolic optimisation was used only on the RZ during the end-systolic optimisation). T_0 for the IZ ($T_{0(IZ)}$) was set as 0 kPa to account for its inability to contract. The parameter values of T_0 (i.e. T_0 for the RZ) and $C_{0(IZ)}$ (i.e. C_0 for the IZ) were estimated by minimising the OBJ. As

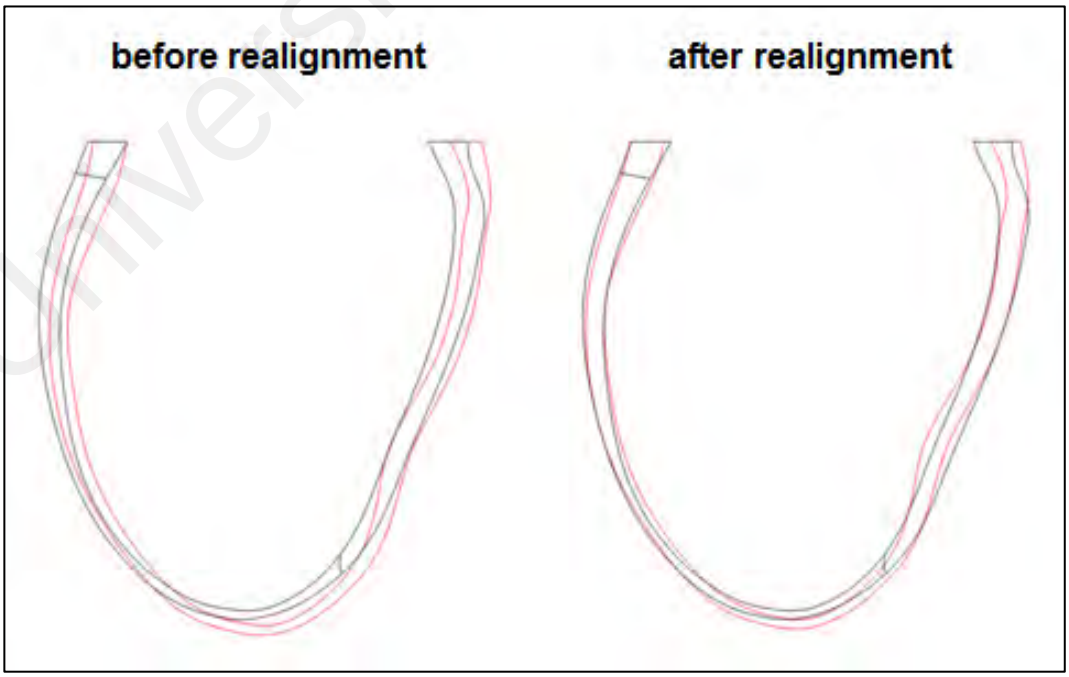

Figure 5.7: Superimposition between the simulated (black) and actual (red) geometries, before and after realignment.

before, realignment of the actual geometry in accordance with the simulated geometry was performed after each optimisation, and the procedures were repeated until the estimated T_0 and $C_{0(IZ)}$ values changed by less than 5%. The optimisations were performed using the Nelder-Mead method, with an optimality tolerance of 1.0×10^{-2}.

5.3.6 Complete Left Ventricular Cycle Simulations

In order to ensure a smooth transition in material properties between the IZ and RZ, a 1 cm bandwidth representing the BZ was introduced in between them, as illustrated in Figure 5.8. Infarct indices, χ, of 1 and 0 represent the IZ and RZ respectively, whilst in-between values represent the BZ. The material properties of the BZ, Ψ_{BZ} (i.e. C_0 and T_0), were assumed to transition linearly from the IZ to the RZ according to the following equation:

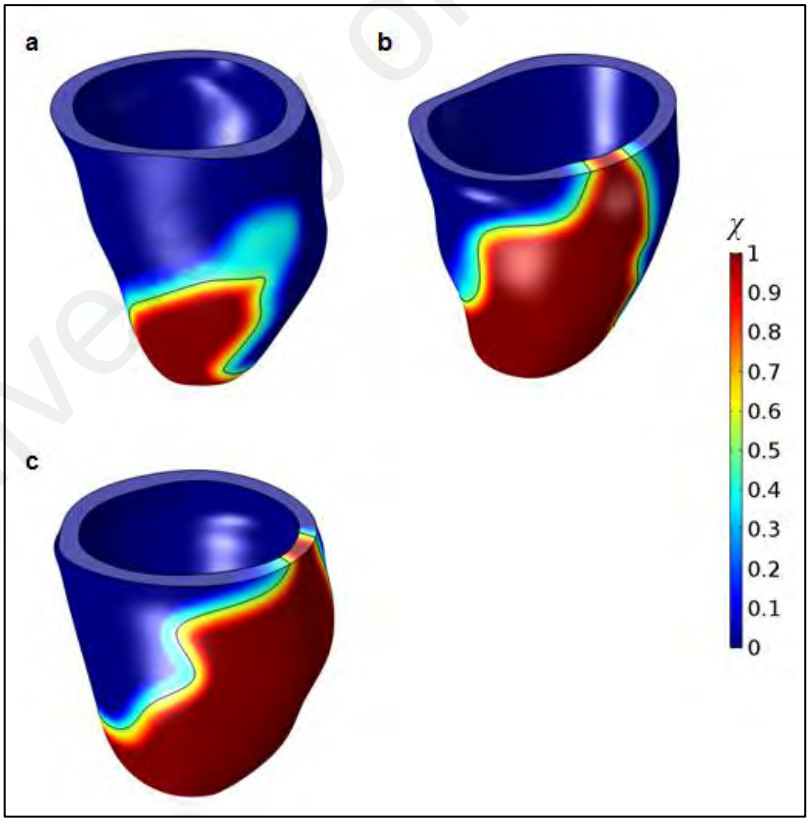

Figure 5.8: Patient-specific LV geometries for patients (a) 1, (b) 2 and (c) 3, with infarct (IZ), border (BZ) and remote (RZ) zones defined. Infarct indices, χ, of 1 and 0 represent the IZ and RZ respectively, whilst in-between values represent the BZ.

$$\Psi_{BZ} = \chi \Psi_{IZ} + (1-\chi)\Psi_{RZ} \tag{5.7}$$

where Ψ_{IZ} and Ψ_{RZ} denote the material properties of IZ and RZ (i.e. C_0 and T_0) respectively.

Using the estimated parameter values obtained from the optimisations, a complete LV cycle was simulated using the boundary conditions described in Section 3.2.6. The parameter values of R_c and R_p in Equations 3.22 and 3.23 respectively, were readjusted such that the LV models exhibited systolic and end-systolic pressures of 120 mmHg and 100 mmHg respectively (Guyton & Hall, 2006).

Three male MI patients {patients 1 and 2: occluded left anterior descending artery (LAD); patient 3: occluded LAD and left circumflex artery (LCx)} with good quality CMR images and no LV thrombus were chosen for the present study. Baseline characteristics of all patients are given in Table 5.1. The LV geometries were meshed using quadratic tetrahedral elements. Mesh size was adjusted until the estimated C_0 in patient 1 changed by less than 1% during the first stage of the optimisation process. The mesh sensitivity test showed that a maximum mesh size of 6.16 mm (physics-controlled normal mesh option) was sufficient for the present work. The meshes generated from the physics-controlled normal and fine mesh options, along with the deformed meshes of patient 1 model (meshed with the physics-controlled normal mesh option) at both end-diastole and end-systole are shown in Figure 5.9. The LV cycles were simulated using the PARDISO solver, with a generalised alpha time stepping method, an absolute tolerance of 1.0×10^{-3} and a time step of 5 ms. The models were solved in COMSOL (v5.2, COMSOL AB, Sweden), using a Workstation equipped with two Intel Xeon E5-2620 6-core 2.00 GHz processors and 128 GB of RAM. It took around 7 hours to compute the optimisation (one optimisation procedure) and 10 hours to simulate a complete LV cycle for each patient.

Table 5.1: Baseline characteristics of patients.

	Patient 1	Patient 2	Patient 3
Age	43	53	67
Gender	Male	Male	Male
Medical history	Dyslipidaemia Hypertension Family history of cardiovascular disease	Dyslipidaemia Hypertension Diabetes	Dyslipidaemia Hypertension Diabetes
Lipid	3.91 (LDL), 5.9 (Total)	3.05 (LDL), 5.4 (Total)	3.06 (LDL), 5.1 (Total)
Smoking	Current	Former	Current
Current medication	Aspirin Statin Beta blocker ACE-inhibitor Ticagrelor Prasugrel	Aspirin Statin Beta blocker ACE-inhibitor Ticagrelor	Aspirin Statin ACE-inhibitor Ticagrelor
Infarcted segments (AHA 17-segment)	8, 9, 14, 15, 17	2, 7, 8, 13, 14, 17	2, 7, 8, 9, 13, 14, 15, 17
Infarct volume percentage	8.8 %	22.2 %	24.6 %
LV and RV functions	• Mild LV diastolic dysfunction • ESV = 41.1 ml • EDV = 106.9 ml • EF = 61.6 % Normal RV functions	• Mild LV diastolic dysfunction • ESV = 74.9 ml • EDV = 140.1 ml • EF = 46.5 % • Reduced RV systolic function	• Mild LV diastolic dysfunction • ESV = 121.5 ml • EDV = 173.5 ml • EF = 30.0 % • Normal RV functions

5.3.7 Data Analysis

In order to assess the occurrence of infarct extension, the same multislice registration-based motion correction algorithm followed by reference LV geometry reconstruction (with NPR) was performed on the CMR images acquired during the second scan. Subsequently, the LV geometries from both scans were realigned by matching their corresponding apex and mid ventricle positions, and shapes.

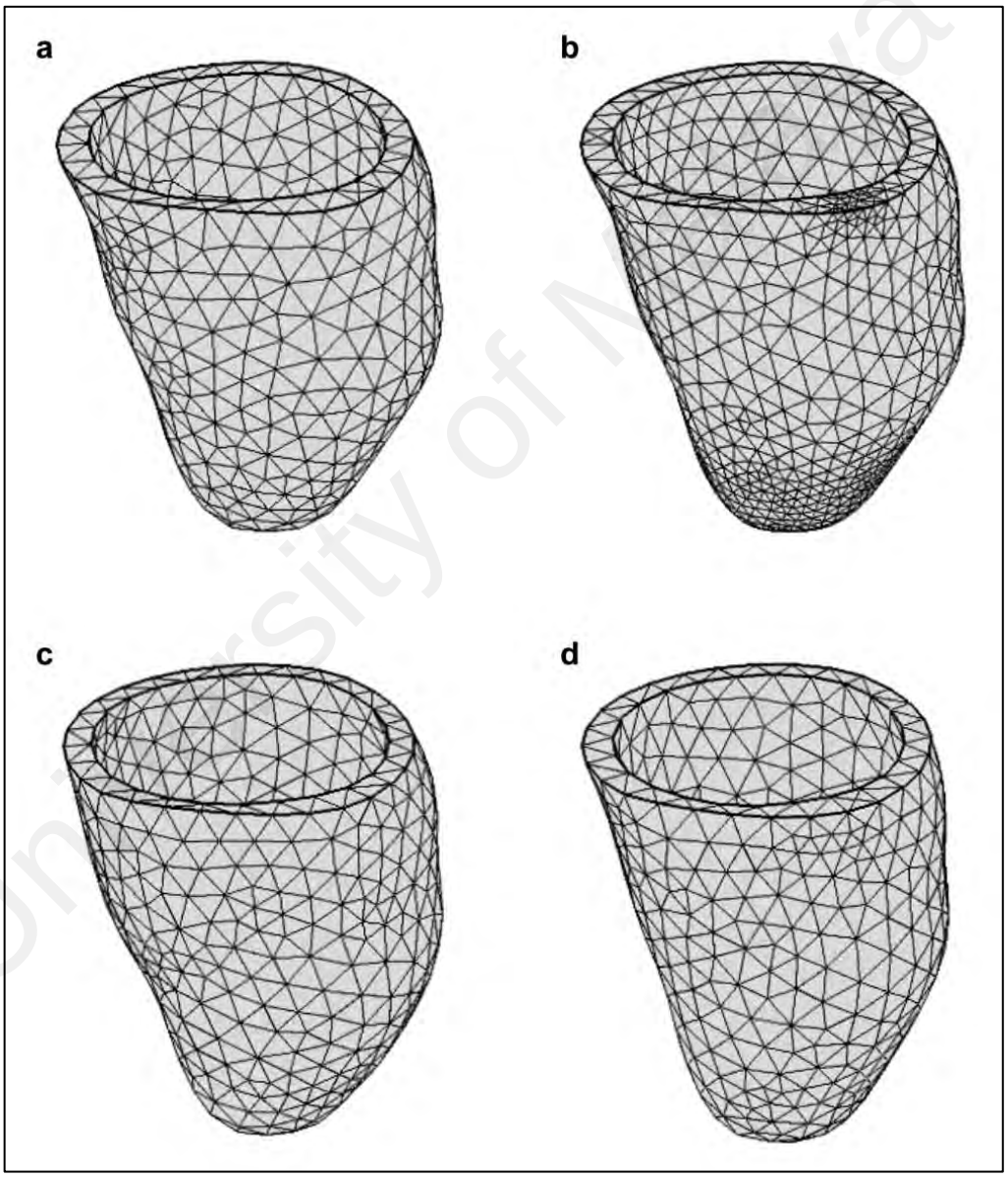

Figure 5.9: Undeformed meshes generated from the physics-controlled (a) normal and (b) fine mesh options. Deformed meshes of patient 1 model (meshed with the physics-controlled normal mesh option) at (c) end-diastole and (d) end-systole.

Following complete LV cycle simulations, the fibre stress-strain (fibre directional Cauchy stress against fibre directional engineering strain) loops (FSSLs), which reflect impairment in regional myocardial mechanics and abnormality in energy dissipation level, were generated for several points at the RZ-BZ border. The FSSL shape, as well as fibre strain and fibre stress, was analysed to investigate its correlation with infarct extension. In order to better quantify the degree of impairment, shown by a deviation of FSSL from the standard rectangular shape, a work density dissipation (WDD) index was proposed. The WDD index for each FSSL was defined as:

$$\mathrm{WDD} = \frac{\omega_{isov} + \omega_{eject}}{\omega_{output}} \tag{5.8}$$

where ω_{isov} and ω_{eject} denote the dissipated work density during the IVC and ejection phases respectively, whilst ω_{output} denotes the work density output by the myocardium. ω_{isov}, ω_{eject} and ω_{output} were represented by the different areas of the FSSL, as shown in Figure 5.10. A higher WDD value signifies worse impairment in myocardial mechanics and energy efficiency. The WDD index value, as well as fibre strain and fibre stress, was analysed to investigate its correlation with infarct extension. The correlation between infarct extension and WDD index value was analysed by conducting a Mann-Whitney *U* test, using the SPSS 23.0 statistical software (SPSS Inc, Chicago, IL). A *P*-value <.05 was considered statistically significant.

5.3.8 Sensitivity Analysis

In order to identify the causal factors leading to impaired regional myocardial mechanics at the RZ-BZ border, a sensitivity analysis was performed by running additional simulations using the optimised parameters for each patient, but with three different model settings: 1) 10 times the $C_{0(IZ)}$ ($10\times C_{0(IZ)}$) to investigate the effect of increased passive stiffness for the IZ, (2) 0.1 times the $C_{0(IZ)}$ ($0.1\times C_{0(IZ)}$) to investigate

the effect of decreased passive stiffness for the IZ and (3) replacing λ with the sarcomere length profile acquired at a selected point in the RZ far away from the IZ ($SL_{(RZ)}$).

5.4 Results

5.4.1 Parameter Optimisation Results

Table 5.2 shows the optimisation errors, indicated by average wall distances between the simulated and actual geometries, for the PR and NPR of each patient. An example of optimisation outcomes, which compares the simulated (black) and actual (red) geometries after the end-diastolic and end-systolic optimisations, is given in Figure 5.11. Generally, all simulated geometries had errors lower than 1 mm on average, relative to their corresponding actual geometries, for both their PRs and NPRs. The only exception was the end-systolic optimisation results for patient 2, which had average errors of 1.084 mm and 1.510 mm for its PR and NPR respectively.

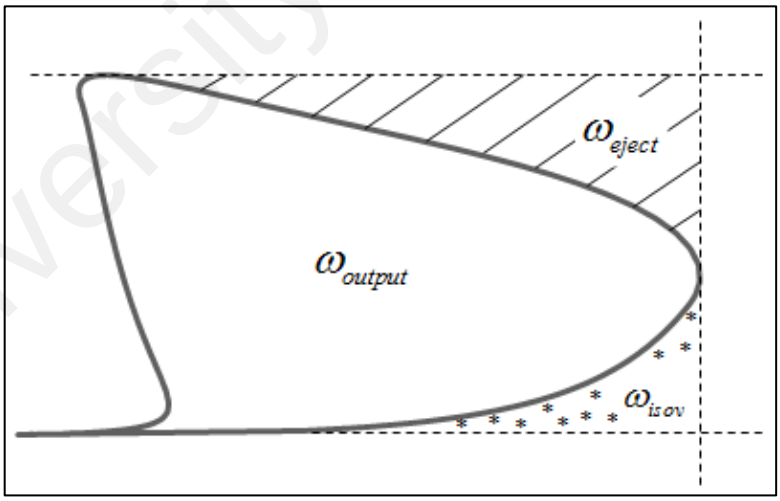

Figure 5.10: The areas of effective (ω_{output}), dissipated isovolumic (ω_{isov}) and dissipated ejection (ω_{eject}) work densities used for the calculation of work density dissipation (WDD) index of fibre stress-strain loop (FSSL), as in Equation 5.8.

Table 5.2: Optimisation errors (indicated by average wall distances between simulated and actual geometries) for the PR and NPR of each patient.

	End-diastole (mm)		End-systole (mm)	
	PR	**NPR**	**PR**	**NPR**
Patient 1	0.878	0.724	0.840	0.560
Patient 2	0.925	0.861	1.084	1.510
Patient 3	0.560	0.696	0.663	0.620

PR: perfused region; NPR: non-perfused region.

Table 5.3 shows the optimised parameter values for $C_{0(RZ)}$ (i.e. C_0 for the RZ), k_0, T_0 and $C_{0(IZ)}$ in each patient. With regards to the passive stiffness of RZ, patient 2 demonstrated the highest $C_{0(RZ)}$, followed by patients 3 and 1. On the contrary, the lowest intrinsic contractility (T_0) was shown in this patient, followed by patients 1 and 3. By comparing the ratio of T_0 to $C_{0(RZ)}$, patient 2 had the lowest $T_0/C_{0(RZ)}$ ratio among all patients, which implied that the LV of patient 2 was the least contractile. Overall, the IZ ($C_{0(IZ)}$) was much stiffer as compared to the RZ ($C_{0(RZ)}$) in all patients (i.e. 46 times greater for patient 2 to nearly 200 times greater for patient 1).

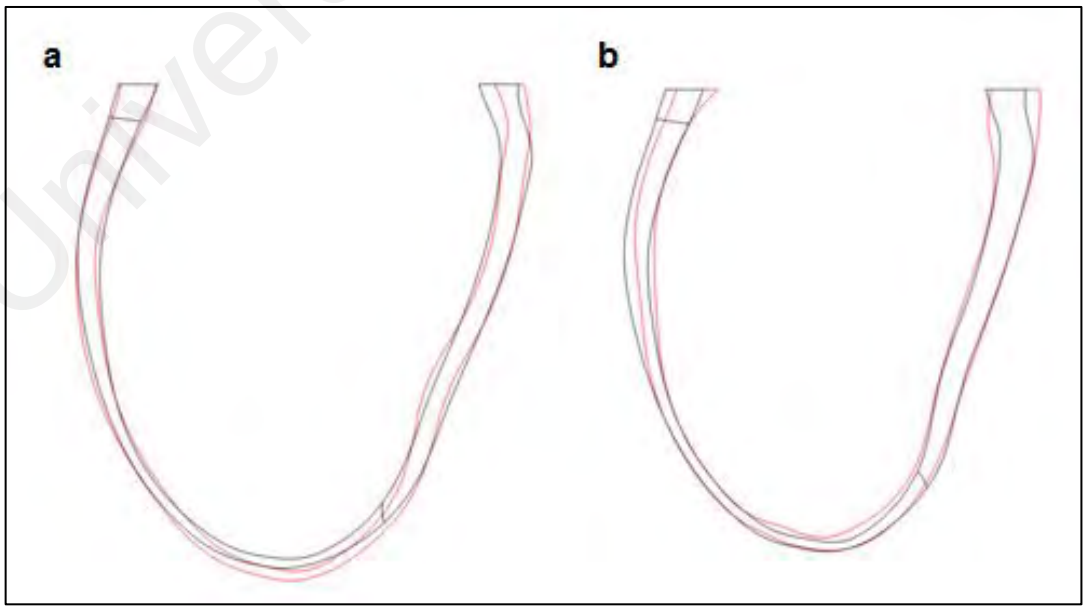

Figure 5.11: Comparison of simulated (black lines) and actual (red lines) geometries after (a) end-diastolic and (b) end-systolic optimisations.

Table 5.3: Estimated parameter values for each patient LV model.

	$C_{0(RZ)}$ (kPa)	k_0 (kN/m^3)	T_0 (Pa)	$C_{0(IZ)}$ (kPa)
Patient 1	1.18	2222.8	245.4	235.2
Patient 2	10.62	330.9	187.5	489.4
Patient 3	5.19	1207.4	717.9	435.0

$C_{0(RZ)}$: material overall stiffness of remote zone; k_0: spring constant applied on the LV basal surface; T_0: Active twitch stress of myocardium; $C_{0(IZ)}$: material overall stiffness of infarct zone.

5.4.2 Post-Infarct Changes in LV Global Function, Wall Thickness and Infarct Extension

Table 5.4 shows the estimates of global LV function (EDV, ESV, SV and EF) from the CMR analysis of each patient at 1st and 2nd scans. The LVs (EDV and ESV) of patients 1 and 3 diminished, whilst patient 2 LV enlarged. However, patients 2 and 3 demonstrated improvement in their global LV systolic function, as reflected by increments in both SV and EF, whilst patient 1 global LV systolic function deteriorated.

Table 5.4: Estimates of global LV function of each patient at 1st and 2nd scans.

	Patient 1		Patient 2		Patient 3	
	1st Scan	2nd Scan	1st Scan	2nd Scan	1st Scan	2nd Scan
EDV (ml)	106.9	76.4	140.1	154.4	173.5	162.0
ESV (ml)	41.1	34.8	74.9	79.1	121.5	90.8
SV (ml)	65.8	41.6	65.2	75.3	52.0	71.2
EF (%)	61.6	54.5	46.5	48.8	30.0	44.0

EDV: end-diastolic volume; ESV: end-systolic volume; SV: stroke volume; EF: ejection fraction.

Figures 5.12, 5.13 and 5.14 illustrate LV wall thickness of patients 1, 2 and 3 respectively at early diastole, during the first and second scans from three different views (nearly 120^{o} apart). During the second scan (i.e. 4 - 5 months after the first scan), an increase in wall thickness was observed throughout the LV in all patients, regardless of LV segments and infarct location.

In order to illustrate the changes in the extent of NPR, LV myocardial perfusion during the first and second scans for all patients is shown in Figure 5.15, with blue and red colours representing PR and NPR respectively. Comparing both scans, several NPRs at the epicardium had disappeared, particularly for patients 1 and 2. This was most likely due to the presence of infarct-related myocardial oedema during the acute phase, which eventually disappeared during the second scan. As the epicardial area was prone to infarct overestimation, and infarct extension mostly initiates from the endocardium, the subendocardium (i.e. the layer located at a distance of 10% wall thickness from the endocardium) was used in all subsequent analyses pertaining to infarct extension.

Figures 5.16a - 5.18a demonstrate the extension of the NPRs at the subendocardium of patients 1, 2 and 3 respectively, from the three different views. The cyan-coloured regions indicate the PRs, whilst the yellow-coloured regions indicate the NPRs, in the first scan. In order to illustrate the changes in the extent of the NPRs during the second scan, black-coloured lines are used to indicate the new borders between the PRs and the NPRs during the second scan (i.e. 4 - 5 months after the first scan). Several points were randomly selected at the RZ-BZ border of simulated LV model of each patient for further analysis. In addition, a control point was also selected in each patient at a location far away from the IZ.

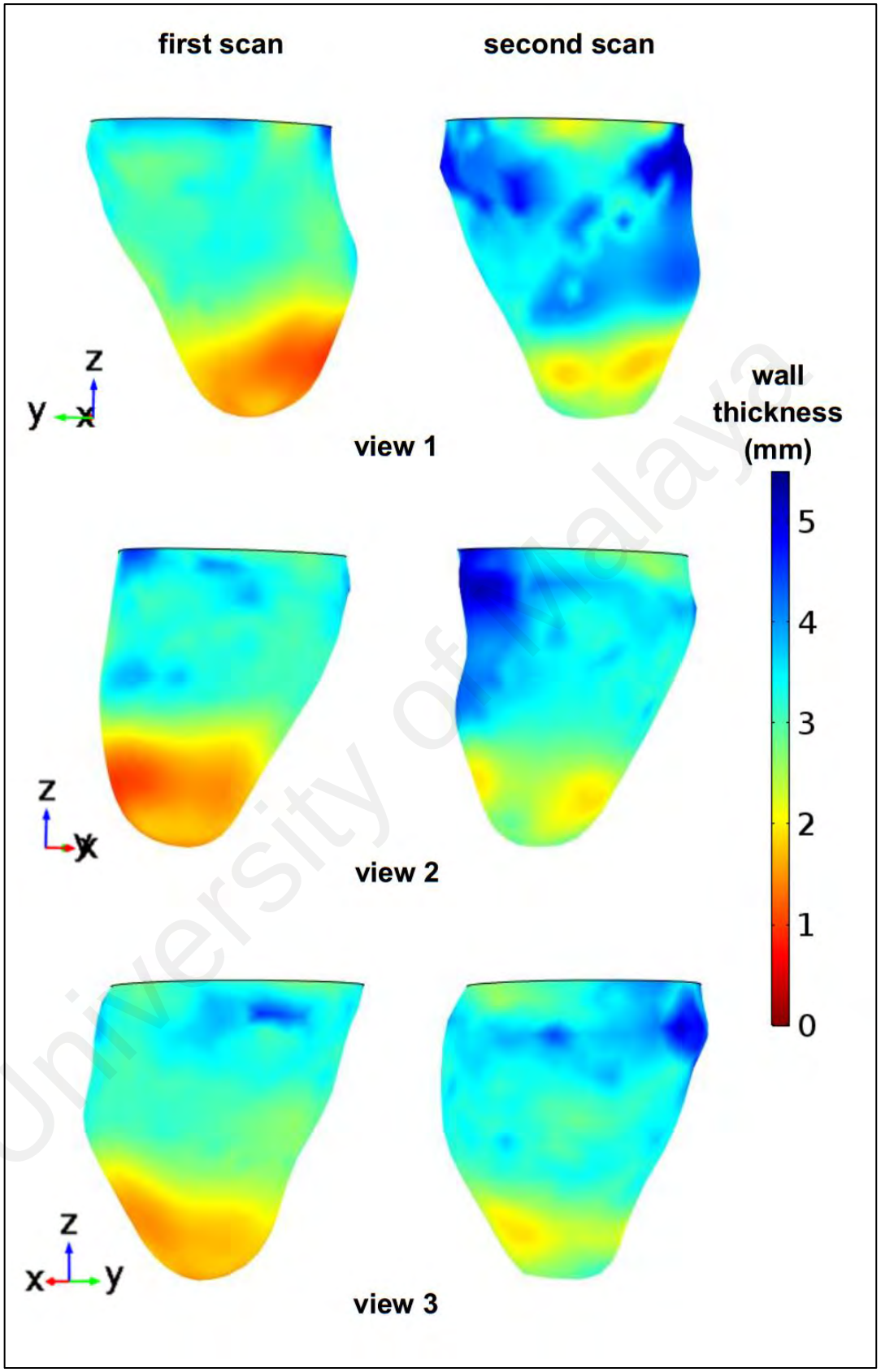

Figure 5.12: LV wall thickness of patient 1 during the first and second scans from 3 different views (nearly 120^{o} apart) at early diastole.

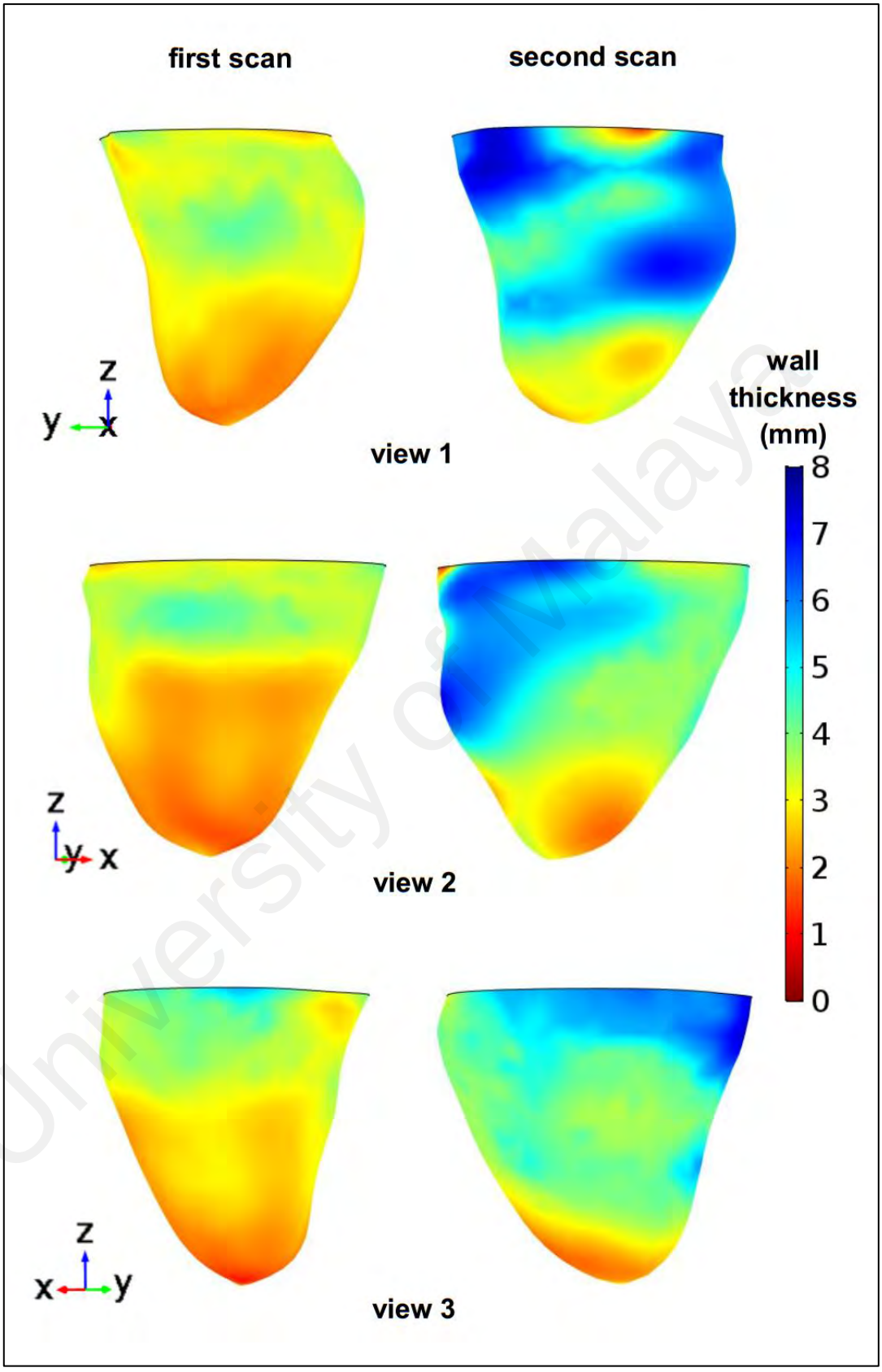

Figure 5.13: LV wall thickness of patient 2 during the first and second scans from 3 different views (nearly 120^{o} apart) at early diastole.

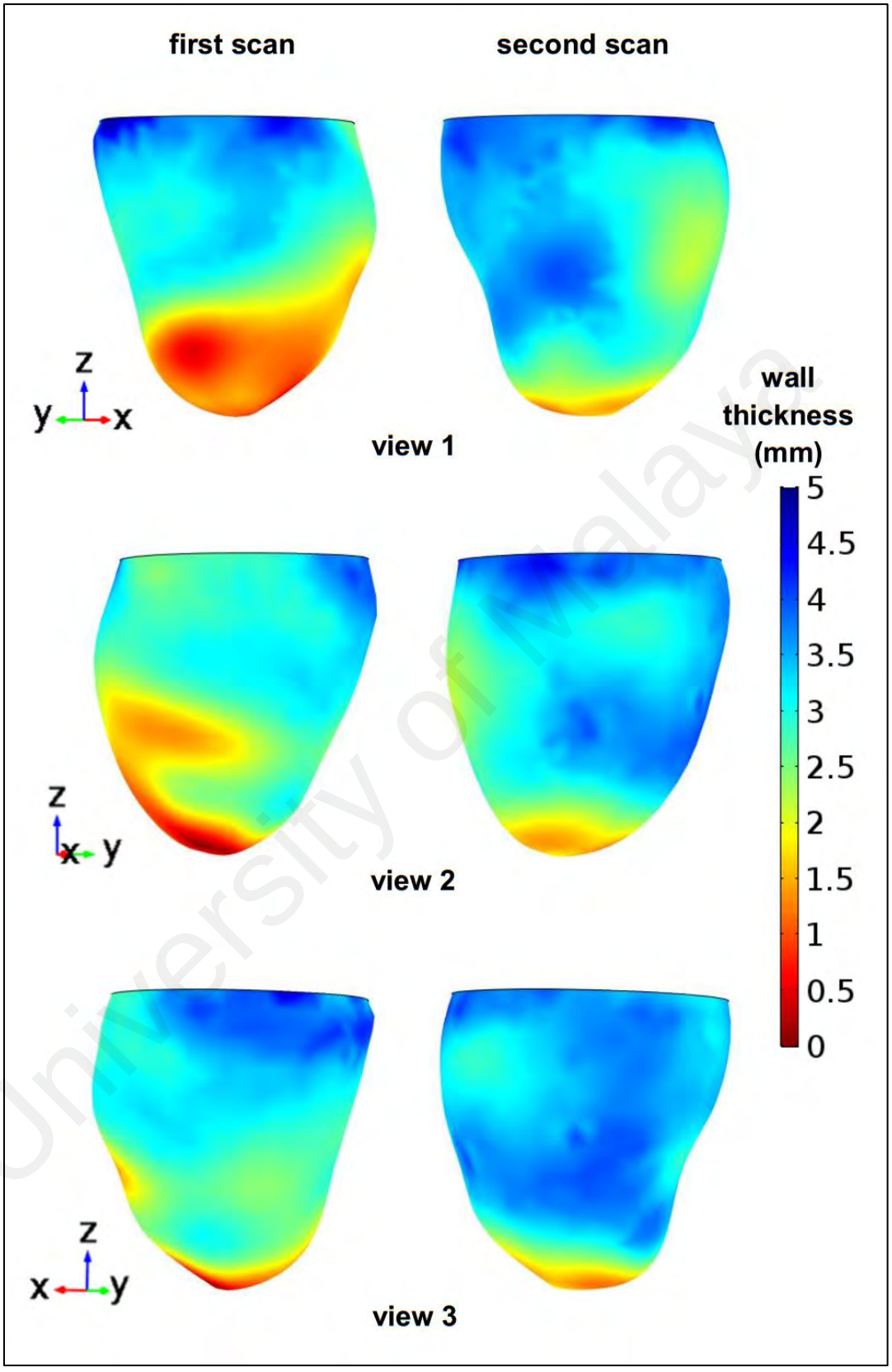

Figure 5.14: LV wall thickness of patient 3 during the first and second scans from 3 different views (nearly 120^{o} apart) at early diastole.

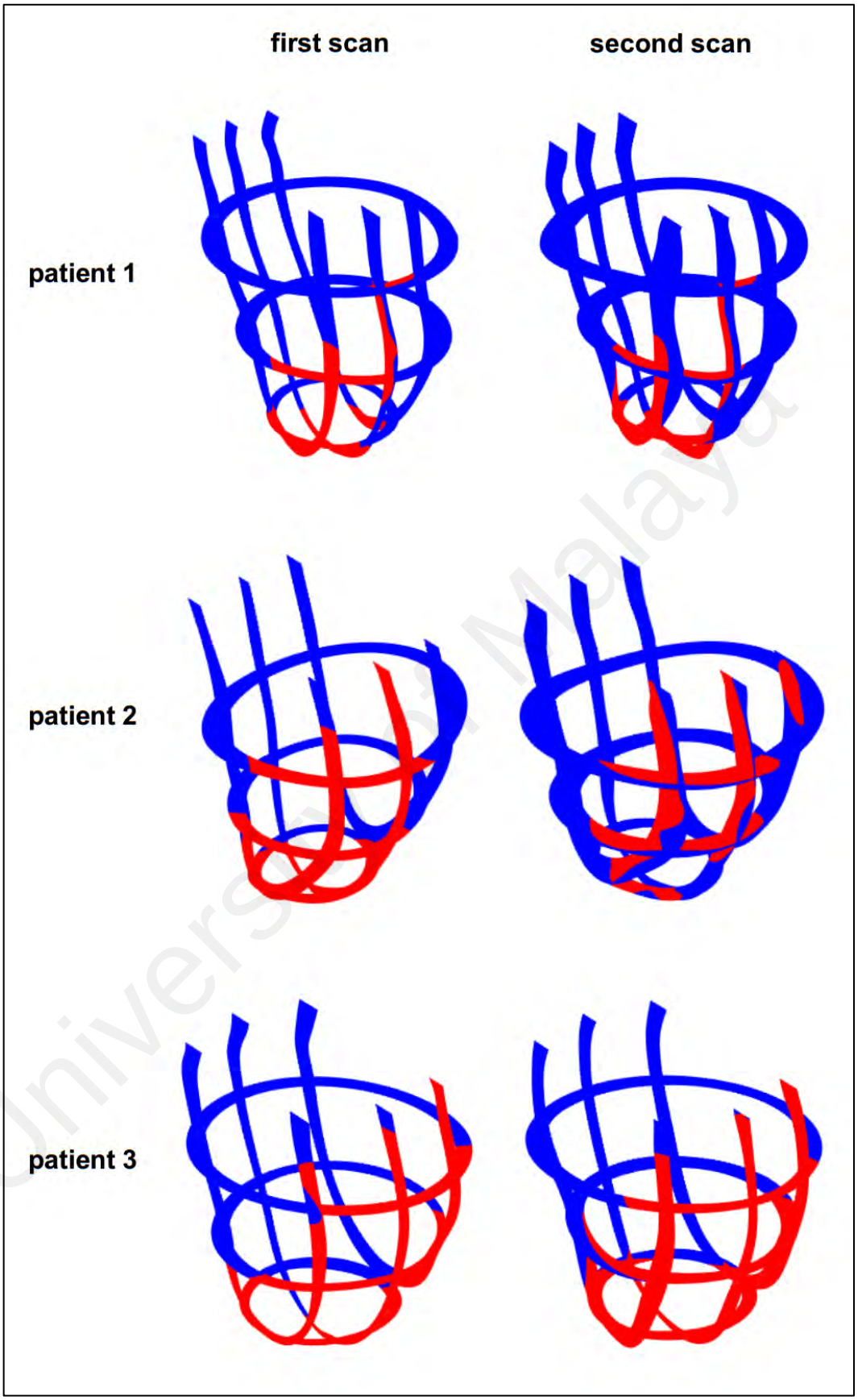

Figure 5.15: LV myocardial perfusion during the first and second scans for all 3 patients, with blue and red colours indicating perfused (PR) and non-perfused (NPR) regions respectively.

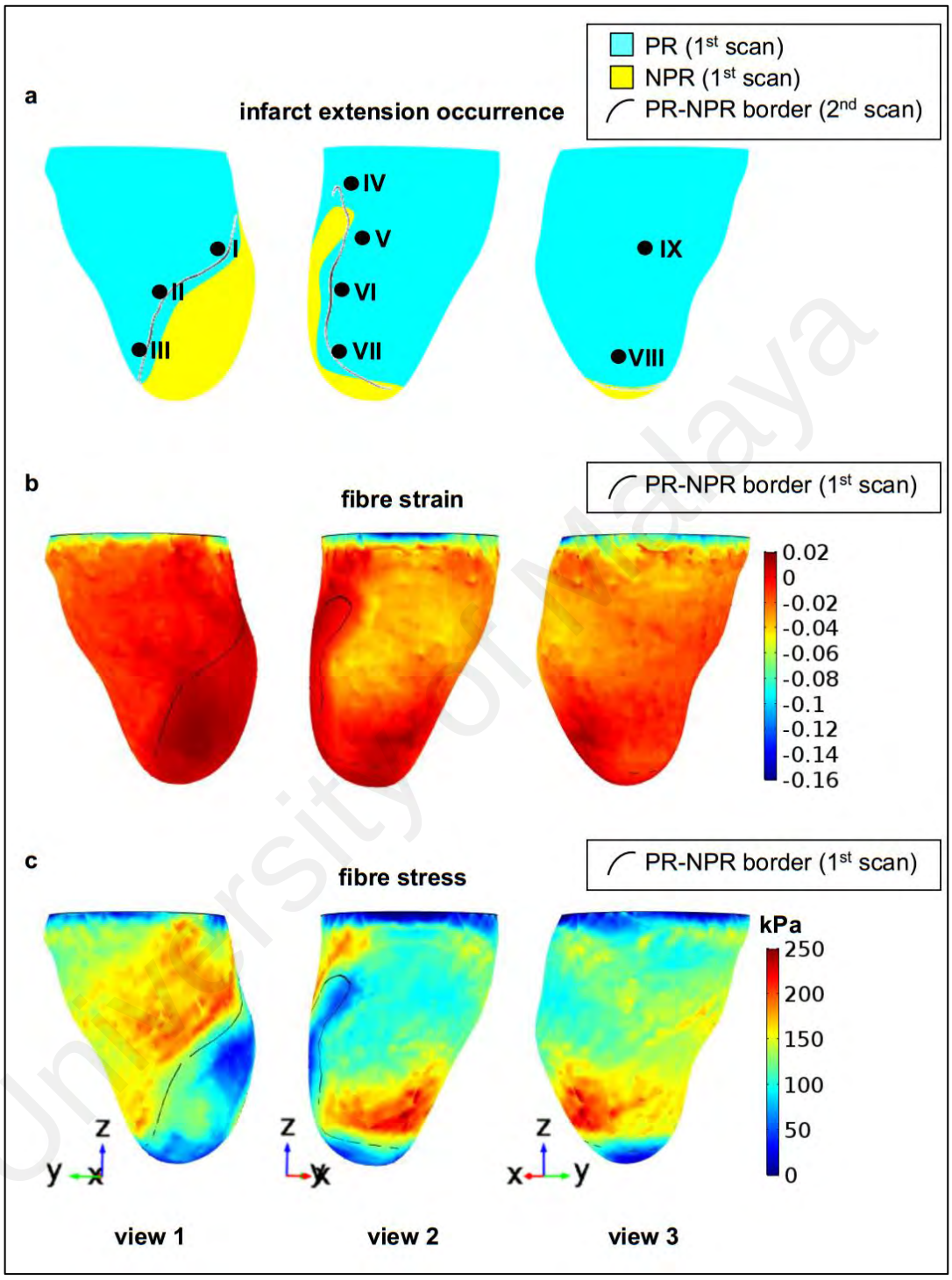

Figure 5.16: (a) Extension of NPR at the subendocardium of patient 1 for both scans. The points denoted with Roman numerals were points used to generate FSSLs shown in Figure 5.19. End-systolic (b) fibre strain and (c) fibre stress distributions at the subendocardium of patient 1 LV model.

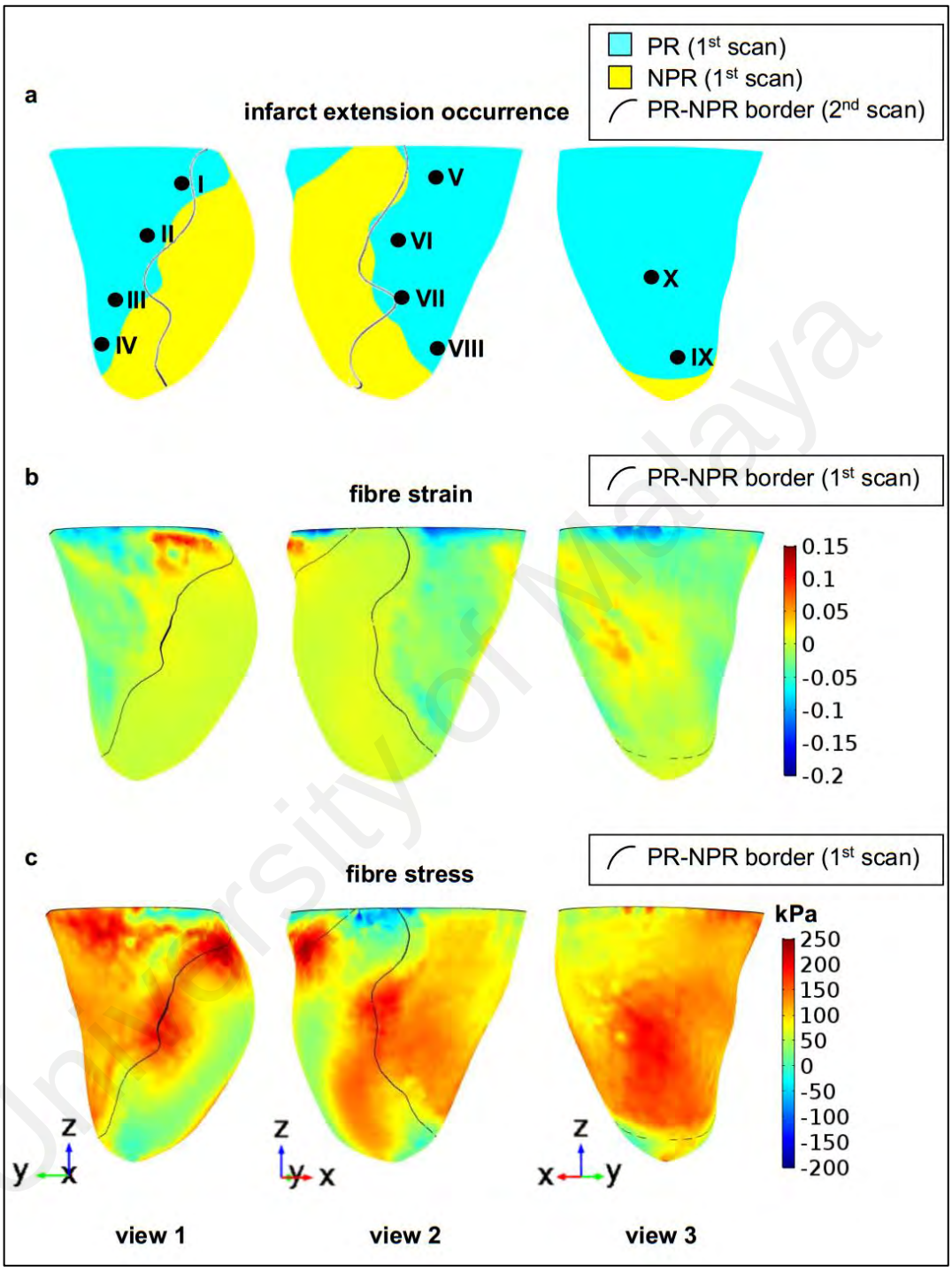

Figure 5.17: (a) Extension of NPR at the subendocardium of patient 2 for both scans. The points denoted with Roman numerals were points used to generate FSSLs shown in Figure 5.20. End-systolic (b) fibre strain and (c) fibre stress distributions at the subendocardium of patient 2 LV model.

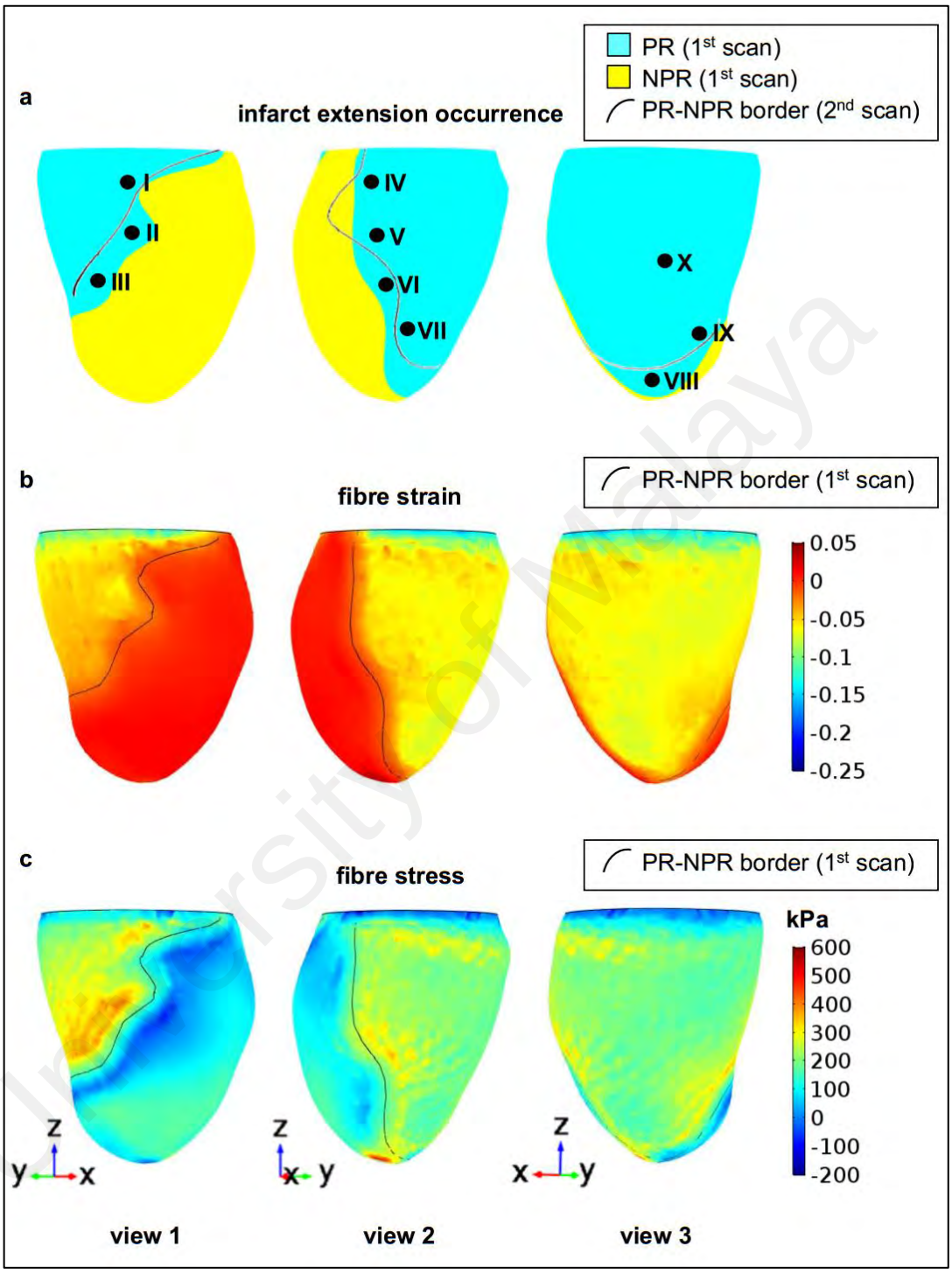

Figure 5.18: (a) Extension of NPR at the subendocardium of patient 3 for both scans. The points denoted with Roman numerals were points used to generate FSSLs shown in Figure 5.21. End-systolic (b) fibre strain and (c) fibre stress distributions at the subendocardium of patient 3 LV model.

For patient 1 (Figure 5.16a), infarct extension was observed at all regions surrounding the NPR (PR-NPR border next to points I - VII, the PR-NPR borders of all patient LV models will be directly referred to the points after this), except for the apex (VIII) and remote (IX) regions. For patient 2 (Figure 5.17a), infarct extension occurred from the base to the lower part of the mid ventricle (points I - III and V - VII). No infarct extension was seen at the apical (IV and VIII), apex (IX) and remote (X) regions. On the other hand, infarct extension was witnessed in almost all regions (points I - IX) surrounding the NPR for patient 3 (Figure 5.18a), except for the remote (X) region.

5.4.3 Correlation between Infarct Extension and Fibre Strain/Stress Distribution

Figures 5.16b and 5.16c illustrate the end-systolic fibre strain and fibre stress distributions on the LV subendocardium in patient 1 respectively, with black lines denoting the border between the PR and NPR during the first scan. It can be observed that although the apex (VIII) region experienced the highest fibre strain and fibre stress, no infarct extension had occurred. Meanwhile, as compared to the other regions surrounding the NPR (points I - VII), which experienced infarct extension, exhibited relatively lower fibre strain and fibre stress. With regards to patient 2 (Figure 5.17), the fibre strain distribution was rather homogeneous throughout the LV, with only points I and X experiencing moderately high fibre strain. While point X had comparatively higher fibre strain, it did not experience infarct extension; unlike points II, III and V - VII, which had infarct extension at relatively low fibre strain level. On the other hand, the fibre stress distribution was not homogeneous, with the greatest fibre stress found around point I, and relatively high fibre stress observed around points II, III, VI, VII, IX and X. Although points IX and X had higher fibre stress as compared to point V, which underwent infarct extension, no infarct extension occurred at these locations. In terms of patient 3 (Figure 5.18), although fibre strain was higher in the NPR as compared to the

PR, its distribution was rather homogeneous. Moderately high fibre stress was observed at certain regions surrounding the NPR. Despite the absence of abnormally high fibre strain or fibre stress in patient 3, almost all regions surrounding the NPR experienced infarct extension.

5.4.4 Correlation between Infarct Extension and Fibre Stress-Strain Loop/Work Density Dissipation

In order to visualise the myocardial mechanics surrounding the NPR throughout the entire LV cycle, the FSSLs were generated at points denoted in Figures 5.16a - 5.18a for all three patients, as shown in Figures 5.19 - 5.21. For patient 1 (Figure 5.19), the FSSLs of points I – III and V - VII appeared to be less rectangular than that of points IV, VIII and IX. Meanwhile, the FSSLs of points I, II, III and V of patient 2 (Figure 5.20) were observed to significantly deviate from the standard rectangular shape. For patient 3 (Figure 5.21), only point X demonstrated a relatively rectangular FSSL.

For better elucidation of the myocardial mechanics impairment, a work density dissipation (WDD) index was calculated for each of the FSSLs generated in Figures 5.19 - 5.21. Figure 5.22 illustrates the WDD index results for all points, with different markers used to distinguish those underwent infarct extension (cross '×') from those did not (diamond '♦'). As shown in the figure, points that experienced infarct extension demonstrated significantly higher (P = .009) WDD values (median = 0.39, Q1-Q3 = 0.30-0.72) compared to those that did not (excluding remote points, median = 0.18, Q1-Q3 = 0.10-0.23). The lowest WDD value was recorded at point VIII of patient 1 (without infarct extension), whilst the highest value was recorded at point III of patient 2 (with infarct extension). Except for a few points (i.e. point IV of patient 1, and points VI and VII of patient 2), all points with infarct extension had WDD indices above 0.239 (i.e. the highest WDD value among all points without infarct extension).

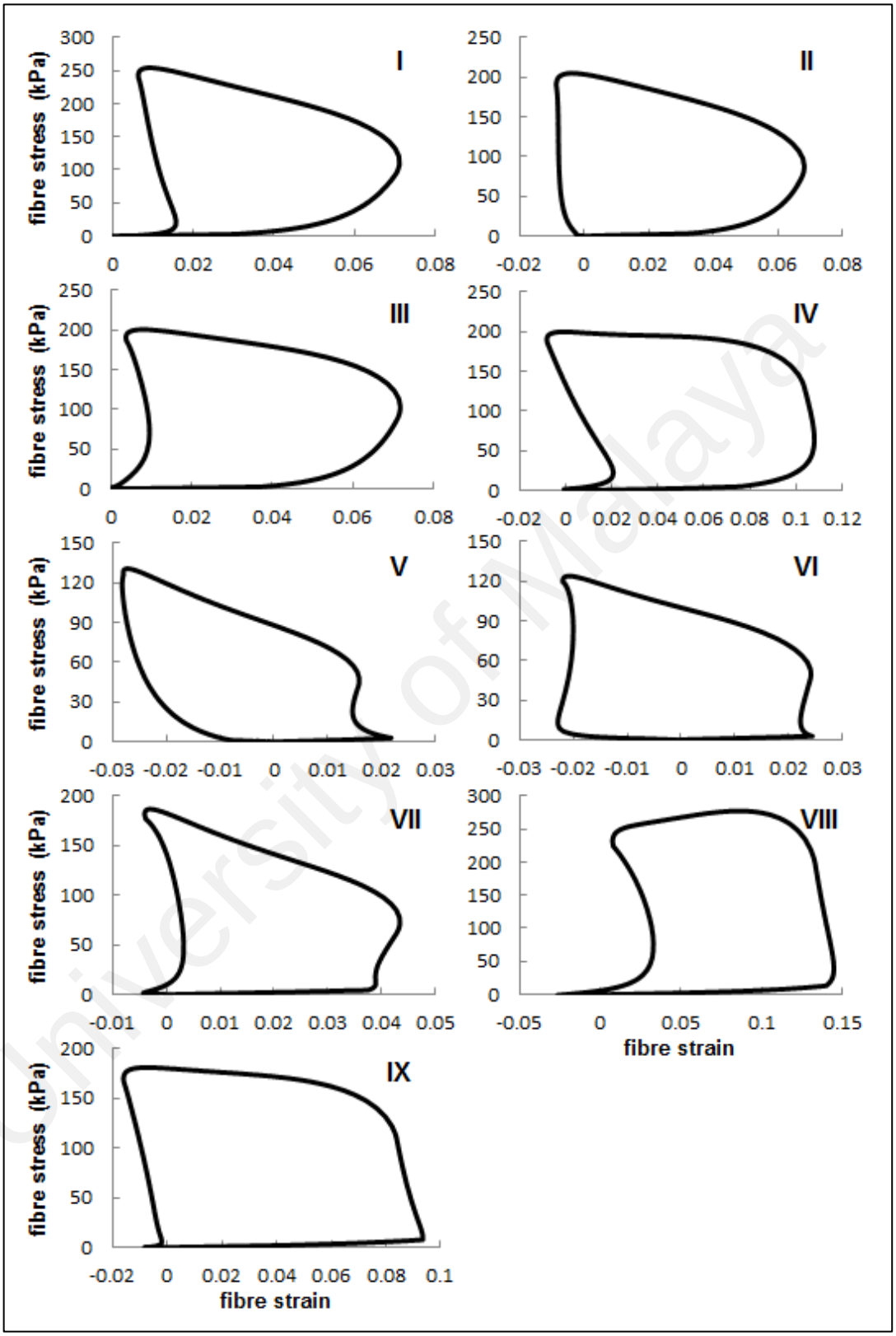

Figure 5.19: FSSLs generated at points denoted in Figure 5.16a (patient 1).

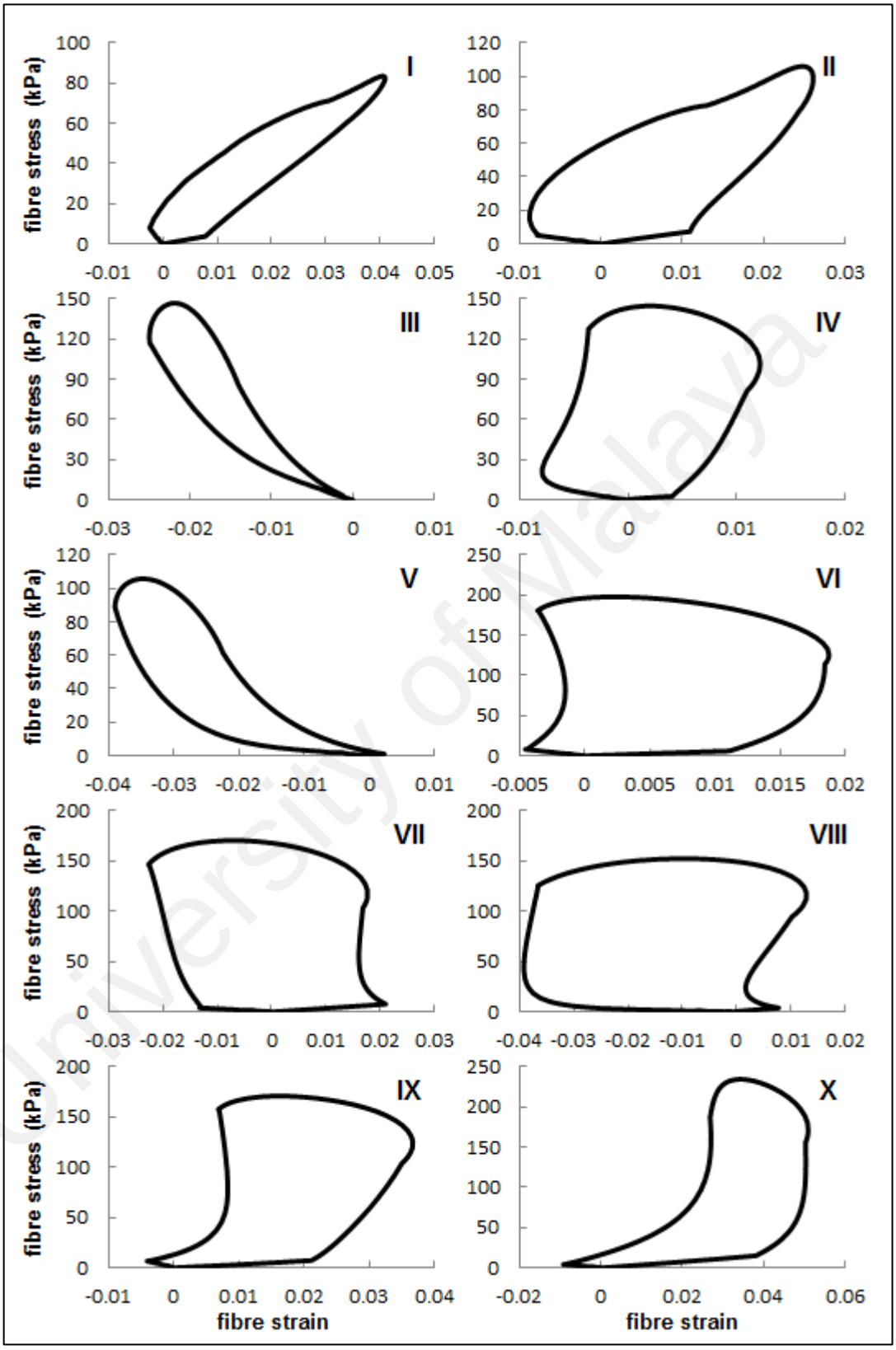

Figure 5.20: FSSLs generated at points denoted in Figure 5.17a (patient 2).

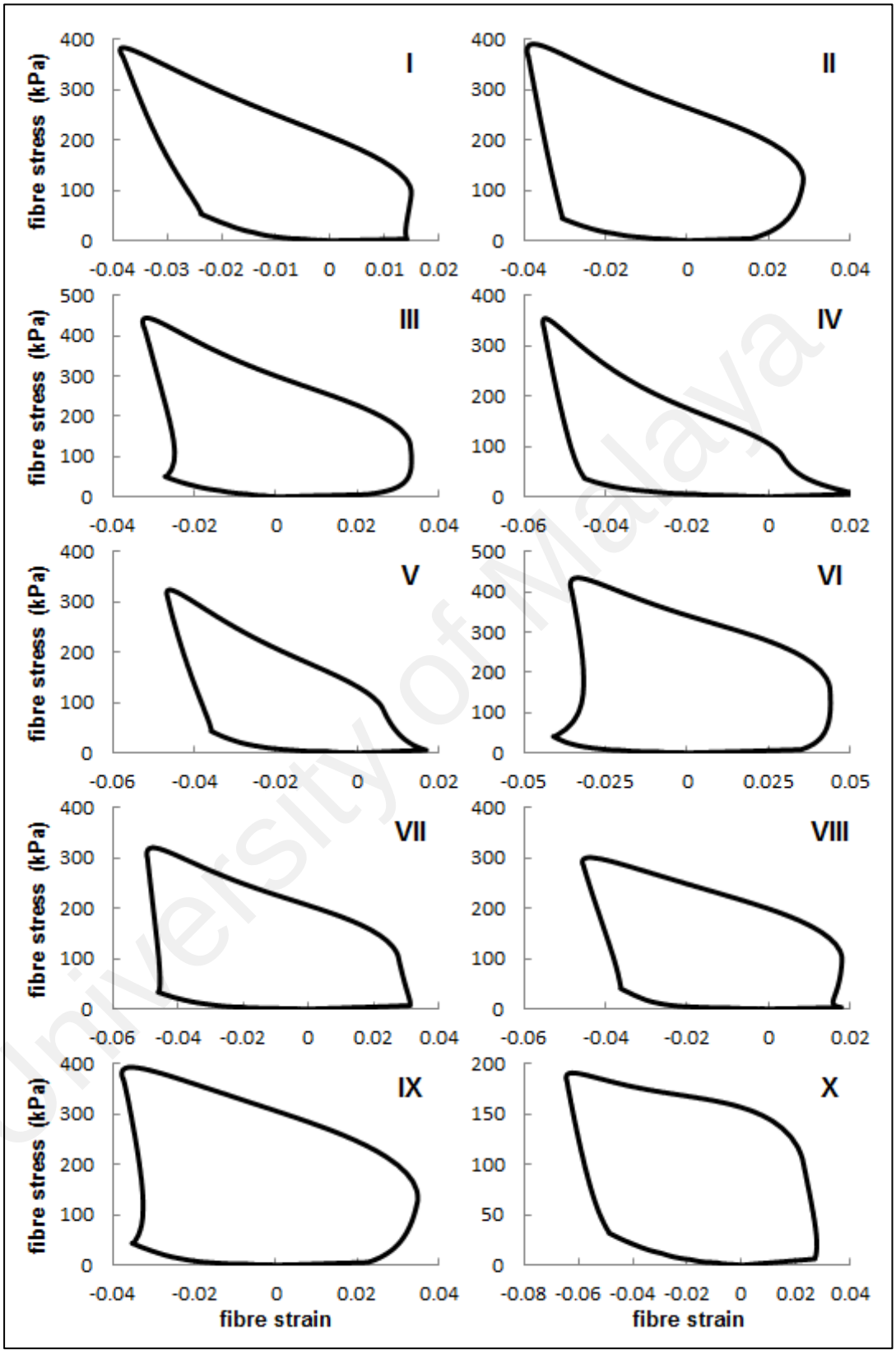

Figure 5.21: FSSLs generated at points denoted in Figure 5.18a (patient 3).

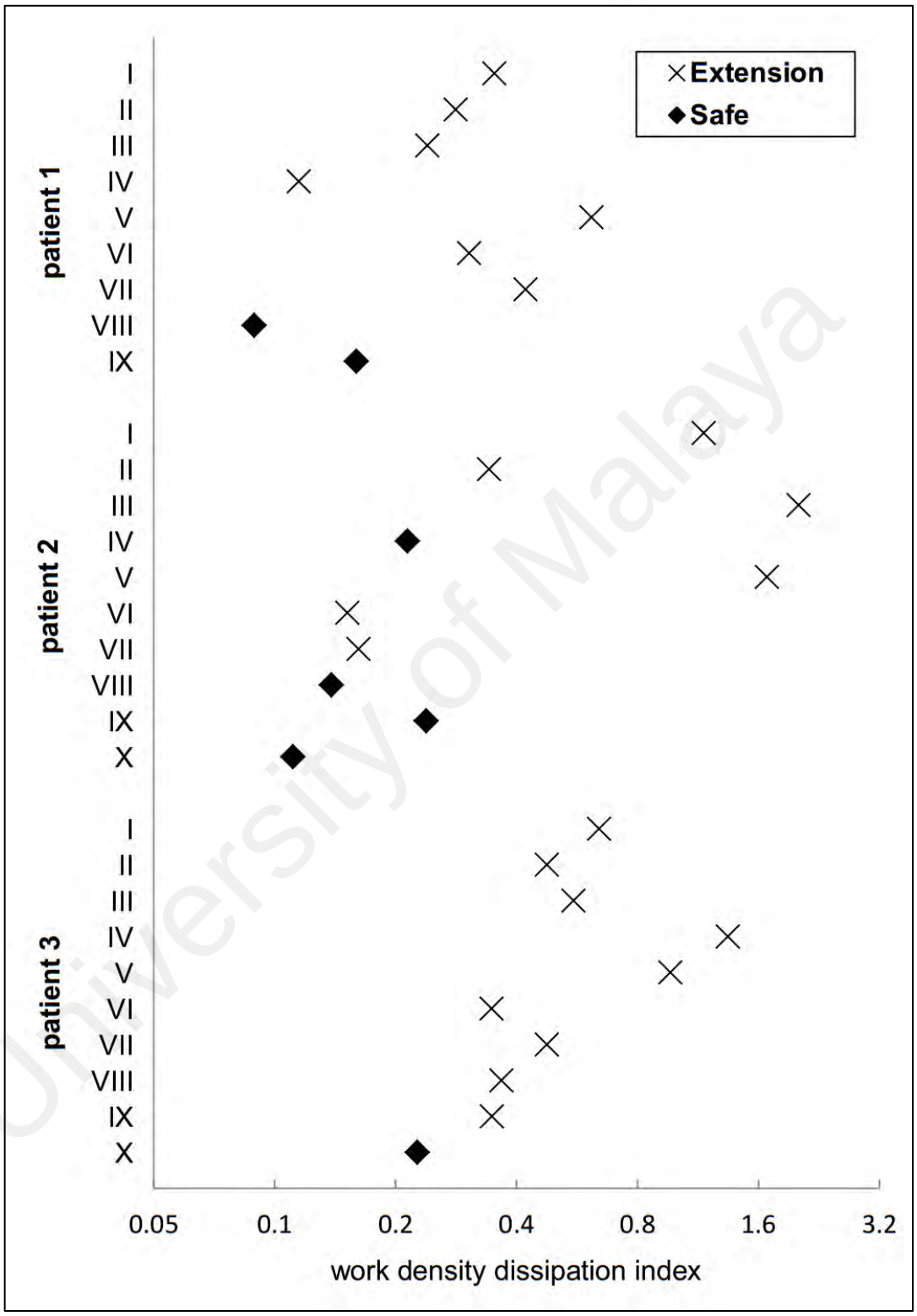

Figure 5.22: WDD index values of all the FSSLs presented in Figures 5.19, 5.20 and 5.21.

5.4.5 Sensitivity Analysis on the Impact of Infarct Stiffness and Sarcomere Length Profile

Figures 5.23 - 5.25 show the effect of varying infarct stiffness ($10\times C_{0(IZ)}$ and $0.1\times C_{0(IZ)}$) and local sarcomere length profile (SL_{RZ}) on the FSSLs at several selected points in each patient, with their WDD indices written in the brackets next to the figure legends. Compared with the control models, a reduction in the infarct stiffness ($0.1\times C_{0(IZ)}$) led to a more rectangular FSSL shape in most locations (except for point IV of patient 1), as reflected by their lower WDD index values. An increase in the infarct stiffness ($10\times C_{0(IZ)}$), on the other hand, caused an opposite phenomenon, with most locations demonstrating an increase in the WDD index values (except for points I and III of patient 2 and point V of patient 3) and less rectangular FSSL shape. With regards to the $SL_{(RZ)}$ models, more rectangular FSSLs and lower WDD index values were observed in most locations as compared to the control models, except for point VI of patient 2 and point VIII of patient 3.

Figures 5.26 and 5.27 illustrate the changes in the WDD index values and end-diastolic fibre strain respectively, of all the 29 selected points (denoted with Roman numerals in Figures 5.16a - 5.18a) for different model settings. Overall, in comparison with the control models, an increase in infarct stiffness elevated the WDD index values despite having a lower maximum WDD index value. On the other hand, a lower infarct stiffness and $SL_{(RZ)}$ had lower WDD index values, relative to the control models. In regards to the end-diastolic fibre strain, an increase in infarct stiffness reduced the end-diastolic fibre strain, whilst a decrease in infarct stiffness elevated the end-diastolic fibre strain.

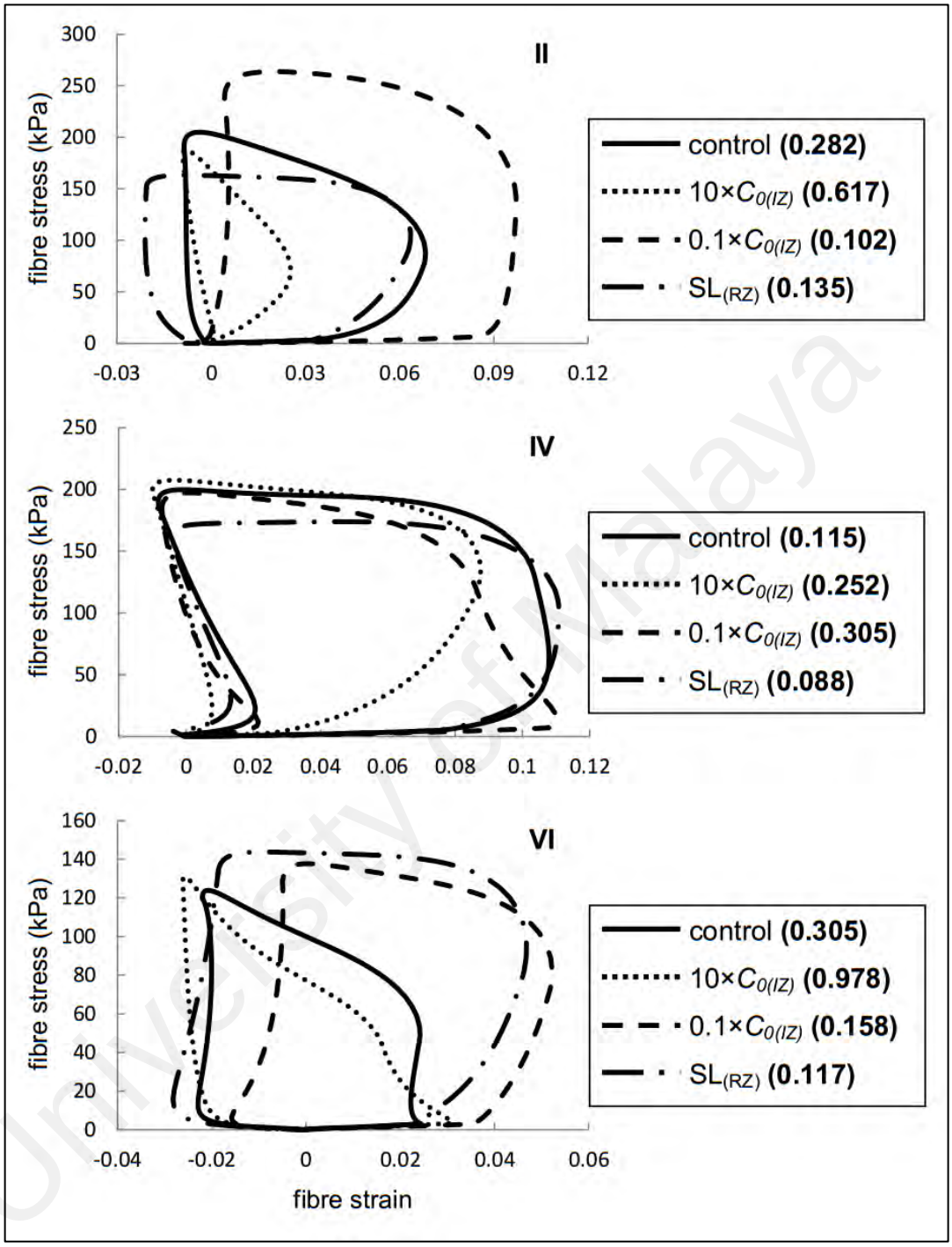

Figure 5.23: Generated FSSLs at the selected points (as denoted by the Roman numerals) of the patient 1 LV model with different settings: control, 10 times the $C_{0(IZ)}$ ($10\times C_{0(IZ)}$), 0.1 times the $C_{0(IZ)}$ ($0.1\times C_{0(IZ)}$) and replacing local sarcomere length profile, λ, with the one obtained at point IX of patient 1 control model (SL_{RZ}). The WDD index of each FSSL is written in parenthesis next to the figure legend.

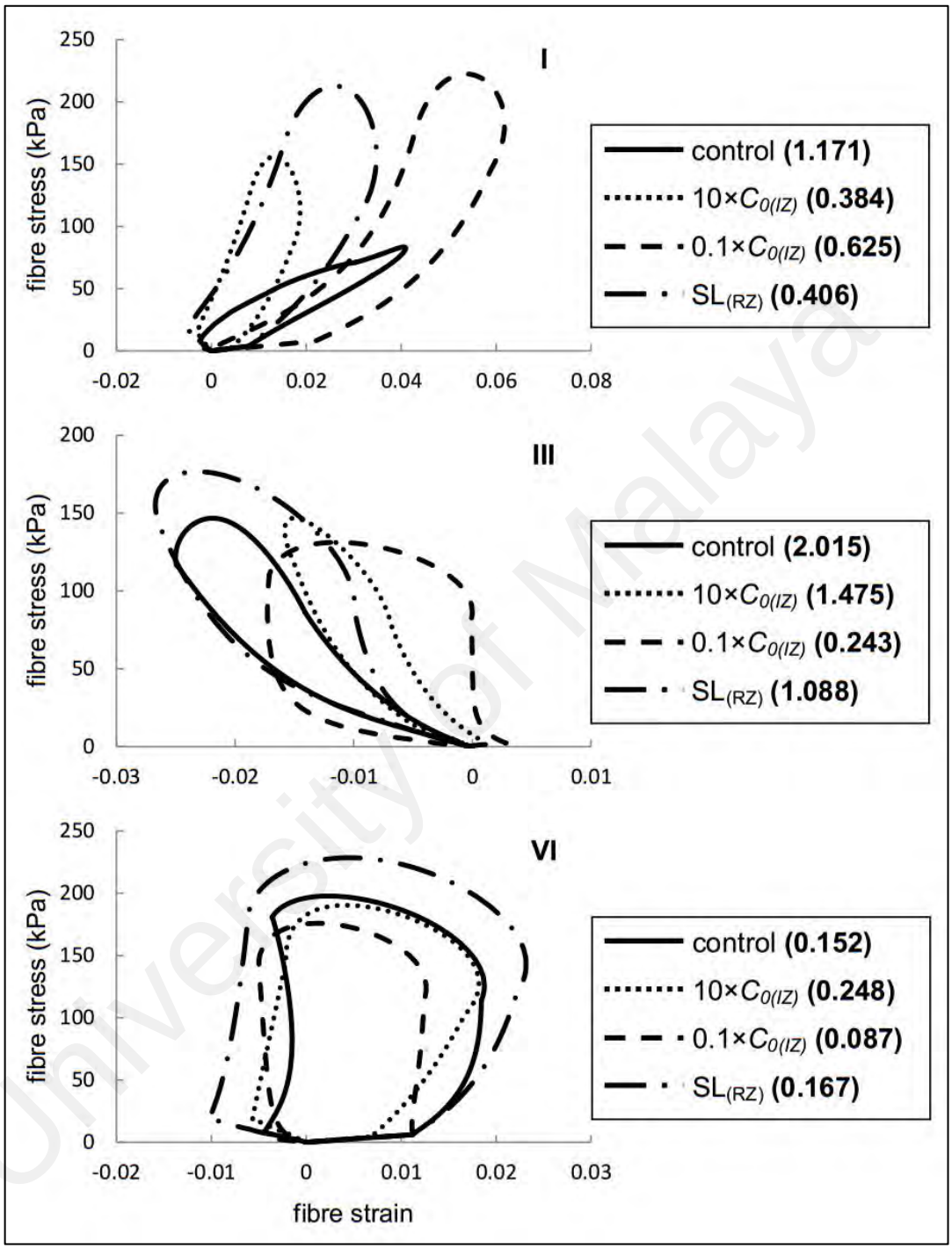

Figure 5.24: Generated FSSLs at the selected points (as denoted by the Roman numerals) of the patient 2 LV model with different settings: control, 10×$C_{0(IZ)}$, 0.1×$C_{0(IZ)}$ and replacing local sarcomere length variable, λ, with the one obtained at point X of patient 2 control model (SL_{RZ}). The WDD index of each FSSL is written in parenthesis next to the figure legend.

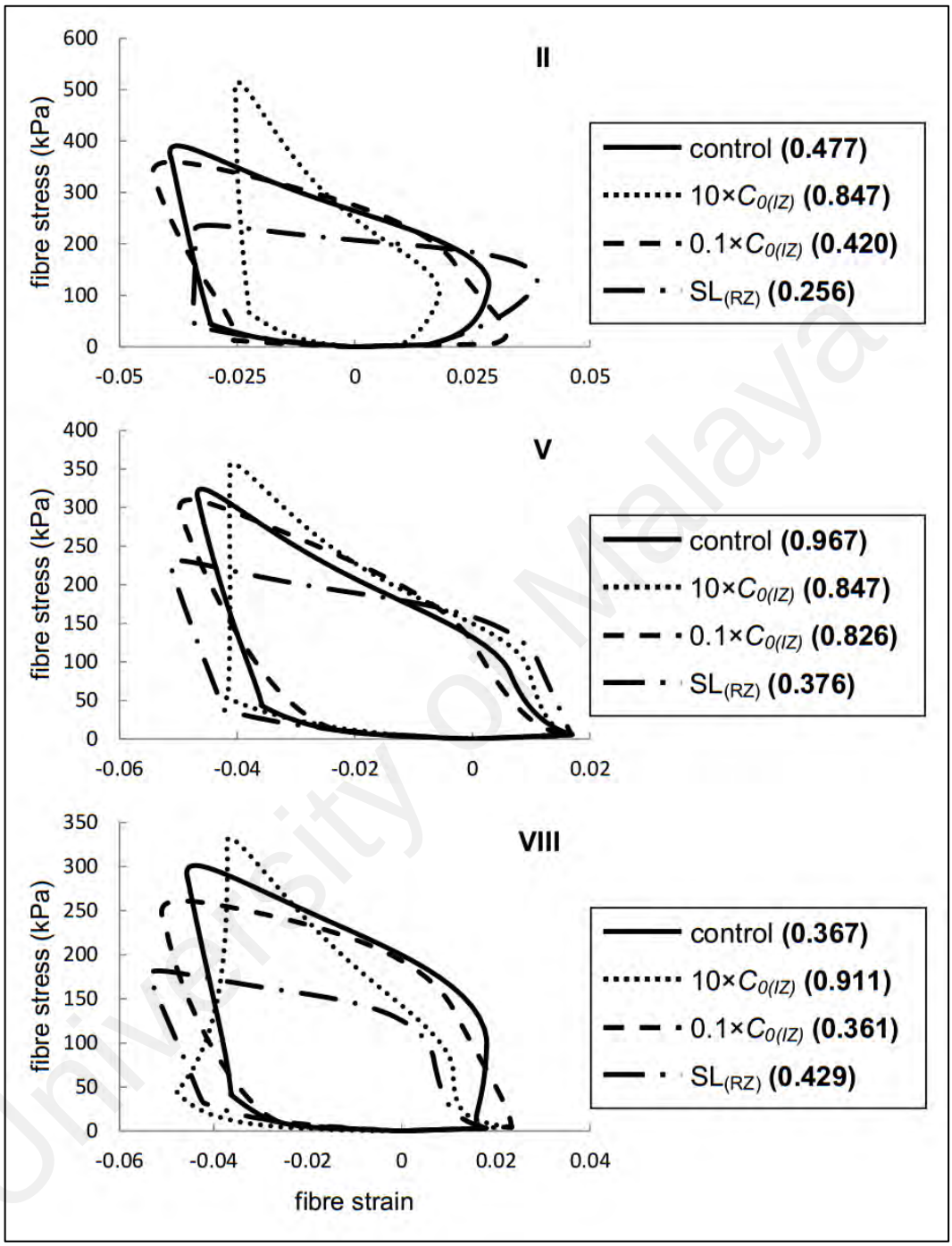

Figure 5.25: Generated FSSLs at the selected points (as denoted by the Roman numerals) of the patient 3 LV model with different settings: control, $10\times C_{0(IZ)}$, $0.1\times C_{0(IZ)}$ and replacing local sarcomere length variable, λ, with the one obtained at point X of patient 3 control model (SL_{RZ}). The WDD index of each FSSL is written in parenthesis next to the figure legend.

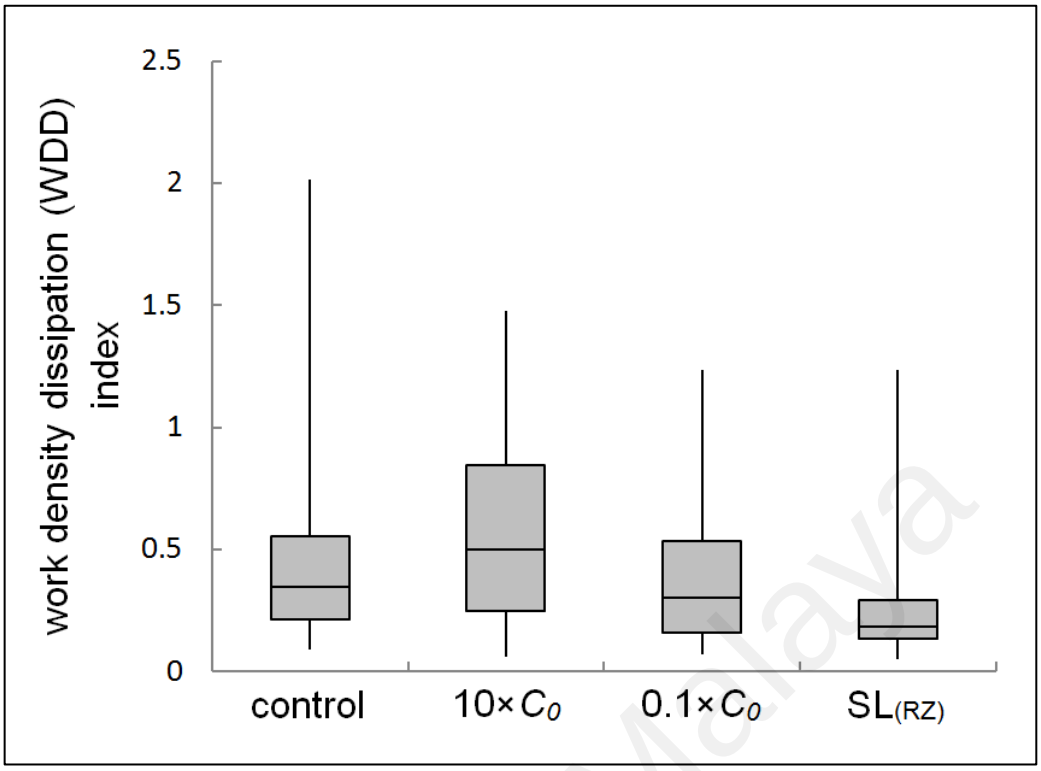

Figure 5.26: Box plot of WDD indices obtained from patient models with different settings.

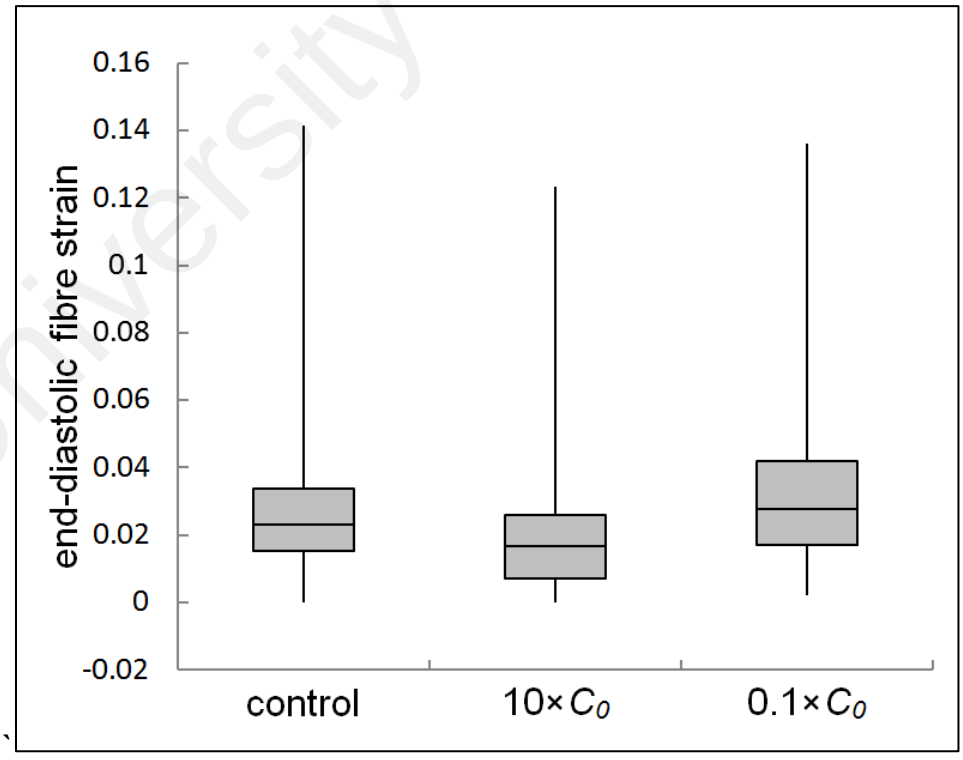

Figure 5.27: Box plot of end-diastolic fibre strain obtained from patient models with different settings.

5.5 Discussion

This study found that WDD, a measure of impaired regional mechanical function based on the FSSL, was correlated with infarct extension, whilst fibre strain and stress distributions were not. The FSSL impairment was reflected in its shape, which deviated from the standard rectangular shape, and its higher WDD index value. Such impairment was, at least in part, caused by inadequate strain during the diastolic phase, which subsequently affected the contractile ability of the myocardium during the IVC and ejection phases.

5.5.1 Optimisation Accuracy

Optimisation of myocardial parameter values was performed using the concept of matching simulated geometry to actual geometry, instead of the conventional displacement data obtained from tagged images. While the extraction of displacement data covering the entire LV cycle from tagged images is challenging due to the tag fading problem, the optimisation method utilised here requires only cine images, thus allowing the optimisation of both diastolic and systolic parameters with ease. Furthermore, 3D displacement data is difficult to extract from conventional 2D tagged images. Geometry matching based on cine images, on the other hand, gives 3D information, which allows the optimisation of myocardial parameters to be more accurate. However, the current approach based on geometry matching does not provide mid-wall information as tagged images do. Nonetheless, mid-wall information does not offer significant advantage in material optimisation involving global parameters (instead of local), as in the present and many past studies (V. Y. Wang et al., 2009; Wenk et al., 2012).

Based on the optimisation results, which yielded errors of only 1.510 mm and 1.084 mm for NPR and PR respectively during the end-systolic optimisation of patient 2, and

errors of less than 1 mm for other optimisations (Table 5.2 and Figure 5.11), it can be concluded that the simulated geometries resembled the actual geometries reasonably well.

5.5.2 Prevention of Infarct Expansion by Infarct Zone Stiffening and Overall Wall Thickening

The parameter optimisation results (Table 5.3) revealed substantially higher passive stiffness for the IZ as compared to the RZ in all patients (46 - 199 times), which was in agreement with previously published studies (Hiesinger et al., 2012; Wenk et al., 2011). Instead of infarct thinning, thickening was observed at the IZ for all the three patients (Figures 5.12 – 5.14), which may be explained by the deposition of extracellular matrix (ECM) in this regions (Cleutjens & Creemers, 2002). The ECM held the IZ myocytes in place, providing adequate stiffness for the IZ to withstand high systolic pressure, preventing the IZ from overdistension, systolic bulging and infarct expansion (French & Kramer, 2007). In addition, RZ thickening was also observed for all the three patients. In order to compensate for the diminished LV function caused by the presence of non-contractile IZ following MI, the viable RZ worked harder to increase its workload, thus giving rise to concentric hypertrophy (Lee et al., 2013).

5.5.3 Correlation between Infarct Extension and Left Ventricular Regional Mechanics

Although several studies have suggested excessive myocardial strain (Pimentel et al., 2001; Tyagi et al., 1998) and stress (Ratcliffe, 2002; Walker et al., 2005) as potential contributors to apoptosis and infarct extension, no evidence has so far been recorded in MI patients. In the present study (Figures 5.16 - 5.18), the observed mismatch between regions with infarct extension and those with high end-systolic fibre strain or fibre stress

suggested that excessive strain or stress is unlikely to be the culprit behind infarct extension.

One of the most notable findings in this study was the significant correlation between the FSSL or WDD index and infarct extension. While the pressure-volume (PV) loop area has been widely used to represent work done by the LV in a cardiac cycle, the FSSL area has been used to indicate stroke work density of myocardium (Watanabe et al., 2004). Figure 5.28a shows an ideal FSSL. During IVC, the active myocardium rapidly generates contraction force against the enclosed ventricular chamber, leading to an increase in the fibre stress and LV pressure while maintaining its fibre strain, as reflected by the vertically rising dashed line in the figure. During the ejection phase, the force generated by the myocardium decreases due to rapid shortening of the cardiac muscle fibre, as described by the force-velocity relations of myocardium (Rice et al., 2008). Consequently, the fibre strain is reduced greatly at a relatively constant fibre stress, as reflected by the horizontal dotted line in the figure.

An impaired FSSL, on the contrary, appears to be less rectangular in shape, as shown in Figure 5.28b. During IVC, the contraction force generated by the regional myocardium is inadequate to maintain its fibre strain against the rapidly rising LV pressure in the enclosed ventricular chamber caused by other actively contracting myocardial tissues. Consequently, these regional muscle tissues are stretched with an increase in fibre strain, thus leading to work dissipation during IVC (defined as ω_{isov}). Depressed shortening and isovolumic stretching of BZ have also been demonstrated in two separate experimental studies (Kramer et al., 1993; Moulton et al., 1995), and these phenomena have been suggested to cause ventricular remodelling. During the ejection phase, the rate of myocardial fibre shortening is impaired, thus leading to a slower rate of reduction in the contraction force (myocardial force-velocity relations), and giving

rise to work dissipation (defined as ω_{eject}), as indicated by a continuous increase in the fibre stress (dotted line in the figure).

In order to examine the correlation between impaired FSSL and infarct extension, FSSLs were generated for points located at the RZ-BZ border, instead of those at the PR-NPR border. This is to ensure that points selected for generating FSSLs have no impairment in the intrinsic contractility (T_0). As such, FSSLs generated from points located at the RZ-BZ border were utilised to correlate with the occurrence of infarct

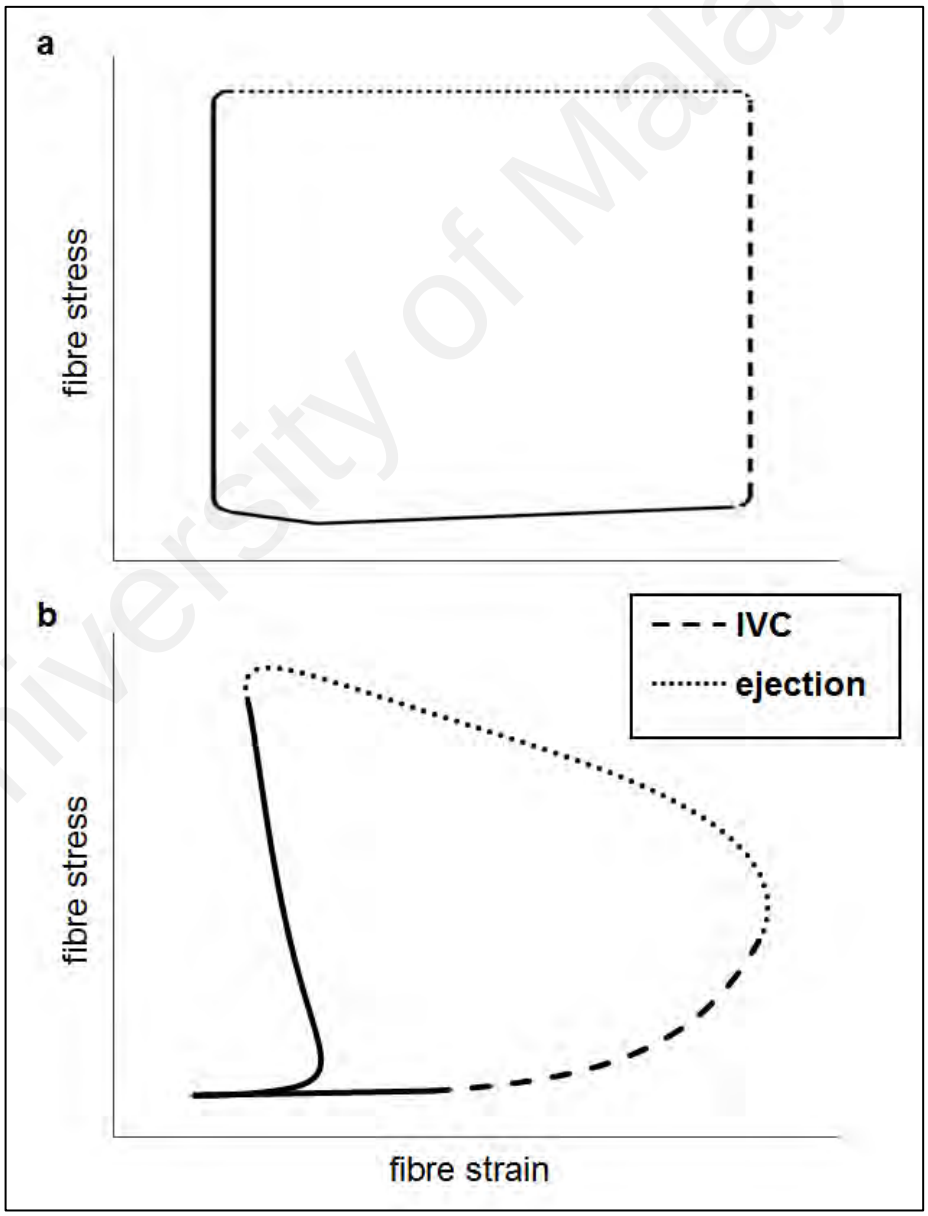

Figure 5.28: (a) An ideal FSSL. (b) An impaired FSSL.

extension at their respective neighbouring PR-NPR border. It is worth noting that based on the results (Figures 5.19 - 5.21), the shape of FSSL was closely related to the occurrence of chronic infarct extension. Regions with FSSLs that significantly deviated from the standard rectangular shape showed higher chances of infarct extension during follow-up.

Regional mechanical impairment was quantified using the WDD index, defined as the ratio of the dissipated work density during IVC and ejection, to work density output by the myocardium (Equation 5.8), was proposed. A higher WDD value signifies worse impairment in myocardial mechanics and energy efficiency. As shown in the result (Figure 5.22), regions with high WDD index values (> 0.24) demonstrated chronic infarct extension. On the other hand, among all ten points with WDD index values lower than 0.24, only three points demonstrated chronic infarct extension. This disparity in observation might arise in part from the possible occurrence of infarct extension surrounding these points at a later time, which was not happening during the first scan. Another possibility is that FSSLs generated from these points were not adequate to reflect the actual impaired mechanics happening at the PR-NPR border next to them.

Based on the above analysis, the inability of the regional myocardial tissue to generate adequate contraction force during IVC, and rapidly shorten during ejection, is responsible for the impaired regional myocardial mechanics and energy efficiency in post-MI patients, which lead to the occurrence of chronic infarct extension. In a previous computational modelling study, J. M. Guccione et al. (2001) found that depressed myocardial intrinsic contractility needs to be pronounced to replicate the experimentally observed isovolumic stretching and impaired myocardial mechanics phenomena in post-MI patients. Nevertheless, the postulation that intrinsic impairment in myocardial contractility accounts for the deterioration in the myocardial mechanics is

inadequate to explain the occurrence of nonischemic infarct extension, as observed in a previous experimental study (Jackson et al., 2002). The present study proved that isovolumic stretching and impaired regional mechanics do not necessarily occur due to impaired myocardial intrinsic contractility, as demonstrated by the impaired FSSLs and abnormally high WDD values at the RZ-BZ border, which was modelled as having a normal T_0, supporting the observation of nonischemic infarct extension.

5.5.4 Causal Factors Leading to Depressed Contractile Ability

Further analysis performed in this study revealed that an increase in IZ stiffness, though helpful in preventing infarct expansion, worsened the regional mechanics of its surrounding contractile myocardium, as illustrated by the less rectangular FSSL shape and higher WDD index values (Figures 5.23 - 5.26). The opposite phenomenon was observed with a reduction in the IZ stiffness. Contractile ability of the myocardium does not depend only on its intrinsic contractility, but also on the end-diastolic length of its muscle fibres, as described by the Frank-Starling law. Therefore, an increase in the IZ stiffness, which reduced the end-diastolic fibre strain (Figure 5.27), decreased the contractile ability of its neighbouring myocardium and increased the work dissipation during the IVC and ejection phases. By independently imposing a predefined, normal sarcomere length profile throughout the myocardium during systole (the $SL_{(RZ)}$ models), the active twitch force of the contractile myocardium was increased in accordance with the Frank-Starling law. Consequently, the WDD index values were decreased, particularly due to an effective reduction in the work dissipation during ejection caused by an increase in the rate of systolic fibre shortening.

The results of the sensitivity analysis above strengthens the argument that the impaired regional myocardial mechanics observed in the contractile myocardium located at the RZ-BZ border was due to, at least in part, a reduction in the end-diastolic

fibre strain, which depressed the contractile ability of the myocardium. As a result of the mechanical interaction between the IZ, BZ and RZ, an overstiff IZ diminishes the end-diastolic fibre strain in the RZ, making it hypocontractile and becoming a part of the BZ over time. In short, infarct extension can be initiated by inadequate end-diastolic fibre strain, a result of the tethering effect between the IZ and RZ, and not necessarily due to myocardial intrinsic contractility impairment. This finding explains the occurrence of nonischemic infarct extension. As far as concerned, this is the first study that demonstrated impaired regional mechanics in the RZ, which was shown to be correlated with infarct extension, and explains the underlying mechanism of nonischemic infarct extension.

This study also explains the ineffectiveness of Dor procedure in enhancing myocardial contractility in the BZ by reducing the LV volume, despite an overall reduction in the end-diastolic and end-systolic stress was achieved (Sun et al., 2010). This is because Dor procedure does not help in restoring depressed end-diastolic fibre strain in the BZ, causing the BZ to continue exhibiting depressed contractile ability and impaired regional mechanics, even with normal intrinsic contractility.

It is worth noting that despite constant stiffness across the IZ in each patient, not all regions surrounding the abnormally stiff IZ experienced impaired myocardial mechanics and infarct extension. Furthermore, overall there was no direct correlation between the end-diastolic fibre strain and WDD index or infarct extension. This could be explained by the fact that the level of end-diastolic fibre strain required to generate adequate contractile force and thereby normal FSSLs at the regional myocardial tissue is affected by its interaction with the neighbouring myocardium. Such an interaction is complicated and multifactorial, including the location of the myocardial tissue, regional infarct transmural extent (TME) and shape, fibre orientation, and LV shape. The

interaction and its impact on the regional myocardial mechanics are beyond the scope of this study.

5.5.5 Inadequacy of Global Parameters in Predicting Left Ventricular Outcome

Since LV pressure measurement is invasive and was thus not performed on patients in this study, fixed end-diastolic and end-systolic LV pressures based on published clinical values were applied on all LV models during the parameter optimisation process. Therefore, the estimated parameter values (i.e. $C_{0(IZ)}$, $C_{0(RZ)}$ and T_0) presented in Table 5.3 could not represent the actual myocardial stiffness and intrinsic contractility of the patient LVs. In spite of this, comparison among the patient LVs with regards to their intrinsic contractility can still be briefly deduced by comparing their T_0 to $C_{0(RZ)}$ ratio. Even though patient 2 had the least contractile LV among all patients, a better outcome was observed in this patient with regards to his infarct extension progression as compared to patient 3. On the other hand, in regards to the global LV function (Table 5.4), patient with physiological function at the 1st scan showed deleterious progress, whilst patients with impaired global function demonstrated improvement. Based on these observations, global indices, such as LV contractility and EF, are inadequate in reflecting the regional myocardial mechanics impairments and predicting LV outcome in post-MI patients.

5.5.6 Clinical Significance

Following an acute MI, there is a high chance that the LV undergoes maladaptive ventricular remodelling, including infarct expansion and extension, which progressively leads to heart failure.

The mechanism underlying infarct expansion is reasonably well known. It starts with a non-contractile infarct, which is unable to withstand high systolic pressure, consequently undergoes distension, systolic bulging, and ultimately infarct expansion

(French & Kramer, 2007). This concept supports the present finding, which revealed that the thickening and stiffening of the scar tissue were effective in preventing infarct expansion. Therefore, any treatments that help in attenuating infarct distension, including thickening and stiffening infarct, are able to prevent, or at least slow down, infarct expansion. Ventricular plication (Schwarz et al., 2000), patches (Leor & Cohen, 2004) and hydrogel injection (Jiang et al., 2009), which help strengthening the infarct to prevent infarct distension, have been demonstrated to aid in preventing or attenuating infarct expansion. Angiotensin converting enzyme (ACE) inhibitors, which help lowering blood pressure and attenuating loading placed on infarct, are normally given to MI patients as early as possible (Antman et al., 2004).

Although highly stiff infarct was shown to be effective in preventing infarct expansion, it can induce another LV complication, namely infarct extension. In the present study, it was elucidated how an excessively stiff IZ could reduce the contractile ability of the neighbouring myocardium, thus leading to an impairment of regional myocardial mechanics, which is correlated with infarct extension. The myocardial contractile ability inadequacy and chronic infarct extension prediction can be evaluated through the FSSL and WDD index.

Although the biological process underlying the transduction of myocardial contractile ability inadequacy to infarct extension is not known, perhaps impaired myocardial contractile ability influences the Ca^{2+} uptake by sarcoplasmic reticulum (SR) after myocardial contraction, subsequently depressing the SR Ca^{2+}-ATPase activity, which is correlated with impaired myocardial contractile function (Hasenfuss et al., 1994) and observed in heart failure cases (Hasenfuss, 1998). Intracellular Ca^{2+}-mishandling is also potent in activating Ca^{2+}-sensitive intracellular signalling factors, such as calcium-calmodulin-dependent phosphatase calcineurin (Lim & Molkentin,

1999; Molkentin et al., 1998; Ritter et al., 2002; Wilkins et al., 2004), Ca^{2+}-dependent protein kinases (Passier et al., 2000; Ramirez et al., 1997) and mitogen-activated protein kinases (Hill & Olson, 2008), which can induce pathologic cardiac growth. Therefore, any treatments aim to restore myocardial contractile ability, including by restoring the end-diastolic fibre strain, will be helpful in restoring regional myocardial mechanics and inhibiting infarct extension.

In summary, in order to prevent both infarct expansion and extension, the IZ should be adequately stiff to withstand the high systolic LV pressure, but not at the expense of reducing the end-diastolic fibre strain and contractile ability of the neighbouring myocardium, in order to maintain normal myocardial mechanics.

5.5.7 Study Limitations

As discussed earlier, since the end-diastolic and end-systolic LV pressures were assumed during the parameter optimisation process, the estimated model parameter values could not represent the actual myocardial stiffness and intrinsic contractility. As a result, the absolute stress values obtained from the simulations could not reflect the actual stress experienced by the patient LVs. Besides, the LV geometry at the second cardiac time point after mitral valve opening was chosen as the reference geometry for model simulations because it is believed that the LV is under minimum stress during this time point. Such minimum stress was ignored in the present study. In addition, the external forces, such as the thoracic pressure and the weight of blood, as well as the residual stresses of the myocardium, were also not included in the models. However, these pressures and stresses are of global factors and would only affect the absolute values of the fibre stress but not its distribution, which was utilised in this study to infer findings. Therefore, the outcomes of this study would not be influenced by these inaccuracies.

Furthermore, as the parameter optimisation approach utilised in this study was based on geometrical similarity, and the same end-diastolic and end-systolic LV pressures were applied during both the parameter optimisation process and full LV cycle simulations, accurate fibre strain, in terms of its absolute values and distribution, could be expected from the simulations. Together with unaffected fibre stress distribution, the simulated regional mechanics, which includes the FSSLs, WDD index values, myocardial contractile ability and end-diastolic fibre strain adequacy, used in this study to interpret the major findings would resemble the actual regional mechanics.

Instead of using patient-specific myocardial fibre orientation, a transmurally changing fibre orientation (from +60° at the endocardium to -60° at the epicardium) was assumed, based on a previous study (Pravdin et al., 2013), which showed fairly consistent fibre orientation across healthy LVs. Although the LV models in this study were based on post-MI patients (within a week from the onset of acute MI), insignificant changes in the fibre orientation were expected as the adaptation process of myocardial fibre orientation takes several months. Therefore, it is reasonable to assume that the fibre orientation remained unchanged, or at least any changes would be minimal, and thus would not have a substantial impact on the present findings.

5.6 Conclusions

In this study, patient-specific LV models, incorporating optimised regional material properties, were successfully developed. The optimisations were performed based on the geometrical similarity concept, instead of conventional tagged images displacement data.

It was found that WDD index and FSSL shape, but not fibre strain and stress, were correlated with infarct extension occurrence. This implies that infarct extension is not explicitly caused by high fibre strain or stress, but rather inadequate contraction force

generation during the IVC and ejection phases. Such inadequacy in the contraction force can be revealed via FSSL and WDD index value, which might serve to predict chronic infarct extension events. More importantly, this study revealed that such contraction force inadequacy may not be solely caused by an intrinsic impairment in the cardiac contractility, but can also be due to inadequate stretch of the myocardium at end-diastole (the Frank-Starling law).

It was also shown in this study that a stiff infarct can prevent infarct expansion. However, an overstiff infarct, via mechanical interaction, causes neighbouring contractile myocardium to exhibit abnormally low strain at end-diastole. As a consequence, the neighbouring myocardium becomes hypocontractile over time, and undergoes nonischemic infarct extension. Meanwhile, the originally hypocontractile BZ progressively becomes less contractile, and eventually turns into a non-contractile infarct via ischemic infarct extension.

CHAPTER 6: CONCLUSIONS

6.1 Conclusions

In this study, an LV modelling framework, which can be used to simulate both generic and patient-specific LV models, has been established. The framework, through its generic counterpart, has been shown to be capable of reproducing physiological LV function, including LV pressure, cavity volume, twisting and wall thickening.

It was found that infarct TME is more important than its size in causing LV regional mechanics impairments. These impairments include the presence of abnormally high stress, elevated myocardial energy expenditure and depressed myocardial energy efficiency at the BZ, which are believed to be capable of inducing infarct extension. The impairments are due to the combined effects of mechanical tethering, a consequence of mechanical interaction between contractile myocardium and non-contractile infarct, and myocardial fibre orientation.

Patient-specific LV models, incorporating optimised regional material properties, were successfully developed and utilised for examining the correlation between infarct extension and myocardial mechanics. Among the observed myocardial mechanics impairments, only depressed myocardial energy efficiency was found to be correlated with infarct extension, but not fibre strain or stress. This outcome questions the common believe that fibre strain or stress alone is capable in inducing infarct extension. The depressed myocardial energy efficiency, which can be revealed via FSSL and WDD index value, is a result of inadequate contraction force generation during the IVC and ejections phases.

The further analysis carried out in the present work also found that the inadequacy in contraction force generation is not necessarily caused by myocardial intrinsic impairment, but can also be due to abnormally low myocardial fibre strain at end-

diastole, which directly affects the contraction force generation in the subsequent systole (according to the Frank-Starling law). Besides, an overstiff infarct, though can prevent infarct expansion, can impair the end-diastolic strain, and so the contraction force generation capability and regional mechanics of the neighbouring myocardium, causing both ischemic and non-ischemic infarct extension. This finding elucidates the occurrence of nonischemic infarct extension, which could not be explained by previous studies.

6.2 Future Works

6.2.1 Geometry

Muscle fibre orientation was defined based on the published literature in this study. In future, patient-specific fibre orientation could be implemented into the model with the use of DT CMR. This would provide quantitatively more accurate results. Besides, the availability of fibre orientation data also allows investigation into the effects of regional mechanics on chronic adaptation of the fibre orientation.

LV deformation might be affected by the presence of RV. Therefore, an RV geometry could be incorporated into the framework presented in this study, extending the framework into a biventricular model. Incorporation of RV would allow the study of its influence on regional mechanics at the RV-LV junction, as well as the septum.

6.2.2 Electrophysiology Model

This study focuses only on the mechanical complications following MI. In future, the simplified electrophysiology formulations in the present framework can be modified to incorporate the mechano-electric feedback characterisations. This would allow the study of electrophysiological complications associated to MI, such as arrhythmias and tachycardia, as well as various treatment strategies, such as cardiac resynchronisation therapy.

6.2.3 Passive Material Model

The myocardium was modelled as a transversely isotropic hyperelastic material in this study. However, as discussed in Section 2.5.3, myocardium is orthotropic (has three characteristic directions) and viscoelastic in nature. To modify the material model into orthotropic, it had to be optimised against the biaxial tensile test results of myocardium, which must include all possible combinations of the three characteristic directions. To incorporate the viscoelastic response of myocardium, a viscous component could be added into each of the characteristic directions, and validated against relaxation and creep curves at different stretch amplitudes for each characteristic direction.

Therefore, experimental studies to better understand the myocardial material properties, particularly the viscoelastic response of myocardium, are beneficial to heart modelling research.

6.2.4 Active Contraction Model

To date, there is no simple phenomenological active stress formulism that adequately characterises the complicated myocardial mechanics. For example, the sarcomere length-force relations and force-velocity relations adopted in this study could not accurately reflect the detailed mechanical behaviour of myocardium. In addition, it still remains unanswered whether the active response of myocardium is also orthotropic, as its passive response.

Therefore, any studies that help in characterising the active orthotropic response of myocardium, as well as formulating phenomenological active stress formulism that adequately represent the complicated active myocardial mechanics, are highly beneficial to facilitate organ-level heart modelling works.

6.2.5 Simulations

To make the experimentally developed material model to be more representative of *in vivo* myocardial characterisation, the material model could be optimised against tagged CMR data, which had to be in 3D form and cover the entire heart cycle with no fading issue.

It is also worthy to extend this work to animal studies, in which the LV pressure throughout the entire LV cycle can be made accessible. This enables a more accurate estimation of the material properties (including the myocardial overall stiffness, C_0, and myocardial intrinsic contractility, T_0), subsequently allowing the model to produce quantitatively more accurate results. Besides, factors such as infarct state, lifestyle and subject age are easier to manipulate in animal studies, thus allowing a better control of the confounding factors.

REFERENCES

Abd-Elmoniem, K. Z., Tomas, M. S., Sasano, T., Soleimanifard, S., Vonken, E.-J. P., Youssef, A., . . . Stuber, M. (2012). Assessment of distribution and evolution of Mechanical dyssynchrony in a porcine model of myocardial infarction by cardiovascular magnetic resonance. *Journal of Cardiovascular Magnetic Resonance, 14*(1), 1-10.

Ahn, K. T., Song, Y. B., Choe, Y. H., Yang, J. H., Hahn, J.-Y., Choi, J.-H., . . . Lee, S. H. (2013). Impact of transmural necrosis on left ventricular remodeling and clinical outcomes in patients undergoing primary percutaneous coronary intervention for ST-segment elevation myocardial infarction. *The International Journal of Cardiovascular Imaging, 29*(4), 835-842.

Aikawa, Y., Rohde, L., Plehn, J., Greaves, S. C., Menapace, F., Arnold, J. M. O., . . . Solomon, S. D. (2001). Regional wall stress predicts ventricular remodeling after anteroseptal myocardial infarction in the Healing and Early Afterload Reducing Trial (HEART): an echocardiography-based structural analysis. *American Heart Journal, 141*(2), 234-242.

Akasaka, Y., Morimoto, N., Ishikawa, Y., Fujita, K., Ito, K., Kimura-Matsumoto, M., . . . Ishii, T. (2006). Myocardial apoptosis associated with the expression of proinflammatory cytokines during the course of myocardial infarction. *Modern Pathology, 19*(4), 588-598.

Aliev, R. R., & Panfilov, A. V. (1996). A simple two-variable model of cardiac excitation. *Chaos, Solitons & Fractals, 7*(3), 293-301.

Ambrosi, D., & Pezzuto, S. (2012). Active stress vs. active strain in mechanobiology: constitutive issues. *Journal of Elasticity, 107*(2), 199-212.

Anand, I. S., & Florea, V. G. (2011). Alterations in Ventricular Structure: Role of Left Ventricular Remodeling. *Heart Failure* (pp. 232-253). Philadelphia, Pennsylvania: Elsevier Inc.

Antman, E. M., Anbe, D. T., Armstrong, P. W., Bates, E. R., Green, L. A., Hand, M., . . . Lamas, G. A. (2004). ACC/AHA guidelines for the management of patients with ST-elevation myocardial infarction—executive summary: a report of the American College of Cardiology/American Heart Association Task Force on Practice Guidelines (Writing Committee to Revise the 1999 Guidelines for the Management of Patients With Acute Myocardial Infarction). *Journal of the American College of Cardiology, 44*(3), 671-719.

Anversa, P., Loud, A. V., Levicky, V., & Guideri, G. (1985). Left ventricular failure induced by myocardial infarction. I. Myocyte hypertrophy. *American Journal of Physiology-Heart and Circulatory Physiology, 248*(6), H876-H882.

Ashikaga, H., Coppola, B. A., Hopenfeld, B., Leifer, E. S., McVeigh, E. R., & Omens, J. H. (2007). Transmural dispersion of myofiber mechanics: implications for electrical heterogeneity in vivo. *Journal of the American College of Cardiology, 49*(8), 909-916.

Ashikaga, H., Mickelsen, S. R., Ennis, D. B., Rodriguez, I., Kellman, P., Wen, H., & McVeigh, E. R. (2005). Electromechanical analysis of infarct border zone in chronic myocardial infarction. *American Journal of Physiology-Heart and Circulatory Physiology, 289*(3), H1099-H1105.

Baines, C. P., & Molkentin, J. D. (2005). STRESS signaling pathways that modulate cardiac myocyte apoptosis. *Journal of Molecular and Cellular Cardiology, 38*(1), 47-62.

Bassani, J., Bassani, R. A., & Bers, D. M. (1994). Relaxation in rabbit and rat cardiac cells: species ‐ dependent differences in cellular mechanisms. *The Journal of Physiology, 476*(2), 279-293.

Bassani, J., Yuan, W., & Bers, D. M. (1995). Fractional SR Ca release is regulated by trigger Ca and SR Ca content in cardiac myocytes. *American Journal of Physiology-Cell Physiology, 268*(5), C1313-C1319.

Becker, M., Ocklenburg, C., Altiok, E., Füting, A., Balzer, J., Krombach, G., . . . Kelm, M. (2009). Impact of infarct transmurality on layer-specific impairment of myocardial function: a myocardial deformation imaging study. *European Heart Journal, 30*(12), 1467-1476.

Beeler, G. W., & Reuter, H. (1977). Reconstruction of the action potential of ventricular myocardial fibres. *The Journal of Physiology, 268*(1), 177-210.

Bers, D. M. (2002). Cardiac excitation–contraction coupling. *Nature, 415*(6868), 198-205.

Berti, V., Sciagrà, R., Acampa, W., Ricci, F., Cerisano, G., Gallicchio, R., . . . Cuocolo, A. (2011). Relationship between infarct size and severity measured by gated SPECT and long-term left ventricular remodelling after acute myocardial infarction. *European Journal of Nuclear Medicine and Molecular Imaging, 38*(6), 1124-1131.

Blom, A. S., Mukherjee, R., Pilla, J. J., Lowry, A. S., Yarbrough, W. M., Mingoia, J. T., . . . Affuso, J. (2005). Cardiac support device modifies left ventricular geometry and myocardial structure after myocardial infarction. *Circulation, 112*(9), 1274-1283.

Cahill, T. J., & Kharbanda, R. K. (2017). Heart failure after myocardial infarction in the era of primary percutaneous coronary intervention: mechanisms, incidence and identification of patients at risk. *World Journal of Cardiology, 9*(5), 407.

Cansız, F. B. C., Dal, H., & Kaliske, M. (2015). An orthotropic viscoelastic material model for passive myocardium: theory and algorithmic treatment. *Computer Methods in Biomechanics and Biomedical Engineering, 18*(11), 1160-1172.

Chabiniok, R., Moireau, P., Lesault, P.-F., Rahmouni, A., Deux, J.-F., & Chapelle, D. (2012). Estimation of tissue contractility from cardiac cine-MRI using a biomechanical heart model. *Biomechanics and Modeling in Mechanobiology, 11*(5), 609-630.

Chien, K. R. (2000). Meeting Koch's postulates for calcium signaling in cardiac hypertrophy. *The Journal of Clinical Investigation, 105*(10), 1339-1342.

Choi, H. F., Rademakers, F. E., & Claus, P. (2011). Left-ventricular shape determines intramyocardial mechanical heterogeneity. *American Journal of Physiology-Heart and Circulatory Physiology, 301*(6), H2351-H2361.

Cleutjens, J. P., & Creemers, E. E. (2002). Integration of concepts: cardiac extracellular matrix remodeling after myocardial infarction. *Journal of Cardiac Failure, 8*(6), S344-S348.

COMSOL. (2012). *COMSOL multiphysics user's guide* (4.3 ed.). United States: COMSOL AB.

Costa, K. D., Holmes, J. W., & McCulloch, A. D. (2001). Modelling cardiac mechanical properties in three dimensions. *Philosophical Transactions of the Royal Society of London A: Mathematical, Physical and Engineering Sciences, 359*(1783), 1233-1250.

Costa, K. D., Hunter, P. J., Rogers, J., Guccione, J. M., Waldman, L., & McCulloch, A. D. (1996). A three-dimensional finite element method for large elastic deformations of ventricular myocardium: I—Cylindrical and spherical polar coordinates. *Journal of Biomechanical Engineering, 118*(4), 452-463.

Creemers, E. E., & Pinto, Y. M. (2010). Molecular mechanisms that control interstitial fibrosis in the pressure-overloaded heart. *Cardiovascular Research, 89*(2), 265-272.

Dall'Armellina, E., Karia, N., Lindsay, A. C., Karamitsos, T. D., Ferreira, V., Robson, M. D., . . . Prendergast, B. D. (2011). Dynamic Changes of Edema and Late Gadolinium Enhancement After Acute Myocardial Infarction and Their Relationship to Functional Recovery and Salvage IndexClinical Perspective. *Circulation: Cardiovascular Imaging, 4*(3), 228-236.

Di Napoli, P., Taccardi, A. A., Grilli, A., Felaco, M., Balbone, A., Angelucci, D., . . . Barsotti, A. (2003). Left ventricular wall stress as a direct correlate of cardiomyocyte apoptosis in patients with severe dilated cardiomyopathy. *American Heart Journal, 146*(6), 1105-1111.

Diwan, A., Krenz, M., Syed, F. M., Wansapura, J., Ren, X., Koesters, A. G., . . . Robbins, J. (2007). Inhibition of ischemic cardiomyocyte apoptosis through targeted ablation of Bnip3 restrains postinfarction remodeling in mice. *The Journal of Clinical Investigation, 117*(10), 2825-2833.

Dor, V. (2001). The endoventricular circular patch plasty ("Dor procedure") in ischemic akinetic dilated ventricles. *Heart Failure Reviews, 6*(3), 187-193.

Dorn, G. W., Robbins, J., & Sugden, P. H. (2003). Phenotyping hypertrophy: eschew obfuscation. *Circulation Research, 92*(11), 1171-1175.

Doyle, M. G. (2011). *Simulation of Myocardium Motion and Blood Flow in the Heart with Fluid-Structure Interaction.* (Doctoral thesis, University of Ottawa, Canada), Retrieved from https://ruor.uottawa.ca/handle/10393/20166.

Erlebacher, J. A., Weiss, J. L., Eaton, L. W., Kallman, C., Weisfeldt, M. L., & Bulkley, B. H. (1982). Late effects of acute infarct dilation on heart size: a two dimensional echocardiographic study. *American Journal of Cardiology, 49*(5), 1120-1126.

Fares, E., & Schröder, W. (2002). A differential equation for approximate wall distance. *International Journal for Numerical Methods in Fluids, 39*(8), 743-762.

Fishbein, M. C., Maclean, D., & Maroko, P. R. (1978). The histopathologic evolution of myocardial infarction. *Chest, 73*(6), 843-849.

FitzHugh, R. (1961). Impulses and physiological states in theoretical models of nerve membrane. *Biophysical Journal, 1*(6), 445-466.

Fomovsky, G. M., Macadangdang, J. R., Ailawadi, G., & Holmes, J. W. (2011). Model-based design of mechanical therapies for myocardial infarction. *Journal of Cardiovascular Translational Research, 4*(1), 82-91.

Frangogiannis, N. G. (2014). The inflammatory response in myocardial injury, repair, and remodelling. *Nature Reviews Cardiology, 11*(5), 255.

Frangogiannis, N. G. (2017). The extracellular matrix in myocardial injury, repair, and remodeling. *The Journal of Clinical Investigation, 127*(5), 1600-1612.

French, B. A., & Kramer, C. M. (2007). Mechanisms of postinfarct left ventricular remodeling. *Drug Discovery Today: Disease Mechanisms, 4*(3), 185-196.

Frey, N., Katus, H. A., Olson, E. N., & Hill, J. A. (2004). Hypertrophy of the heart: a new therapeutic target? *Circulation, 109*(13), 1580-1589.

Fukuda, N., Sasaki, D., Ishiwata, S. i., & Kurihara, S. (2001). Length dependence of tension generation in rat skinned cardiac muscle: role of titin in the Frank-Starling mechanism of the heart. *Circulation, 104*(14), 1639-1645.

Gaasch, W. H., Zile, M. R., Hoshino, P. K., Apstein, C. S., & Blaustein, A. S. (1989). Stress-shortening relations and myocardial blood flow in compensated and failing canine hearts with pressure-overload hypertrophy. *Circulation, 79*(4), 872-883.

Gajarsa, J. J., & Kloner, R. A. (2011). Left ventricular remodeling in the post-infarction heart: a review of cellular, molecular mechanisms, and therapeutic modalities. *Heart Failure Reviews, 16*(1), 13-21.

Gao, H., Aderhold, A., Mangion, K., Luo, X., Husmeier, D., & Berry, C. (2017). Changes and classification in myocardial contractile function in the left ventricle following acute myocardial infarction. *Journal of The Royal Society Interface, 14*(132), 20170203.

Geselowitz, D. B., & Miller, W. (1983). A bidomain model for anisotropic cardiac muscle. *Annals of Biomedical Engineering, 11*(3-4), 191-206.

Gilson, W. D., Epstein, F. H., Yang, Z., Xu, Y., Prasad, K.-M. R., Toufektsian, M.-C., . . . French, B. A. (2007). Borderzone contractile dysfunction is transiently attenuated and left ventricular structural remodeling is markedly reduced following reperfused myocardial infarction in inducible nitric oxide synthase knockout mice. *Journal of the American College of Cardiology, 50*(18), 1799-1807.

Grossman, W., Jones, D., & McLaurin, L. (1975). Wall stress and patterns of hypertrophy in the human left ventricle. *The Journal of Clinical Investigation, 56*(1), 56-64.

Guccione, J., Waldman, L., & McCulloch, A. (1993). Mechanics of active contraction in cardiac muscle: Part II—Cylindrical models of the systolic left ventricle. *Journal of Biomechanical Engineering, 115*(1), 82-90.

Guccione, J. M., Costa, K. D., & McCulloch, A. D. (1995). Finite element stress analysis of left ventricular mechanics in the beating dog heart. *Journal of Biomechanics, 28*(10), 1167-1177.

Guccione, J. M., McCulloch, A. D., & Waldman, L. (1991). Passive material properties of intact ventricular myocardium determined from a cylindrical model. *Journal of Biomechanical Engineering, 113*(1), 42-55.

Guccione, J. M., Moonly, S. M., Moustakidis, P., Costa, K. D., Moulton, M. J., Ratcliffe, M. B., & Pasque, M. K. (2001). Mechanism underlying mechanical dysfunction in the border zone of left ventricular aneurysm: a finite element model study. *The Annals of Thoracic Surgery, 71*(2), 654-662.

Gupta, K. B., Ratcliffe, M. B., Fallert, M. A., Edmunds, L., & Bogen, D. K. (1994). Changes in passive mechanical stiffness of myocardial tissue with aneurysm formation. *Circulation, 89*(5), 2315-2326.

Guyton, A., & Hall, J. (2006). *Textbook of medical physiology* (11th ed.). Philadelphia, Pennsylvania: Elsevier Inc.

Hasenfuss, G. (1998). Alterations of calcium-regulatory proteins in heart failure. *Cardiovascular Research, 37*(2), 279-289.

Hasenfuss, G., Reinecke, H., Studer, R., Meyer, M., Pieske, B., Holtz, J., . . . Drexler, H. (1994). Relation between myocardial function and expression of sarcoplasmic reticulum Ca (2+)-ATPase in failing and nonfailing human myocardium. *Circulation Research, 75*(3), 434-442.

Helm, P., Beg, M. F., Miller, M. I., & Winslow, R. L. (2005). Measuring and mapping cardiac fiber and laminar architecture using diffusion tensor MR imaging. *Annals of the New York Academy of Sciences, 1047*(1), 296-307.

Hiesinger, W., Brukman, M. J., McCormick, R. C., Fitzpatrick III, J. R., Frederick, J. R., Yang, E. C., . . . Atluri, P. (2012). Myocardial tissue elastic properties determined by atomic force microscopy after stromal cell–derived factor 1α angiogenic therapy for acute myocardial infarction in a murine model. *The Journal of Thoracic and Cardiovascular Surgery, 143*(4), 962-966.

Hill, J. A., & Olson, E. N. (2008). Cardiac plasticity. *New England Journal of Medicine, 358*(13), 1370-1380.

Hodgkin, A. L., & Huxley, A. F. (1952). A quantitative description of membrane current and its application to conduction and excitation in nerve. *The Journal of Physiology, 117*(4), 500-544.

Holzapfel, G. A., & Ogden, R. W. (2009). Constitutive modelling of passive myocardium: a structurally based framework for material characterization. *Philosophical Transactions of the Royal Society of London A: Mathematical, Physical and Engineering Sciences, 367*(1902), 3445-3475.

Humphrey, J., Strumpf, R., & Yin, F. (1990). Determination of a constitutive relation for passive myocardium: I. A new functional form. *Journal of Biomechanical Engineering, 112*(3), 333-339.

Hutchins, G. M., & Bulkley, B. H. (1978). Infarct expansion versus extension: two different complications of acute myocardial infarction. *The American Journal of Cardiology, 41*(7), 1127-1132.

Intrigila, B., Melatti, I., Tofani, A., & Macchiarelli, G. (2007). Computational models of myocardial endomysial collagen arrangement. *Computer Methods and Programs in Biomedicine, 86*(3), 232-244.

Jackson, B. M., Gorman, J. H., Moainie, S. L., Guy, T. S., Narula, N., Narula, J., . . . Gorman, R. C. (2002). Extension of borderzone myocardium in postinfarction dilated cardiomyopathy. *Journal of the American College of Cardiology, 40*(6), 1160-1167.

Jiang, X. J., Wang, T., Li, X. Y., Wu, D. Q., Zheng, Z. B., Zhang, J. F., . . . Huang, C. (2009). Injection of a novel synthetic hydrogel preserves left ventricle function after myocardial infarction. *Journal of Biomedical Materials Research Part A, 90*(2), 472-477.

Jie, X., Gurev, V., & Trayanova, N. (2010). Mechanisms of mechanically induced spontaneous arrhythmias in acute regional ischemia. *Circulation Research, 106*(1), 185-192.

Katz, A. M., & Rolett, E. L. (2015). Heart failure: when form fails to follow function. *European Heart Journal, 37*(5), 449-454.

Kaul, S. (1995). There may be more to myocardial viability than meets the eye! *Circulation, 92*(10), 2790-2793.

Kerckhoffs, R. C. P., McCulloch, A. D., Omens, J. H., & Mulligan, L. J. (2009). Effects of biventricular pacing and scar size in a computational model of the failing heart with left bundle branch block. *Medical Image Analysis, 13*(2), 362-369.

Kerckhoffs, R. C. P., Omens, J. H., McCulloch, A. D., & Mulligan, L. J. (2010). Ventricular dilation and electrical dyssynchrony synergistically increase regional mechanical non-uniformity but not mechanical dyssynchrony: a computational model. *Circulation: Heart Failure, 3*(4), 528-536.

Klabunde, R. E. (2011). *Cardiovascular physiology concepts*. New York, NY: Lippincott Williams & Wilkins.

Kozlovskis, P. L., Silver, J., Rubin, R., Wong, S., Gaide, M., Bassett, A., . . . Myerburg, R. (1984). Regional variations in myosin heavy chain concentration after healing of experimental myocardial infarction in cats. *Journal of Molecular and Cellular Cardiology, 16*(6), 559-566.

Kramer, C. M., Lima, J., Reichek, N., Ferrari, V. A., Llaneras, M. R., Palmon, L. C., . . . Axel, L. (1993). Regional differences in function within noninfarcted myocardium during left ventricular remodeling. *Circulation, 88*(3), 1279-1288.

Kroon, W., Delhaas, T., Bovendeerd, P., & Arts, T. (2009). Computational analysis of the myocardial structure: Adaptation of cardiac myofiber orientations through deformation. *Medical Image Analysis, 13*(2), 346-353.

Land, S., Park-Holohan, S.-J., Smith, N. P., dos Remedios, C. G., Kentish, J. C., & Niederer, S. A. (2017). A model of cardiac contraction based on novel measurements of tension development in human cardiomyocytes. *Journal of Molecular and Cellular Cardiology, 106*, 68-83.

Lang, R. M., Bierig, M., Devereux, R. B., Flachskampf, F. A., Foster, E., Pellikka, P. A., . . . Shanewise, J. (2006). Recommendations for chamber quantification. *European Journal of Echocardiography, 7*(2), 79-108.

Lee, P. T., Dweck, M. R., Prasher, S., Shah, A., Humphries, S. E., Pennell, D. J., . . . Payne, J. R. (2013). Left ventricular wall thickness and the presence of asymmetric hypertrophy in healthy young army recruits: data from the LARGE heart study. *Circulation: Cardiovascular Imaging, 6*(2), 262-267.

Leor, J., & Cohen, S. (2004). Myocardial tissue engineering: creating a muscle patch for a wounded heart. *Annals of the New York Academy of Sciences, 1015*(1), 312-319.

LeWinter, M. M., & Granzier, H. L. (2014). Cardiac titin and heart disease. *Journal of Cardiovascular Pharmacology, 63*(3), 207.

Liew, Y., McLaughlin, R., Chan, B., Aziz, Y. A., Chee, K., Ung, N., . . . Lim, E. (2015). Motion corrected LV quantification based on 3D modelling for improved functional assessment in cardiac MRI. *Physics in Medicine & Biology, 60*(7), 2715-2733.

Lim, H. W., & Molkentin, J. D. (1999). Calcineurin and human heart failure. *Nature Medicine, 5*(3), 246-247.

Lima, J., Becker, L. C., Melin, J. A., Lima, S., Kallman, C. A., Weisfeldt, M. L., & Weiss, J. L. (1985). Impaired thickening of nonischemic myocardium during acute regional ischemia in the dog. *Circulation, 71*(5), 1048-1059.

Linzbach, A. (1960). Heart failure from the point of view of quantitative anatomy. *The American Journal of Cardiology, 5*(3), 370-382.

Lopez-Perez, A., Sebastian, R., & Ferrero, J. M. (2015). Three-dimensional cardiac computational modelling: methods, features and applications. *Biomedical Engineering Online, 14*(1), 35.

Makela, T., Clarysse, P., Sipila, O., Pauna, N., Pham, Q. C., Katila, T., & Magnin, I. E. (2002). A review of cardiac image registration methods. *IEEE Transactions on Medical Imaging, 21*(9), 1011-1021.

Mann, D. L. (2003). Stress-activated cytokines and the heart: from adaptation to maladaptation. *Annual Review of Physiology, 65*(1), 81-101.

Masci, P. G., Ganame, J., Francone, M., Desmet, W., Lorenzoni, V., Iacucci, I., . . . Agati, L. (2011). Relationship between location and size of myocardial infarction and their reciprocal influences on post-infarction left ventricular remodelling. *European Heart Journal, 32*(13), 1640-1648.

Matsui, Y., Takagi, H., Qu, X., Abdellatif, M., Sakoda, H., Asano, T., . . . Sadoshima, J. (2007). Distinct roles of autophagy in the heart during ischemia and reperfusion: roles of AMP-activated protein kinase and Beclin 1 in mediating autophagy. *Circulation Research, 100*(6), 914-922.

McDonald, K. S., Hanft, L. M., Domeier, T. L., & Emter, C. A. (2012). Length and PKA dependence of force generation and loaded shortening in porcine cardiac myocytes. *Biochemistry Research International, 2012*(2012), 1-12.

Mckay, R. G., Pfeffer, M. A., Pasternak, R. C., Markis, J. E., Come, P. C., Nakao, S., . . . Grossman, W. (1986). Left ventricular remodeling after myocardial infarction: a corollary to infarct expansion. *Circulation, 74*(4), 693-702.

Minamisawa, S., Hoshijima, M., Chu, G., Ward, C. A., Frank, K., Gu, Y., . . . Kranias, E. G. (1999). Chronic phospholamban–sarcoplasmic reticulum calcium ATPase interaction is the critical calcium cycling defect in dilated cardiomyopathy. *Cell, 99*(3), 313-322.

Mitchell, C. C., & Schaeffer, D. G. (2003). A two-current model for the dynamics of cardiac membrane. *Bulletin of Mathematical Biology, 65*(5), 767-793.

Miyamoto, M. I., Del Monte, F., Schmidt, U., DiSalvo, T. S., Kang, Z. B., Matsui, T., . . . Hajjar, R. J. (2000). Adenoviral gene transfer of SERCA2a improves left-ventricular function in aortic-banded rats in transition to heart failure. *Proceedings of the National Academy of Sciences, 97*(2), 793-798.

Molkentin, J. D., Lu, J.-R., Antos, C. L., Markham, B., Richardson, J., Robbins, J., . . . Olson, E. N. (1998). A calcineurin-dependent transcriptional pathway for cardiac hypertrophy. *Cell, 93*(2), 215-228.

Moulton, M. J., Downing, S. W., Creswell, L. L., Fishman, D. S., Amsterdam, D. M., Szabó, B. A., . . . Pasque, M. K. (1995). Mechanical dysfunction in the border zone of an ovine model of left ventricular aneurysm. *The Annals of Thoracic Surgery, 60*(4), 986-998.

Muller, J. E., Rude, R. E., Braunwald, E., Hartwell, T. D., Roberts, R., Sobel, B. E., . . . Stone, P. H. (1988). Myocardial infarct extension: occurrence, outcome, and risk factors in the Multicenter Investigation of Limitation of Infarct Size. *Annals of Internal Medicine, 108*(1), 1-6.

Mullins, P. D., & Bondarenko, V. E. (2013). A mathematical model of the mouse ventricular myocyte contraction. *PLoS One, 8*(5), e63141.

Murphy-Ullrich, J. E. (2001). The de-adhesive activity of matricellular proteins: is intermediate cell adhesion an adaptive state? *The Journal of Clinical Investigation, 107*(7), 785-790.

Nakao, K., Minobe, W., Roden, R., Bristow, M. R., & Leinwand, L. A. (1997). Myosin heavy chain gene expression in human heart failure. *The Journal of Clinical Investigation, 100*(9), 2362-2370.

Nash, M. P., & Panfilov, A. V. (2004). Electromechanical model of excitable tissue to study reentrant cardiac arrhythmias. *Progress in Biophysics and Molecular Biology, 85*(2-3), 501-522.

Nelson, D. M., Ma, Z., Fujimoto, K. L., Hashizume, R., & Wagner, W. R. (2011). Intra-myocardial biomaterial injection therapy in the treatment of heart failure: Materials, outcomes and challenges. *Acta Biomaterialia, 7*(1), 1-15.

Notomi, Y., Setser, R. M., Shiota, T., Martin-Miklovic, M. G., Weaver, J. A., Popovic, Z. B., . . . Thomas, J. D. (2005). Assessment of left ventricular torsional deformation by Doppler tissue imaging: validation study with tagged magnetic resonance imaging. *Circulation, 111*(9), 1141-1147.

O'Hara, T., Virág, L., Varró, A., & Rudy, Y. (2011). Simulation of the undiseased human cardiac ventricular action potential: model formulation and experimental validation. *PLoS Computational Biology, 7*(5), e1002061.

O'Regan, D. P., Shi, W., Ariff, B., Baksi, A. J., Durighel, G., Rueckert, D., & Cook, S. A. (2012). Remodeling after acute myocardial infarction: mapping ventricular dilatation using three dimensional CMR image registration. *Journal of Cardiovascular Magnetic Resonance, 14*(1), 41.

Olivetti, G., Capasso, J. M., Sonnenblick, E. H., & Anversa, P. (1990). Side-to-side slippage of myocytes participates in ventricular wall remodeling acutely after myocardial infarction in rats. *Circulation Research, 67*(1), 23-34.

Opie, L. H., Commerford, P. J., Gersh, B. J., & Pfeffer, M. A. (2006). Controversies in ventricular remodelling. *The Lancet, 367*(9507), 356-367.

Ørn, S., Manhenke, C., Anand, I. S., Squire, I., Nagel, E., Edvardsen, T., & Dickstein, K. (2007). Effect of left ventricular scar size, location, and transmurality on left ventricular remodeling with healed myocardial infarction. *The American Journal of Cardiology, 99*(8), 1109-1114.

Pandian, N. G., Skorton, D. J., Collins, S. M., Falsetti, H. L., Burke, E. R., & Kerber, R. E. (1983). Heterogeneity of left ventricular segmental wall thickening and excursion in 2-dimensional echocardiograms of normal human subjects. *The American Journal of Cardiology, 51*(10), 1667-1673.

Passier, R., Zeng, H., Frey, N., Naya, F. J., Nicol, R. L., McKinsey, T. A., . . . Olson, E. N. (2000). CaM kinase signaling induces cardiac hypertrophy and activates the MEF2 transcription factor in vivo. *The Journal of Clinical Investigation, 105*(10), 1395-1406.

Peterson, B. Z., DeMaria, C. D., & Yue, D. T. (1999). Calmodulin is the Ca2+ sensor for Ca2+-dependent inactivation of L-type calcium channels. *Neuron, 22*(3), 549-558.

Pfeffer, J. M., Pfeffer, M. A., Fletcher, P. J., & Braunwald, E. (1991). Progressive ventricular remodeling in rat with myocardial infarction. *American Journal of Physiology-Heart and Circulatory Physiology, 260*(5), H1406-H1414.

Pfeffer, M. A., & Braunwald, E. (1990). Ventricular remodeling after myocardial infarction. Experimental observations and clinical implications. *Circulation, 81*(4), 1161-1172.

Pfeffer, M. A., Lamas, G. A., Vaughan, D. E., Parisi, A. F., & Braunwald, E. (1988). Effect of captopril on progressive ventricular dilatation after anterior myocardial infarction. *New England Journal of Medicine, 319*(2), 80-86.

Pimentel, D. R., Amin, J. K., Xiao, L., Miller, T., Viereck, J., Oliver-Krasinski, J., . . . Singh, K. (2001). Reactive oxygen species mediate amplitude-dependent hypertrophic and apoptotic responses to mechanical stretch in cardiac myocytes. *Circulation Research, 89*(5), 453-460.

Potse, M., Dubé, B., Richer, J., Vinet, A., & Gulrajani, R. M. (2006). A comparison of monodomain and bidomain reaction-diffusion models for action potential propagation in the human heart. *IEEE Transactions on Biomedical Engineering, 53*(12), 2425-2435.

Pravdin, S. F., Berdyshev, V. I., Panfilov, A. V., Katsnelson, L. B., Solovyova, O., & Markhasin, V. S. (2013). Mathematical model of the anatomy and fibre orientation field of the left ventricle of the heart. *Biomedical Engineering Online, 12*(1), 54.

Purslow, P. P. (2008). The extracellular matrix of skeletal and cardiac muscle. In P. Fratzl (Ed.), *Collagen structure and mechanics* (pp. 325-358). New York, NY: Springer Science+Business Media.

Ramanathan, C., Jia, P., Ghanem, R., Ryu, K., & Rudy, Y. (2006). Activation and repolarization of the normal human heart under complete physiological conditions. *Proceedings of the National Academy of Sciences, 103*(16), 6309-6314.

Ramirez, M. T., Zhao, X.-L., Schulman, H., & Brown, J. H. (1997). The nuclear δB isoform of Ca2+/calmodulin-dependent protein kinase II regulates atrial natriuretic factor gene expression in ventricular myocytes. *Journal of Biological Chemistry, 272*(49), 31203-31208.

Ratcliffe, M. B. (2002). Non-ischemic infarct extension: a new type of infarct enlargement and a potential therapeutic target. *Journal of the American College of Cardiology, 40*(6), 1168-1171.

Rice, J. J., Wang, F., Bers, D. M., & De Tombe, P. P. (2008). Approximate model of cooperative activation and crossbridge cycling in cardiac muscle using ordinary differential equations. *Biophysical Journal, 95*(5), 2368-2390.

Ritter, O., Hack, S., Schuh, K., Röthlein, N., Perrot, A., Osterziel, K. J., . . . Neyses, L. (2002). Calcineurin in human heart hypertrophy. *Circulation, 105*(19), 2265-2269.

Robinson, T. F., Geraci, M. A., Sonnenblick, E. H., & Factor, S. M. (1988). Coiled perimysial fibers of papillary muscle in rat heart: morphology, distribution, and changes in configuration. *Circulation Research, 63*(3), 577-592.

Roth, B. J. (1988). The electrical potential produced by a strand of cardiac muscle: a bidomain analysis. *Annals of Biomedical Engineering, 16*(6), 609-637.

Sabbah, H. N., Sharov, V. G., Lesch, M., & Goldstein, S. (1995). Progression of heart failure: a role for interstitial fibrosis. *Molecular and Cellular Biochemistry, 147*(1), 29-34.

Sadoshima, J., & Izumo, S. (1997). The cellular and molecular response of cardiac myocytes to mechanical stress. *Annual Review of Physiology, 59*(1), 551-571.

Sakai, K., Watanabe, K., & Millard, R. W. (1985). Defining the mechanical border zone: a study in the pig heart. *American Journal of Physiology-Heart and Circulatory Physiology, 249*(1), H88-H94.

Schlosser, T., Pagonidis, K., Herborn, C. U., Hunold, P., Waltering, K.-U., Lauenstein, T. C., & Barkhausen, J. (2005). Assessment of left ventricular parameters using 16-MDCT and new software for endocardial and epicardial border delineation. *American Journal of Roentgenology, 184*(3), 765-773.

Schuster, E. H., & Bulkley, B. H. (1979). Expansion of transmural myocardial infarction: a pathophysiologic factor in cardiac rupture. *Circulation, 60*(7), 1532-1538.

Schwarz, E. R., Speakman, M. T., & Kloner, R. A. (2000). A new model of ventricular plication: a suturing technique to decrease left ventricular dimensions, improve contractility, and attenuate ventricular remodeling after myocardial infarction in the rat heart. *Journal of Cardiovascular Pharmacology and Therapeutics, 5*(1), 41-49.

Sermesant, M., Chabiniok, R., Chinchapatnam, P., Mansi, T., Billet, F., Moireau, P., . . . Rhode, K. (2012). Patient-specific electromechanical models of the heart for the prediction of pacing acute effects in CRT: a preliminary clinical validation. *Medical Image Analysis, 16*(1), 201-215.

Serneri, G. G. N., Modesti, P. A., Boddi, M., Cecioni, I., Paniccia, R., Coppo, M., . . . Papa, L. (1999). Cardiac growth factors in human hypertrophy: relations with myocardial contractility and wall stress. *Circulation Research, 85*(1), 57-67.

Shannon, T. R., Ginsburg, K. S., & Bers, D. M. (2000). Potentiation of fractional sarcoplasmic reticulum calcium release by total and free intra-sarcoplasmic reticulum calcium concentration. *Biophysical Journal, 78*(1), 334-343.

Shimkunas, R., Zhang, Z., Wenk, J. F., Soleimani, M., Khazalpour, M., Acevedo-Bolton, G., . . . Wallace, A. W. (2013). Left ventricular myocardial contractility is depressed in the borderzone after posterolateral myocardial infarction. *The Annals of Thoracic Surgery, 95*(5), 1619-1625.

Shinde, A. V., & Frangogiannis, N. G. (2014). Fibroblasts in myocardial infarction: a role in inflammation and repair. *Journal of Molecular and Cellular Cardiology, 70*, 74-82.

Shinde, A. V., Humeres, C., & Frangogiannis, N. G. (2017). The role of α-smooth muscle actin in fibroblast-mediated matrix contraction and remodeling. *Biochimica et Biophysica Acta (BBA)-Molecular Basis of Disease, 1863*(1), 298-309.

Shiojima, I., Sato, K., Izumiya, Y., Schiekofer, S., Ito, M., Liao, R., . . . Walsh, K. (2005). Disruption of coordinated cardiac hypertrophy and angiogenesis contributes to the transition to heart failure. *The Journal of Clinical Investigation, 115*(8), 2108-2118.

Sipido, K. R., Callewaert, G., & Carmeliet, E. (1995). Inhibition and rapid recovery of Ca2+ current during Ca2+ release from sarcoplasmic reticulum in guinea pig ventricular myocytes. *Circulation Research, 76*(1), 102-109.

Sipido, K. R., Carmeliet, E., & Van de Werf, F. (1998). T‐type Ca2+ current as a trigger for Ca2+ release from the sarcoplasmic reticulum in guinea‐pig ventricular myocytes. *The Journal of Physiology, 508*(2), 439-451.

Sipido, K. R., Maes, M., & Van de Werf, F. (1997). Low efficiency of Ca2+ entry through the Na+-Ca2+ exchanger as trigger for Ca2+ release from the sarcoplasmic reticulum: a comparison between L-type Ca2+ current and reverse-mode Na+-Ca2+ exchange. *Circulation Research, 81*(6), 1034-1044.

Streeter, D. D., Spotnitz, H. M., Patel, D. P., Ross, J., & Sonnenblick, E. H. (1969). Fiber orientation in the canine left ventricle during diastole and systole. *Circulation Research, 24*(3), 339-347.

Sugden, P. H. (2001). Mechanotransduction in cardiomyocyte hypertrophy. *Circulation, 103*(10), 1375-1377.

Sun, K., Zhang, Z., Suzuki, T., Wenk, J. F., Stander, N., Einstein, D. R., . . . Ratcliffe, M. B. (2010). Dor procedure for dyskinetic anteroapical myocardial infarction fails to improve contractility in the border zone. *The Journal of Thoracic and Cardiovascular Surgery, 140*(1), 233-239.

Tang, D., Yang, C., Geva, T., Gaudette, G., & Pedro, J. (2011). Multi-physics MRI-based two-layer fluid–structure interaction anisotropic models of human right and left ventricles with different patch materials: cardiac function assessment and mechanical stress analysis. *Computers & Structures, 89*(11-12), 1059-1068.

Theroux, P., Ross, J., Franklin, D., Covell, J., Bloor, C., & Sasayama, S. (1977). Regional myocardial function and dimensions early and late after myocardial infarction in the unanesthetized dog. *Circulation Research, 40*(2), 158-165.

Tortora, G. J., & Derrickson, B. (2012). *The cardiovascular system: The heart* (13th ed.). United States of America: John Wiley & Sons.

Trayanova, N., Li, W., Eason, J., & Kohl, P. (2004). Effect of stretch-activated channels on defibrillation efficacy. *Heart Rhythm, 1*(1), 67-77.

Trayanova, N. A. (2011). Whole-heart modeling: applications to cardiac electrophysiology and electromechanics. *Circulation Research, 108*(1), 113-128.

Tyagi, S. C., Lewis, K., Pikes, D., Marcello, A., Mujumdar, V. S., Smiley, L. M., & Moore, C. K. (1998). Stretch‐induced membrane type matrix metalloproteinase and tissue plasminogen activator in cardiac fibroblast cells. *Journal of Cellular Physiology, 176*(2), 374-382.

Usyk, T., Mazhari, R., & McCulloch, A. (2000). Effect of laminar orthotropic myofiber architecture on regional stress and strain in the canine left ventricle. *Journal of Elasticity and the Physical Science of Solids, 61*(1-3), 143-164.

Walker, J. C., Ratcliffe, M. B., Zhang, P., Wallace, A. W., Fata, B., Hsu, E. W., . . . Guccione, J. M. (2005). MRI-based finite-element analysis of left ventricular aneurysm. *American Journal of Physiology-Heart and Circulatory Physiology, 289*(2), H692-H700.

Walker, J. C., Ratcliffe, M. B., Zhang, P., Wallace, A. W., Hsu, E. W., Saloner, D. A., & Guccione, J. M. (2008). Magnetic resonance imaging-based finite element stress analysis after linear repair of left ventricular aneurysm. *The Journal of Thoracic and Cardiovascular Surgery, 135*(5), 1094-1102.

Wall, S. T., Guccione, J. M., Ratcliffe, M. B., & Sundnes, J. S. (2011). Electromechanical feedback with reduced cellular connectivity alters electrical activity in an infarct injured left ventricle: a finite element model study. *American Journal of Physiology-Heart and Circulatory Physiology, 302*(1), H206-H214.

Wang, J., Khoury, D. S., Yue, Y., Torre-Amione, G., & Nagueh, S. F. (2008). Preserved left ventricular twist and circumferential deformation, but depressed longitudinal and radial deformation in patients with diastolic heart failure. *European Heart Journal, 29*(10), 1283-1289.

Wang, V. Y., Lam, H., Ennis, D. B., Cowan, B. R., Young, A. A., & Nash, M. P. (2009). Modelling passive diastolic mechanics with quantitative MRI of cardiac structure and function. *Medical Image Analysis, 13*(5), 773-784.

Watanabe, H., Sugano, T., Sugiura, S., & Hisada, T. (2004). Finite element analysis of ventricular wall motion and intra-ventricular blood flow in heart with myocardial infarction. *JSME International Journal Series C Mechanical Systems, Machine Elements and Manufacturing, 47*(4), 1019-1026.

Weber, K. T. (1997). Extracellular matrix remodeling in heart failure: a role for de novo angiotensin II generation. *Circulation, 96*(11), 4065-4082.

Weisman, H. F., Bush, D. E., Mannisi, J. A., Weisfeldt, M. L., & Healy, B. (1988). Cellular mechanisms of myocardial infarct expansion. *Circulation, 78*(1), 186-201.

Wenk, J. F., Eslami, P., Zhang, Z., Xu, C., Kuhl, E., Gorman III, J. H., . . . Guccione, J. M. (2011). A novel method for quantifying the in-vivo mechanical effect of material injected into a myocardial infarction. *The Annals of Thoracic Surgery, 92*(3), 935-941.

Wenk, J. F., Klepach, D., Lee, L. C., Zhang, Z., Ge, L., Tseng, E. E., . . . Gorman, R. C. (2012). First evidence of depressed contractility in the border zone of a human myocardial infarction. *The Annals of Thoracic Surgery, 93*(4), 1188-1193.

White, H. D., & Chew, D. P. (2008). Acute myocardial infarction. *The Lancet, 372*(9638), 570-584.

Whiteley, J. P. (2006). An efficient numerical technique for the solution of the monodomain and bidomain equations. *IEEE Transactions on Biomedical Engineering, 53*(11), 2139-2147.

Whittaker, P., Boughner, D. R., & Kloner, R. A. (1991). Role of collagen in acute myocardial infarct expansion. *Circulation, 84*(5), 2123-2134.

Wilkins, B. J., Dai, Y.-S., Bueno, O. F., Parsons, S. A., Xu, J., Plank, D. M., . . . Molkentin, J. D. (2004). Calcineurin/NFAT coupling participates in pathological, but not physiological, cardiac hypertrophy. *Circulation Research, 94*(1), 110-118.

Wu, E., Ortiz, J. T., Tejedor, P., Lee, D. C., Bucciarelli-Ducci, C., Kansal, P., . . . Klocke, F. J. (2008). Infarct size by contrast enhanced cardiac magnetic resonance is a stronger predictor of outcomes than left ventricular ejection fraction or end-systolic volume index: prospective cohort study. *Heart, 94*(6), 730-736.

Zhang, Z., Sun, K., Saloner, D., Wallace, A. W., Ge, L., Baker, A., . . . Ratcliffe, M. B. (2012). The benefit of enhanced contractility in the infarct borderzone: a virtual experiment. *Frontiers in Physiology, 3*(86), 1-6.

Zhang, Z., Tendulkar, A., Sun, K., Saloner, D. A., Wallace, A. W., Ge, L., . . . Ratcliffe, M. B. (2011). Comparison of the Young-Laplace law and finite element based calculation of ventricular wall stress: implications for postinfarct and surgical ventricular remodeling. *The Annals of Thoracic Surgery, 91*(1), 150-156.

Zhou, Z., & January, C. T. (1998). Both T-and L-type Ca2+ channels can contribute to excitation-contraction coupling in cardiac Purkinje cells. *Biophysical Journal, 74*(4), 1830-1839.

Zhu, H., Tannous, P., Johnstone, J. L., Kong, Y., Shelton, J. M., Richardson, J. A., . . . Hill, J. A. (2007). Cardiac autophagy is a maladaptive response to hemodynamic stress. *The Journal of Clinical Investigation, 117*(7), 1782-1793.

Zou, Y., Akazawa, H., Qin, Y., Sano, M., Takano, H., Minamino, T., . . . Kudoh, S. (2004). Mechanical stress activates angiotensin II type 1 receptor without the involvement of angiotensin II. *Nature Cell Biology, 6*(6), 499-506.

Zühlke, R. D., Pitt, G. S., Deisseroth, K., Tsien, R. W., & Reuter, H. (1999). Calmodulin supports both inactivation and facilitation of L-type calcium channels. *Nature, 399*(6732), 159-162.

LIST OF PUBLICATIONS AND PAPERS PRESENTED

Leong, C. N., Al Abed, A., Lim, E., Lovell, N. H., Marasco, S., Hashim, S. A., & Dokos, S. (2015). Electromechanics modeling of the effects of myocardial infarction on left ventricular function. In *Engineering in Medicine and Biology Society (EMBC), 2015 37th Annual International Conference of the IEEE* (pp. 5684-5687). IEEE.

Leong, C. N., Lim, E., Andriyana, A., Al Abed, A., Lovell, N. H., Hayward, C., . . . Dokos, S. (2017). The role of infarct transmural extent in infarct extension: A computational study. *International Journal for Numerical Methods in Biomedical Engineering, 33*(2), e02794.

Leong, C. N., Dokos, S., Andriyana, A., Liew, Y. M., Chan, B. T., Abdul Aziz, Y. F., . . . Lim, E. (2020). The role of end-diastolic myocardial fibre stretch on infarct extension. *International Journal for Numerical Methods in Biomedical Engineering, 36*(1), e3291.

Chan, B. T., Bakir, A. A., Al Abed, A., Dokos, S., Leong, C. N., Ooi, E. H., . . . Lim, E. (2019). Impact of myocardial infarction on intraventricular vortex and flow energetics assessed using computational simulations. *International Journal for Numerical Methods in Biomedical Engineering*, *35*(6), e3204.

Leong, C. O., Leong, C. N., Al Abed, A., Bakir, A. A., Liew, Y. M., Dokos, S. & Lim, E. (2019). Computational modelling of the effect of infarct stiffness on regional myocardial mechanics. In *Engineering in Medicine and Biology Society (EMBC), 2019 41st Annual International Conference of the IEEE* (pp. 6952-6955). IEEE.